

ON THE PHYSICS AND CHEMISTRY OF THE ICE SHELL
AND SUB-SURFACE OCEAN OF EUROPA

A DISSERTATION
SUBMITTED TO THE DEPARTMENT OF GEOLOGICAL &
ENVIRONMENTAL SCIENCES
AND THE COMMITTEE ON GRADUATE STUDIES
OF STANFORD UNIVERSITY
IN PARTIAL FULFILLMENT OF THE REQUIREMENTS
FOR THE DEGREE OF
DOCTOR OF PHILOSOPHY

Kevin Peter Hand
September 2007

UMI Number: 3281853

INFORMATION TO USERS

The quality of this reproduction is dependent upon the quality of the copy submitted. Broken or indistinct print, colored or poor quality illustrations and photographs, print bleed-through, substandard margins, and improper alignment can adversely affect reproduction.

In the unlikely event that the author did not send a complete manuscript and there are missing pages, these will be noted. Also, if unauthorized copyright material had to be removed, a note will indicate the deletion.

UMI[®]

UMI Microform 3281853

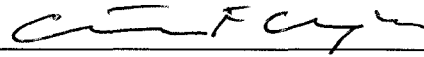
Copyright 2007 by ProQuest Information and Learning Company.

All rights reserved. This microform edition is protected against unauthorized copying under Title 17, United States Code.

ProQuest Information and Learning Company
300 North Zeeb Road
P.O. Box 1346
Ann Arbor, MI 48106-1346

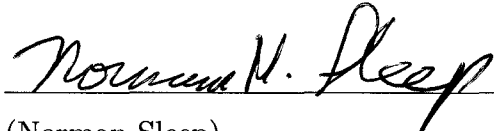
© Copyright by Kevin Peter Hand 2007
All Rights Reserved

I certify that I have read this dissertation and that, in my opinion, it is fully adequate in scope and quality as a dissertation for the degree of Doctor of Philosophy.



(Christopher F. Chyba) Principal Adviser

I certify that I have read this dissertation and that, in my opinion, it is fully adequate in scope and quality as a dissertation for the degree of Doctor of Philosophy.



(Norman Sleep)

I certify that I have read this dissertation and that, in my opinion, it is fully adequate in scope and quality as a dissertation for the degree of Doctor of Philosophy.



(Page C. Chamberlain)

Approved for the University Committee on Graduate Studies.

Preface

Europa, Jupiter's second large moon, almost certainly harbors a global sub-surface ocean containing 2–3 times the volume of all the liquid water on Earth. This ocean has likely persisted for the history of the solar system and as such it presents a compelling world in our search for life beyond Earth.

In the work presented here, results from the *Galileo* spacecraft magnetometer were used to investigate the sub-surface ocean chemistry and to derive relationships for salinity and ice layer thickness as a function of induced amplitude response. The best fit to the currently available data was found to be a 4 km ice shell and near-saturation salt concentrations in the ocean. These results hold for both the 3-layer spherical model (mantle-ocean-ice) and a 5-layer half-space model (adding an ionosphere and core). This is the first empirical constraint provided for the ice shell thickness independent of surface geology and thermal models. Interestingly, results for salt concentration imply that contemporary Europa could be suitable for halophilic organisms, but it may be too salty to allow for the origin of life as we know it.

Along with numerical modeling of the magnetic field interactions, a cryostat-coupled vacuum chamber with a high-energy electron gun was constructed to investigate magnetospheric interactions of the energetic particles with the surface ice of Europa and other icy satellites. The focus of this work was on electrons in the ~ 10 keV range and ices at temperatures of 80–120 K and pressures of 10^{-9} torr.

Laboratory investigations of H_2O_2 production and saturation levels were conducted for a range of temperatures, beam currents, and electron energies. Most significantly, experimental results were combined with a mathematical model for total H_2O_2 production and destruction over the range of incident electrons energies

($\sim 0.1 - 10^4$ keV). Integrating down through the surface ice we find that sub-surface H_2O_2 concentrations could be significantly larger than the observed surface abundance (several percent versus 0.13% by number relative to water).

Ice mixtures of H_2O and either CO_2 , propane, propene, butane, (1-,2-)butene, and ammonia were irradiated to examine the resulting organic chemistry and possible pre-biotic chemistry. Radiolysis with CO_2 yielded only CO and carbonic acid, with minor amounts of formaldehyde possibly present. No residues were left on the substrate after these experiments. During radiolysis of all hydrocarbon mixtures we observed the evolution of CO_2 and methane coupled with polymerization of the short-chain alkane or alkene. In the case of alkenes, the π bond was seen to rapidly disappear with increased dose. Refractory residues were left on the gold target mirrors and subsequent analysis indicated long aliphatic mixtures with alcohols, aldehydes, and esters. Adding ammonia to the initial ice mixture yields the cyanate ion, formamide, nitriles, and a tentative identification of racemic alanine.

Considering the problem of observed, condensed phase oxygen on the surface of Europa, we show that mixed clathrate hydrates of O_2 , CO_2 , and SO_2 could provide the necessary trapping mechanism for retaining O_2 . Calculations for oxidant delivery to the sub-surface ocean - accounting for consumption by geologically produced reductants - show that Europa's ocean is not likely to be oxidant limited. Were biology to be present, the chemical energy available through delivery of radiolytically produced surface oxidants could be great enough to support organisms comparable to terrestrial ocean macrofauna.

This issue of biomarkers on the surface of Europa was explored by irradiating *Bacillus pumilus* spores in the Europa simulation chamber. Results indicate that the amide bands associated with α -helical proteins and β -pleated sheets survive irradiation and could serve as possible spectroscopic biosignatures, allowing differentiation of abiotic organic chemistry from biologically driven chemistry. The phosphodiester bonds of nucleic acids may serve a similar purpose, but more work needs to be done with abiotic residues containing phosphorous. Finally, the technological challenges facing future spacecraft missions aiming to search for life on Europa are considered.

Acknowledgements

This thesis is dedicated to my parents, Peter and MaryBeth Hand, for their incredible ability to provide a childhood few in fences but full of nets. Thank you for carefully tending the seeds of curiosity, imagination, and wonder.

With them comes great gratitude to my siblings for all the support they have given me through the years. My older brother Sean is largely responsible for exposing me to science ideas and books at a young age, my sister Meaghan for making sure I didn't turn out to be too much of a 'dork', and my younger brother PJ for always being up for a bit of exploration. Together we shared a wonderful childhood.

The community in which I grew up, and the landscape in which I was raised, did much to form the person I have become. The clear night skies of Vermont romanced my imagination at a young age and drew my attention to the prospect of life elsewhere. Add in a few books by Carl Sagan, plus the *Cosmos* series, and I was hooked.

But such ideas would have been little fun had I not had a cadre of friends with which to explore them. To my lifelong friends from Manchester - and specifically to Stephen Drunsic, Stephen Williams, and Scott Faraci - I am forever indebted for memories of innumerable tree forts, toboggan rides, haunted houses, attempted bull fights, hallowed trees, camping trips, rocket launches gone awry, BB pellets to the head and elsewhere, the Bushwacker, and a four-foot-tall killer cole slaw riding a Big Wheels bike. It is a minor miracle that we made it past age ten. To Alicia Williams, who has been there since the start and who has always reeled in us derelict boys, a special thanks.

Good teachers cannot be praised enough. I was fortunate to have several that left an indelible positive mark on my developing young mind. Mrs. Dorfman deserves

thanks for motivating me and my fellow students to learn our multiplication tables by offering ice cream sundays in return; the prospect of free food continued to serve as a motivating element throughout graduate school. To Donna Williams, teacher, friend, and mother of one of my dearest friends - she knew how to guide, challenge, and instruct us without any condescension; we were not her students, we were her peers. She had an incredible capacity to instill in us the need to think critically about the world around us.

Mike Cepuran deserves special acknowledgment. Mike was my science teacher during junior high. He was a mythical figure to the grades below - a Paul Bunyan with a roaring laugh that shook the building - and his science room was full of fossils, old machines, and other scientific curiosities. To the young minds and fertile imaginations that walked into his classroom, it might as well have been a candy store and Mike the candyman. It was through Mike's inspiration that I spent hours wandering the forests learning the leaves of all the trees. It was through Mike's inspiration that we explored the tools and technology of the past to learn about the present and think about the future. It was in Mike's classroom where we gathered and witnessed the explosion of the *Challenger* space shuttle - a moment of great sadness, but one which Mike would use, not to criticize the risks, but instead to underscore the incredible complexity of human exploration and discovery. Exploration and discovery is difficult - it has never been easy, and it never will be. But the pursuit of knowledge, the urge to explore and discover, to push our imagination - despite the risks - is part of what makes us so uniquely human. Mike, you're the one that started weaving the web of connections in my brain, giving me a whole new window on the universe. I can't thank you enough for that.

In high school the science resources were limited, but one teacher knew, with incredible precision, how to tap into other dimensions of my imagination. Bob Leslie, english teacher extraordinaire, always enjoyed assigning me horrendously long and involved books, and when I would complain he would laugh his 'cat-ate-a-canary' laugh and mock me with a 'So it goes, so it goes' or 'Poot-tee-weet'. Without fail, I would read the book and my world would be transformed. Bob fostered in me not just a love of literature, but more importantly, an aesthetic for life - a simultaneous

appreciation for the absurd and a love of all that is truly beautiful. Thanks Bob, even with a PhD I can tell you that there is still no truth beyond magic.

To Bev, Bob's wonderful bride, a dear friend, and a great math teacher, thanks for being a bridge between the numbers and the letters in my life. To Betsy Hubner and Marilyn Hopkins, my art teachers, my creativity is still my keystone. To Bill Muench, though never a teacher of mine, you now carry the torch of inspiration!

Largely because of Bob's insistence, and because I knew it was Mike's alma mater, I found myself at Dartmouth for my undergraduate work. As a physics student, nothing was more valuable to me than the friendships developed through late-night sessions on problem sets, clear nights at the telescope, and flying-circus-of-physics lunches. Najam Haider and Iago Lowe, you'd both make my physics all-star team any day. Sure, we'd lose to Big Al and crew, but we'd have a good time anyway. Rick, you could coach us.

Outside the classroom, my friends in the outing club - with whom I endeavored in the exploration of this planet - share with me some of the most serene, joyous, and harrowing experiences of my life. To Tyler Stableford, Noah Goldberg, Tony Mamone, Scott Porter, Jim Hourdequin, Margaret Wheeler, and Brad Molyneaux, when the mothership comes, I'll be sure to save you guys a seat.

Along with my contemporaries at Dartmouth, one alumnus and I shared a very comforting bond. The physics department graciously granted me office space beneath the telescope on the hill. Not surprisingly, I found myself spending many late nights in my office, doing homework, writing my thesis, etc. I would often procrastinate by opening the dome to spy on Jupiter, Saturn, or Mars. I kept a sleeping bag in my office so that when the hour got too late I could curl up on a leafy patch between the trees. A statue of Robert Frost sitting on a stump was erected not far from where I used to sleep. He was a welcome friend during those cool, crisp sunrises. 'Morning Bob, what'ya working on today?' A good friend in spirit. Frost once said that he hoped he could 'lodge a few poems where they can't be gotten rid of easily'. As a scientist, I can only hope that I might do the same with a few ideas or discoveries.

Stirling Colgate was my introduction to the real world of science, and what an introduction it was. I interned with Stirling at Los Alamos and was exposed, for

the first time in my life, to all the ins and outs and ups and downs of science as a profession. He was a wonderful influence and his passion for science and big ideas proved to me that inspiration could outlive cynicism. Among many other things, he taught me to do order-of-magnitude calculations in my head, shared with me his amazing dynamo machine, and fostered in me a love of paleolithic art. Stirling's colleagues in the Theoretical Astrophysics group (TA-6) were equally welcoming and encouraging.

Academically, I owe much to Stanford University's Department of Geological and Environmental Sciences, and to the Mechanical Engineering Department. The ME218 course series was arguably the highest density learning experience of my academic career. An experience made all the better by the great camaraderie of my fellow students, in particular Alex Tung, Louis Burgos, Frederick Winston, and Sally Madsen. Oh, and The Roth and The Hag should be acknowledged for, among many other things, their commitment to quality burritos.

The geology department has been wonderfully nurturing. Without Elaine Andersen and Jenn Powell I would have fallen through the cracks on many, many occasions. They kept my head above water and threw me a life-preserver whenever I started to sink into the bureaucratic quicksand. Thanks for pulling me through, I feel as though you've both earned a PhD along with me.

Page Chamberlain, Dennis Bird, and Norm Sleep have all provided guidance and encouragement to the astronomer turned geologist. Dennis' geochemistry class is not to be missed. While Dennis 'burned chalk' my eyes were opened to the way in which a geologist views the world. Many of the concepts and laws I had learned as a physics student now moved into the complexity of the landscape around me.

Page encouraged me to teach with him and to learn by TA-ing his classes. Between the courses and the lab work I think I managed to stay just far enough ahead of the students to keep them satisfied that I knew what I was talking about. When in doubt, Page encouraged me to just tell them about Europa. Norm has been critical to my thinking as a planetary scientist and astrobiologist. He combines creativity and mathematical rigor unlike anyone I've ever met, and he always made time for me when I needed to think things through and hash out the details with him. To fellow

graduate students Carrie Whitehill and Fraser Thomson I owe a deep thanks for all the support - always there whenever I needed you.

The Princeton Department of Astrophysical Sciences has been a gracious host to me during my final year of graduate work. Specifically, David Spergel and Ed Turner have been very kind in welcoming me into the department and helping me navigate my way through the myriad changes in academic landscape. Chris and I went from a department in which we were the outliers because we were studying things larger than anyone else (*i.e.* planets instead of mountains and continents), to a department in which we were the outliers because we were study things smaller than anyone else (*i.e.* planets instead of galaxies and things of a cosmological scale). David and Ed helped dovetail me into the department and I thank them for their kindness and consideration. To Amaya Moro-Martin, Ali Nouri, Victoria Langland, and especially to Sylvia Smullin, thanks for the continuing encouragement, support, and friendship.

My early days at NASA and SETI were marked by a number of very positive influences. Foremost was Doug O’Handley, responsible for my introduction to NASA through the NASA Ames Astrobiology Academy. Over the years David Morrison, Jeff Cuzzi, Lynn Harper, Greg Schmidt, Shirley Berthold, Rita Briggs, Muriel Ross, Jeff Smith, Lynn Rothschild, and Shirley Burg have all pointed the way somehow. Max Bernstein, to borrow a phrase from my advisor’s acknowledgements, has also steered me, though it’s harder to say where. To Tori Hoehler, Matt Jardin, and Rob Morris, I am indebted for many insightful conversations and an equal number of good adventures.

The SETI Institute has long been a family to me, beginning with the time when I tracked down Jill Tarter at her office, after she gave an open invitation to me and my fellow interns at Ames. No one else wanted to come with me, so later that week I made the pilgrimage to Landings Drive alone. I was a bit shy and awestruck by the experience of finally seeing the Institute, and when I found Jill she was in sixth gear and looked like she hadn’t slept for days. She was very welcoming, but she apologized for not being able to show me around. Instead she brought me into the control room, sat me down, and told me to pipe in with questions whenever I got confused about what she and her colleague were doing. It was obvious that something

was happening and I definitely didn't want to interrupt. I sat there and watched as real, live waterfall plots came streaming in and appeared on the monitor. It turns out that I had appeared at Jill's door in the midst of the 1997 SOHO signal confusion. What timing! If only it had been the real thing. Since those days, Jill, Tom Pierson, Taylor Bucci, Cynthia Phillips, Pamela Harman, Laurance Doyle, and others at the institute have been wonderful colleagues and friends. To Andrew Howard, a great partner in alien endeavors, I look forward to hearing what those nano-second pulses have to say.

With regard to funding, I owe thanks to NASA's Graduate Student Research Fellowship program (*i.e.* the American tax payer), NASA's Exobiology Program (*i.e.* the American tax payer), Stanford's geology department, and to my advisor. I've been very fortunate to live in a country where I can make a living working on these profound questions and challenges, and I am very grateful for that opportunity.

I should also make a special note to the Agouron Institute and to the tutelage of Ken Neelson, Andy Knoll, and John Grotzinger. Through the generosity of Agouron I have had the chance to greatly advance my understanding of biology and in particular geobiology. Learning from the likes of Ken, Andy, and John - in the lab and in the field - was one of the highlights of my graduate experience.

My work in Africa with Cosmos Education has continually rejuvenated me. To my friends and colleagues both here and abroad, and to the students with whom we have worked, I am indebted for endless inspiration. O'brien Daka has been a special source of inspiration. His is the smile of Africa, full of hope and dreams. Someday, my friend, you will be a doctor. I hold that promise dear.

Bob Carlson has been an incredible mentor, colleague, and friend. The depth of knowledge that Bob harbors about the solar system and spectroscopy is truly astounding. Ask Bob a question on these topics and he'll glance upward, rub his thumb and fingers together, and a few moments later he'll have an answer for you that's almost certain to be correct to within a factor of a few. But expertise aside, Bob is an amazing human being. I often tell people that Bob is 60-something going on 30-something. We've hiked, camped, and climbed together in some of the most extraordinary places on the planet, and wherever we go, whatever we do, Bob always

has an excitement and optimism that is infectious. He has been critical to my research and to my perspective as a young scientist. Through his guidance, I feel that I have gained a sense of hope about what might be possible in my years to come with NASA.

Alas, I come to the advisor. The story of how I came to work with Chris is the story of a young man's quest for a mentor. I had been working at NASA Ames after completing my undergraduate work, and while I enjoyed parts of the work I found myself rather uninspired. After a year and a half I left Ames to go travel and to gain some perspective on life. Many stories could fill the pages between the time when I left Ames and the point at which I found myself standing outside on a castle balcony atop the 'Most Serene Republic of San Marino'. I was there for a small conference on SETI. Claudio Maccone had sent me an email about the meeting and I was hitch-hiking through Italy anyway, so the timing worked out. In any case, it was at that meeting that I had the good fortune of intersecting, right there on that cobblestone balcony, with one of NASA's grey-beards, Dr. Gerry Soffen. I had gotten to know Gerry through participation in the NASA Academy program (his brainchild) several years before. Gerry, by just about all measures, was an agent provocateur for the next generation of NASA. He had been in the thick of it during the heyday of Viking and he was sad to see NASA lose its way on scientific questions as compelling as the search for life elsewhere. To me, and I'm sure to many of my young NASA contemporaries, he was a Yoda.

So there I was, a weary traveller taking a break from listening to research on aliens, enjoying a cloudy red sunset over the hills of San Marino, when Gerry steps out for some fresh air. We get through the small talk pretty quickly and come to the issue of my future. Time for the Oracle to speak. Gerry waxes on about all the interesting things going on in astrobiology and I listen carefully as he describes the path ahead, and the life ahead, for each area of research. At some point I interrupt him and describe a bit more of what I'm looking for in life. How I want to be an apprentice, not a grad student. How I want to learn not just about a specific area of research, but also about how it all fits together with the past, the present, and the future of humanity's pursuit of knowledge. I ramble on about some of the experiences I've had, some of the people who have influenced me, and my general philosophy of

life, the universe, and everything.

Gerry grumbles and plays with his spiraling fu-manchu beard. I can see the gears of his brain churning behind his eyes. Finally, the answer pops out like coins from a one-arm jack hitting three roses: ‘You need to go work with Chris Chyba.’

Now up until that point I had known only the published name of Chris Chyba. I had never met him, nor had I heard him speak. But it clicked. Chris was working on things of great interest to me - the origin of life and Europa to be specific - but beyond that I knew, only very vaguely at that point, of his policy work and his more humanitarian interests. I knew a little bit of his reputation, not just as a good scientist, but also as a man of considerable wisdom for his age. Coupled with all of that, he had recently relocated to both Stanford and the SETI Institute.

As I continued my back-packing adventures, the idea of working with Chris germinated and when I returned to the US my friend Taylor Bucci at the SETI Institute arranged for a meeting. I didn’t know what to expect, but by some miracle I found myself working for Chris that summer, marking the beginning of our many years together as mentor and apprentice.

Chris has been a truly remarkable influence in my personal, professional, and intellectual development. Part of the reason I thought I might actually be useful as a scientist was because of my creativity, yet all too often I had met or worked with people who, while incredibly intelligent, lacked the spark of creativity needed to come up with new and interesting ideas. At times I found it frustrating. With Chris, that all changed. Our brainstorming sessions throughout the years have been nothing short of phenomenal. Sometimes enlightening, sometimes discouraging, sometimes just downright painful to the cortex - but always phenomenal. We’ve worked through so many things on the board, on paper, and through late-night emails. The sadness of moving on from my graduate work and Chris’ mentorship is largely placated by the fact we have years of back-logged ideas yet to work through.

Though my scientific and academic experiences with Chris were fantastic, I must say that the most enjoyable experience I’ve had with Chris is watching him become a father. Benjamin has continually brought sleepless, baggy, eyes to both Chris and Deborah, but with that has come a profound joy that trumps the weight of the world.

Given my experiences with both Chris and Deborah, it thrills me to see them bring a child into their life.

Chris once told me something that Carl had once said to him: that the more one learns about the world, the more one understands the incredible need to treat each other well - the need to be kind to our fellow inhabitants on this pale blue dot. I've had the incredible fortune, through parents, siblings, friends, teachers and mentors, to grow and benefit from such kindness. I can only hope that in the years to come I will have the chance to return such kindness, to pass on some wisdom, and to lodge a little hope, inspiration, and love where they can't be gotten rid of easily.

Contents

| | |
|---|------------|
| Preface | v |
| Acknowledgements | vii |
| 1 Introduction | 1 |
| 1.1 The stars of Medici | 1 |
| 1.2 Europa in the context of Astrobiology | 3 |
| 1.3 The Liquid Water Environment of Europa | 5 |
| 1.4 Energy Constraints on Habitability | 6 |
| 1.5 Steps toward Life and Life Detection | 8 |
| 2 Jovian magnetic field | 9 |
| 2.1 The Primary Field | 9 |
| 2.2 The Induced Magnetic Field of Europa | 11 |
| 2.2.1 Observational Constraints on Amplitude Response | 20 |
| 2.3 Energetic Particle Environment | 24 |
| 3 Empirical constraints on ocean salinity | 31 |
| 3.1 Conductivity vs Concentration | 32 |
| 3.2 Amplitude constraints | 36 |
| 3.2.1 Amplitude response $A \leq 0.9$ | 38 |
| 3.2.2 Amplitude response $A = 0.97 \pm 0.02$ | 39 |
| 3.3 Adding a conducting core, mantle, and ionosphere | 51 |
| 3.4 Implications for ice shell thickness | 55 |

| | | |
|----------|--|-----------|
| 3.5 | Density constraints | 58 |
| 3.6 | Implications for habitability | 60 |
| 3.7 | Conclusion | 62 |
| 4 | The case against MgSO₄ | 65 |
| 4.1 | Ocean Derived from Chondrites | 66 |
| 4.2 | Compositional Constraints | 67 |
| 4.3 | Steady-State Ocean Chemistry of Europa | 69 |
| 4.3.1 | Magnesium | 71 |
| 4.3.2 | Candidate Cations? | 85 |
| 4.3.3 | Abundant Anions? | 86 |
| 4.4 | Surface Observations | 87 |
| 4.5 | Consistency with Magnetometer Data | 88 |
| 4.6 | Conclusion | 88 |
| 5 | Simulation of electron irradiation | 91 |
| 5.1 | Laboratory studies of electron radiolysis | 91 |
| 5.2 | Experimental set-up | 92 |
| 5.2.1 | Hardware | 92 |
| 5.2.2 | Software | 95 |
| 6 | H₂O₂ production with temperature and depth | 99 |
| 6.1 | Introduction | 100 |
| 6.2 | Experiment Details | 103 |
| 6.3 | Results | 105 |
| 6.3.1 | Temperature dependence of H ₂ O ₂ production | 105 |
| 6.3.2 | H ₂ O ₂ production and electron beam current | 110 |
| 6.3.3 | H ₂ O ₂ production and electron energy | 113 |
| 6.4 | Discussion | 117 |
| 6.4.1 | H ₂ O ₂ production as a function of depth into ice | 117 |
| 6.5 | Conclusion | 124 |
| 6.5.1 | Implications for Icy Satellites | 124 |

| | | |
|----------|--|------------|
| 7 | Phase and stability of oxidants | 127 |
| 7.1 | Conditions for clathrate hydrate formation | 128 |
| 7.2 | Clathrate stability | 130 |
| 7.3 | Radiolytic production | 132 |
| 7.3.1 | Oxygen | 133 |
| 7.3.2 | Sulfur dioxide | 137 |
| 7.3.3 | Carbon dioxide | 138 |
| 7.3.4 | Combined oxidant abundance | 139 |
| 7.4 | T-P in ice shell | 139 |
| 7.5 | Clathrates of O ₂ , CO ₂ , and SO ₂ | 140 |
| 7.5.1 | Oxygen clathrates | 140 |
| 7.5.2 | Carbon dioxide clathrate | 147 |
| 7.5.3 | Sulfur dioxide clathrate | 148 |
| 7.5.4 | Mixed clathrate | 148 |
| 7.6 | Implications for the ice shell | 153 |
| 7.7 | Conclusion | 158 |
| 8 | Surface Chemistry | 161 |
| 8.1 | Oxidants | 162 |
| 8.2 | Reductants and Radiolysis of H ₂ O + CO ₂ | 167 |
| 8.3 | Abiotic sinks for surface oxidants | 174 |
| 8.4 | Timescales for Delivery | 176 |
| 8.4.1 | Thin Shells | 177 |
| 8.4.2 | Thick Shells | 179 |
| 8.5 | Conclusion | 183 |
| 9 | Radiolysis of H₂O + Hydrocarbons | 187 |
| 9.1 | In-situ analysis of radiolytic evolution | 190 |
| 9.1.1 | Propane vs. Propene | 190 |
| 9.1.2 | Four Carbon Compounds | 202 |
| 9.2 | Hydrocarbon residue analysis | 210 |
| 9.3 | Conclusion | 223 |

| | |
|---|------------|
| 10 Radiolysis of NH₃-rich ices | 229 |
| 10.1 In-situ analysis of radiolytic evolution | 229 |
| 10.2 Residue analysis | 239 |
| 10.3 Conclusion | 244 |
| 11 Biomarkers on Europa | 247 |
| 11.1 Irradiation of <i>Bacillus pumilus</i> spores | 248 |
| 11.2 Implications for the search for life on Europa | 264 |

List of Tables

| | | |
|-----|---|-----|
| 2.1 | Observational Constraints on Amplitude Response | 21 |
| 3.1 | Europa's induced amplitude response | 43 |
| 3.2 | Density constraints on salt concentration | 59 |
| 4.1 | The chemistry of Europa's ocean | 67 |
| 4.2 | Solar elemental abundance ratios | 69 |
| 4.3 | Hydrothermal fluxes and magnesium sources and sinks | 83 |
| 6.1 | H ₂ O ₂ G-values and cross-sections | 110 |
| 7.1 | Properties of Clathrates and Ice | 154 |
| 8.1 | Spectral lines for single-carbon compounds in ice | 171 |
| 8.2 | Timescales for various processes on Europa | 177 |
| 9.1 | Interatomic bonds and associated parameters for C, H, and O | 200 |
| 9.2 | Hydrocarbon irradiation table | 223 |
| 9.3 | Hydrocarbon irradiation table (cont.) | 224 |

List of Figures

| | | |
|-----|--|----|
| 1.1 | The Stars of Medici | 2 |
| 1.2 | Habitability of Europa | 4 |
| 2.1 | Jovian magnetic field configuration | 11 |
| 2.2 | Jovian magnetic field and Europa | 13 |
| 2.3 | Energy flux on Europa | 25 |
| 2.4 | Ranges of Energetic Particles | 27 |
| 2.5 | Ranges for Energetic Electrons | 29 |
| 2.6 | Surface radiation on Europa | 30 |
| 3.1 | Specific conductivity of an aqueous solution as a function of sea salt or MgSO ₄ concentration | 35 |
| 3.2 | Ocean depth-salt concentration relationship for an induced magnetic field amplitude of $A = 0.7$ | 40 |
| 3.3 | Ocean depth-salt concentration relationship for an induced magnetic field amplitude of $A = 0.8$ | 41 |
| 3.4 | Ocean depth-salt concentration relationship for an induced magnetic field amplitude of $A = 0.9$ | 42 |
| 3.5 | Amplitude, A , as a function of conductivity, ocean thickness, and ice shell thickness | 47 |
| 3.6 | Amplitude, A , for a five-layer half-space model | 48 |
| 3.7 | Contours of conductivity as a function of amplitude and ocean thick- ness for a 10 km ice shell | 49 |

| | | |
|------|--|-----|
| 3.8 | Contours of conductivity as a function of amplitude and ocean thickness for a 30 km ice shell | 50 |
| 3.9 | Influence of a conducting core and mantle on amplitude | 53 |
| 3.10 | Influence of an ionosphere on amplitude | 56 |
| 3.11 | Comparison of amplitudes, A, for models with and without conducting ionosphere | 57 |
| 4.1 | Serpentinization and Mg ²⁺ concentration in solution | 76 |
| 4.2 | Mg ²⁺ concentration in seawater+rock experiments | 79 |
| 4.3 | Mg ²⁺ activity as a function of T and P | 81 |
| 4.4 | MgSO ₄ in ocean vs. vent water flux | 84 |
| 4.5 | Conductivity vs. H ₂ SO ₄ Concentration | 89 |
| 5.1 | Laboratory set-up: Vacuum chamber with gas manifold | 94 |
| 5.2 | Laboratory set-up: Chamber shown along with rack-mounted computer and controllers | 96 |
| 5.3 | Cross-sectional diagram of the chamber set-up | 97 |
| 6.1 | O ₂ production pathways | 100 |
| 6.2 | Stopping power of energetic particles | 102 |
| 6.3 | The 2850 cm ⁻¹ band of H ₂ O ₂ | 104 |
| 6.4 | Hydrogen peroxide production as a function of temperature | 106 |
| 6.5 | H ₂ O ₂ G-values at different temperatures | 107 |
| 6.6 | Comparison of experimental results and published H ₂ O ₂ G-values | 109 |
| 6.7 | Production of H ₂ O ₂ as a function of electron beam current | 111 |
| 6.8 | H ₂ O ₂ saturation for several different values of electron beam current | 112 |
| 6.9 | Hydrogen peroxide production as a function of incident electron energy | 113 |
| 6.10 | H ₂ O ₂ G-values as a function of initial electron energy | 114 |
| 6.11 | $\Gamma(E_0)$ vs E_0 | 115 |
| 6.12 | Diagram of electron penetration into surface ice on Europa | 118 |
| 6.13 | Volume production, Q(x) from 1-100 μm into the ice | 120 |
| 6.14 | Volume destruction, L(x) from 1-100 μm into the ice | 122 |

| | | |
|------|---|-----|
| 6.15 | Steady-state H ₂ O ₂ concentrations from 1-100 μm into the ice | 123 |
| 7.1 | Clathrate cages of SI and SII clathrates | 129 |
| 7.2 | Radiolytic production of O ₂ | 134 |
| 7.3 | Dissociation pressure curves for O ₂ , CO ₂ , and SO ₂ | 142 |
| 7.4 | Mixed hydrate dissociation pressure curve for O ₂ , CO ₂ , and SO ₂ | 144 |
| 7.5 | Mixed hydrate dissociation pressure curve (10 km ice) | 145 |
| 7.6 | Mixed hydrate dissociation pressure curve (30 km ice) | 146 |
| 8.1 | Chemical map of Europa's surface | 162 |
| 8.2 | Moles per year of compounds vs. delivery period | 165 |
| 8.3 | Oxygen delivery to the ocean, no sinks | 166 |
| 8.4 | Oxidation states of carbon and sulfur compounds | 168 |
| 8.5 | Spectra of H ₂ O+CO ₂ ice irradiation | 169 |
| 8.6 | Production of H ₂ CO ₃ and CO | 172 |
| 8.7 | Oxygen delivery to ocean, with sinks | 185 |
| 9.1 | Irradiated alkanes and alkenes | 188 |
| 9.2 | Reference spectra for carbon compounds in ice | 189 |
| 9.3 | Propane irradiation sequence (500-4000 cm ⁻¹) | 191 |
| 9.4 | H ₂ O+C ₃ H ₈ : Integrated bands vs. Dose | 193 |
| 9.5 | H ₂ O+Propene irradiation sequence (500-4000 cm ⁻¹) | 194 |
| 9.6 | H ₂ O+Propene irradiation sequence (2500-3900 cm ⁻¹) | 195 |
| 9.7 | H ₂ O+Propene irradiation sequence (600-1800 cm ⁻¹) | 196 |
| 9.8 | H ₂ O+Propene: Integrated bands vs. Dose | 198 |
| 9.9 | Comparison of H ₂ O+C ₃ H ₈ and H ₂ O+C ₃ H ₆ ice irradiation | 199 |
| 9.10 | Comparison of H ₂ O+C ₃ H ₈ and H ₂ O+C ₃ H ₆ (2800-3050 cm ⁻¹) | 200 |
| 9.11 | Comparison of H ₂ O+C ₃ H ₈ and H ₂ O+C ₃ H ₆ (1000-1700 cm ⁻¹) | 201 |
| 9.12 | Irradiation of H ₂ O + Butane (500-4000 cm ⁻¹) | 203 |
| 9.13 | Irradiation of H ₂ O + Isobutane (500-4000 cm ⁻¹) | 204 |
| 9.14 | Irradiation of H ₂ O + Isobutane (2600-4000 cm ⁻¹) | 204 |
| 9.15 | Irradiation of H ₂ O + Isobutane (500-1800 cm ⁻¹) | 205 |

| | |
|---|-----|
| 9.16 Irradiation of H ₂ O + 1-Butene (500-4000 cm ⁻¹) | 206 |
| 9.17 Irradiation of H ₂ O + 1-Butene film (2700-3600 cm ⁻¹) | 207 |
| 9.18 Irradiation of H ₂ O + 1-Butene film (600-1700 cm ⁻¹) | 208 |
| 9.19 H ₂ O + 1-Butene: Integrated bands vs. Dose | 209 |
| 9.20 RGA results for H ₂ O + Isobutane, m/z: 0-100 | 211 |
| 9.21 RGA results for H ₂ O + Isobutane, m/z: 50-100 | 212 |
| 9.22 RGA results: Volatiles from warming H ₂ O + Propane ice | 214 |
| 9.23 Hydrocarbon residues | 215 |
| 9.24 Hydrocarbon residues (under microscope) | 216 |
| 9.25 FTIR of hydrocarbon residues from alkene irradiation | 217 |
| 9.26 FTIR of hydrocarbon residue from alkene irradiation | 218 |
| 9.27 MALDI residue analysis | 219 |
| 9.28 MALDI spectrum of residue from irradiation of H ₂ O+Propane | 220 |
| 9.29 MALDI spectrum of H ₂ O+ 1-Butene residue | 221 |
| 9.30 MALDI spectrum of H ₂ O + Propene residue | 222 |
| | |
| 10.1 Spectra of irradiated H ₂ O+CO ₂ +NH ₃ ice | 230 |
| 10.2 Spectra of irradiated H ₂ O+NH ₃ +C ₃ H ₈ ice | 231 |
| 10.3 Spectra of irradiated H ₂ O+NH ₃ +C ₃ H ₆ ice | 232 |
| 10.4 Spectra of irradiated H ₂ O+NH ₃ +C ₃ H ₆ ice, (2700-3200 cm ⁻¹) | 233 |
| 10.5 Spectra of irradiated H ₂ O+NH ₃ +C ₃ H ₆ ice, (600-2200 cm ⁻¹) | 234 |
| 10.6 Integrated bands vs. Dose for H ₂ O+NH ₃ +C ₃ H ₈ ice film | 235 |
| 10.7 H ₂ O+NH ₃ +C ₃ H ₆ , integrated RGA | 237 |
| 10.8 H ₂ O+NH ₃ +C ₃ H ₆ , integrated RGA (zoom) | 238 |
| 10.9 H ₂ O+NH ₃ +C ₃ H ₈ ice residue analysis, FTIR | 240 |
| 10.10 H ₂ O+NH ₃ +C ₃ H ₈ ice residue analysis, HPLC | 242 |
| | |
| 11.1 Irradiation of <i>Bacillus pumilus</i> spores at 100 K (500-3600 cm ⁻¹) | 248 |
| 11.2 Irradiation of <i>Bacillus pumilus</i> spores at 100 K (2750-3100 cm ⁻¹) | 249 |
| 11.3 Irradiation of <i>Bacillus pumilus</i> spores at 100 K (700-1800 cm ⁻¹) | 250 |
| 11.4 RGA: <i>B. pumilus</i> during irradiation | 251 |
| 11.5 RGA: <i>B. pumilus</i> during 8 minute warming period | 253 |

| | |
|---|-----|
| 11.6 RGA: <i>B. pumilus</i> data integrated from 100-300 K | 254 |
| 11.7 FTIR: Spectrum of <i>B. pumilus</i> residue (600-3700 cm ⁻¹) | 255 |
| 11.8 FTIR: Spectrum of <i>B. pumilus</i> residue (800-1800 cm ⁻¹) | 257 |
| 11.9 MALDI: <i>B. pumilus</i> with no irradiation (m/z 0-2500) | 261 |
| 11.10 MALDI: <i>B. pumilus</i> with 20 keV electron irradiation (m/z 0-2500) . | 262 |
| 11.11 MALDI: <i>B. pumilus</i> with no irradiation (m/z 40-140) | 263 |
| 11.12 MALDI: <i>B. pumilus</i> post-irradiation (m/z 40-140) | 264 |

Chapter 1

Introduction

“...our own eyes show us four stars which wander around Jupiter as does the Moon around the Earth, while all together trace out a grand revolution about the Sun in the space of twelve years.” – Galileo Galilei, 1610

1.1 The stars of Medici

On January 7th, 1610, the Galilean satellites came into existence, at least as far as human awareness is concerned (Figure 1.1). For about a week they were thought to be stars. By that point, however, Galileo Galilei had collected enough data to convince himself that the small, curiously aligned points of light he was seeing were not just stars, they were planets. With even more data, he would reach the conclusion that he was indeed witnessing the orbit of four large moons around the planet Jupiter (Galileo and Drake, 1957).

This conclusion was perhaps one of the strongest nails in the coffin of the Aristotelian world view. Just a few decades later, Newton would famously stand on the shoulders of predecessors like Galileo and the Universe would never be the same. The laws of physics now permeated the Universe and over the course of the three centuries to follow humanity would come to discover that the principles of other sciences, like chemistry and geology, could also be applied to other worlds and wonders of the Universe. Of the major branches of science – and more to the point, of the major ways of

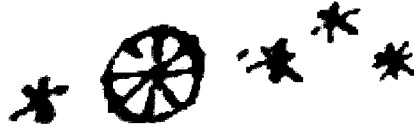


Figure 1.1: The Stars of Medici as depicted by Galileo in one of the first ‘images’ of Europa. The circle at center represents Jupiter and the four large moons are drawn as stars. This sketch, from one of Galileo’s early notebooks, is from Fahie (1903). No information is provided about which ‘star’ represents which moon and this configuration provides little in the way of clues that can be coupled with our contemporary knowledge of orbital dynamics (*e.g.* Laplace resonance). Nevertheless, Galileo did tend to draw the brightest moon with additional ‘points’ and Europa has the highest albedo of any of Jupiter’s moons ($\alpha_g = 0.68$, (Bagenal et al., 2004)). For this reason I would wager that Europa is on the far right, leading to a configuration that is likely (from L–R), Io, Ganymede, Callisto, and Europa, though Io and Ganymede could be interchanged.

understanding how matter and energy interact – biology remains the last to extend its reach beyond our terrestrial confines. Here we may find ourselves returning once again to the Stars of Medici, for it is here – as I argue in this thesis – within the world of Europa, that we may discover life beyond Earth.

Our knowledge of Europa is sufficiently advanced, and our understanding of biology is such, that we can now put forward the testable hypothesis that Europa is habitable. Future spacecraft missions will be capable of answering these questions. The discovery of a second origin of life on this world would close that critical gap in our understanding of the coupled physical, chemical, geological, and ultimately biological evolution of the Universe in which we live. With that single discovery, the entire Universe becomes habitable. Conversely, the failure to find life on Europa, or other seemingly habitable niches in the solar system, would call into question our understanding of the most fundamental links between chemical evolution and biological evolution. What seemed to be an inevitable progression here on Earth now takes on the crown of biological singularity. Both outcomes are equally profound.

To close this brief historical introduction on a perhaps mundane, but nevertheless

enlightening note, I return to the name¹. Though what were once the Medicean stars had – and I predict may continue to have – a profound effect on our understanding of the Universe in which we live, it is worth noting the rather academically astute motivation behind Galileo’s choice of name. There was no romantic vision of the Cosmos or glorified connection to history behind his decision. The fact of the matter is that his teaching load was interfering with his ability to do research and his salary could barely support his research. He needed time and money and for this reason he coined the name of ‘Medicean Stars’ to honor the Medici family and in particular, Cosimo II de’ Medici . Cosimo, a former student of Galileo’s, was now the Grand Duke of Tuscany and Galileo hoped this gesture would bear him the goodwill of the family. It did, and Galileo relocated from Padua to Florence with a significant pay raise (Geymonat, 1965). Alas, while the science may change and be revolutionized, the challenges of life in academia and doing research persist. If only getting a mission to Europa was as easy as naming the spacecraft after a politician.

1.2 Europa in the context of astrobiology

Jupiter’s second large moon, the ice-covered Europa, is subject to a number of interesting physical phenomena which, when combined, may lead to a habitable sub-surface environment. It is the topic of this dissertation to explore, both through numerical models and laboratory analysis, several of these phenomena and to assess the effects on the surface and sub-surface physics and chemistry.

As we approach the 400th anniversary of the discovery of Europa (Galileo and Drake, 1957), the evidence for a contemporary, global liquid water ocean beneath the ice of Europa has reached near incontrovertable levels. Multiple lines of empirical evidence (Kivelson et al., 1997; Khurana et al., 1998; Carr et al., 1998; Pappalardo et al., 1998) and numerical modeling (Cassen et al., 1979, 1980; Squyres et al., 1983) point to this conclusion. Meanwhile, alternative hypotheses have been proposed,

¹Note that the origin of the now common names for the individual moons – Io, Europa, Ganymede, and Callisto – is credited to Simon Marius, a Galileo contemporary who claimed to have priority in the discovery of the moons. His notes, however, show that at best he made one observation in the days after Galileo’s discovery.

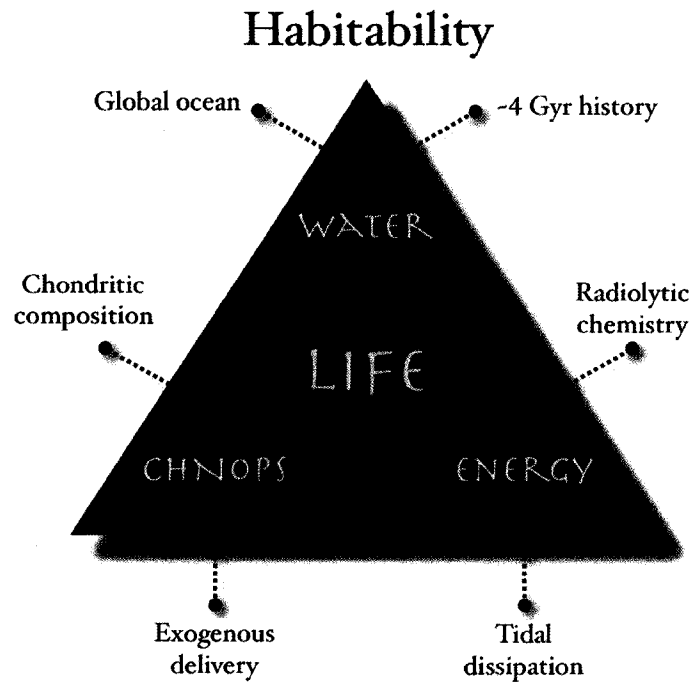


Figure 1.2: At present, our understanding of the conditions necessary for life can be distilled down to three broad requirements: 1) a sustained liquid water environment, 2) a suite of elements critical for building life (e.g. C, H, N, O, P, S), and 3) a source of energy that can be utilized by life. Here we show how these ‘pillars of habitability’ intersect with our current understanding of the conditions on, and within, Europa.

tested, and almost entirely rejected based on a failure to explain the observations (Pappalardo et al., 1999; Spohn and Schubert, 2003; Moore, 2006).

While the presence of liquid water may be a harbinger for habitability, it is by no means a sufficient condition for habitability. Our understanding of life here on Earth has taught us that at least two additional conditions must be met: 1) the environment must provide an inventory of so-called biogenic elements, (C, H, O, N, P, and S), and 2) the environment must exist in a state of energetic disequilibrium. Figure 1.2 provides a diagram of these three ‘pillars’ of habitability. Here we note that the word habitability necessitates further distinction. An environment can be said to be habitable if extant life could survive in that environment. Alternatively, an environment could be said to be habitable if life can originate and survive within

that environment. The first allows for contamination while the second requires an independent origin. From the standpoint of modern biology, we have a reasonable understanding of the first aspect of habitability (see *e.g.* Rothschild and Mancinelli (2001)), but a rather poorly constrained understanding of the second (see *e.g.* Nisbet and Sleep (2001); Chyba and McDonald (1995)).

As we extend our understanding of biology to worlds beyond the Earth, the prospect of discovering a second, independent origin for life sits as the Holy Grail for defining whether we live in a biological universe or one in which we - *i.e.* life on Earth - represent the cosmic anomaly. Several worlds, including Mars, Titan, and Enceladus, offer interesting environments in which to probe this question. But of the variety of worlds in our solar system, Europa represents the premier location to search for a second origin of life. It is host to the handful of broad requirements thought to be necessary for the emergence of life, and it is protected - both by distance and radiation - from the potentially contaminating influence of ejecta from Earth. Europa offers the unique opportunity to explore questions not just of life beyond Earth, but also those pertaining to the uniqueness of our terrestrial DNA, RNA, ATP and protein based biochemistry.

1.3 The Liquid Water Environment of Europa

The sub-surface ocean of Europa has likely been in existence throughout the history of the solar system and the water within that ocean has likely been in contact with chemically-rich rocks for much of that time. To assess the liquid water environment of contemporary Europa, in Chapters 3 and 4 we analyze the chemistry of Europa's ocean and explore the role of an active seafloor on the bulk ocean chemistry throughout the ocean's history. Also of potentially great significance to the chemistry of the ocean is the fact that the surface ice of Europa has been exposed the radiation environment of Jupiter's magnetic field and consequently made rich with oxidants. The question of delivery of surface oxidants to the ocean is addressed in Chapter 8.

Though our understanding of the limits of life - both in the context of origins and habitability - is incomplete, our results indicate that Europa could support life as we

know it. Furthermore, it is plausible to presume that Europa has been habitable for much of its history. As we will show in Chapter 3, the modern ocean of Europa may be too saline for the origin of life as we know it, but this does not preclude origins in a less saline micro-environment, either past or present.

1.4 Energy Constraints on Habitability

While the mantra of ‘follow the water’ has been the call of NASA’s search for life beyond Earth, this mantra is really a subset of the mantra ‘follow the energy’. Life as we know it - that is, all life on Earth - requires just two forms of energy: thermal energy for melting water, and chemical energy for maintaining and regulating processes considered essential for life. Organisms that directly absorb light do so as a means of producing utilizable chemical energy, stored in ATP.

The existence of liquid water on any world requires an investment of energy in our contemporary cold universe (2.725 ± 0.002 K) (Mather et al., 1999). Liquid water implies at least $6006.8 \text{ J mol}^{-1}$ of pure water in order to convert 273.16 K ice to liquid water (Haida et al., 1974). Traditional definitions of the habitable zone have, in part, been restricted to liquid water on the surface of Earth-like planets made possible in part by atmospheric heating from the parent star (Kasting et al., 1993). Such definitions do not adequately account for the energy sources that may be responsible for maintaining the majority of liquid water in our solar system, if not the universe: tidal and radiogenic energy.

Within the jovian system, generating thermal energy through tidal dissipation and radioactive decay (following initial accretional heating) accounts for what are likely our solar systems three largest oceans. At present, the evidence amassed from the *Galileo* mission leads to the conclusion that liquid water oceans within Europa, Ganymede, and Callisto may harbor a total volume of liquid water 30-35 times that of the Earth’s ocean (Spohn and Schubert, 2003).

Despite the fact that these moons likely contain large oceans (Zimmer et al., 2000) and bulk chemical compositions with a suite of biogenic elements (Kargel, 1991; Kargel et al., 2000), the availability of chemical energy may be a limiting factor

for habitability. Of the three worlds, the young surface age of Europa (30-70 Myr, Zahnle et al. (2003)) provides some indication that geological processes may be active on a global scale and could serve to maintain chemical disequilibrium in the ocean. Based on the argument that no reductant-oxidant chemical pairing could persist on Europa, some workers have argued that the ocean is thermodynamically dead (Gaidos et al., 1999). McCollom (1999), Zolotov and Shock (2003), and Zolotov and Shock (2004), however, have analyzed the geochemical possibilities for maintaining chemical disequilibrium in a hydrothermally active euroman ocean and find that energetic niches for microbial life could persist, provided hydrothermal activity is maintained through time. Methanogenesis and sulfate reduction are argued to be viable pathways for life, perhaps supporting 10^5 kg yr⁻¹ of biomass (McCollom, 1999). By comparison, terrestrial production is $\sim 10^{14}$ kg yr⁻¹ globally, with perhaps $\sim 10^{10}$ kg yr⁻¹ from hydrothermal vents (McCollom, 1999). Ultimately, however, these systems may be oxidant limited.

But the *Galileo* results (Carlson et al., 1999a) and more recent ground-based results (Spencer and Calvin, 2002), have made a strong case for an oxidant-laden surface on Europa. The predominant source of the oxidants is the radiolytic chemistry resulting from the bombardment of the surface ice by energetic electrons and ions entrained in the Jovian magnetic field (Johnson et al., 2004). Chyba (2000) and Chyba and Phillips (2001) have examined the potential role that surface radiolysis may play in creating an environment of chemical disequilibrium in the putative ocean of Europa. Though their results are contingent on an active surface that delivers surface material to the sub-surface, the conclusion is that radiolytically produced oxidants could serve to greatly enhance chemical disequilibrium within the ocean and significantly enhance the habitability of the ocean.

In Chapters 6, 7, 8 and 9 we examine, through laboratory experiments and numerical models, the role of high-energy electron radiolysis on the chemistry of the surface of Europa. We then consider the potential consequences of such chemistry on the sub-surface ocean. We show that the abundance of oxidants produced in the surface ice suggests that the availability of oxidants is unlikely to be a limiting factor for either abiotic or biological reactions. Delivery of radiolytic oxidants to the ocean

could mean the difference between an ocean that could be inhabited by single-celled microbes and an ocean that can support complex, multi-cellular life forms.

1.5 Steps toward Life and Life Detection

Robotic exploration in the coming decade must include Europa (NRC, 2003). Be it an orbiting spacecraft, a lander, or - hopefully - a combination of both, these missions will pose great challenges for the field of astrobiology. The near-term missions to Europa will not directly sample the ocean water (unless serendipity lends a hand) and thus our knowledge of any subsurface biochemistry will be limited by our ability to deconvolve the abiotic radiolytic surface chemistry from the biochemistry. Biological material exposed to the harsh radiation environment of the european surface will be modified and the resulting biosignature, if any, could be indistinguishable from abiotic organic chemistry driven by radiolysis on the surface of Europa.

In Chapter 8 we examine, through laboratory experiments, the abiotic radiolytic organic chemistry that could result from $\text{H}_2\text{O}+\text{CO}_2$ ices at european temperatures and pressures. We then move to experiments on more complex ices where the initial conditions include organics (Chapter 9). Specifically, we examine ices with short-chain alkanes (propane, butane, and isobutane) and alkenes (propene, 1-butene, and 2-butene). Ammonia is then added to the system (Chapter 10) and the resulting compounds are examined in the context of prebiotic chemistry.

Finally, in Chapter 11 we analyze bacterial spores irradiated under european conditions. The resulting chemistry is then compared to that of the abiotic organic chemistry and we assess the potential for distinguishing biomarkers. We conclude by exploring the difficulties, advantages, and disadvantages of searching for biosignatures on Europa from orbit and from a lander on the surface.

Chapter 2

The Jovian Magnetic Field and Interactions with Europa

The numerical and experimental investigations of Europa, as described in this thesis, depend on our present understanding of the Jovian magnetic field and the interactions of that field with both the surface and interior of Europa. Here I review these processes to provide background and motivation for the work that follows.

2.1 The Primary Field

A liquid metallic hydrogen dynamo within Jupiter is the likely source of the primary magnetic field of Jupiter. The region of the dynamo extends from $\sim 0.15R_J$ to $\sim 0.85R_J$ within Jupiter (where the mean $R_J = 69,911 \pm 6$ km), creating a magnetic field at the equatorial surface of 4.3×10^{-4} Tesla (4.3 Gauss).

The orientation of the field is tilted 9.4-9.6° from the rotation axis of Jupiter and is offset from the center of Jupiter by 0.12-0.13 R_J , depending on the model of choice (see, for instance the chapters and appendices within Bagenal et al. (2004)). Figure 2.1 illustrates the general configuration of the field with respect to a Jupiter-centered coordinate system. As Jupiter rotates on its axis every 9.92 hours the co-rotating field sweeps past all of the jovian satellites except for Metis and Adrastea, both of which have orbital periods of just over seven hours (Bagenal et al., 2004). Amalthea, the

largest of the four innermost satellites, orbits with a period (11.95h) slightly greater than that of an orbit synchronous with Jupiter's rotation. All of the other 63 known moons of Jupiter lag behind the co-rotating field as they orbit Jupiter.

Available spacecraft data (*Pioneer 10*, *Pioneer 11*, *Voyager 1*, *Voyager 2*, *Ulysses*, and *Galileo*) provide enough information to usefully describe the spatial distribution of the magnetic field resulting from the jovian dynamo. The field is described by a potential of the form (Khurana et al., 2004; Guillot et al., 2004),

$$\Phi = \sum_{i=1}^{\infty} \left(\frac{R_J}{r} \right)^{l+1} \sum_{m=0}^l P_l^m(\cos\theta) (g_l^m \cos(m\lambda) + h_l^m \sin(m\lambda)) \quad (2.1)$$

Here r is the distance from the center of Jupiter and θ and λ are the colatitude (*i.e.* θ at the poles of planet is 0°) and longitude of the moon's position. The associated Schmidt normalized Legendre polynomials of order m and degree l are represented by P_l^m , and the empirically determined Schmidt coefficients are represented by g_m^l and h_m^l . Physically, the term with $m = 0$ and $l = 1$ represents the axial dipole term of the magnetic field resulting from the dynamo. As the order and degree of the terms increases the ability to empirically resolve the coefficients based on the available data decreases. For this reason most models for Jupiter are constrained to $m = 3$ and $l = 3$. Solving for the magnetic field strength at Europa ($r = 9.38R_J$, $\theta = 90^\circ$, $\phi = 0$) yields $|\mathbf{B}| = 520$ nT (using Schmidt coefficients for the VIP 4 model as given in Connerney et al. (1998)).

The magnetosphere of Jupiter - defined by the extent of the region in which the jovian magnetic field dominates over the background solar wind - occupies a tear-dropped shaped region with a radius of some $\sim 45 - 100 R_J$ on the sub-solar side and a tail which extends for some $\sim 7000 R_J$, or ~ 3.3 AU (Khurana et al., 2004). During conjunction with Saturn, the tail region of the jovian magnetosphere can reach into the saturnian magnetosphere.

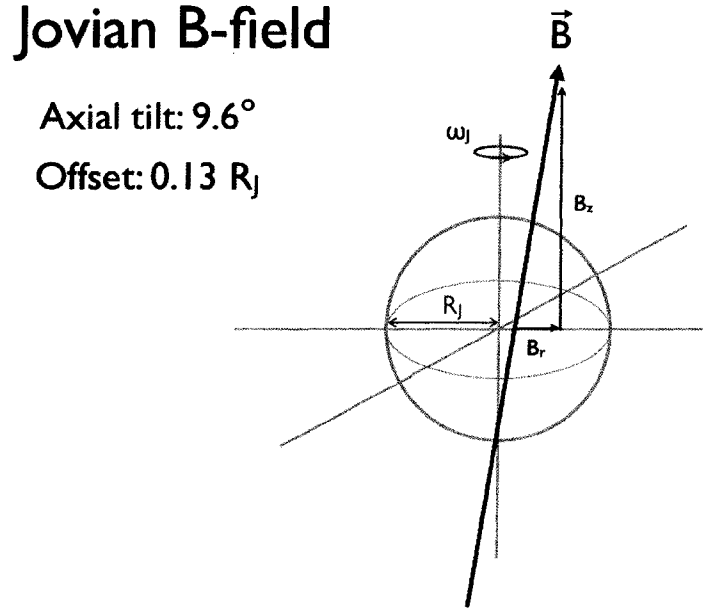


Figure 2.1: Jovian magnetic field configuration showing the primary dipole, the offset, and the angular frequency, ω_J .

2.2 The Induced Magnetic Field of Europa

The 3.55 day orbital period of Europa results in a synodic period of 11.2 hours for the rotation of the jovian magnetic field past Europa. As a result of the 9.6° tilt and $0.13 R_J$ offset of the magnetic field, Europa experiences a time-varying change in the component of the magnetic field aligned along the Jupiter-Europa axis (hereafter, the y-axis). Figure 2.2 shows the configuration of the satellite with respect to the jovian field.

During the 11 Europa fly-bys of the *Galileo* spacecraft, the onboard magnetometer returned data during 8 of the encounters and detected fluctuations in the surrounding magnetic field consistent with a time-varying response to the primary field of Jupiter (Khurana et al., 1998; Kivelson et al., 2000). This leads to the idea of an induced magnetic field, generated by a conducting layer internal to Europa, responding to the $\partial B/\partial t$ of the external primary field of Jupiter.

We can better understand this interaction by first considering Maxwell's equations, given here in the most general differential form,

$$\nabla \times \mathbf{H} = \mathbf{J} + \frac{\partial \mathbf{D}}{\partial t} \quad (2.2)$$

$$\nabla \times \mathbf{E} = -\frac{\partial \mathbf{B}}{\partial t} \quad (2.3)$$

$$\nabla \cdot \mathbf{B} = 0 \quad (2.4)$$

$$\nabla \cdot \mathbf{D} = q \quad (2.5)$$

where \mathbf{H} represents the magnetic field intensity (in units of A m^{-1}), \mathbf{B} is the magnetic induction (in T), \mathbf{E} is the electric field intensity (in V m^{-1}), and \mathbf{D} is the electric displacement (in C m^{-2}). The density of electric charges is represented by q and \mathbf{J} is the current density. In addition to Maxwell's equations, we need Ohm's Law,

$$\mathbf{J} = \sigma \mathbf{E} \quad (2.6)$$

For the case of induction in the near surface of Europa we are dealing with a non-magnetic material. Therefore the relation between the induction and field intensity simplifies to $\mathbf{B} = \mu_0 (\mathbf{H} + \mathbf{M}) = \mu_0 \mathbf{H}$. (Here \mathbf{M} is the magnetisation vector in A m^{-1} .) We are also considering a medium in which the current from conduction, \mathbf{J} , is much greater than the displacement current $\partial \mathbf{D} / \partial t$. Finally, we note that we are not going to consider currents due to the motion of the conductive media itself. Including this component adds a $\sigma (\mathbf{v} \times \mathbf{B})$ term to Ohm's Law and consequently a curl term to the diffusion equation. Ignoring this term amounts to assuming a small magnetic Reynold's number for the conducting media - a fair assumption for non-metallic conductors. Given the above constraints, we can rewrite Maxwell's equations as,

$$\nabla \times \mathbf{B} = \mu_0 \sigma \mathbf{E} \quad (2.7)$$

Jupiter-Europa B-field interactions

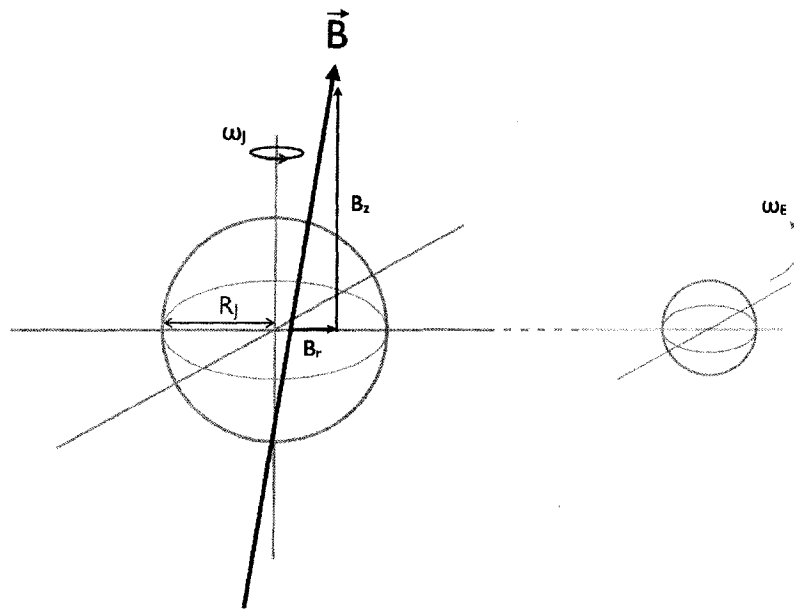


Figure 2.2: The jovian magnetic field and the relative motion of Jupiter, Europa and the flow of the magnetic field. Here we use the EPhiO Cartesian coordinate system to describe the relative motion of Europa, Jupiter, and the flow of the magnetic field. The x -axis is along the line of Europa's orbital motion (and the flow of the field past Europa), the y -axis is along the Jupiter-Europa line, and the z -axis is along the spin axis of Europa (Schilling et al., 2004).

$$\nabla \times \mathbf{E} = -\frac{\partial \mathbf{B}}{\partial t} \quad (2.8)$$

$$\nabla \cdot \mathbf{B} = 0 \quad (2.9)$$

$$\nabla \cdot \mathbf{E} = \frac{q}{\epsilon_0} \quad (2.10)$$

Following Parkinson (1983) we can now take the curl of 2.7, substitute 2.8 and use 2.9 to yield,

$$\nabla \times (\nabla \times \mathbf{B}) = -\mu_0 \sigma \frac{\partial \mathbf{B}}{\partial t}$$

$$\nabla \nabla \cdot \mathbf{B} - \nabla^2 \mathbf{B} = -\mu_0 \sigma \frac{\partial \mathbf{B}}{\partial t}$$

$$\nabla^2 \mathbf{B} = \mu_0 \sigma \frac{\partial \mathbf{B}}{\partial t} \quad (2.11)$$

The final expression, 2.11, is the diffusion equation for induction in a stationary conductor within a time-varying magnetic field. We can represent the simple case of a magnetic field varying as a single sine wave of frequency ω by $B(x, t) = B_0 e^{-i\omega t} e^{ikx}$. Equation 2.11 then becomes,

$$\nabla^2 \mathbf{B} = k^2 \mathbf{B} \quad (2.12)$$

where $k = \pm(1-i)\sqrt{\omega\mu_0\sigma/2} = \pm(1-i)s$. Physically, the parameter s is termed the skin depth and specifies the distance into the conductor at which the amplitude of the field is reduced by $1 - e^{-1}$. The real part of k must be chosen to be negative in order for the solution to be physically realistic; a positive real k would correspond to the field increasing exponentially with depth.

The field within a conducting sphere can be represented in spherical polar coordinates as the sum of forces parallel and forces perpendicular to the radial line of the

sphere. The field can then be written as

$$\mathbf{B} = \mathbf{B}_T + \mathbf{B}_P = \nabla \times T\mathbf{r} + \nabla \times (\nabla \times T\mathbf{r}) \quad (2.13)$$

The subscripts T and P denote the toroidal (perpendicular) and poloidal (parallel) fields. The expressions for the fields on the right-hand side of Eq. 2.13 come from the definition of the vector potential, \mathbf{A} , for the field,

$$\mathbf{B} = \nabla \times \mathbf{A} = \nabla \times (T\mathbf{r}) + \nabla \times (\nabla P \times \mathbf{r}) \quad (2.14)$$

where T and P are the scalar potentials for the toroidal and poloidal fields respectively. In spherical coordinates, \mathbf{B}_T and \mathbf{B}_P can then be expressed as,

$$\mathbf{B}_T = \nabla \times T\mathbf{r} = (r^2 \sin \theta)^{-1} \begin{vmatrix} \hat{\mathbf{r}} & \hat{\theta} & \hat{\phi} \\ \partial/\partial r & \partial/\partial \theta & \partial/\partial \phi \\ T\mathbf{r} & r^2 T & r^2 \sin(\theta) T \end{vmatrix}$$

$$\mathbf{B}_T = \frac{1}{\sin(\theta)} \frac{\partial T}{\partial \phi} \hat{\theta} - \frac{\partial T}{\partial \theta} \hat{\phi} \quad (2.15)$$

and similarly,

$$\begin{aligned} \mathbf{B}_P &= \nabla \times (\nabla \times P\mathbf{r}) \\ &= (r \sin \theta)^{-1} (\partial/\partial \theta (\sin \theta \partial P/\partial r) + (\sin \theta)^{-1} \partial^2 P/\partial \phi^2) \hat{\mathbf{r}} \\ &\quad + r^{-1} (\partial/\partial \theta (\partial(rP)/\partial r)) \hat{\theta} \\ &\quad + (r \sin \theta)^{-1} (\partial/\partial \phi) (\partial(rP)/\partial r) \hat{\phi} \\ &= (r^{-1} D^2 P) \hat{\mathbf{r}} + (r^{-1} \partial V/\partial \theta) \hat{\theta} + ((r \sin \theta)^{-1} \partial V/\partial \phi) \hat{\phi} \end{aligned} \quad (2.16)$$

where,

$$V = (\partial/\partial r) (rP) \quad (2.17)$$

and,

$$D^2 = (\sin \theta)^{-1}(\partial/\partial\theta)(\sin \theta \partial/\partial\theta) + (\sin^2\theta)^{-1}\partial^2/\partial\phi^2 \quad (2.18)$$

When acting on the surface spherical harmonics, $S_n(\theta, \phi)$, separation of variables in Laplace's equation shows that the operator D^2 yields,

$$D^2 S_n = -n(n+1) S_n \quad (2.19)$$

For the case of a uniform conducting sphere, the toroidal field is neither detectable outside of the sphere or capable of being induced by an external field. Considering the application to Europa, we are then concerned only with the poloidal field arising from the interior of Europa resulting from interaction with the external jovian field. We can take a jovian primary field potential (where $\mathbf{B}_J = -\nabla B_J$) of the form, $B_J = CF(r)S_n^m(\theta, \phi)e^{-i\omega t}$. The radial component is represented by the function F and the angular components by the spherical harmonics, S_n^m . Due to the symmetry of the problem, the orders m of the harmonics can be omitted. C is a complex constant. Within the conductor (*i.e.* Europa) we then find the expression for the behavior of the induced poloidal field as determined by the diffusion equation, 2.12, which governs the behavior of the primary field within the conductor. Following 2.16 and ignoring the time dependency then leads to,

$$B_{J_r} = Cr^{-1}n(n+1)F(r)S_n$$

$$B_{J_\theta} = Cr^{-1}d(rF)/dr \partial S_n/\partial\theta \quad (2.20)$$

$$B_{J_\phi} = C(r \sin \theta)^{-1}d(rF)/dr \partial S_n/\partial\phi$$

Using these expressions in the diffusion equation then leads to the following differential equation for F ,

$$\frac{d^2 F}{dr^2} + \frac{2}{r} \frac{dF}{dr} + \left(k^2 - \frac{n(n+1)}{r^2} \right) F = 0, \quad (2.21)$$

which, by comparison with Bessel's equation,

$$\frac{d^2 f}{dx^2} + \frac{1}{x} \frac{df}{dx} + f \left(1 - \frac{(n + \frac{1}{2})^2}{x^2} \right) = 0 \quad (2.22)$$

is known to have solutions of the form,

$$f(x) = J_{n+\frac{1}{2}}(x). \quad (2.23)$$

Here the $J_{n+\frac{1}{2}}(x)$ are, for example,

$$J_{\frac{1}{2}}(x) = \sqrt{\frac{2}{\pi x}} \sin x$$

$$J_{-\frac{1}{2}}(x) = \sqrt{\frac{2}{\pi x}} \cos x$$

$$J_{\frac{3}{2}}(x) = \sqrt{\frac{2}{\pi x}} \left(\frac{\sin x}{x} - \cos x \right)$$

$$J_{-\frac{3}{2}}(x) = \sqrt{\frac{2}{\pi x}} \left(-\frac{\cos x}{x} - \sin x \right) \quad (2.24)$$

Following Parkinson (1983), higher-orders and derivatives can be found with,

$$J_{m+1}(x) = \frac{2m}{x} J_m(x) - J_{m-1}(x) \quad (2.25)$$

and,

$$\frac{d}{dx} J_m(x) = J_{m-1}(x) - \frac{m}{x} J_m(x) = \frac{1}{2} (J_{m-1}(x) - J_{m+1}(x)) \quad (2.26)$$

respectively. The solutions for F in Eq. 2.21 are then,

$$F(r) = \frac{1}{\sqrt{rk}} J_{n+\frac{1}{2}}(rk) \quad (2.27)$$

and,

$$F(r) = \frac{1}{\sqrt{rk}} J_{-n-\frac{1}{2}}(rk). \quad (2.28)$$

The second solution, Eq. 2.28, goes to infinity for $r \rightarrow 0$ and is thus non-physical.

With the spherical harmonics, Eq. 2.27, and Eq.'s 2.20 we have now defined the behavior of the induced field within the conductor. External to the conducting sphere, *i.e.* at distance a where $a > r$, the radius of the sphere, the total potential can be described as (Parkinson, 1983),

$$B_{Total} = a \left(\frac{r}{a}\right)^n S_n(\theta, \phi) B_{Primary} + a \left(\frac{a}{r}\right)^{n+1} S_n(\theta, \phi) B_{Induced} \quad (2.29)$$

Taking the negative of the gradient for each component and solving for the combined field at the surface, $r = a$, then leads to,

$$B_r = ((n+1)B_{Induced} - nB_{Primary}) S_n(\theta, \phi),$$

$$B_\theta = -(B_{Induced} + B_{Primary}) \frac{\partial S_n}{\partial \theta}, \quad (2.30)$$

$$B_\phi = -(B_{Induced} + B_{Primary}) \frac{1}{\sin \theta} \frac{\partial S_n}{\partial \phi}.$$

At the interface between the solid surface (*i.e.* ice) and the surrounding space, the poloidal field must be continuous. Given this boundary condition, the individual components from equations 2.30 and 2.20 can then yield,

$$\frac{C}{a} n(n+1)F = (n+1)B_{Induced} - nB_{Primary} \quad (2.31)$$

$$\frac{C}{a} \frac{d(rF)}{dr} = -(B_{Induced} + B_{Primary}) \quad (2.32)$$

$$\frac{C}{a} \frac{d(rF)}{dr} = -(B_{Induced} + B_{Primary}) \quad (2.33)$$

where, by following Eq. 2.26 and using a change of variable, the expression $d(rF)/dr$ expands to,

$$\frac{d(rF)}{dr} = (rk)^{\frac{1}{2}} J_{n-\frac{1}{2}}(rk) - n(rk)^{-\frac{1}{2}} J_{n+\frac{1}{2}}(rk). \quad (2.34)$$

Next we solve Eqs. 2.31 and 2.32 for C/a and equate the results. Here we use J_+ and J_- to denote $J_{n+\frac{1}{2}}$ and $J_{n-\frac{1}{2}}$ respectively and we denote \sqrt{ak} by α . We also contract $B_{Primary}$ and $B_{Induced}$ to B_P and B_I respectively.

$$\frac{(n+1)B_I - nB_P}{\frac{n(n+1)}{\alpha} J_+} = \frac{-B_P - B_I}{(\alpha J_- - \frac{n}{\alpha} J_+)}, \quad (2.35)$$

Collecting B terms on the right-hand side, expanding the left-hand side, and multiplying the equation by $(n+1)$ yields,

$$\frac{\alpha^2 J_-}{n J_+} - 1 = \frac{-1 - \frac{B_I}{B_P}}{\frac{B_I}{B_P} - \frac{n}{n+1}}. \quad (2.36)$$

Bringing the 1 on the LHS to the RHS, simplifying the fraction and rearranging then leads to,

$$\frac{B_I}{B_P} = -\frac{nJ_+}{\alpha^2 J_-} - \frac{n^2 J_+}{(n+1)\alpha^2 J_-} + \frac{n}{n+1}. \quad (2.37)$$

Upon further simplification,

$$\frac{B_I}{B_P} = \frac{n\alpha^2 J_- - 2n^2 J_+ - nJ_+}{(n+1)\alpha^2 J_-} \quad (2.38)$$

$$\frac{B_I}{B_P} = \frac{n\alpha^2 J_- - (2n+1)nJ_+}{(n+1)\alpha^2 J_-} \quad (2.39)$$

I note here that Eq. (390) of Parkinson (1983) shows J_+ in the denominator and after several thorough reviews of my derivation, I believe that the Parkinson text contains a typo and the equation I derived is correct with J_- in the denominator.

Substituting a , k and the Bessel functions back into Eq. 2.39,

$$\frac{B_I}{B_P} = \frac{nakJ_{n-\frac{1}{2}}(ak) - (2n+1)nJ_{n+\frac{1}{2}}(ak)}{(n+1)akJ_{n-\frac{1}{2}}(ak)}. \quad (2.40)$$

Using Eq. 2.25 allows further simplification of the Bessel functions,

$$\frac{B_I}{B_P} = -\frac{nJ_{n+\frac{3}{2}}(ak)}{(n+1)J_{n-\frac{1}{2}}(ak)}. \quad (2.41)$$

The expression in Eq. 2.41 provides the ratio of the fields for induction in a uniform conducting sphere. This expression can be used to find $B_{Induced}$ and C , and using Eq.'s 2.30 and 2.20 the components of the combined magnetic field can be calculated. In Chapter 3 we use a similar expression, as derived by Zimmer et al. (2000), to describe a three-layer spherical model for Europa. The layers described are the ice shell, ocean, and mantle. Zimmer et al. (2000) set the conductivity of the ice and mantle to zero, thereby simplifying the solution. We build on their model and then employ a five-layer half space model to examine the added influence of a conducting core and a conducting ionosphere on the ratio of the induced field to the primary field.

2.2.1 Observational Constraints on Amplitude Response

Much of Chapter 3 depends on results from the *Galileo* magnetometer team's analysis of the magnetic field data around Europa. Here we review this work to provide a foundation for our subsequent analysis.

During most of *Galileo*'s orbit, the magnetometer recorded data at 24 s intervals, but during closest approaches this sampling rate was increased to 0.33 s (Kivelson et al., 1997). Close approaches were generally 20-30 minutes in length with minimum altitudes above Europa of ~ 200 -3500 km (Schilling et al., 2004). The early passes, and the early evidence for an induced magnetic field, were presented by Kivelson et al. (1997), Khurana et al. (1998), Kivelson et al. (1999), and Kivelson et al. (2000), but the work constraining the amplitude response is mostly found in the later works of Zimmer et al. (2000) and Schilling et al. (2004).

| Model | Summed <i>rmsw</i> | Condition number | g_1^0 (nT) | g_1^1 (nT) | h_1^1 (nT) | A |
|--------------------|-----------------------|---------------------|-----------------|-----------------|-----------------|-----------------|
| 1 Dip+UMF | 27 | 10.9 | 38 ± 5 | 68 ± 3 | 14 ± 3 | 0 |
| 2 Dip+Ind+UMF | 20 | 16.9 | 53 ± 3 | -1 ± 2 | 15 ± 2 | 1.10 ± 0.02 |
| 3 Dip+Quad+UMF | 21 | 20.2 | -17 ± 6 | 80 ± 3 | -1 ± 3 | 0 |
| 4 Dip+Quad+Ind+UMF | 17 | 24.5 | 31 ± 5 | 22 ± 3 | 7 ± 2 | 1.00 ± 0.03 |
| 5 Dip+AWM+Ind | 20 | 6.9 | 12 ± 3 | 20 ± 1 | 0 \pm | 0.96 ± 0.03 |
| 6 Dip+Quad+Ind+AWM | 16 | 10.2 | 42 ± 3 | 7 ± 1 | -14 ± 3 | 1.00 ± 0.03 |
| 7 Ind+AWM | 21 | 3.5 | 0 | 0 | 0 | 0.98 ± 0.01 |

Table 2.1: Results of the models considered by Schilling et al. (2004). Dip: Fixed dipole moment; Quad: Fixed quadrupole moment; UMF: Uniform magnetic field; Ind: Induced field; AWM: Alfven wing model. The *rms* values are weighted (hence *rmsw*) according to the maximum perturbation and thereby the altitude of closest approach. Condition numbers of ≤ 60 are desired for inversion of planetary fields. A value close to 1 indicates an accurate inversion.

The formalism followed by Zimmer et al. (2000) is the same as described in Section 2.2 and which is described in part in Chapter 3. For this reason we limit the discussion here to the Zimmer et al. (2000) conclusion that the amplitude of the induced field must fall between 0.7 and 1.0, and the phase lag of that response is close to zero. The model field was compared to the data but little to no analysis of the quality of the fit was provided. Aside from confirming the need for an internal near-surface conducting layer (*i.e.* salty ocean) as a mechanism for providing the observed changes in the magnetic field, the utility of the Zimmer et al. (2000) results was to set a lower limit on the inductive response.

Schilling et al. (2004) set out to quantify the internal dipole moment of Europa and in so doing they set a much tighter constraint on the inductive response. They concluded that the internal moment is probably zero, but if it does exist it is likely a dipole of magnitude of fewer than 25 nT. The amplitude of the inductive response was found to be 0.97 ± 0.02 . Table 2.1 provides information on each of the models considered by Schilling et al. (2004). Below we describe these models in detail.

The data used for the fit of the Schilling et al. (2004) models was selected based on proximity of the flyby (< 1800 km, in order to reduce S/N) and magnetospheric latitude (selecting for latitudes > 0 , in order to minimize perturbations from the

plasma sheet and pick-up ions). Though the E12 flyby had the closest approach (204.0 km), it was rejected since it passed by Europa at the same time as Europa was crossing the equator of the magnetosphere. The magnetospheric latitude of that flyby was 0.91° . The four flybys chosen by Schilling et al. (2004) were E4, E14, E19, and E26. The closest approach and magnetospheric latitude for each of these was 695.1 km at 6.54° , 1647.1 km at 9.15° , 1442.4 km at 4.83° , and 346.4 km at -9.51° , respectively.

For each of the passes, the data well prior to and well past closest approach were used to establish a background field and a polynomial fit was then used to extract the background field from the observed variation during close approach. The difference between the data and the fit, denoted $\delta\mathbf{B}^i$ where i represents one of the four passes, was then weighted according to the largest perturbation found in each pass. The weighting was inversely proportional to the magnitude of the perturbation and it was intended to prevent a single pass with a large variation from dominating the results. The weighting factor is given by (Schilling et al., 2004),

$$w_i = \frac{|\delta B_{max}^i|}{\sqrt{\frac{1}{4} \sum_i (\delta B_{max}^i)^2}}. \quad (2.42)$$

The diagonal matrix, \mathbf{W} , of the weights w_i^{-1} can then be combined with the data matrix, $\delta\mathbf{B}$, and a matrix \mathbf{A} of the spatial dependence of the data, to yield a matrix, \mathbf{x} , of the coefficients for the model field.

$$\mathbf{x} = (\mathbf{W}\mathbf{A}^T\mathbf{W}\mathbf{A})^{-1} \mathbf{W}\mathbf{A}^T\mathbf{W}\delta\mathbf{B} \quad (2.43)$$

where \mathbf{T} denotes the transpose of matrix \mathbf{A} . The coefficients and model were then checked against the data by calculating the *rms* deviation, again weighted against maximum perturbation to the field,

$$rmsw = \sqrt{\sum_{i,n} \left(\frac{\delta B_{data}^{in} - \delta B_{model}^{in}}{w_i^2} \right)^2 \frac{1}{4N}}. \quad (2.44)$$

Five different types of contributions to the field were considered and they were combined in a number of different permutations, all with the aim of finding the best fit to the available data. Along with dipole and quadrupole components, contributions from a uniform magnetic field (UMF), an induced magnetic field, and Alfvén wings (AWM) were examined. The UMF is allowed to vary from pass to pass and it is simply a way of accommodating the observed time varying signature. It has no physical basis other than serving as a first-order approximation to external effects such as plasma currents. The AWM accommodates for interactions between the plasma of the magnetosphere and the ionosphere of Europa. The model used by Schilling et al. (2004) is based on that of Khurana et al. (1997) and involves representing the currents as wires tracing out cylinders that intersect at Europa and extend along the positive x direction with angles of $\pm 20^\circ$.

The seven different combinations modeled by Schilling et al. (2004) are listed in Table 2.1 along with the $rmsw$ as per Eq. 2.44 and select coefficients from the model results. Also listed is the condition number of the matrix \mathbf{A} . This is the ratio of the largest to the smallest eigenvalues and if this ratio is close to one then the inversion of \mathbf{A} has yielded accurate results. Values ≤ 60 are desired for limited data of planetary fields.

The g_1^0 , g_1^1 , and h_1^1 coefficients listed in Table 2.1 correspond to the z , y , and x -components of the dipole moment. For the case of model 1, this results in a field with equatorial surface strength of 79 nT inclined 61° from the z -axis and inclined 12° from the y -axis in the direction of positive x . Similarly, model 5 yields an equatorial surface field magnitude of 23 nT, with the dipole tilted 59° from positive z along the positive y directions (*i.e.* toward Jupiter). In the results for model 2, Schilling et al. (2004) find $A = 1.1$ but they comment that this is ‘unphysically high unless the currents flow in an extended ionosphere’. They go on to comment that Zimmer et al. (2000) argue that this is not possible given the low conductivity of the ionosphere. Our analysis in Chapter 3 corroborates this conclusion.

Considering the fit results and the combination of the $rmsw$ and condition number parameters, Schilling et al. (2004) choose models 5 and 7 as their best modeling fits to the data. They conclude that the internal moment is very likely small and that

the AWM serves an important role in modeling the external field contribution. The dominant contribution, however, comes from the response of the induced field. The lowest possible value allowed by the Schilling et al. (2004) results is $A = 0.93$ and this comes from accounting for the uncertainty in the Dip+AWM+Ind field model. All other results indicate a value of A close to one.

The conclusion reached by Schilling et al. (2004), *i.e.* that $A = 0.97 \pm 0.02$, is a conclusion we will use to determine the implications of our modeling work in the following chapter. At present, the only work providing the necessary input for our models is the work of Zimmer et al. (2000) and Schilling et al. (2004). We are therefore limited to these published results but look forward to further analyses and refinement of the amplitude parameter.

2.3 The Energetic Particle Environment of the Inner Jovian Magnetosphere

While the numerical modeling work of this thesis depends largely on Maxwell's equations and the physics therein, the laboratory work described in this thesis requires an understanding of energetic particles contained within the field. As a result of being situated deep within the Jovian magnetosphere, the surface of Europa is exposed to high energy, charged particle irradiation. The incident particle flux of 7.9×10^{10} keV $\text{cm}^{-2} \text{s}^{-1}$ is dominated by electrons in the keV to MeV range (Cooper et al., 2001). Ions of H^+ , O^{n+} , and S^{n+} , account for approximately 21.5% of this energy. Photons add an additional 8×10^{12} keV $\text{cm}^{-2} \text{s}^{-1}$ to the surface radiation environment (4×10^{10} keV $\text{cm}^{-2} \text{s}^{-1}$ of which is from <2800 Å, the wavelength upper limit for the dissociation of water).

Largely due to variations in mass, charge, and velocity, the ions and electrons gyrate around the magnetic field lines with different respective radii (hereafter gyroradii). The ions, being heavier, have gyroradii comparable to the radius of Europa, whereas the near-massless electrons typically have gyroradii in the range of a few kilometers (Johnson et al., 2004). As a result, incident ions are, for the most part,

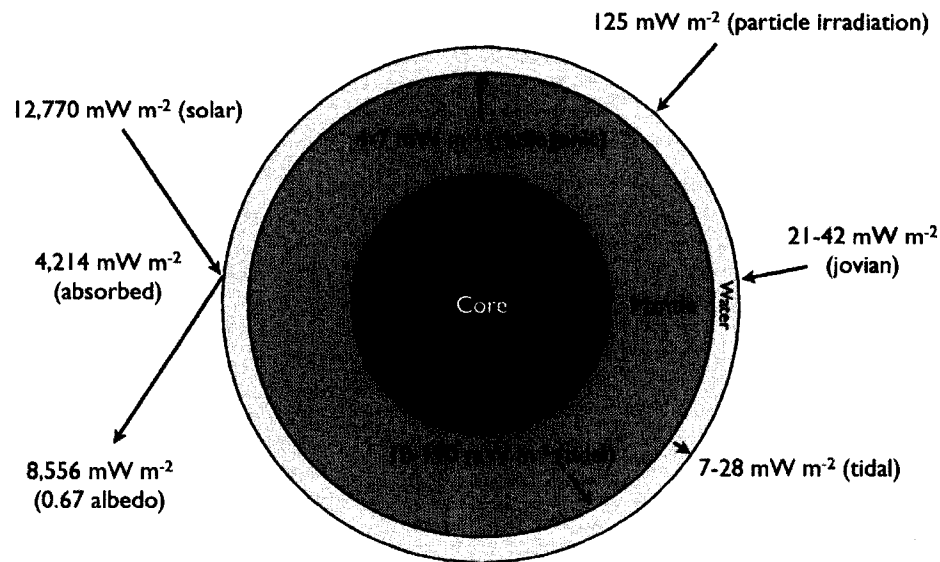


Figure 2.3: The energy budget of Europa. Sources include external (solar, jovian, particles) and internal (radiogenic, tidal). Europa's energetic particle flux is $\sim 0.037\%$ that of Earth's average incident solar flux. The solar flux is the flux on the moon's cross-section divided by the total surface area.

distributed globally whereas the bulk of the electrons are deposited on the trailing hemisphere of Europa as the Jovian magnetic field sweeps past Europa during its ~ 11 hour synodic rotation period (Cooper et al., 2001). It is on the trailing hemisphere where the large 'bull's-eye' of discolored, non-ice material is found, prompting some to suggest a strong connection between the discoloration and radiolysis resulting from electron bombardment (Johnson et al., 1998).

The total energetic flux resulting from incident ions, protons, and electrons, imparts an average of 125 mW m^{-2} to the surface of Europa (Cooper et al., 2001). By comparison, the average solar flux is 12.8 W m^{-2} , of which $\sim 60 \text{ mW m}^{-2}$ is due to UV-C (a small portion of which is capable of H_2O photolysis). An additional ~ 21 to

$\sim 42 \text{ mW m}^{-2}$ comes from Jupiter. (This is the combination of reflected and thermal radiation, with the upper limit being set by reflection from the full disk of Jupiter. Since Europa is tidally locked to Jupiter, the sub-jovian hemisphere is the primary beneficiary of this radiation.) By comparison, average insolation over the surface of the Earth is $\sim 340 \text{ W m}^{-2}$, with roughly 240 W m^{-2} being absorbed by the atmosphere or surface (Wielicki et al., 1995, 2005). Figure 2.3 shows a full accounting for all known energy sources on Europa.

The solar energy incident on Europa is ~ 100 times that delivered by charged particle irradiation, but most of the solar flux is reflected back to space (Europa's albedo is ~ 0.67). The remaining energy does not penetrate far into the ice and is rapidly reradiated as heat from the $\sim 70\text{--}130 \text{ K}$ surface (Spencer et al., 1999). Only shorter wavelength UV-C photons serve to effectively store energy in the ice by breaking and making new chemical bonds.

The population of charged particles, on the other hand, is dominated by energetic electrons that can penetrate deeper into the ice layer while exciting and dissociating water into reactive components (*e.g.* OH^- , H^+). Unlike the massive energetic ions and protons, the electrons are capable of penetrating several microns to several tens of centimeters below the surface. In addition, while protons and ions do not penetrate far into the ice, they create cascades of secondary electrons that can penetrate much deeper than the parent ion. Figure 2.4 shows data from the National Institute of Standards and Technology.

The mean projected range, \overline{R}_p , for energetic electrons with average initial energy, E_A , entering the ice normal to the surface is (Johnson, 1990),

$$\overline{R}_p(E_A) = [n_{Ice}\sigma]^{-1} + \int \frac{d\sigma}{\sigma} \overline{R}_p(E_A - \Delta E) \cos\theta(\Delta E). \quad (2.45)$$

The particle cross-section and differential cross-section are given by σ and $d\sigma$ respectively and the number density for ice is given by n_{Ice} . Here the first term represents the mean-free-path until the first collision and the integral represents the average distance traveled for all possible pathways through the ice after the first collision, with an energy ΔE lost with a probability $d\sigma/\sigma$ for each collision. If there are zero

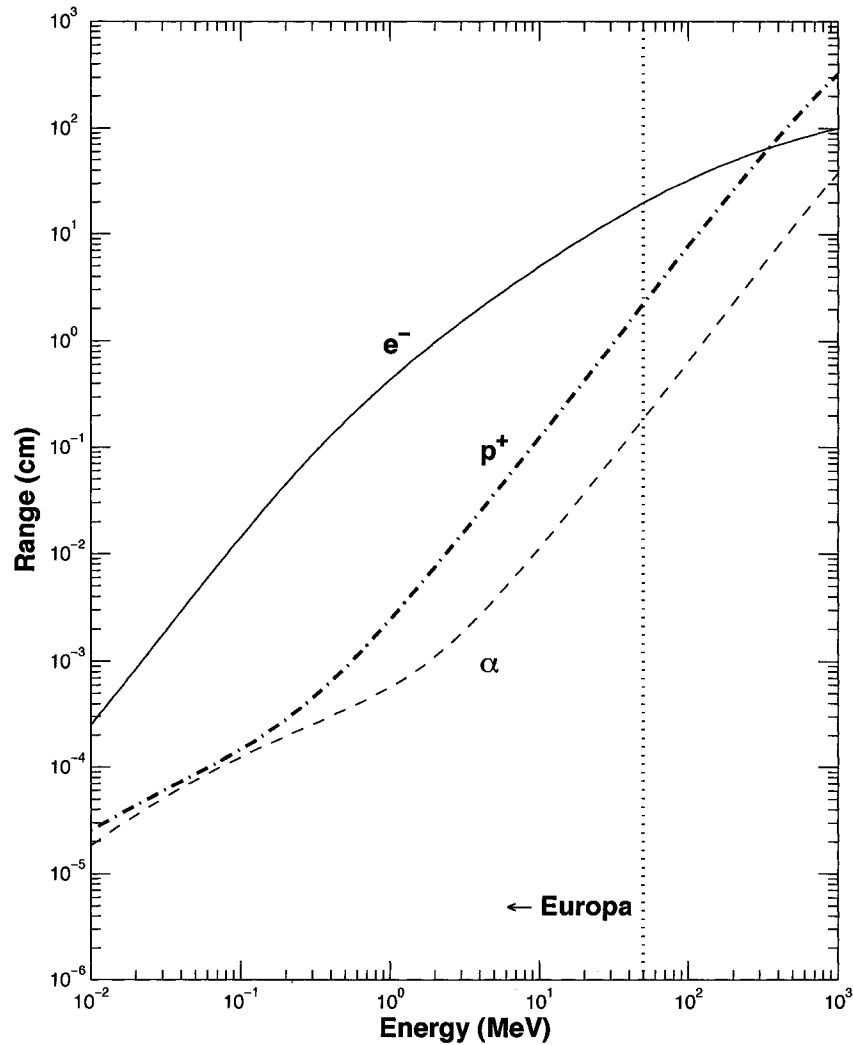


Figure 2.4: Comparison of ranges of electrons, protons, and α particles into unit density water. The ions at Europa are primarily S^{n+} and O^{n+} and have projected ranges much less than that of the the helium ions (*i.e.* α). Data are from Berger et al. (2005).

deflections from the normal during the collisions, then $\theta = 0$ and the cosine term goes to one, yielding the maximum penetration depth. In Figure 2.5 we plot empirical approximations to the equation above for the mean projected range of high-energy electrons in ice of unit density and a density for ice of 1.3 g cm^{-3} (corresponding to the upper density limit for Europa's ice shell in the range considered by Anderson et al. (1998)). As is shown, the most energetic electrons ($\sim 10 \text{ MeV}$) will penetrate a few to a few tens of centimeters into the ice, even for ice densities considerably higher than 1 g cm^{-3} . By comparison, even the most energetic ions (H^+) will only penetrate a few millimeters below the surface (Figure 2.4).

The chemistry resulting from the surface radiation of the ice is the topic of laboratory experiments described in Chapters 8–10. The potential impact that this chemistry has on the sub-surface ocean is depicted in Figure 2.6. Here we illustrate the energetic particle environment of the european surface and the possibility for sub-surface delivery of the radiolytic products via fracturing in the ice. Oxidants and other biochemically useful compounds may be cycled into the ocean during periods of active geology on Europa. Finally, we note that photosynthesis cannot strictly be ruled out for young cracks on Europa (Reynolds et al., 1983). This would of course be a means for biology to directly harness the surface energy without any need for radiolytically produced intermediaries.

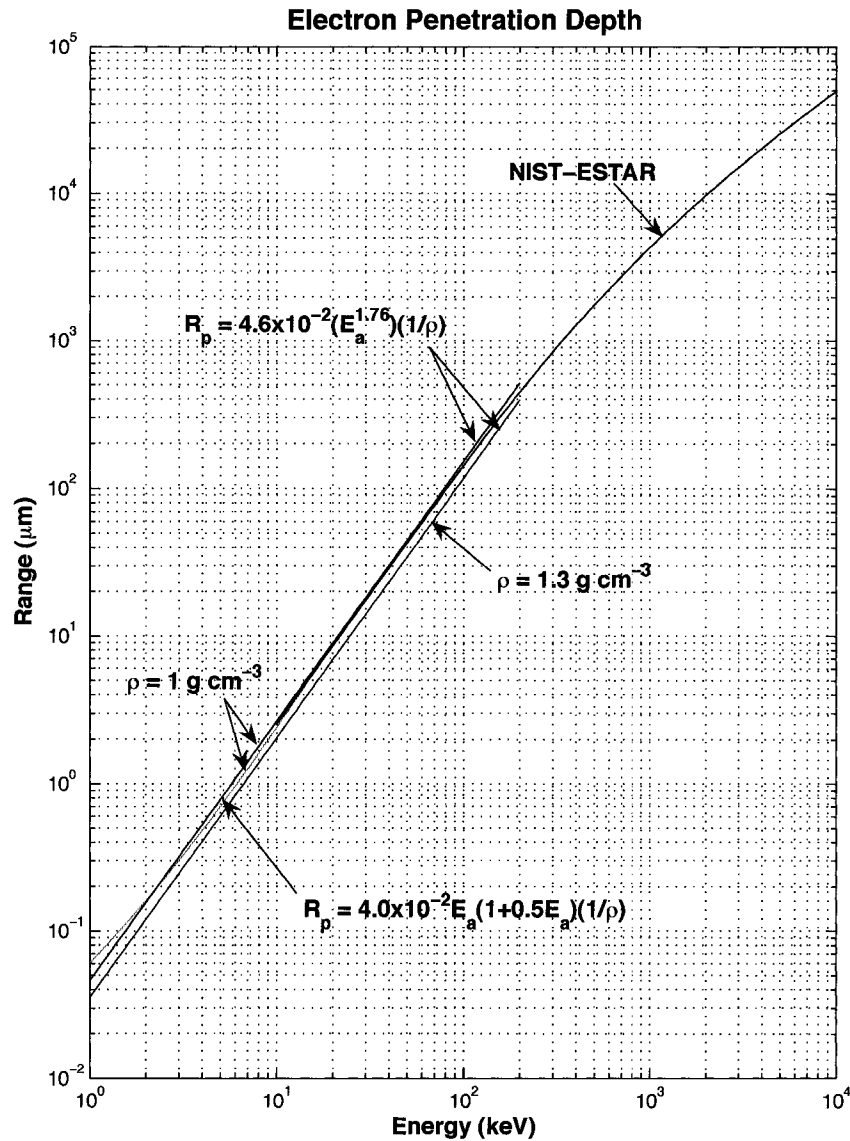


Figure 2.5: Electrons comprise 80% of the energy flux from energetic particles (Cooper et al., 2001). Projected ranges into the ice, R_p , are calculated based on Johnson (1990) for unit density ice (blue) and higher density ice (1.3 g cm^{-3}). The higher density curve accommodates for high concentrations of the observed sulfur hydrate (Carlson et al., 2005; McCord et al., 1998a). For electron energies $>200 \text{ keV}$ we have used the NIST-ESTAR database (Berger et al., 2005).

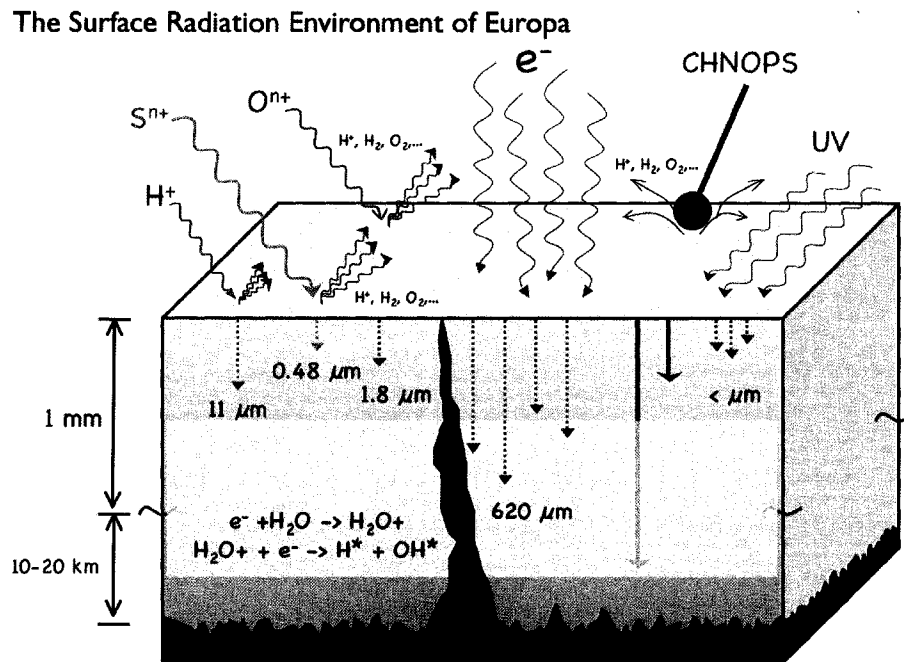


Figure 2.6: Model for radiolytic surface chemistry and subsequent delivery to the putative subsurface ocean. Oxidants produced at the surface and subsequently delivered to the putative subsurface ocean could provide a source of chemical energy for biological activity. Mean particle penetration depths are taken from Cooper et al. (2001).

Chapter 3

Empirical constraints on ocean salinity¹

Both the salt concentration (defined as g dissolved salts per kg of H₂O ($\text{kg}_{\text{H}_2\text{O}}^{-1}$)) of Europa's ocean, and the overlying ice shell thickness, have been only poorly constrained. Experimental (Fanale et al., 2001) and theoretical (Kargel et al., 2000; Zolotov and Shock, 2001; McKinnon and Zolensky, 2003) compositional studies that assume that Europa's salts derive from the leaching or aqueous alteration of carbonaceous chondrites suggest that Europa's ocean should have magnesium (Mg^{2+}) as the dominant cation and sulfate (SO_4^{2-}) as the dominant anion. These results are broadly consistent with *Galileo* spacecraft observations of the near-infrared ice absorption bands (1.0 μm , 1.25 μm , 1.5 μm , and 2.0 μm) of Europa's surface (McCord et al., 1999), although there are alternative models for the identification of these bands (Carlson et al., 1999b; Dalton et al., 2003). Total extraction models can yield salt concentrations as high as $\sim 560 \text{ g MgSO}_4 \text{ kg}_{\text{H}_2\text{O}}^{-1}$ (Kargel et al., 2000) or even higher, 50-50 mixtures of $1000 \text{ g MgSO}_4 \text{ kg}_{\text{H}_2\text{O}}^{-1}$ (Zolotov and Shock, 2001). Zolotov and Shock (2001) preferred partial extraction model gives $7.6 \text{ g MgSO}_4 \text{ kg}_{\text{H}_2\text{O}}^{-1}$, with other models ranging as low as $0.018 \text{ g MgSO}_4 \text{ kg}_{\text{H}_2\text{O}}^{-1}$, corresponding to $0.0036 \text{ g Mg}^{2+} \text{ kg}_{\text{H}_2\text{O}}^{-1}$. McKinnon and Zolensky (2003), arguing against a sulfate-rich model, conclude that MgSO_4 concentrations should lie below $\sim 100 \text{ g MgSO}_4 \text{ kg}_{\text{H}_2\text{O}}^{-1}$. That is, compositional

¹This chapter is an extended version of the manuscript Hand and Chyba (2007)

models currently in the literature allow an almost five order of magnitude range in the possible MgSO_4 concentration in Europa's ocean.

Constraints on the ice shell thickness are currently limited by surface observations and, broadly, by the gravity data (Anderson et al., 1998). Analyses of european surface features (Greeley et al., 2004; Greenberg et al., 2002), crater morphologies (Turtle and Pierazzo, 2001), ice convection models (Pappalardo et al., 1998), and thermal models (Ojakangas and Stevenson, 1989) point to an ice shell thickness in the range of ~ 3 km to > 30 km. Comparison of *Voyager* and *Galileo* image data provide no evidence for contemporary, active resurfacing (Phillips et al., 2000). Differences in the interpretation of lineae, cycloids, ridges, and chaos features are hard to resolve without additional data and without knowledge of the age of the features. Some workers have made a case that while some of the observed features fit a thin-shell model, such features could be indicative of a thin-shell epoch occurring tens of millions of years ago (Pappalardo et al., 1998). Contemporary Europa could have a thick ice shell (> 30 km) with thin-shell features literally frozen in time on the surface. Thermal-orbital evolution models support this possibility (Husmann and Spohn, 2004; Husmann et al., 2002).

Here we address empirical constraints on the ice shell thickness by examining the relationship between the induced magnetic field signature of Europa and the conductivity of the putative subsurface ocean. We are able to set limits on the inductive response of the ocean, thereby necessitating a thin ice shell in order to explain the observed induced magnetic field.

3.1 Conductivity vs Concentration

The conductivity of Europa's ocean, inferred from fitting *Galileo* spacecraft magnetometer measurements to a near-surface conducting layer, must exceed 58 mS m^{-1} in order to explain the observed induced magnetic field (Zimmer et al., 2000). However, coupling the magnetometer measurements to the gravity data, thereby constraining the hydrosphere to be < 200 km thick (Anderson et al., 1998), requires the conductivity of the ocean to exceed 72 mS m^{-1} (Zimmer et al., 2000). More recent modelling

work by Schilling and Neubauer (2005) argues for a minimum conductivity of 250 mS m⁻¹. If Europa's ocean had the composition of seawater (dominated by the salt NaCl), empirical fits for standard seawater conductivity as a function of salinity and temperature could be used to determine salinity (defined as g salt per kg of solution) (Poisson, 1980; Denny, 1993). For the case T = 0 °C (a reasonable first estimate for european sea temperatures, though see Melosh et al. (2004) for more detail), salinity s and conductivity σ are related via

$$s = 35[A_1(R_0^{5/2} - R_0) + A_2(R_0^2 - R_0) + A_3(R_0^{3/2} - R_0) + R_0] - 15R_0(R_0 - 1)(B_0 + R_0^{1/2}B_1R_0), \quad (3.1)$$

where $R_0 = 0.3443\sigma$ for σ in S m⁻¹, $A_1=0.08887$, $A_2=-0.2368$, $A_3=0.4450$, $B_0=0.03579$, and $B_1=-0.001529$. For a solution of terrestrial seawater ions at 0 °C, $\sigma = 72$ mS m⁻¹ corresponds to $s = 0.68$ g kg⁻¹, or about fifty times below the salinity of Earth's ocean. At a conductivity of $\sigma = 250$ mS m⁻¹ the salinity rises to 2.5 g kg⁻¹, still over twelve times less than that of the terrestrial ocean.

However, most models (Kargel et al., 2000; McKinnon and Zolensky, 2003; Zolotov and Shock, 2001) as well as aqueous leaching experiments (Fanale et al., 2001) suggest MgSO₄, not NaCl, as the dominant salt in Europa's ocean. Therefore, we have searched the literature to obtain concentration-conductivity data for MgSO₄. In Figure 3.1 we plot the available conductivity-concentration data for MgSO₄ along with, for comparison, Eq. 3.2 for terrestrial ocean conductivity-salinity. Figure 3.1 shows magnetometer constraints for conductivity as well as some published compositional model constraints on salinity. Conductivity data at 0 °C (Washburn and Klemenc, 1936; Bremner et al., 1939) have been combined with data taken at 25 °C (Calvert et al., 1958; Pethybridge and Taba, 1977; Dunsmore and James, 1951; Harkins and Paine, 1919; Fisher, 1962; Fisher and Fox, 1979) that we have scaled to 0 °C by multiplying the 25 °C conductivity data by a scaling factor of 0.525. This scaling is possible because Washburn and Klemenc (1936) report conductivity-concentration data for both 0 °C and 25 °C across the concentration range from 0.6 g MgSO₄ kg_{H₂O}⁻¹

to $60 \text{ g MgSO}_4 \text{ kg}_{\text{H}_2\text{O}}^{-1}$. The scaling factor was calculated by finding the ratio of conductivities for $T = 0 \text{ }^\circ\text{C}$ and $T = 25 \text{ }^\circ\text{C}$ for a given salt concentration. The average of the nine ratios available from the Washburn and Klemenc (1936) data was used as our final scaling factor. The fact that the temperature-scaled data fall along the curve sketched by the more sparse Washburn and Klemenc (1936) $0 \text{ }^\circ\text{C}$ and the Bremner et al. (1939) $0 \text{ }^\circ\text{C}$ data suggests that this temperature scaling has been done correctly. We fit a third-degree polynomial to the data,

$$C = c_3\sigma^3 + c_2\sigma^2 + c_1\sigma + c_0, \quad (3.2)$$

finding the coefficients, $c_3 = -1.7268$, $c_2 = 12.0161$, $c_1 = 15.2108$, $c_0 = -0.0129$, where C is concentration and σ is conductivity. Errors for values calculated using the polynomial fit are on the order of a few percent across the range of conductivities considered here.

From Eq. 3.2 or Figure 3.1, we see that the lower conductivity limit of 58 mS m^{-1} corresponds to a minimum MgSO_4 concentration of $0.91 \text{ g MgSO}_4 \text{ kg}_{\text{H}_2\text{O}}^{-1}$. With the added constraint of a hydrosphere $< 200 \text{ km}$ thick ($\sigma > 72 \text{ mS m}^{-1}$), we find a minimum salt concentration of $1.1 \text{ g MgSO}_4 \text{ kg}_{\text{H}_2\text{O}}^{-1}$. This value is a factor of 50 greater than the lower limit partial extraction model of Zolotov and Shock (2001) so that the lowest extraction models are excluded by the data. The lower limit on σ proposed by Schilling and Neubauer (2005), based on longer period wave propagation, requires $4.5 \text{ g MgSO}_4 \text{ kg}_{\text{H}_2\text{O}}^{-1}$. Zimmer et al. (2000) do not explicitly provide an upper limit to the conductivity of the ocean. However, they determine that an ocean of terrestrial salinity ($s = 35$, or a concentration of $34 \text{ g sea salt per kg of water (kg}_{\text{H}_2\text{O}}^{-1})$ at $0 \text{ }^\circ\text{C}$, corresponding to 2.75 S m^{-1}) would imply a near-surface ocean of only 3.5 km thickness. (An insulating ice shell is ignored in their model; they therefore treat the uppermost 3.5 km of Europa as conducting.) A shell of conductivity 2.75 S m^{-1} would require $96.8 \text{ g MgSO}_4 \text{ kg}_{\text{H}_2\text{O}}^{-1}$.

In summary, the range of empirically supported MgSO_4 salt concentrations permitted by Figure 3.1 and previously published conductivity constraints falls between $1.1 \text{ g MgSO}_4 \text{ kg}_{\text{H}_2\text{O}}^{-1}$ and $96.8 \text{ g MgSO}_4 \text{ kg}_{\text{H}_2\text{O}}^{-1}$. Note that the high-end value is not

well constrained by values in the literature. Therefore in subsequent sections we work to provide a stronger constraint on this value and show that empirical constraints from *Gablio*, combined with physical limitations on the conductivity resulting from salinity, necessitate a thin ice shell.

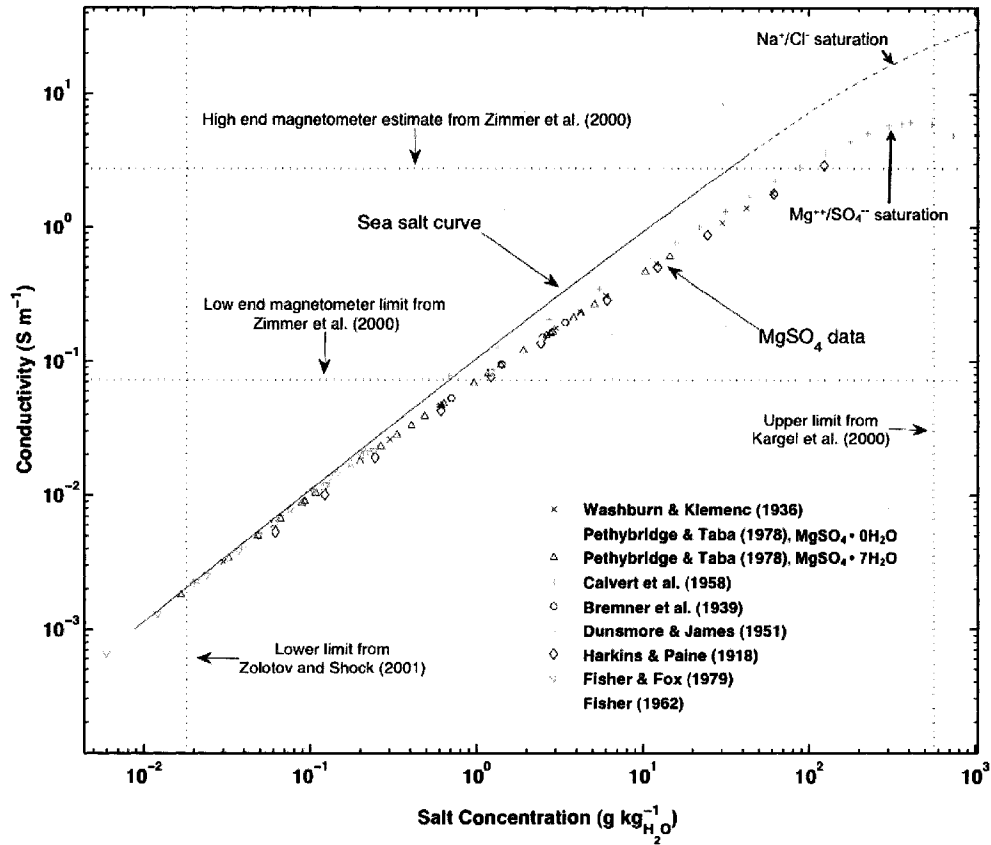


Figure 3.1: Specific conductivity of an aqueous solution as a function of sea salt or MgSO_4 concentration. The sea salt curve was calculated using the polynomial of Poisson (1980) (see text). The region of the curve beyond $42 \text{ g salt kg}_{\text{H}_2\text{O}}^{-1}$ is shown in dashes in order to emphasize that this region extends beyond the data of Poisson (1980). Data from Washburn and Klemenc (1936) and Bremner et al. (1939) represent actual measurements of a magnesium sulfate solution at 0°C . All other data represents measurements made at 25°C and then scaled to at 0°C by using a scaling factor derived from the 0°C and 25°C data of Washburn and Klemenc (1936). Limits for the dissolution of NaCl ($304 \text{ g kg}_{\text{H}_2\text{O}}^{-1}$) and MgSO_4 ($282 \text{ g kg}_{\text{H}_2\text{O}}^{-1}$) are shown.

3.2 Amplitude constraints

We derive a first set of limits for conductivity by combining information from Zimmer et al. (2000) with the gravity measurement constraints of Anderson et al. (1998), viz. that the total thickness of Europa's ice plus liquid water shell must lie in the range 80 km to 170 km.

We solve for the induced magnetic field amplitude for a range of ocean thicknesses and ice shell thickness. The total magnetic field, as observed by the Galileo spacecraft, consists of the primary field of Jupiter plus the secondary, induced field of Europa: $B = B_{primary} + B_{secondary}$. The induced magnetic field is a function of the primary field, and in the three-shell model (ice, ocean, and mantle) of Zimmer et al. (2000) this field is a dipole field (Srivastava, 1966; Parkinson, 1983) and can be expressed as

$$\mathbf{B}_{secondary} = -Ae^{-i(\omega t - \phi)} B_{primary} [3(\mathbf{r} \cdot \mathbf{e}_0)r - r^2 \mathbf{e}_0] r_m^2 / (2r^5) \quad (3.3)$$

The amplitude A , and phase ϕ , of the induced magnetic field are found by combining Maxwell's equations and Ohm's law, and solving the resulting diffusion equation:

$$\nabla^2 \mathbf{B} = \mu_0 \sigma \frac{\partial \mathbf{B}}{\partial t} \quad (3.4)$$

where μ_0 is the vacuum permeability and σ is the conductivity. For nested spheres, Eq. 3.3 may be solved by separation of variables; the radial component of the solution is given by Bessel's equation and continuity of \mathbf{B} across the spherical boundaries yields recursion formulae (Srivastava, 1966; Parkinson, 1983). For a three-shell spherical model where the conducting ocean is nested between an insulating interior and an insulating ice shell, A and ϕ are given by (Zimmer et al., 2000):

$$Ae^{i\phi} = \left(\frac{r_0}{r_m} \right)^3 \frac{R J_{\frac{5}{2}}(r_0 k) - J_{-\frac{5}{2}}(r_0 k)}{R J_{\frac{1}{2}}(r_0 k) - J_{-\frac{1}{2}}(r_0 k)} \quad (3.5)$$

where

$$R = \frac{r_1 k J_{-\frac{5}{2}}(r_1 k)}{3J_{\frac{3}{2}}(r_1 k) - r_1 k J_{\frac{1}{2}}(r_1 k)} \quad (3.6)$$

Here the J_n denote Bessel functions of the first kind and order n . The radius of Europa, the radius to the ocean surface, and the radius to the ocean floor are symbolized by r_m , r_o , and r_1 , respectively. The complex parameter k is a measure of the extent to which the time-varying field penetrates the conductor, here taken to be the ocean. The field oscillation frequency ω and conductivity σ determine k :

$$k = (1 - i)\sqrt{\mu_0\sigma\omega/2} \quad (3.7)$$

We calculate A for a range of ocean thicknesses, ice thicknesses, and ocean conductivities. In this first model, the ice shell and mantle are assumed to have zero conductivity; we solve for a conductive mantle later in this work. For small σ (≤ 1 S m⁻¹) we solve for A exactly. As σ increases, however, the terms in the numerator and denominator of Eq. 3.5 rapidly approach zero, creating a region of numerical instability. For large σ we use an approximation to Eq. 3.5 wherein the highest-order (smallest) terms are discarded. This approximation is good for $\sigma \geq 0.1$ S m⁻¹ and is derived by eliminating terms of order x^2 and higher in the denominator of Eq. 3.5, where $x = r_0k$ or r_1k . With this approximation, Eq. 3.5 simplifies to

$$Ae^{i\phi} \approx \left(\frac{r_o}{r_m}\right)^3 \left(\frac{r_1}{r_o - \left(\frac{r_0r_1k}{3}\right)\tan(k(r_o - r_1))} - 1\right) + O\left(\frac{1}{x^2}\right). \quad (3.8)$$

Using Eq. 3.7 and an 11.2-hour synodic period for the primary field oscillation, we find

$$|x| = r_0|k| \approx r_1|k| \approx 10\sigma^{1/2} \quad (3.9)$$

with σ in S m⁻¹. Therefore $O(1/x^2) \approx 10^{-2}\sigma^{-1}$ (σ in S m⁻¹), and Eq. 3.8 is a good approximation to Eq. 3.5 provided $\sigma \geq 0.1$ S m⁻¹. Explicit numerical ratioing of A from Eq. 3.8 to A from Eq. 3.5 verifies this analytical prediction. The solution for A is found by expanding Eq. 3.8 into real and imaginary components, and then eliminating ϕ in order to solve for A . Figures 3.2, 3.3, and 3.4 were plotted using the exact solution for A , whereas in Figures 3.5 and 3.6 we use the above approximation.

Zimmer et al. (2000) concluded that induced field amplitudes of $A < 0.7$ are hard to reconcile with the *Galileo* observations; so in all cases we have solved for

conductivity variations with $A \geq 0.7$. Furthermore, amplitudes for $A > 1.0$ imply significant conductivity outside the moon (e.g. ionosphere, cloud of pick-up ions) and Zimmer et al. (2000) argue that the observed magnetic signature does not fit such a model. We nevertheless address the possible contribution of an ionosphere in a subsequent section. More recent work using a least-squares fit to the magnetometer data (Schilling et al., 2004) concludes that $A = 0.97 \pm 0.02$. Here we examine how variations in the amplitude A , coupled with variations in the ice shell and ocean thicknesses, constrain the salt concentration in the putative ocean.

3.2.1 Amplitude response $A \leq 0.9$

First, we examine the low-end case of $A = 0.7$. Results are shown in Figure 3.2. The range of ocean thicknesses shown in Figure 3.2 covers the range allowed by the gravity data (Anderson et al., 1998). Lines of constant ice shell thickness are shown for shells ranging from 0 to 50 km thickness. For the case of a 100 km thick ocean with ice shells of different thicknesses, the resulting salt concentrations all fall below $2.7 \text{ g MgSO}_4 \text{ kg}_{H_2O}^{-1}$. Note that even for the case of a 50 km ice shell overlying a 50 km ocean, the required salt concentration when $A = 0.7$ still falls below $5 \text{ g MgSO}_4 \text{ kg}_{H_2O}^{-1}$.

Considering some of the cases permitted by the two extremes of the gravity data, we have calculated that a 160 km liquid water ocean beneath a 10 km ice shell would require a concentration of $1.3 \text{ g MgSO}_4 \text{ kg}_{H_2O}^{-1}$ ($\sigma \sim 88 \text{ mS m}^{-1}$). Similarly, for the lower-limit case of an 80 km hydrosphere, we find that a 60 km-thick ice shell with a 20 km liquid water conducting layer at the bottom would require $15.6 \text{ g MgSO}_4 \text{ kg}_{H_2O}^{-1}$ ($\sigma \sim 0.69 \text{ S m}^{-1}$) whereas an ice shell of 10 km with a 70 km ocean requires only $2.8 \text{ g MgSO}_4 \text{ kg}_{H_2O}^{-1}$ ($\sigma \sim 165 \text{ mS m}^{-1}$). That is, for the case of $A = 0.7$, even the extreme choices permitted by the gravity data give low MgSO_4 concentrations, in the range 1 to $16 \text{ g kg}_{H_2O}^{-1}$.

As we increase the amplitude response, A , the conductive layer approaches a perfect conductor ($A = 1.0$). Solutions for $A = 0.8$ and $A = 0.9$ are shown in Figures 3.3 and 3.4, respectively. Examining the case of a 10 km ice shell overlying a 100 km

thick ocean, we find that for $A = 0.8$ the required salt concentration is $3.2 \text{ g MgSO}_4 \text{ kg}_{H_2O}^{-1}$ while for $A = 0.9$, the requirement increases to $10 \text{ g MgSO}_4 \text{ kg}_{H_2O}^{-1}$. Both values are still significantly lower than the sea salt concentration of the terrestrial ocean. Increasing the ice shell to 50 km thickness pushes the salt concentration up to $5.6 \text{ g MgSO}_4 \text{ kg}_{H_2O}^{-1}$ for the case of $A = 0.8$. Under the same circumstances, raising A to 0.9 requires increasing the conductivity to $\sim 175 \text{ S m}^{-1}$ (see Figure 3.5). This value is far beyond the conductive capabilities of salt ions in water, so these parameter combinations are not permitted. We explore these issues in depth in subsequent sections.

3.2.2 Amplitude response $A = 0.97 \pm 0.02$

As A increases toward 1.0, salt concentrations must concomitantly increase. While Zimmer et al. (2000) argued that A must lie in the range $0.7 \leq A \leq 1.0$, more recent work by Schilling et al. (2004) suggests that $A = 0.97 \pm 0.02$. In Figures 3.5-3.8 we extend the range of conductivities to include large values for σ and we show how the combination of ocean thickness, ice shell thickness, and conductivity determine the amplitude of the induced magnetic field. We explore the range of physically plausible conditions that could allow such a high value of A . Ultimately we show that because there is an upper limit on the conductivity of the ocean placed by the salt ion saturation, values of $A = 0.97 \pm 0.02$ are only possible if the ice shell is thin.

In Figures 3.5 and 3.6, three models for the ocean thickness are considered: 80 km, 100 km, and 120 km, and in each case we examine the solutions for ice shell thicknesses of 0, 10, 30, and 50 km. At conductivities below 1.2 S m^{-1} the ocean thickness plays an important role in determining the amplitude. However, beyond 1.2 S m^{-1} the ice shell thickness dominates the amplitude response. As shown in Figures 3.5 and 3.6, when $\sigma > 2 \text{ S m}^{-1}$ ice shells of greater thickness require higher oceanic conductivities in order to achieve the same amplitude response. As conductivity increases, the amplitude slowly approaches the idealized perfect conductor case of $A = 1.0$. Here we solve for values of σ up to 300 S m^{-1} (~ 120 times the conductivity of Earth's ocean), at which point the maximum achievable amplitude response is $A =$

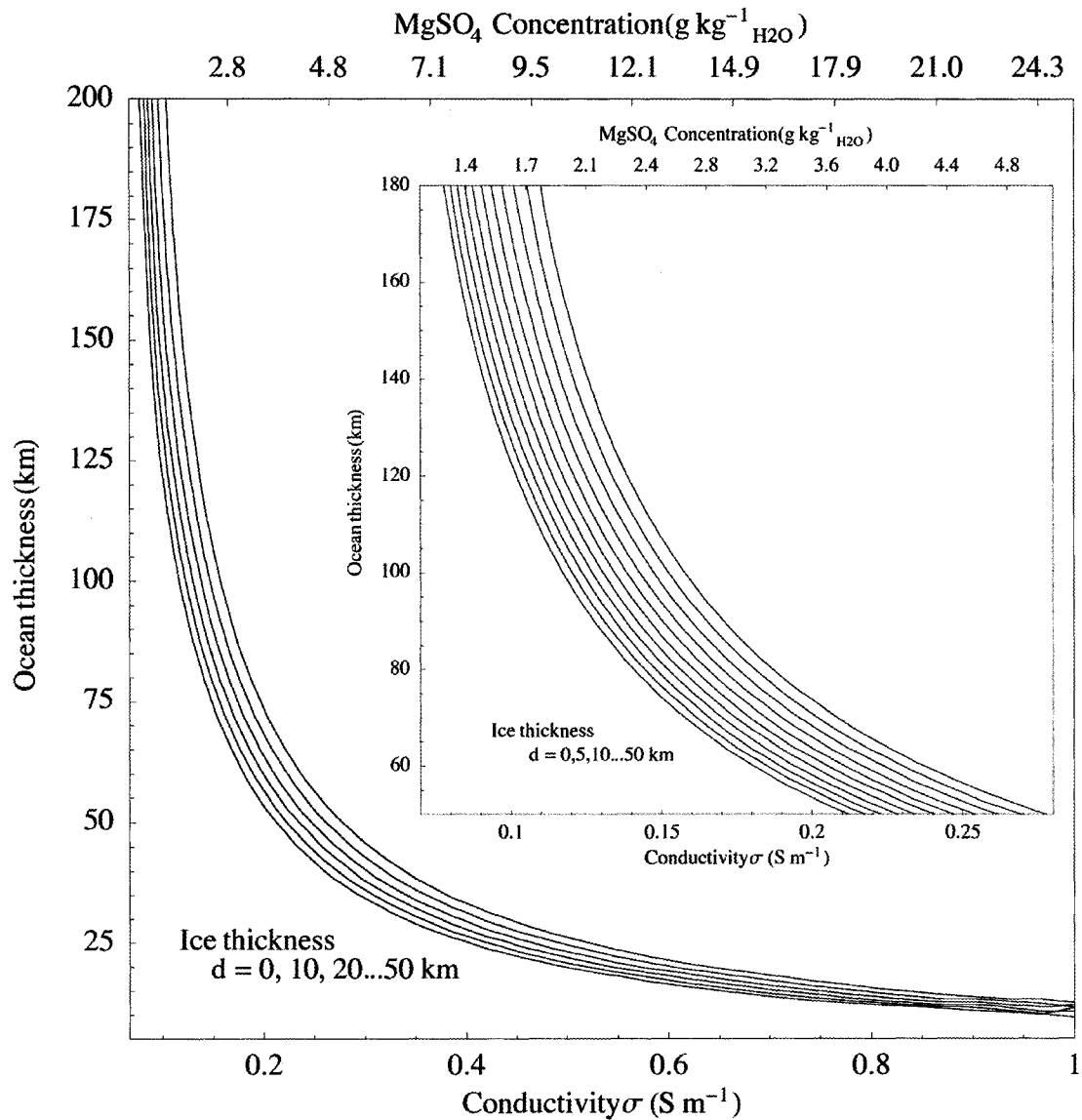


Figure 3.2: Ocean depth-salt concentration relationship for an induced magnetic field amplitude of $A = 0.7$. Magnesium sulfate concentrations (g per kg water) for varying ocean thicknesses were calculated (see text) for a variety of ice shell thicknesses. The plot shows lines of constant ice thickness. Starting from the left, lines are given for no ice shell (0 km) on up to a 50 km ice shell, in 10 km increments. The inset plot details the 50 - 180 km ocean thickness region and shows lines of ice shell thickness ranging from 0 km to 50 km in 5 km increments. All of the solutions shown in the inset plot would be considered freshwater, or nearly freshwater (*i.e.* oligohaline or mildly brackish), by Earth standards.

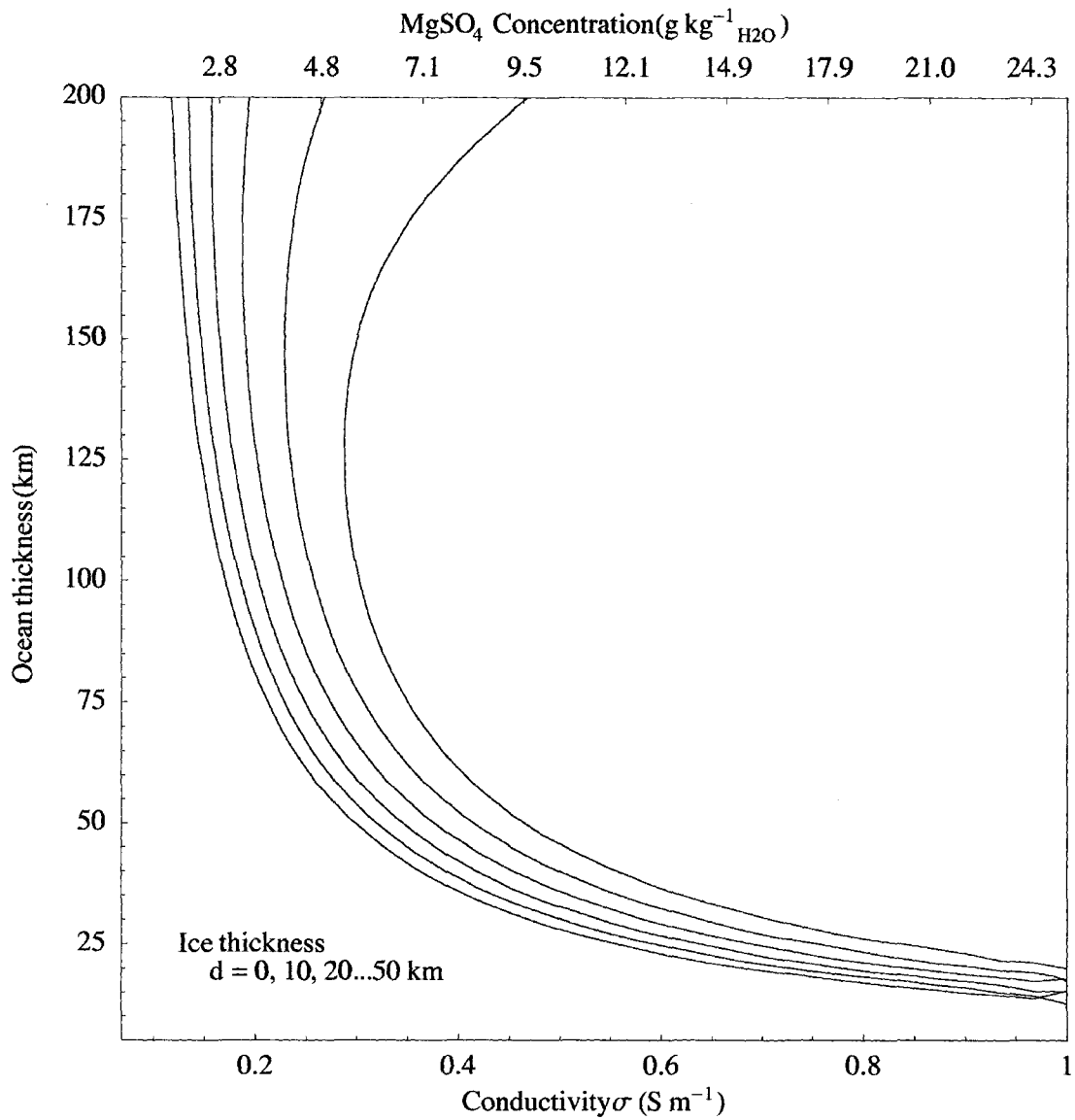


Figure 3.3: Ocean depth-salinity relationship for an induced magnetic field amplitude of $A = 0.8$. Magnesium sulfate concentrations (g per kg water) for varying ocean thicknesses were calculated (see text) for a variety of ice shell thicknesses. The plot shows lines of constant ice thickness. Starting from the left, lines are given for no ice shell (0 km) on up to a 50 km ice shell, at 10 km increments.

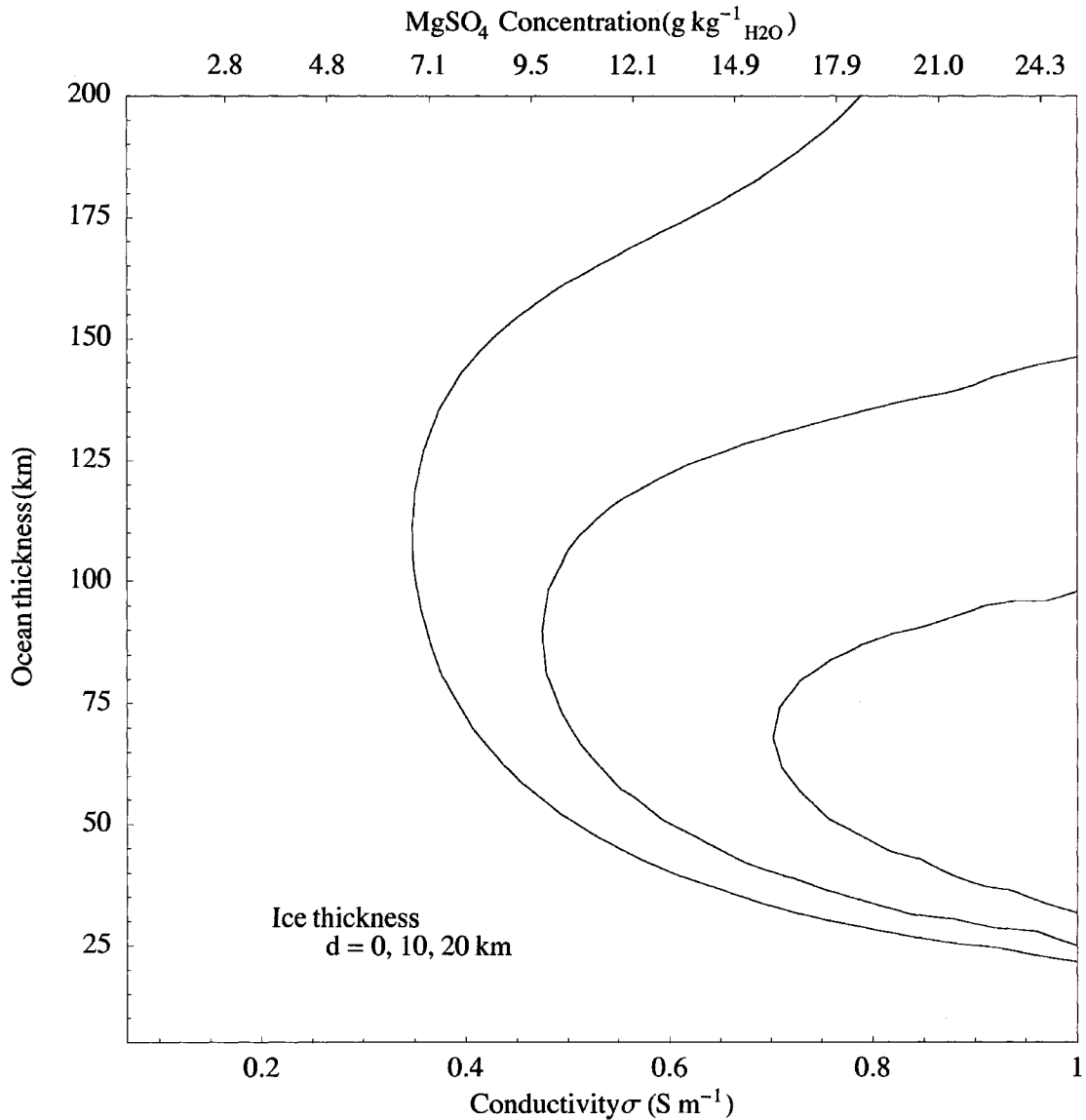


Figure 3.4: Ocean depth-salt concentration relationship for an induced magnetic field amplitude of $A = 0.9$. Magnesium sulfate concentrations (g per kg water) for varying ocean thicknesses were calculated (see text) for a variety of ice shell thicknesses. The plot shows lines of constant ice thickness. Starting from the left, lines are given for no ice shell (0 km), a 10 km shell, and a 20 km shell. The double-valued shape of the curves is due to skin depth effects in amplitude and phase (see text).

| Ocean thickness (km) | Ice thickness (km) | Amplitude of induced magnetic field (A) | | | | | |
|----------------------|--------------------|---|-----------|-----------|-----------|------------|------------|
| | | Salt concentration (g salt $\text{kg}_{\text{H}_2\text{O}}^{-1}$) [Conductivity, S m^{-1}] | | | | | |
| | | 1.14 [0.072] | 5 [0.250] | 100 [3.0] | 282 [6.0] | 304 [18.0] | 350 [23.0] |
| 60 | 0 | 0.38 | 0.8 | 0.96 | 0.97 | 0.98 | 0.98 |
| | 10 | 0.37 | 0.78 | 0.94 | 0.95 | 0.96 | 0.96 |
| | 30 | 0.35 | 0.75 | 0.91 | 0.91 | 0.92 | 0.92 |
| | 50 | 0.33 | 0.71 | 0.87 | 0.88 | 0.89 | 0.89 |
| 80 | 0 | 0.46 | 0.84 | 0.95 | 0.96 | 0.98 | 0.98 |
| | 10 | 0.45 | 0.83 | 0.94 | 0.94 | 0.96 | 0.96 |
| | 30 | 0.43 | 0.79 | 0.9 | 0.91 | 0.92 | 0.92 |
| | 50 | 0.41 | 0.76 | 0.86 | 0.87 | 0.87 | 0.89 |
| 100 | 0 | 0.53 | 0.87 | 0.95 | 0.96 | 0.98 | 0.98 |
| | 10 | 0.52 | 0.85 | 0.93 | 0.94 | 0.96 | 0.96 |
| | 30 | 0.49 | 0.81 | 0.89 | 0.91 | 0.92 | 0.92 |
| | 50 | 0.47 | 0.78 | 0.86 | 0.87 | 0.89 | 0.89 |
| 120 | 0 | 0.59 | 0.88 | 0.95 | 0.96 | 0.98 | 0.98 |
| | 10 | 0.57 | 0.86 | 0.93 | 0.94 | 0.96 | 0.96 |
| | 30 | 0.54 | 0.82 | 0.89 | 0.91 | 0.92 | 0.92 |
| | 50 | 0.52 | 0.79 | 0.86 | 0.87 | 0.89 | 0.89 |
| 150 | 0 | 0.64 | 0.88 | 0.95 | 0.96 | 0.98 | 0.98 |
| | 10 | 0.63 | 0.86 | 0.93 | 0.94 | 0.96 | 0.96 |
| | 30 | 0.6 | 0.82 | 0.89 | 0.91 | 0.92 | 0.92 |
| | 50 | 0.57 | 0.79 | 0.86 | 0.87 | 0.89 | 0.89 |

Table 3.1: Induced amplitude response, A , is provided for a variety of MgSO_4 concentrations, ocean thicknesses, and ice shell thicknesses. The salt concentrations shown here correspond to: 1) the low-end conductivity limit of Zimmer et al. (2000), 2) the low-end conductivity limit of Schilling and Neubauer (2005), 3) the high-end estimate for MgSO_4 concentration of McKinnon and Zolensky (2003), 4) the saturation concentration of NaCl , and 5) the ionic saturation concentration for MgSO_4 . Errors in the salt concentration, primarily resulting from the polynomial fit, are on the order of ± 0.1 grams $\text{MgSO}_4 \text{ kg}_{\text{H}_2\text{O}}^{-1}$.

0.99. This is for no ice shell ($d = 0$), obviously not physically plausible. If we instead consider the case of $d = 10$ km, then at $\sigma = 300 \text{ S m}^{-1}$ we find $A = 0.97$. Similarly, for $d = 30$ km and $d = 50$ km we find $A = 0.94$ and $A = 0.90$, respectively.

In practice there are solubility limits on how much salt can be added to water and thus there are limits to how high the conductivity can be driven by the concentration of salt ions. Saturation for the dissolved ionic form of MgSO_4 occurs at $\sim 282 \text{ g MgSO}_4 \text{ kg}_{\text{H}_2\text{O}}^{-1}$ (Hogenboom et al., 1995; Kargel, 1991) and for NaCl saturation occurs at $\sim 304 \text{ g NaCl kg}_{\text{H}_2\text{O}}^{-1}$ at 25°C (Oren, 2001). Hydrated forms of MgSO_4 may exist in suspension in the water (*e.g.* $\text{MgSO}_4 \cdot 7\text{H}_2\text{O}$), but these forms do not contribute to the conductivity of the ocean water. In addition, as the salt concentration increases the viscosity of the solution also increases, reducing the mobility of the ions and limiting the conductivity (Anderko and Lencka, 1997). At low temperatures, increasing pressure over the range 0-400 MPa has little effect on conductivity (Quist and Marshall, 1968). The ~ 5 -200 MPa range within Europa's ocean should thus cause little variation in conductivity. Hypersaline environments on Earth are rarely above a few Siemens per meter. For example, the brine of Mono Lake in Northern California is reported to be 8.57 S m^{-1} (at 25°C) (Jellison et al., 1999), and the brine saturated sediments of Lake Magadi in Southwest Kenya are measured to be $\sim 11 \text{ S m}^{-1}$ (34°C) (Jones et al., 1998).

The saturation limits for salt concentration impose limits on the conductivity ($\sim 6 \text{ S m}^{-1}$ for MgSO_4 and $\sim 18 \text{ S m}^{-1}$ for sea salt) that are hard to reconcile with the high amplitude requirement of $A \sim 0.97$. In Figures 3.5 and 3.6 we show the upper limit for conductivity of an MgSO_4 or NaCl solution. As is shown, the intersection of these lines with $A = 0.97$ yields an ice shell of thickness equal to, or less than, 4 km. Taking the lower end of the error bar, $A = 0.95$, we find that at most the ice shell is 7 km (MgSO_4) to 15 km (NaCl) thick. Even if a solution of conductivity 30 S m^{-1} were physically plausible, we would still have upper limits on the ice shell thickness of ~ 6 km and ~ 17 km for $A = 0.97$ and $A = 0.95$ respectively (for NaCl). Additionally, it should be noted that salt concentrations of $\geq 300 \text{ g per kg of H}_2\text{O}$ would push the density of the solution beyond those permissible by the 3-shell internal modelling results of Anderson et al. (1998). This density constraint is not terribly strict -

alternative interior models fitting for the bulk density and moment of inertia could allow for higher density outer shells - but it does provide another piece of information pertaining to the bulk properties of putative ocean. We examine the role of density in 3.5.

Does the above analysis demonstrate that Europa's ice shell must be ≤ 15 km? While Schilling et al. (2004) conclude that $A = 0.97 \pm 0.02$, this value is derived by comparing two different models for the external and internal magnetic fields in and around Europa. In the first case, Europa is allowed to have an internal permanent dipole moment with a surface magnitude of 23 nT and a tilt of 59° from the Europa's spin axis. From this fit to the magnetometer data, they find that $A = 0.96 \pm 0.03$. In other words, if we allow Europa to have an internal magnetic field, we can push the amplitude down to 0.93. Even for this low of a value for A , we find that the ice shell must be equal to, or less than 26 km thick. In their model without an internal dipole, Schilling et al. (2004) find that $A = 0.98 \pm 0.01$. Here the lower limit of $A = 0.97$ again leads us to an ice shell of ≤ 4 km for the case of NaCl. At $A = 0.98$, the ice shell can be only meters thick. Ultimately, the work of Schilling et al. (2004) is data limited - only four Galileo passes of Europa were close enough to satisfy their criterion. However, in their rigorous analysis and fitting of models so as to minimize root-mean square fits to the data, they conclude that $A = 0.97 \pm 0.02$, taking all models into account. In this case, the ice must indeed be ≤ 15 km.

In Figures 3.7 and 3.8 we show how varying the ocean thickness affects the amplitude response. Contours for the saturation limits on conductivity, along with several other conductivity contours of interest are shown. In Figure 3.7 the ice shell thickness is 10 km, whereas in the Figure 3.8 the ice shell is 30 km thick. These contours reveal that for conductivities of a few Siemens per meter the inductive response actually decreases as we increase the thickness of the conducting layer (*i.e.* the ocean thickness). This is likely a skin depth effect, and can be understood semi-quantitatively in the following way. In the case of a plane conductor, the solution to Eq. 3.4 is simply (*e.g.* Parkinson (1983)):

$$B = B_0 e^{-z/\delta} e^{-i(\omega t - z/\delta)}, \quad (3.10)$$

where $z = 0$ at the boundary of the conductor and increases positively into the conductor, and

$$\delta = (\mu_0 \sigma \omega / 2)^{-1/2}, \quad (3.11)$$

is the skin depth. For every increment δ of depth z into the conductor, the amplitude decreases by a factor of e and the phase changes by one radian. Therefore increasingly deep layers of the conductor both contribute less to the amplitude, and contribute increasingly destructively (out of phase). For $\sigma=1$ and 10 S m^{-1} , $\delta=101 \text{ km}$ and 32 km , respectively, consistent with the behaviour seen in Figures. 3.3–3.8.

Of course, a nested spherical shell model for Europa requires that Eq. 3.4 be solved in spherical coordinates, and the solution is Eq. 3.5, not Eq. 3.10. However, Eqs. 3.10 and 3.11 will provide a good local approximation for the solution into the spherical conductor provided that (Srivastava, 1966):

$$\sigma \gg 2 / (\mu \sigma \omega r^2). \quad (3.12)$$

In this case, the real part of $kr \gg 1$, allowing us to drop the first derivative term in the Bessel equation solution to the radial part of Eq. 3.4, and the system has solutions given by Eqs. 3.10 and 3.11 (Srivastava, 1966). For Europa, $r = 1560 \text{ km}$ and $\omega = 2\pi/P = 1.6 \times 10^{-4}$ where $P = 4.03 \times 10^4 \text{ s} = 11.2 \text{ hr}$ is Jupiters synodic rotation period. Eq. 3.12 will therefore hold when $\sigma \gg 10^{-3} \text{ S m}^{-1}$, which will be the case for the conductivities of interest here. Therefore Eqs. 3.10 and 3.11 provide good insight into the decay and phase change of the magnetic field as it extends down into Europa's ocean.

For certain combinations of σ and ocean thickness, the induced response at depth will cancel part of the induced response generated near the surface; this behaviour explains, *e.g.*, the shape of the curves in Figs. 3.7 and 3.8. For large conductivity the skin depth goes to zero - all of the induced response is generated near the surface - and cancellation effects are avoided. A curious consequence of this behaviour is that if the salinity of the putative european ocean is comparable to that of the Earth's ocean (with σ of a few S m^{-1}), then thinner oceans provide a better fit to the high amplitude requirement of Schilling et al. (2004).

Table 3.1 summarizes the relationship between layers on our 3-layer model, providing values of A for a variety of plausible combinations of ice thickness, ocean thickness, and conductivity. Again, A can only exceed 0.95 for thin ice shells and near-saturation salt concentrations, regardless of which scenario is considered.

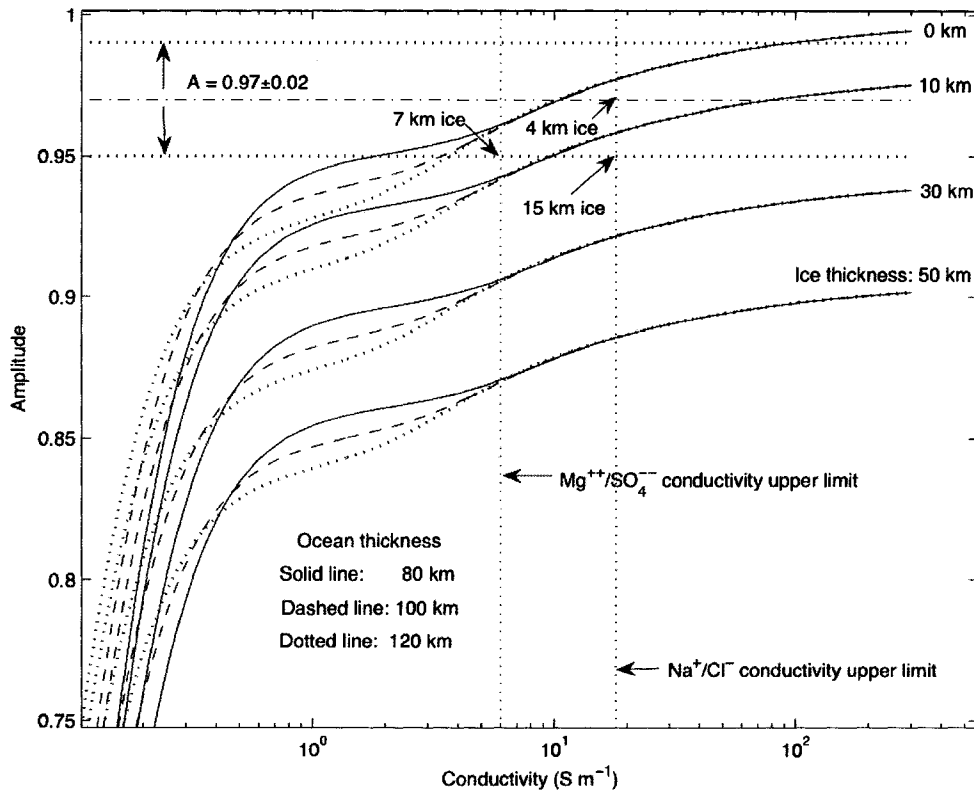


Figure 3.5: Amplitude, A , as a function of conductivity, ocean thickness, and ice shell thickness. At low conductivities the ocean thickness dominates the amplitude response, however, as the conductivity of the solution increases, ocean thickness becomes less important and the thickness of the non-conducting ice shell dominates the inductive amplitude response. Here we show a three-layer spherical model with non-conducting ice shell and mantle. The only solutions consistent with the magnetometer data (Schilling et al. (2004) requires $A = 0.97 \pm 0.02$) and the gravity data (Anderson et al., 1998) are those in which the ice shell is thin (between 0 and 15 km thick). The optimal fit for an ocean dominated by NaCl is 4 km thickness. The maximum allowable ice shell thickness for an MgSO_4 dominated ocean is 7 km.

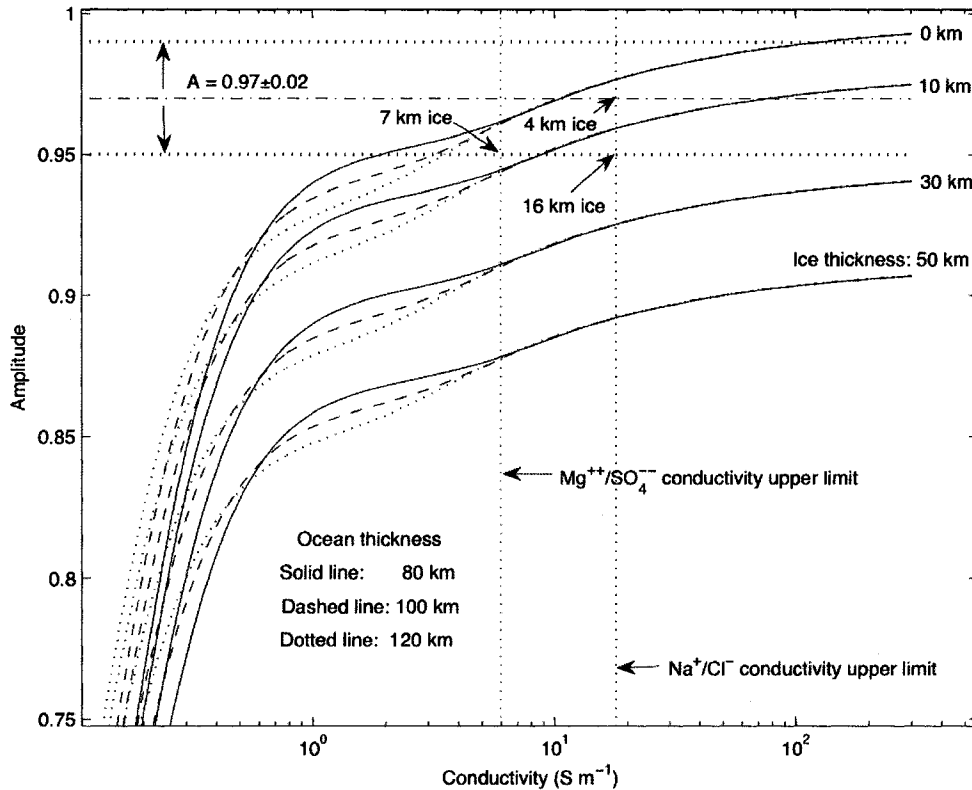


Figure 3.6: Five-layer half-space model showing A , as a function of conductivity, ocean thickness, and ice shell thickness. Results are very similar to the three-layer spherical model. Values for the conductivity of individual layers are: $\sigma_{Ionosphere} = 2 \times 10^{-4} \text{ S m}^{-1}$; $\sigma_{Ice} = 1 \times 10^{-10} \text{ S m}^{-1}$; $\sigma_{Mantle} = 0.01 \text{ S m}^{-1}$; $\sigma_{Core} = 3.3 \times 10^5 \text{ S m}^{-1}$. Again the optimal fit to the magnetometer data is achieved with a 4 km thick ice shell. The maximum thickness allowed by the error bars is 16 km, slightly more than calculated with the three-layer spherical model. This difference is primarily due to conductivity limits for the half-space model (see text).

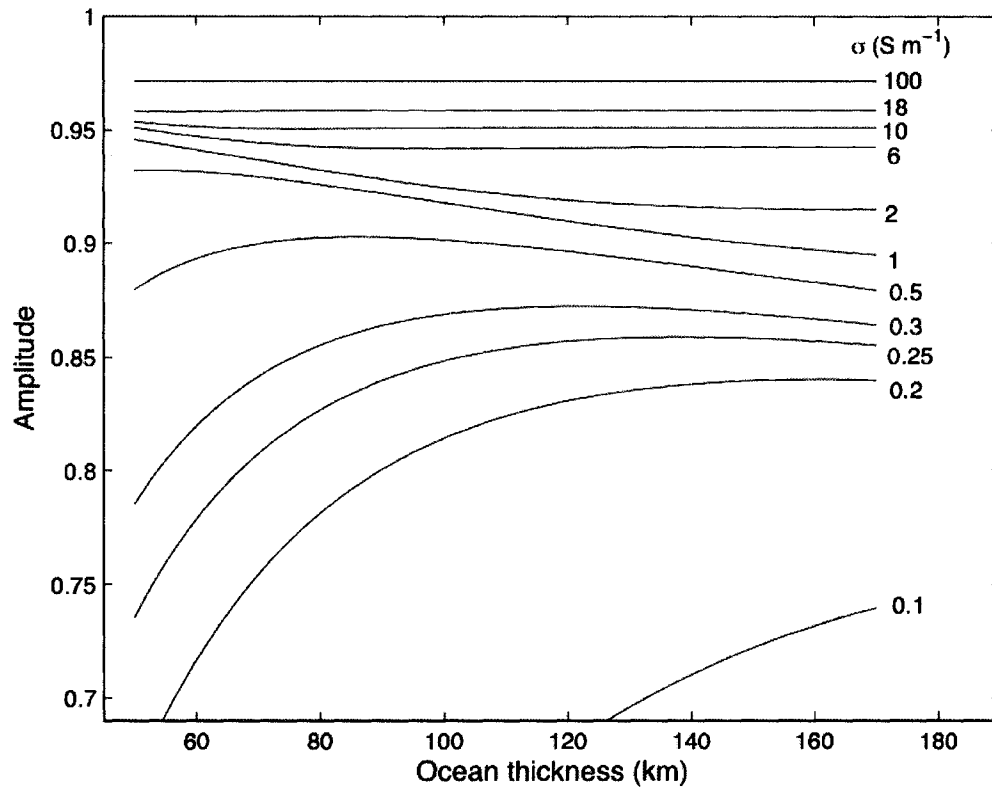


Figure 3.7: Contours of conductivity as a function of amplitude and ocean thickness. The ice thickness in all cases is assumed to be 10 km.

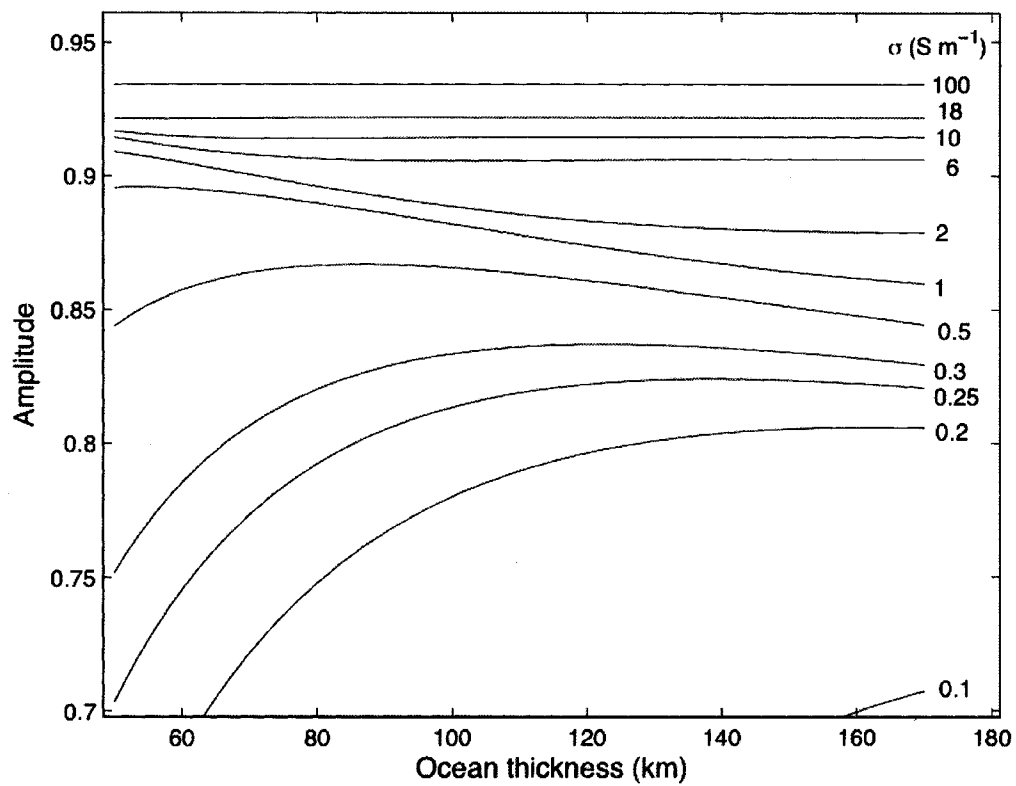


Figure 3.8: Contours of conductivity as a function of amplitude and ocean thickness. The ice thickness in all cases is assumed to be 30 km.

3.3 Adding a conducting core, mantle, and ionosphere

We have shown that the three-layer model can only fit the magnetometer amplitude constraints if the conductivity is high and the ice shell thin. Here we explore the influence of a conducting ionosphere, mantle, and core on the induced field response. We use a plane stratified half-space (Parkinson, 1983; Srivastava, 1965) instead of a spherical model. As previously shown, this model is a good approximation for Europa for conductivities greater than approximately 10^{-3} S m^{-1} . This leads to a planar approximation with m shells and a recursive expression for the ratio of the induced to external fields given by,

$$\frac{B_i}{B_e} = \frac{R_1 (\alpha_1 - \nu) - \alpha_1 + \nu}{R_1 (\alpha_1 - \nu) - \alpha_1 + \nu} \quad (3.13)$$

where

$$R_j = e^{2\alpha_j z_j} \frac{R_{j+1} (\alpha_j + \alpha_{j+1}) + (\alpha_j - \alpha_{j+1}) e^{2\alpha_{j+1} z_j}}{R_{j+1} (\alpha_j - \alpha_{j+1}) + (\alpha_j + \alpha_{j+1}) e^{2\alpha_{j+1} z_j}}, \quad (3.14)$$

and the recursion is initiated by

$$R_{m-1} = e^{2\alpha_{m-1} z_{m-1}} \frac{\alpha_{m-1} + \alpha_m}{\alpha_{m-1} - \alpha_m}. \quad (3.15)$$

Here $\alpha_m = \sqrt{\nu^2 + k_m^2}$ where k_m is given by Eq. 3.7 and ν is a constant resulting from separation of variables when solving the half-space model (Price, 1962). Physically, the value $2\pi/\nu$ is a measure of the horizontal scale and uniformity of the source field (Srivastava, 1965; Price, 1962), with $\nu = 0$ representing no spatial variation in the field (Cagniard, 1953). Price (1962) however showed that even very small values of ν are important for accurate modelling. For the case of the Earth, Price finds the smallest permissible value of ν to be found by setting $2\pi/\nu$ equal to the circumference of the Earth. The largest value is found by setting $2\pi/\nu$ equal to a few times the height of the terrestrial ionosphere. Following Srivastava (1965) we take where n is the order of the Bessel function, so $n = 1$ for the external dipole field. This leads to a good match with the 3-layer spherical model, though for thick ice shells ($>30 \text{ km}$) the

results yield slightly higher values for the amplitude. This is in part due to the fact that adding the very low-conductivity ice layer means adding a layer that does not satisfy the conductivity criteria for the half-space model. The net effect is that our 5-layer model over-estimates the amplitude response and consequently over-estimates the ice shell thickness. Even so, the 5-layer model still predicts an ice shell of < 16 km, with a best-fit at 4 km. Figure 3.6 shows these results.

In Figure 3.9 we show amplitude profiles for several different combinations of ionosphere, mantle, and core conductivity. For ocean conductivities greater than ~ 3 S m^{-1} , the contribution from these additional layers is negligible. Below this value, the core and mantle are seen to have a strong influence on amplitude. The effect of induction in the core and mantle is primarily destructive interference with induction in the ocean. The result is that for a given ocean conductivity, a conductive core (and/or mantle) lowers the amplitude response of the total induced field. Values for both layer conductivity and layer thickness were varied based on published estimates (Zimmer et al., 2000; Saur et al., 1998; Parkinson, 1983; Petrenko and Whitworth, 1999; Anderson et al., 1998; Stacey, 1992). Though we have shown results for mantle conductivity of 200 S m^{-1} (dash-dotted line) this is a very high-end value that would likely only persist for the upper few kilometers of oceanic crust. Measurements of terrestrial mantle conductivity suggest that a ~ 600 km thick mantle would likely have a bulk conductivity in the range of 0.01 S m^{-1} (solid line) (Parkinson, 1983; Stacey, 1992). Comparisons with electrical properties of chondrites indicate that such conductivities are also compatible with a mantle of chondritic origin (Campbell and Ulrichs, 1969). Thus, as is shown in Figure 3.9, we expect that on Europa the amplitude response at low ocean conductivities will be dominated by the core. In all cases, we find that adding conductive mantle and core layers to our model does not significantly influence the amplitude response in the region where $A = 0.97 \pm 0.02$.

The case of a conducting ionosphere is treated separately. First we note that in order to properly compare the amplitude response with and without an ionosphere, we must scale the models with an ionosphere by a factor of $\sim (r_0/r_m)^3$. Here r_0 is the total thickness and r_m is the thickness without the ionosphere. This scaling normalizes A for thickness variations between the models, and in so doing reveals amplitude

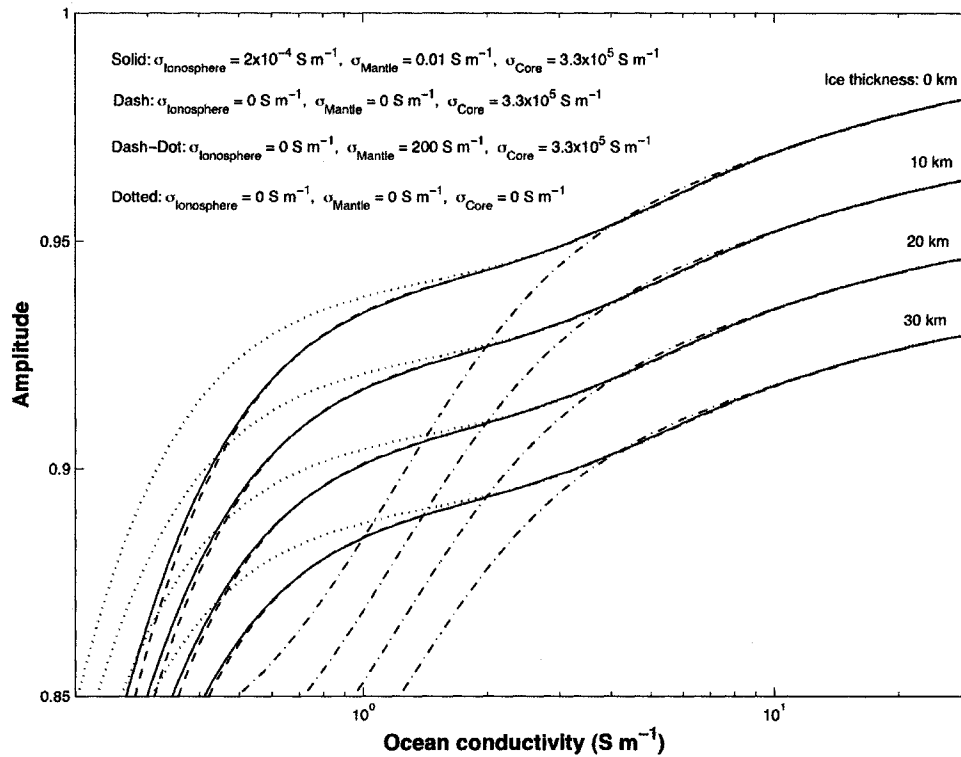


Figure 3.9: Adding a conducting core and mantle influences the total amplitude response when the ocean conductivity is small. Even for models with a very conducting core and mantle, the amplitude in the region $A \geq 0.95$ is dominated by the conductivity of the ocean and the ice shell thickness.

differences resulting from ionospheric conductivity. The scaling factor allows us to compare with published values of A , all of which are calculated for B_{ind}/B_{ext} at the surface of Europa. The cube of the ratio accounts for the $1/r^3$ change in the external and induced fields as one moves from the ice surface to the top of the ionosphere. The scaling factor is chosen such that at zero ionospheric conductivity, the ratio of the amplitudes for models with and without an ionosphere is one.

Estimates for ionospheric conductivity range from $< 5 \times 10^{-5}$ to 2×10^{-4} S m $^{-1}$ (Khurana et al., 2004; Saur et al., 1998; Zimmer et al., 2000). We take 300 km as our nominal ionosphere thickness (Zimmer et al., 2000), but we find that this parameter can be changed without impacting the results, provided the conductivity is constrained to the range above.

Figure 3.10 shows that even with the high-end value of 2×10^{-4} S m $^{-1}$ for ionospheric conductivity, there is negligible effect on the amplitude response. Only when the conductivity is approximately two orders of magnitude higher do we see significant changes in the amplitude response. In Figure 3.11 we show this relationship by plotting the conductivity of the ionosphere versus the ratio of the amplitudes for a model with an ionosphere to that without a conducting ionosphere. At high conductivities for the ionosphere, the amplitude ratio becomes greater than one, indicating that the ionosphere could drive the amplitude response to very high values if such conductivities were physically plausible. Only when the ocean conductivity is very low (e.g. 0.1 S m $^{-1}$) do we begin to see some influence of the ionosphere at realistic values for ionospheric conductivity. Even then, the net effect does not help us resolve the issue of the observed high values for the amplitude response. At very low ocean conductivities a conducting ionosphere can influence the amplitude response, but since the ocean conductivity is so low, the amplitude response is limited to values below $A \sim 0.7$. In other words, adding a conductive ionosphere could alter our interpretation of the broad range of allowed amplitudes, $0.7 < A < 1.0$ (Zimmer et al., 2000), but it has no influence when considering the much tighter constraints, $A = 0.97 \pm 0.02$, of Schilling et al. (2004).

In summary, even when we add a conducting core, mantle, and ionosphere, we find that the critical factors for achieving high values of A are the ocean conductivity

and ice shell thickness.

3.4 Implications for ice shell thickness

We have shown that for the lower end limits of the Zimmer et al. (2000) model ($0.7 < A < 0.9$) many of the most plausible solutions yield oceanic salt concentrations of less than ~ 15 g $\text{MgSO}_4 \text{ kg}_{\text{H}_2\text{O}}^{-1}$, and solutions of < 3 $\text{MgSO}_4 \text{ kg}_{\text{H}_2\text{O}}^{-1}$ are entirely possible. In other words, by terrestrial standards, the putative ocean of Europa could be much less saline than our ocean and for some solutions it could even qualify as a freshwater ocean. However, given the interplay of the conductivity, ocean thickness, and ice shell thickness in this model, we find that in order to satisfy the *Galileo*-constrained amplitude response of $A = 0.97 \pm 0.02$ (Schilling et al., 2004), the ice shell must be ≤ 15 km thick, irrespective of ocean thickness. For an ice shell of near-zero conductivity ($\sigma_{\text{Ice}} = 1 \times 10^{-10} \text{ S m}^{-1}$), we find that an ice shell thickness of ~ 4 km - comparable to that of the Antarctic ice sheet - best satisfies the $A = 0.97$ requirement. Even if we account for changes in the ice shell conductivity resulting from variations in temperature with depth, allowing the conductivity to reach $\sim 10^{-4} \text{ S m}^{-1}$ (Addison, 1969; Moore et al., 1994), we find no change in our results.

For a three-shell gravity model, the combined ocean plus ice thickness must be greater than 80 km (Anderson et al., 1998), thus implying an ocean at least 70 km thick. Trading liquid water for ice (*e.g.* 50 km water and 30 km ice) results in a poor amplitude response, one only satisfied by the lower end fits to the *Galileo* magnetometer data (Zimmer et al., 2000). If one considers the MgSO_4 constraints suggested by McKinnon and Zolensky (2003) of < 100 g $\text{MgSO}_4 \text{ kg}_{\text{H}_2\text{O}}^{-1}$, it is then impossible to satisfy the $A \sim 0.97$ constraint of Schilling et al. (2004) with the model of Zimmer et al. (2000). At $100 \text{ g MgSO}_4 \text{ kg}_{\text{H}_2\text{O}}^{-1}$ ($\sim 3.0 \text{ S m}^{-1}$) the largest amplitude response is $A = 0.94$ when the ice shell thickness is set to zero.

An upper limit on salinity is set by the saturation limits of the various salt ions. With Mg^{2+} and SO_4^{2-} as the primary cation and anion, saturation is reached at approximately $282 \text{ g MgSO}_4 \text{ kg}_{\text{H}_2\text{O}}^{-1}$ in Europa's ocean. If more MgSO_4 is added it forms a hydrate and does not dissolve. Models of plume currents in the European ocean

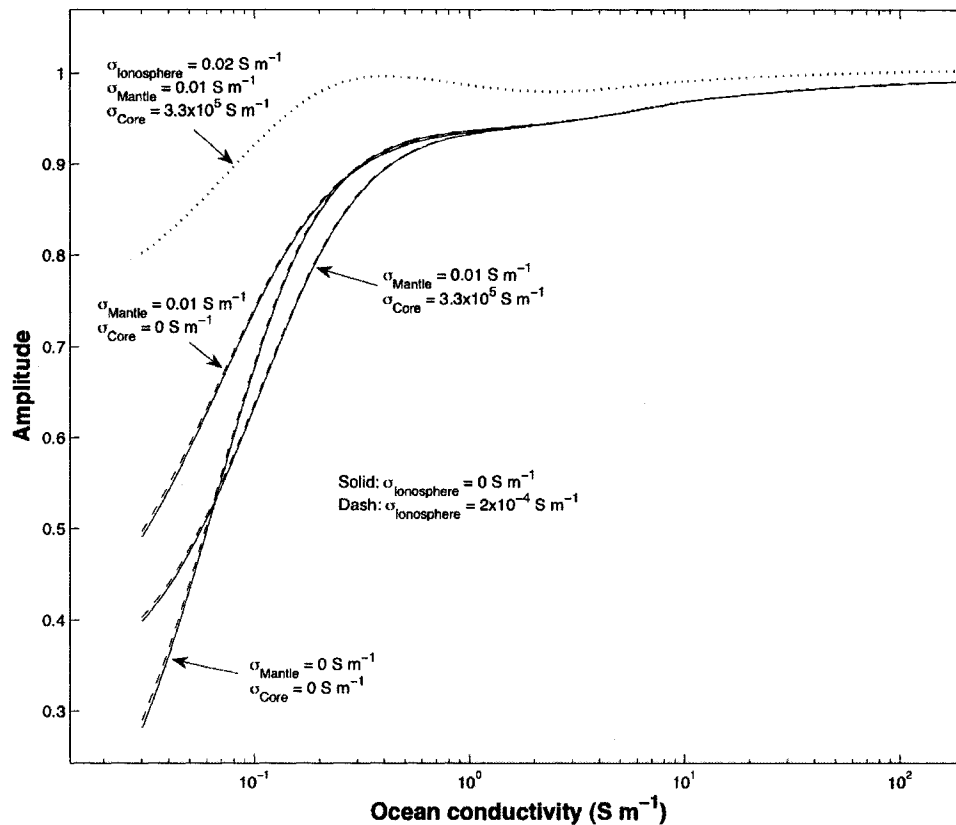


Figure 3.10: Adding an ionosphere to our model results in little change to the amplitude profile for all reasonable values of ionospheric conductivity ($\leq 2 \times 10^{-4} \text{ S m}^{-1}$). The dashed lines show results for models with an ionosphere of conductivity $2 \times 10^{-4} \text{ S m}^{-1}$ and the solid lines show results for an ionosphere of zero conductivity. As shown by the dotted line, it is only when the ionosphere reaches physically implausible levels of conductivity that an influence on the amplitude is observed. In all cases the ionosphere is 300 km thick, the ice has zero thickness, and the ocean is 100 km thick. The amplitude has been normalized for comparison to published values of A (see text).

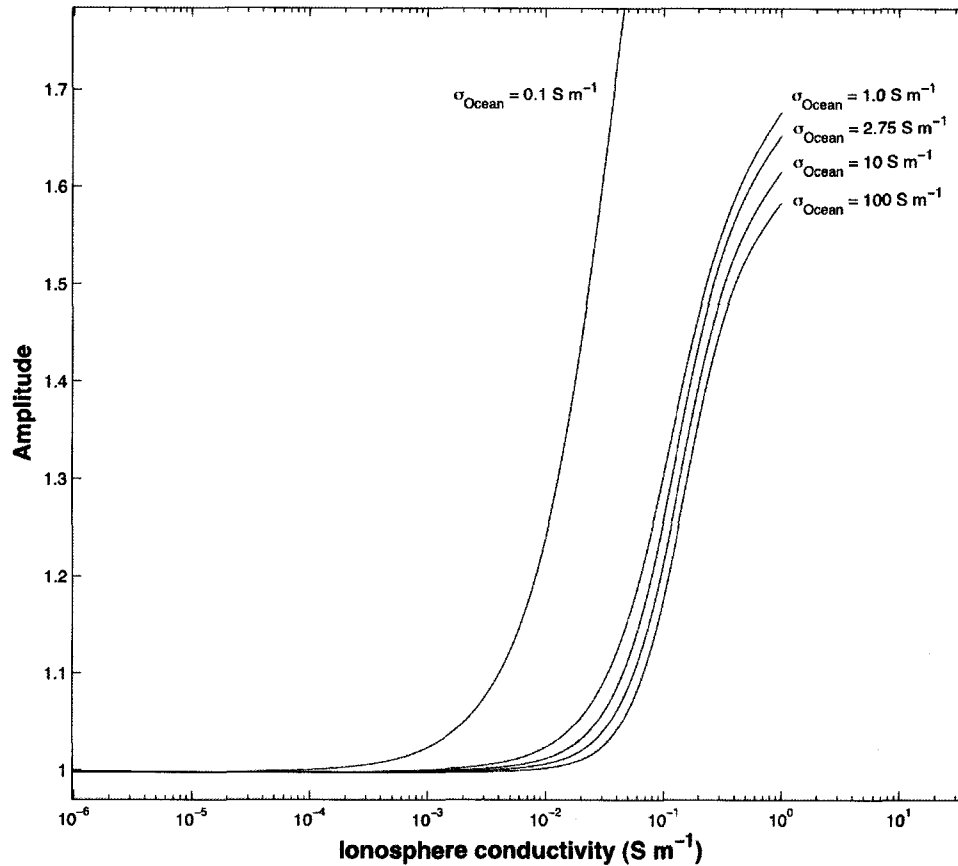


Figure 3.11: Comparison of amplitudes, A , for models with and without conducting ionosphere. Here we define the ratio of the amplitudes as A_{IC}/A_{I0} , where A_{IC} is the amplitude for a model with a conducting ionosphere and A_{I0} is the amplitude for a model without a conducting ionosphere. We then plot this ratio as a function of ionospheric conductivity for several different choices of ocean conductivity. In all cases the ratio is very close to unity for reasonable choices of ionospheric conductivity ($\leq 2 \times 10^{-4} \text{ S m}^{-1}$). The ionosphere shows a stronger effect for small values of ocean conductivity; however, such low values for the ocean conductivity are not consistent with the empirical constraints on the observed amplitude (Zimmer et al., 2000; Schilling et al., 2004).

indicate that such material is unlikely to remain in suspension and will most likely precipitate to the ocean floor (Goodman et al., 2004). Consequently, adding more than $282 \text{ g MgSO}_4 \text{ kg}_{\text{H}_2\text{O}}^{-1}$ does not help explain the induced magnetic field response of Europa. The conductivity can be pushed higher by considering sea salt (*e.g.* Na^+ and Cl^-), but even with then the conductivity of the solution will not exceed tens of Siemens per meter. As a result, invoking a salty ocean to explain the observed induced magnetic field fails unless the ice shell is thin or the amplitude is less than that determined by Schilling et al. (2004). In order to have a thick ice shell (≥ 30 km), the induced amplitude must be less than 0.92, contradictory to the results of Schilling et al. (2004).

3.5 Density constraints

While the magnetometer data cannot explicitly rule out an ocean with a very high salt concentration (*i.e.* $> 300 \text{ g MgSO}_4 \text{ kg}_{\text{H}_2\text{O}}^{-1}$, where here we consider both dissolved Mg^{2+} , SO_4^{2-} and hydrated MgSO_4 in suspension), we can look to the gravity data for some insight as to how high salt concentrations affect the density of the outer-most layer and ultimately the 3-layer model of Anderson et al. (1998). In their analysis, Anderson et al. (1998) argue that the measured value for the C_{22} coefficient for the gravitational potential of Europa is best fit by an outer layer with a bulk density in the range of 900 kg m^{-3} to 1300 kg m^{-3} . While the resolution for the moment of inertia cannot differentiate between the density of ice and water, it can be used to exclude thick oceans with a very high salt concentration. Anderson et al. (1998) choose 1300 kg m^{-3} as representative of an ice-rock mixture, but a hypersaline ocean could push densities higher and affect the mantle/core densities and distribution in the 3-layer model.

The critical measurement from the radio Doppler observation constrains the normalized (to a sphere) axial moment of inertia to 0.346 ± 0.005 . From this we calculate the maximum allowable oceanic salt concentration for several representative models. Here we use an ice density of 920 kg m^{-3} and calculate the bulk outer shell density for the combined ocean and ice shell. Table 3.2 shows how variations in oceanic salt

| Salt concentration required to achieve a bulk density of 1300 kg m^{-3} | | |
|---|--------------------------|---|
| Ocean thickness (km) | Ice shell thickness (km) | Salt concentration (g per kg H_2O) |
| 70 | 4 | 323 |
| | 10 | 357 |
| | 20 | 415 |
| | 30 | 474 |
| | 50 | 594 |
| 100 | 4 | 316 |
| | 10 | 341 |
| | 20 | 382 |
| | 30 | 424 |
| | 50 | 510 |
| 150 | 4 | 311 |
| | 10 | 328 |
| | 20 | 357 |
| | 30 | 386 |
| | 50 | 445 |

Table 3.2: Density constraints on salt concentration in Europa's ocean. Salt concentrations are calculated for various ocean and ice shell models with the constraint being that the bulk density (ice + water) equal 1300 kg m^{-3} . The ice density was taken to be 920 kg m^{-3} and liquid water density was taken to be 1000 kg m^{-3} . Thick ice shells and thin oceans permit the highest values. Many of the values shown here are beyond ion saturation for MgSO_4 (282 g per kg water), and are thus only plausible if ocean currents are sufficient to keep hydrated salts in suspension.

concentration affect bulk density for three cases of ocean thickness (70 km, 100 km, and 150 km). As is expected, increasing the ice shell thickness dilutes the bulk density and thus oceans with very high salt concentrations are only feasible for models that include a thick ice shell. For instance, if we take a 100 km ocean with a 20 km ice shell, the maximum oceanic salt concentration that still yields a bulk density (ocean + ice) of less than 1300 kg m^{-3} is 382 g per kg H_2O . For a 10 km ice shell this number reduces to 341 g per kg H_2O . Reducing the ocean thickness reduces the bulk density, thus in the lower-limit case of a 70 km ocean with 10 km shell (for a total thickness of 80 km, as per Anderson et al. (1998)) we find that the maximum allowable salt concentration is 357 g per kg H_2O . If we accept the limits of Anderson et al. (1998) and if we accept the $A = 0.97$ requirement of Schilling et al. (2004) then the ice shell on Europa must be ~ 4 km and the maximum oceanic salt concentration must be less than 321 g per kg H_2O (here we use an ocean of 76 km thick). The MgSO_4 eutectic ($\sim 22\%$ wt MgSO_4) corresponds to a solution density of 1240 kg m^{-3} (Kargel, 1991). Thus, if MgSO_4 is the dominant salt and density constraints limit the concentration to ~ 350 g per kg H_2O , then an additional 68 grams of salt per kg H_2O could reside in suspension (*e.g.* hydrated MgSO_4) or in dissolved form (*e.g.* Na^+ and Cl^-). If these additional salts are dissolved sea salt and if we assume their contribution to the overall conductivity is simply additive, then these ions add $\sim 5 \text{ S m}^{-1}$ to the overall oceanic conductivity. Even in this case the total conductivity of $\sim 23 \text{ S m}^{-1}$ still falls well within our analysis of conductivities up to 300 S m^{-1} . In order for an ocean with 282 g MgSO_4 and 68 g sea salt per kg H_2O to yield an amplitude response of $A = 0.97$, the ice shell must be less than 10 km thick.

3.6 Implications for habitability

If the ice and liquid water layers on Europa fall within the limits of Fig. 3.2 ($A = 0.7$) then, by standard definitions of 'freshwater' environments on Earth (broadly meaning $< 3 \text{ g salt kg}_{\text{H}_2\text{O}}^{-1}$ (Barlow, 2003)), Europa's ocean would be a freshwater ocean, though admittedly more salty than most terrestrial lakes. Indeed, in this case, the putative global ocean of Europa could be more like the mildly saline environment of Pyramid

Lake, Nevada than like the Earth's ocean. While the drinking water regulations of the U. S. Environmental Protection Agency recommend no more than 0.25 grams of sulfate per kilogram of water, adult humans can acclimatize to drinking water with nearly $2 \text{ g MgSO}_4 \text{ kg}_{\text{H}_2\text{O}}^{-1}$ without much discomfort (EPA, 2004; CDC-EPA, 1999). Animal toxicity (the lethal dose for 50% of the population) is in the range of $6 \text{ g MgSO}_4 \text{ kg}_{\text{H}_2\text{O}}^{-1}$ (CDC-EPA, 1999), but most livestock are satisfied provided the total salt concentration is less than 5 grams per kilogram of water (ESB-NAS, 1972). If we assume the low amplitude regime for our solution ($A < 0.8$) then it is possible that human or beast could drink the water of Europa.

What are the implications for habitability for $A = 0.97$? Terrestrial halophilic microorganisms are capable of surviving at NaCl saturation (Oren, 2002, 1994). Among these are microbes from each domain of life (*Archaea*, *Bacteria*, and *Eucarya*). Metabolic pathways for these microbes include oxygenic and anoxygenic photosynthesis (*Dunaliella salina*, *Halorhodospira halphila*), aerobic respiration (*Halobacterium salinarum*), and fermentation (*Halobacterium salinarum*). Obviously, photosynthesis is an unlikely metabolic pathway if the ice is more than a few tens of meters thick, but respiration and fermentation could be possible, especially if radiolytically produced oxidants are delivered to the sub-surface (Chyba, 2000; Chyba and Hand, 2001). Methanogens – sometimes considered a plausible model for euroman life (McCollom, 1999) – are capable of surviving in solutions near NaCl saturation if methanol or methylated amines are available (Oren, 2001). Data for MgSO_4 tolerance is limited, but microbes such as *Halobacterium sodomense* are known to survive in solutions above 2 M Mg^{2+} (equivalent to $\sim 260 \text{ g MgSO}_4 \text{ kg}_{\text{H}_2\text{O}}^{-1}$) (Oren, 1994). Thus on Europa, where the high amplitude constraint necessitates a high salt concentration, the habitability of the ocean may be limited but the conditions would not appear to exclude life as we know it.

But habitability for life is not the same as suitability for the origin of life. Experimental investigations of the influence of ionic inorganic solutes on self-assembly of monocarboxylic acid vesicles, and the nonenzymatic, nontemplated polymerization of activated RNA monomers may support the contention that life originated in a freshwater solution (Monnard et al., 2002). In these prebiotic simulation experiments,

sodium chloride or sea salt concentrations as low as 25 mM NaCl (1.5 g per kg of H₂O) were found to ‘substantially’ reduce oligomerization, with higher concentrations having worse effects. But these experiments have not yet been performed with MgSO₄. With regard to vesicle formation, if the ratio of the cation to amphiphile falls below ~ 1 , then it becomes possible for the excess amphiphile to form membranes; above ~ 2 and the amphiphile precipitates and no membrane formation occurs. The Monnard et al. (2002) results therefore suggest that the upper range of salinities implied by the *Galileo* magnetometer experiments could pose a serious challenge to the origin of life in Europa’s bulk ocean, were abiotic RNA oligomerization or amphiphile membrane formation on the critical path to the origin of life, and if the experimental results for NaCl carry over to MgSO₄.

3.7 Conclusion

Aside from surface imagery, the magnetometer results are the only dataset that provides information about the relationship between the ice shell and putative subsurface ocean. In the analyses presented here we have provided empirical constraints on both the salinity of the euroman ocean and the overlying ice shell thickness. By the low-end, poorly constrained analysis where $0.7 \leq A \leq 1.0$ (Zimmer et al., 2000) we find that a freshwater ocean is possible on Europa. By the tighter Schilling et al. (2004) constraints of $A = 0.97 \pm 0.02$, our results show that an ice shell of thickness ≤ 4 km, overlying a very salty ocean, is the best fit to the data. Thicknesses ranging from 0 to 15 km are permissible if one allows for the ± 0.02 uncertainties in the magnetic field signature. These results apply to present day Europa and are independent of any geological interpretation of surface features.

While our work provides new insight into the nature of the ice shell and ocean, we note two limiting factors in our models, the first of which is the focus of subsequent studies. First, we have assumed that the bulk ocean temperature is ~ 273 K. For a given salt concentration, higher temperatures would mean higher conductivity. If the ocean is stratified and contains layers of significant thickness with temperatures

slightly higher than 273 K, then such layers would have slightly higher conductivity. Using this relationship, a magnetometer on a future spacecraft mission could potentially help determine ocean structure and temperature profile.

The second limiting factor is simply the constraint on the amplitude. With additional analysis of the *Galileo* data, some greater resolution on this issue may be achieved. However, final answers to the questions of Europa's ice shell thickness, ocean chemistry, and habitability, await a future spacecraft mission.

Chapter 4

Chemical composition and the case against MgSO_4

The sub-surface ocean of Europa may contain near saturation levels of dissolved salts (Hand and Chyba, 2007). Based on chondrite elemental abundances and leaching experiments, many workers have argued that the predominant salt in the ocean is likely to be MgSO_4 (Fanale et al., 2001; Kargel et al., 2000; Zolotov and Shock, 2001; McKinnon and Zolensky, 2003). The case for a sulfate cation is strengthened by the spectroscopic evidence of hydrated sulfate material on the surface (McCord et al., 1998a; Carlson et al., 1999b). Empirical evidence for a dominant cation is considerably weaker. Candidates include H^+ , Mg^{2+} , and Na^+ , with Mg^{2+} being the favored cation largely because of its abundance in chondrites. Magnesium, however, should be efficiently removed from solution. Reaction of the seawater with the seafloor - either through hot active hydrothermal systems or low-temperature systems - will remove Mg^{2+} leaving Na^+ as the dominant cation. Here we model metasomatism for several different thermal models of Europa's oceanic crust and show that persistence of magnesium at high levels in solution in the ocean is unlikely. The sulfate anion is also efficiently removed during hydrothermal alteration and is replaced by sulfide, but importantly, unlike magnesium, the sulfur itself is not removed. The abundance of chlorine, as constrained by a chondritic composition for Europa, is insufficient to reach the high salt concentrations needed to explain the magnetometer results (Hand

and Chyba, 2007). The abundance of additional key ions, such as Ca^{2+} and K^+ , is also considered in the context of ocean chemistry and geological interactions. Finally, the high salt concentrations implied by the magnetometer results (Hand and Chyba, 2007) contradict the preferred ‘ K_{1a} ’ extraction model of Zolotov and Shock (2001) (12.3 g salt per kg water). We use a similar extraction model to that of Zolotov and Shock (2001) in order to achieve a salt water solution that is both geochemically consistent and in agreement with the empirical constraints set by the *Galileo* magnetometer data.

4.1 Initial Conditions: An Ocean Derived from Chondrites

The composition of Europa is generally believed to be similar to that of chondritic material (Fanale et al., 2001; Kargel et al., 2000). The formation of the Galilean satellites in the jovian subnebula likely leads to differentiation and dehydration in the case of Io, differentiation in the case of Europa, and varying levels of differentiation for both Ganymede and Callisto (Greeley et al., 2004). The subsurface ocean on Europa therefore represents an aqueous solution derived from the chemistry of chondrites. The extent of chemical extraction and alteration is poorly constrained, but several workers have used leaching results and numerical models to derive estimates for the ocean chemistry (Fanale et al., 2001; Kargel et al., 2000; Zolotov and Shock, 2001; McKinnon and Zolensky, 2003). Table 4.1 provides a summary of these results.

In most cases magnesium is found to be the dominant cation and in all cases sulfate is found to be the dominant anion. By comparison with chondritic abundances this is not surprising. However, as pointed out by McKinnon and Zolensky (2003), the leaching results of Fanale et al. (2001) are not a good model for primordial leaching on Europa. In particular, the experiments were exposed to air (*i.e.* 21% O_2) and the temperature and pressure of the experiments were considerably lower than that expected for differentiation during the formation of Europa ($T = 373$ K, $P = 1$ bar for experiments of Fanale et al. (2001), versus $T \sim 1700$ K, $P \sim 50$ kbar for the mantle

| Solution | Na ⁺ | Ca ²⁺ | Mg ²⁺ | K ⁺ | Cl ⁻ | SO ₄ ²⁻ | CO ₃ ²⁻ | Total |
|------------------------------|-----------------|------------------|------------------|----------------|-----------------|-------------------------------|-------------------------------|--------|
| (F01), leach | 1.12 | 0.802 | 0.758 | 0.079 | 0.179 | 6.36 | NA | 9.30 |
| (F01), 1 st brine | 6.04 | 4.60 | 4.91 | 0.401 | 0.720 | 42.8 | NA | 59.47 |
| (F01), 3 rd brine | 1.52 | 0.182 | 0.195 | 0.109 | 0.178 | 6.80 | NA | 8.98 |
| (K00) | | | | | | | | >500 |
| (ZS01), K _{1a} | 1.129 | 0.3863 | 1.525 | 0.0768 | 0.740 | 8.412 | NA | 12.27 |
| (MZ03) | | | <17 | | | <67 | NA | ≤ 100 |
| Earth seawater | 11 | 0.41 | 1.3 | 0.4 | 19 | 2.7* | 0.132* | 34.582 |
| Earth seawater† | 95.43 | 3.56 | 11.28 | 3.47 | 164.83 | 23.42 | 1.15 | 300 |
| CV chondrite | 44 | 240 | 1800 | 4.6 | 3.2 | 840* | 340* | 3272 |

Table 4.1: The chemistry of Europa’s ocean based on several different published models and comparisons with Earth’s ocean and chondritic abundances. The composition of terrestrial seawater is shown for comparison. Quantities are all given in units of ($g\ kg_{H_2O}^{-1}$). *Based on S, C abundances and scaling SO_4 , CO_3 accordingly. † Scaled to $300\ g\ kg_{H_2O}^{-1}$. Citations are as follows: (F01), Fanale et al. (2001); (K00), Kargel et al. (2000); (ZS01), Zolotov and Shock (2001); and (MZ03), McKinnon and Zolensky (2003).

region on Europa during formation (Hussmann and Spohn, 2004)).

Though not likely to be directly applicable to the formation of icy satellites, the leaching and extraction models yield the only empirically-based starting points for considering the chemical evolution of the europian ocean. We use these models as initial conditions for our analysis of the steady state chemistry. In order to satisfy the *Galileo* magnetometer results (Hand and Chyba, 2007; Schilling et al., 2004) we also include several saturated solutions.

4.2 Compositional Constraints

The presence of near-saturation levels of magnesium sulfate in the ocean raises the question of magnesium availability, both for the ocean and for the silicate mantle. Kuskov and Kronrod (2005) have argued for a CM, CV, or L/LL chondritic composition for Europa. The CM carbonaceous chondrites, named for the Mighei meteorite found in the Ukraine, are rich in hydrated silicates, pyroxene, and olivine (Lodders and Fegley, 1998). The CV chondrites, named for the 1910 Vigarano meteorite of

Italy, are dominated by olivine and sulfide. The low iron (L) and low iron, low metal (LL) chondrites contain mostly hypersthene, olivine, and iron-nickel (Lodders and Fegley, 1998). For Europa's bulk composition, this leads to between 11.5 (CM) and 15.3 (LL) weight percent Mg^{2+} , or a total of 5.5×10^{21} - 7.33×10^{21} kg of magnesium. Combining geophysical and geochemical constraints, these workers also argue for a metallic core radius to Europa radius ratio (R_c/R_E) of 0.29-0.43. According to Sohl et al. (2002), these radius constraints would lead to mantle olivine compositions with varying proportions of fayalite (Fe_2SiO_4) and forsterite (Mg_2SiO_4). With an R_c/R_E of 0.29 and a 150 km water layer, the mantle could have as much as 33 wt% fayalite (with 67 wt% forsterite). With a ratio of 0.43 and a 120 km water layer, the mantle would have at most 5% fayalite (95% forsterite). These two cases provide upper and lower bounds on the mantle composition. By comparison, on Earth the mantle olivine contains $\sim 90\%$ forsterite and $\sim 10\%$ fayalite (Turcotte and Schubert, 2002).

In the first case, the 955 km mantle with 67 wt% forsterite would require 9.55×10^{21} kg of magnesium. This is more than the chondritic supply derived above and implies that little, if any, Mg^{2+} would be available for the ocean. In the second case, the larger core and thinner ice shell require a mantle of lower density. The 95 wt% forsterite mantle consumes 1.21×10^{22} kg of magnesium, well above that available from an initially chondritic composition.

But how much Mg^{2+} would Europa's ocean require? A 150 km outer shell of ice and liquid water with 50 g of $MgSO_4$ per kg of water (yielding the 1050 kg m^{-3} density used by Sohl et al. (2002)) requires a total of 4.16×10^{16} kg of magnesium. The conductivity requirements set by the magnetometer data require near saturation levels of $MgSO_4$ (~ 300 g per kg water) (Hand and Chyba, 2007). This leads to $\sim 2.5 \times 10^{17}$ kg of magnesium in a 150 km water shell. In either case, the ocean requires only a small fraction of a percent of the total available Mg^{2+} . While the mantle likely harbors almost all of the Mg^{2+} , it only takes a trace amount to achieve a highly saline ocean. Therefore, from the standpoint of initial conditions there are no useful compositional limits on the magnesium cation abundance in the ocean. Interestingly, however, for a given R_c/R_E , increasing the density of the water layer while maintaining constant thickness requires decreasing the mantle density. The trade-off for magnesium sinks

| Ratio | Mg/Si | Na/Si | Ca/Si | K/Si | Cl/Si | S/Si | Fe/Si |
|-------|-------|-----------------------|-----------------------|----------------------|----------------------|--------|--------|
| | 1.023 | 5.75×10^{-2} | 6.46×10^{-2} | 3.7×10^{-3} | 5.2×10^{-3} | 0.4467 | 0.8913 |

Table 4.2: Solar abundance ratios for select elements relevant to Europa’s ocean. Values calculated based on the selected solar spectroscopic and meteorite analyses compiled by Lodders and Fegley (1998).

is therefore not self-consistent - increasing the water density consumes Mg^{2+} while decreasing the mantle density also consumes Mg^{2+} (replacing fayalite with forsterite).

We make an additional check on cation availability by considering solar abundances. Table 4.2 provides ratios of select elements to silicon based on solar abundances Lodders and Fegley (1998). The Mg/Si ratio of ~ 1 implies that olivine ($[Mg,Fe]/Si = 2$) may be present with considerable hypersthene ($[Mg,Fe]/Si = 1$), consistent with the L and LL models of Kuskov and Kronrod (2005). The high solar abundance ratio of Mg/Si indicates that there is enough magnesium to supply both the mantle rocks and to saturate the ocean.

4.3 Modeling the Steady-State Ocean Chemistry of Europa

The bulk composition of the Earth is also believed to have been derived from chondrites (Holland, 1984). Over the history of the Earth, however, the steady-state chemistry of our ocean has changed considerably due to interactions with the mantle, continental crust, and atmosphere. While much remains to be understood about the detailed stages of chemical evolution in our ocean, most models and empirical studies indicate that during all but the earliest stages of ocean evolution the chemistry of the ocean has differed considerably from what would be expected from a chondritic leaching model. Thus, while different processes may be driving the ocean chemistry of Europa, our experience here on Earth leads us to conclude that models for deriving ocean chemistry based largely on leaching models could lead to erroneous conclusions about the steady-state ocean chemistry. If such assumptions were valid, then we

could expect a terrestrial ocean dominated by salts of chondritic abundance. This, of course, is not the case on Earth.

The work of Zolotov and Shock (2001) is arguably the most comprehensive and applicable model for contemporary salt concentrations on Europa. Working from data on chemical extraction to the ocean and crust from the bulk silicate Earth and other major geological regions within our own planet, Zolotov and Shock (2001) arrive at a model for comparable extraction and differentiation within Europa. They consider several different possibilities for extraction into the ocean, but their preferred model achieves a bulk salt concentration, dominated by Mg^{2+} and SO_4^{2-} , of only 12.3 grams of salt per kilogram of water. Implicit in some of their models are several of the geochemical cycles operating here on Earth, *e.g.* continental weathering and hydrothermal circulation. Because of this implicit accounting for geochemical cycles, their models are preferable to the bulk leaching models (Kargel et al., 2000; Fanale et al., 2001), but there are still several shortcomings.

Working from their K_1 model for extraction into the upper continental crust and ocean, Zolotov and Shock (2001) arrive at their preferred K_{1a} model by scaling the potassium abundance to match the observed Na/K atomic ratio of 25 Brown (2001). Calcium and sulfate are adjusted for consistency with gypsum saturation at European temperatures and pressures. Finally, magnesium is increased to achieve charge balance. We find the above procedure to be a valid and interesting approach to quantifying the salt content of the ocean, but it represents only one possible solution. The Na/K relationship deserves a more careful treatment, as does the Ca^{2+} and Mg^{2+} relationship. Furthermore, dissolved carbon and the associated anions were ignored in the work of Zolotov and Shock (2001).

In the work presented here we adopt a sources and sinks model comparable to those used for a full accounting of terrestrial oceanic salts. We examine processes that have defined terrestrial ocean chemistry and focus on those processes that may be applicable to Europa. Two different temperature regimes are used for geochemical cycling through the oceanic crust and we examine the possible role of cycling with the ice shell as both a source and sink term for various ions. The focus is on Mg^{2+} , but the availability and residence times of other ions and anions is also considered. Based

on our accounting for sources and sinks, we then return to the model of Zolotov and Shock (2001) with the goal of achieving consistency across models. We conclude by calculating the total combined dissolved ionic composition of Europa's ocean.

4.3.1 Magnesium

Mass balance for magnesium in Europa's ocean can be expressed as (adapted from Holland (1984)),

$$m_{Mg^{2+}}^{CW} \frac{dV_{CW}}{dt} + \Theta_{Exo} \cong m_{Mg^{2+}}^{Ocean} \frac{dV_{HB}}{dt} + m_{Mg^{2+}}^{Ocean} \frac{dV_{LB}}{dt} + m_{Mg^{2+}}^{Ocean} \frac{dV_P}{dt} + \Phi_{Dolomite} + \Gamma_{Sputtering} \quad (4.1)$$

where $m_{Mg^{2+}}^{CW}$ is the concentration ($g\ kg^{-1}$) of magnesium ions entering the ocean via continental weathering, $\frac{dV_{CW}}{dt}$ is the flux of water ($kg\ yr^{-1}$) from continental weathering, Θ_{Exo} is the delivery flux ($kg\ yr^{-1}$) from exogenous sources, $m_{Mg^{2+}}^{Ocean}$ is the magnesium ion concentration ($g\ kg^{-1}$) in the ocean water, $\frac{dV_{HB}}{dt}$ and $\frac{dV_{LB}}{dt}$ represent the flux of ocean water through high-temperature and low-temperature basalts respectively, $\frac{dV_P}{dt}$ represents the flux of water reacting with mantle peridotites, and $\Phi_{Dolomite}$ is the rate of magnesium ion removal ($kg\ yr^{-1}$) resulting from dolomite formation. The loss term, $\Gamma_{Sputtering}$, accounts for losses at the surface of Europa due to sputtering by energetic ions from interactions with the Jovian magnetic field.

Unlike the Earth, where continental weathering supplies Mg^{2+} to the oceans via rivers, Europa has no obvious large source terms for magnesium. While it is possible that continental weathering could occur on Europa, *e.g.* mountain ranges piercing into the ice shell, the smooth european surface and the evidence for nonsynchronous rotation (Hoppa et al., 1999, 2001) make a strong case for a global liquid water ocean with little to no contact between the ice shell and subsurface rocks. We set the continental weathering source term to zero.

The exogenous source term, Θ_{Exo} , accounts for the contemporary surface flux of $\sim 45\ g\ s^{-1}$ of $\sim 100\ \mu m$ diameter meteoritic material Johnson et al. (2004). If material delivered to the surface does indeed reach the ocean, then this flux can be taken as the flux to the ocean, independent of the surface age (*i.e.* the surface age cancels out when calculating the flux to the ocean). For the CI, CM, CV, L, and LL chondrites

the weight percent range for magnesium (9.7-15.3 wt% Lodders and Fegley (1998)), the source flux is then approximately 5 g s^{-1} , $5 \times 10^4 \text{ kg yr}^{-1}$, or an added 1.7×10^{-21} grams of Mg^{2+} per second per kilogram of water. Even over the 4.5 Gyr history of the solar system this amounts to at most a few tenths of a milligram of Mg^{2+} per kilogram of water. The added flux during the early history of the solar system is unlikely to have increased this number by more than an order of magnitude. Consequently, this term is significant only for low-end limits on the abundance of Mg^{2+} in solution.

The sputtering loss term, $\Gamma_{Sputtering}$, is also found to be insignificant for the bulk ocean chemistry. Leblanc et al. (2002) have shown that there is a net loss of $\sim 5 - 10 \times 10^6$ sodium atoms per square centimeter per second from the surface of Europa. Over the history of the solar system this translates to a loss of $\sim 3 \text{ mg}$ of Na^+ per kilogram of ocean water. While the observed sodium cloud Brown (2001) is hard to rectify without an endogenous source (*e.g.* dissolved salts in the ocean, (Leblanc et al., 2002)), it has little implication for the bulk salt concentration. This term is also insignificant for magnesium, which is heavier than Na^+ and also potentially less prone to sputtering loss (Johnson et al., 2004).

With little in the way of sources terms, the steady state concentration of magnesium in solution is then largely a function of the starting concentration and the rates at which the sink terms extract magnesium from the ocean water. For the present analysis we ignore dolomite formation as a sink; the formation of this carbonate on Earth remains a point of considerable debate and the biogenicity of some dolomites complicates the matter. Thus little can be said about dolomite on Europa.

Using leaching and extraction models as initial conditions for salinity, we can rewrite Eq. 4.1 as a function of time and then calculate elemental abundances for a range of source and sink values throughout the history of Europa's ocean,

$$m_t = m_{t=0} - \left(m_{t-1} \frac{dV_{HB}}{dt} + m_{t-1} \frac{dV_{LB}}{dt} + m_{t-1} \frac{dV_P}{dt} \right) \frac{t}{M_{Ocean}}. \quad (4.2)$$

Here m is the moles of salt per kilogram of water at time t , $t = 0$, and $t - 1$, with t being the present and $t = 0$ being the starting point for initiating the source and sinks model (*e.g.* post-accretion, $\sim 4 \text{ Ga}$). The term M_{Ocean} is the mass of Europa's ocean in kilograms.

For the reaction of ocean water with basalt, as expressed by $\frac{dV_{HB}}{dt}$, $\frac{dV_{LB}}{dt}$ and $\frac{dV_P}{dt}$, temperature is the most important factor both in determining the chemical pathways, the reaction rates and ion exchange (Holland, 1984). Other important factors include the water to rock mass ratio (hereafter, w/r), and initial mineralogy (Bischoff and Dickson, 1975; Mottl and Wheat, 1994). Reactions between seawater and oceanic basalts and peridotites over a wide range of temperatures and pressures show a relatively rapid depletion of Mg^{2+} in the resulting aqueous solution (Bischoff and Dickson, 1975; Mottl and Holland, 1978; Seyfried Jr and Mottl, 1982; Janecky and Seyfried Jr, 1986). On Earth these reactions serve as a sink for some 5.3×10^{10} kg Mg^{2+} yr^{-1} , accounting for much of the terrestrial river flux of magnesium (12.9×10^{10} kg Mg^{2+} yr^{-1}) (Mottl and Wheat, 1994).

The sink terms in Eq. 4.1 and Eq. 4.2 represent three different temperature regimes for extracting magnesium from the ocean water. Understanding the role of each mechanism requires understanding the heat flow on the sea floor of Europa, both past and present. The contemporary seafloor of the Earth has three broad regimes for seafloor geochemistry: 1) the hot mid-ocean ridge axes ($T \sim 350$ °C), 2) the low-temperature ridge flanks ($T \sim 100$ - 300 °C), and 3) the cold ocean basins ($T < 100$ °C) (Mottl and Wheat, 1994). In the work presented here, we examine the low and high end regimes for the case of Europa.

Estimates for Europa's oceanic crust range from hydrothermally active (Thomson and Delaney, 2001; McCollom, 1999; Goodman et al., 2004; Lowell and DuBose, 2005) to possibly inactive (McKinnon and Zolensky, 2003). The temperature of the oceanic crust on Europa is unknown, but numerical models and observational results can help us put upper and lower limits on this number. On the low end, we take radiogenic decay as the only source of heating. If this is the case, then the heat flux at the ocean floor from a Europa of chondritic composition is ~ 8 mW m^{-2} , for a total heat production rate of 2.1×10^{11} W (Hussmann and Spohn, 2004). Four billion years ago this source would have generated roughly an order of magnitude more heat at the ocean floor, depending on the abundance of short-lived radionuclides such as aluminum-26.

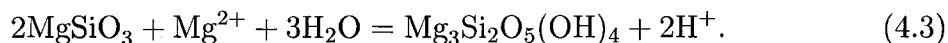
Dissipation of tidal energy in the mantle may be the dominant heat source for

hydrothermal activity. In their modelling of the orbital evolution of Io and Europa, Hussmann and Spohn (2004) consider several different scenarios for dissipation. If all of the tidal energy is dissipated in the mantle, they find heat production during the first ~ 2 Ga to be in excess of 10^{13} W (350 mW m^{-2}). With a convecting mantle, heat production stays well above 10^{13} W for the first ~ 3.8 Ga of Europa's orbital evolution. Contemporary heating in this case is $\sim 5 \times 10^{11}$ W. The reality of the situation is that tidal heating likely occurs in both the ice layer and the mantle, and the partitioning of dissipation between these two layers has changed with time. Nevertheless, the low-end set by radiogenic heating and the high end set by total tidal dissipation in the mantle gives us a range of temperature regimes for Mg^{2+} removal. In the sections to follow we consider this range of regimes and put limits on the geological uptake of Mg^{2+} . In so doing, we constrain the Mg^{2+} currently in solution in the ocean and find that in all cases it is geochemically implausible that Europa's ocean contains large quantities of magnesium in solution.

Cold basins and exothermic reactions

As a lower limit for magnesium extraction from the ocean water we consider all of Europa's seafloor to fall in the cold basin regime. We take exothermic serpentinization of mantle peridotites to be the only mechanism whereby magnesium is removed from the ocean water. Sites such as Lost City along the Atlantic Massif (Kelley et al., 2001) may serve as a good analog, though some debate remains as to the role of mantle heating in this system (Allen and Seyfried, 2004).

Laboratory measurements have shown this process to be an important sink for Mg^{2+} in seawater (Janecky and Seyfried Jr, 1986), with the conversion of enstatite into serpentine being represented by,



Simultaneously, in the absence of a free magnesium ion the following reaction liberates aqueous silica,



During their experiments Janecky and Seyfried Jr (1986) observed the dissolution of large amounts of olivine ($(Mg,Fe)_2SiO_4$) and enstatite ($MgSiO_3$) and small amounts of diopside ($CaMgSi_2O_6$). Reaction of forsterite (Mg_2SiO_4) within olivine can consume the hydrogen and silica produced in the above reactions, while fayalite (Fe_2SiO_4) dissolution will consume magnesium and produce iron in solution, which then precipitates as magnetite (Fe_3O_4),

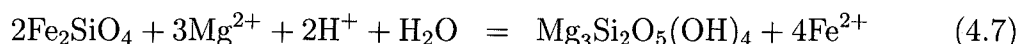
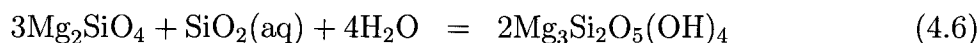
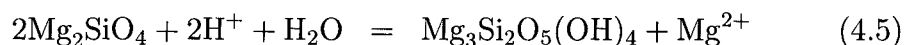


Figure 4.1 shows the results of the Janecky and Seyfried Jr (1986) experiments with lherzolite (mantle rock rich in olivine, orthopyroxene, and clinopyroxene) and dunite (also a mantle rock rich in olivine) in reaction with seawater at temperatures and pressures appropriate for terrestrial seafloor systems. The magnesium in solution is consumed on geologically rapid timescales and Janecky and Seyfried Jr (1986) comment that the reactions did not likely go to completion. Similar work with a lower water to rock mass ratio (<3) apparently achieved complete removal of Mg^{2+} from solution but this work was only published in abstract form (Sakai et al., 1979).

Based on the reaction of Mg^{2+} with enstatite (4.3) and fayalite (4.7) we can quantify an idealized scenario in which the reaction goes to completion for a given amount of available rock. Mass balance for the above equations shows that one gram of these ultramafic rocks can consume ~ 0.15 grams of Mg^{2+} . For a cubic centimeter of rock, with density 3.5 g cm^{-3} , this leads to 0.525 g Mg^{2+} consumed. If, as in the experiments, the water to rock ratio is ten, then in our idealized scenario one gram of rock interacting with ten grams of water could completely deplete the water of Mg^{2+}

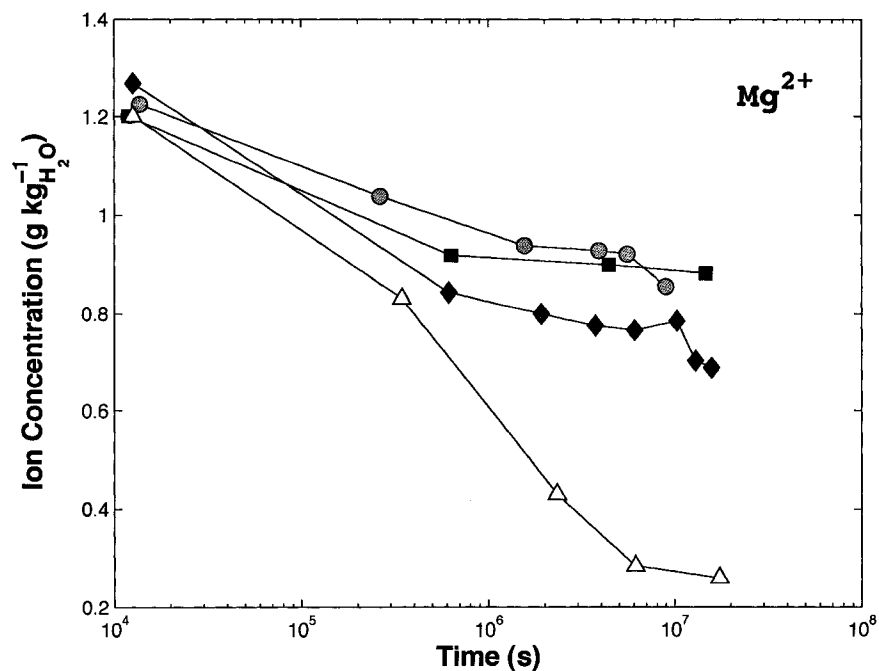


Figure 4.1: Data from Janecky and Seyfried Jr (1986) showing consumption of magnesium ions during laboratory experiments on serpentinization reactions. Red diamonds: lherzolite + seawater at 300 °C, 500 bars, $w/r=10$. Blue squares: lherzolite+seawater at 300 °C, 500 bars, $w/r=30$. Green circles: dunite+seawater at 300 °C, 500 bars, $w/r=10$. Yellow triangles: lherzolite+seawater at 200 °C, 500 bars, $w/r=10$.

if the concentration is less than 0.015 grams of Mg^{2+} per gram of water. Similarly, one kilogram of water, containing 15 grams of Mg^{2+} , could be depleted of Mg^{2+} by 100 grams of rock, or a 1 cm rock column of 28.6 cm depth (*i.e.* 100 g / 3.5 g cm^{-3}). One kilogram of water corresponds to a one centimeter water column ten meters in height. To put this another way, in an idealized scenario where the rock is completely serpentinized, a rock crust of 28.6 cm depth could deplete a 10 m deep ocean of 15 grams of Mg^{2+} per kg of ocean water. Though Janecky and Seyfried Jr (1986) suspected their reaction would ultimately go to completion, if we just take their data at face value and estimate the process to only draw down the Mg^{2+} concentration by $\sim 40\%$, then a 1 cm \times 28.6 cm rock column would only be able to deplete six grams of Mg^{2+} per kilogram of water. (Note, this scenario would be the same as saying that the reaction only occurs in 40% of the rock.) Taking as our range the conservative, data constrained value of 6 g Mg^{2+} $\text{kg}_{\text{H}_2\text{O}}^{-1}$ per 28.6 cm rock depth and our idealized value of 15 g Mg^{2+} $\text{kg}_{\text{H}_2\text{O}}^{-1}$ per cm rock depth, then for every 10 m of water a 1 cm crust of rock can deplete the water of 0.21-0.52 g Mg^{2+} $\text{kg}_{\text{H}_2\text{O}}^{-1}$.

Using these values, we can then calculate the depth of ocean crust required in order to deplete a Mg^{2+} -rich ocean on Europa. For an ocean with MgSO_4 saturation of 282 g MgSO_4 $\text{kg}_{\text{H}_2\text{O}}^{-1}$, the Mg^{2+} concentration is 57 g Mg^{2+} $\text{kg}_{\text{H}_2\text{O}}^{-1}$. For every 10 m of ocean water, a rock crust of 1.1–2.7 m will be required to deplete the water of magnesium. For an ocean of 100 km depth, a total ocean crust of 11–27 km thickness would be required in order to deplete the entire ocean of Mg^{2+} through serpentinization.

Is it likely that water within Europa's ocean could interact with rocks at such depth? Serpentinization is a self-limiting process in that the formation of the lizardite seals the peridotites off from the overlying seawater, thus closing the reaction and preventing further extraction of Mg^{2+} . Tidal tectonics and thermal cracking could, however, offset this process. Estimates for tidal and thermal cracking of Europa's seafloor are poorly constrained but are generally considered to be in the range of ~ 1 -10 km (McKinnon and Zolensky (2003) and N. Sleep, personal communication). Thus, the above numbers for total Mg^{2+} depletion through serpentinization are a factor of a few, to an order of magnitude, too large. If tides maintained cracking in the mantle to 1–10 km depth, then for a 100 km ocean we find w/r ratios of 32.5

and 3.27, respectively. A w/r of 10, comparable to the experiments of Janecky and Seyfried Jr (1986), requires mixing to a depth of 3.25 km in the mantle. On the low end, depletion of Mg^{2+} limited to 1 km of crustal rock yields a loss of 2.1–5.2 grams of Mg^{2+} per kg of water. This translates to 10.4–25.75 $\text{MgSO}_4 \text{ kg}_{\text{H}_2\text{O}}^{-1}$. On the high end, depletion of Mg^{2+} by 10 km of crustal rock yields a loss of 21–52 grams of Mg^{2+} per kg of water. This translates to 104–257 $\text{MgSO}_4 \text{ kg}_{\text{H}_2\text{O}}^{-1}$.

Based on the above calculations, we find that even for a ‘cold’ euroman seafloor in which hydrothermal reactions are limited to the exothermic processes of serpentinization, the magnesium concentration in the ocean water is likely to be depleted. The extent of Mg^{2+} depletion is primarily a function of the depth to which ocean water can react with mantle rocks. The most conservative estimates assume that the water-rock reactions are not driven to completion, and that only 1 km of the ocean floor crust has reacted with the ocean. For these scenarios, an ocean initially containing 282 g $\text{MgSO}_4 \text{ kg}_{\text{H}_2\text{O}}^{-1}$ would be depleted to levels of 255–270 g $\text{MgSO}_4 \text{ kg}_{\text{H}_2\text{O}}^{-1}$.

If, however, ocean water can react with rocks to a depth of 10 km, then the ocean could be largely depleted of Mg^{2+} . Oceanic concentrations of MgSO_4 in these models range from 25–178 g $\text{MgSO}_4 \text{ kg}_{\text{H}_2\text{O}}^{-1}$.

Axial flow through high-temperature basalts

For this case we treat the seafloor of Europa as comparable to that of the Earth’s seafloor, *i.e.* it is, or has been in the past, an active geological environment with rapid, high-temperature reactions between seawater and crustal rocks. Though contemporary Europa may be devoid of such activity, it is important to consider that active tectonic periods in Europa’s past could well have served to define contemporary ocean chemistry. Indeed, the case of a convecting mantle on Europa, as treated by Hussmann and Spohn (2004), is the closest approximation to an Earth-like seafloor on Europa.

Reactions between terrestrial seawater and oceanic basalt at high-temperature consume magnesium ions via production of smectite and chlorite (Seyfried Jr and Mottl, 1982). Much of the magnesium goes into brucite ($\text{Mg}(\text{OH})_2$) layering within

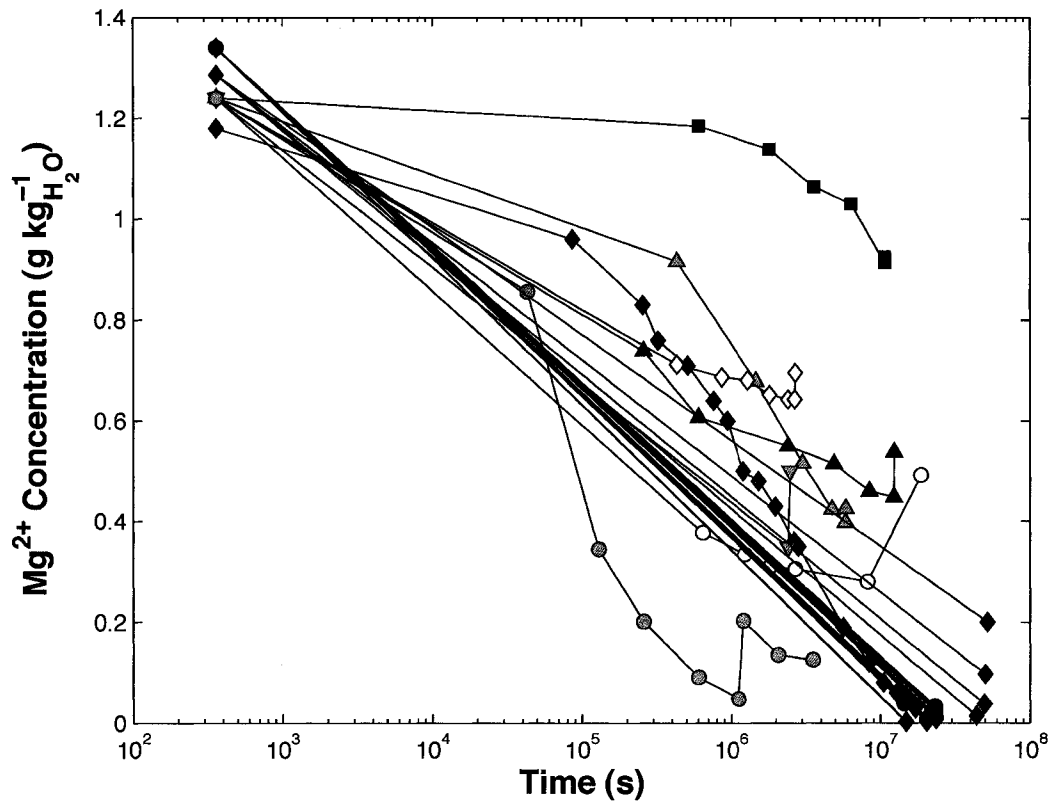
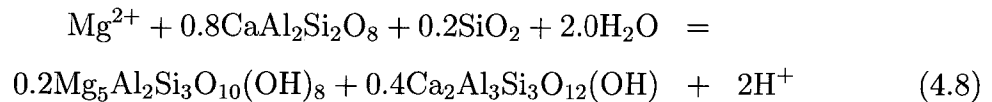


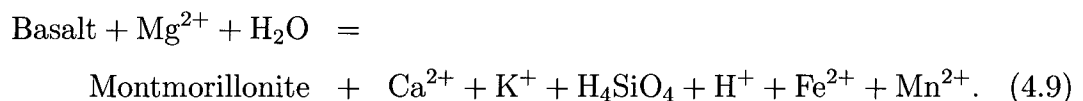
Figure 4.2: Data of seawater + rock experiments for temperatures of 100-500 °C and pressures of 500-1000 bars. Rapid decline of Mg^{2+} concentration was seen in almost all of the experiments. Data are as follows: red diamonds, 200 °C, 500 bar, (Bischoff and Dickson, 1975); blue squares, 150 °C, 500 bar, $w/r = 62$; green triangles, 300 °C, 500 bars, $w/r = 62$; yellow circles, 300 °C, 500 bar, $w/r = 62$; green inverted triangles, 300 °C, 500 bar, $w/r = 62$; blue triangles, 300 °C, 500 bar, $w/r = 62$; yellow diamonds, 300 °C, 500 bar, $w/r = 125$; green circles, 300 °C, 500 bar, $w/r = 50$, all from Seyfried Jr and Mottl (1982); black diamonds, 200–500 °C, 500–700 bar, $w/r = 1$; red circles, 500 °C, 1000 bar, $w/r = 1$, all from Mottl and Holland (1978).

secondary phyllosilicates. As an example, the plagioclase anorthite reacts with seawater at high temperature to yield the magnesium consuming phyllosilicate clinochlore (Seyfried Jr, 1987),



Bischoff and Dickson (1975), Mottl and Holland (1978), and Seyfried Jr and Mottl (1982) have shown such processes to be an effective magnesium sink for temperatures 150-500 °C and pressures of 500-1000 bar. Bischoff and Dickson (1975) find that 98% of the original Mg^{2+} is removed during seawater + basalt reaction at 200 °C and 500 bars. Similarly, Mottl and Holland (1978) find that 97% of the magnesium is consumed. Figure 4.2 shows a compilation of data for magnesium loss during seawater-rock experiments under a variety of conditions. Rock types for these experiments included diabase and basaltic glasses. Temperatures ranged from 150–500 °C and pressures ranged from 500–1000 bar. The water to rock ratios varied from 1–125. All of the experiments were run over time periods of months to years, and in all cases the magnesium ion concentration was seen to drop to levels near zero. The only notable exception to this result were the Seyfried Jr and Mottl (1982) experiments with basaltic glass at 150 °C, 500 bar, and $w/r = 62$ (shown as blue squares). Temperature was likely the critical limiting factor in that experiment as all other results, by those workers and others, show that for $T = 200$ °C and greater, Mg^{2+} depletion is efficient. Some of the Seyfried Jr and Mottl (1982) data show an increase in Mg^{2+} concentration at the end of the experiment (*e.g.* the data in yellow circles). This was due to a quenching process whereby the sample temperature was rapidly decreased to 25 °C. Despite these few excursions, the data all reflect the fact that magnesium ions will not last long in water in contact with rock at high temperatures and pressures.

Bischoff and Dickson (1975) summarize the removal of magnesium as,



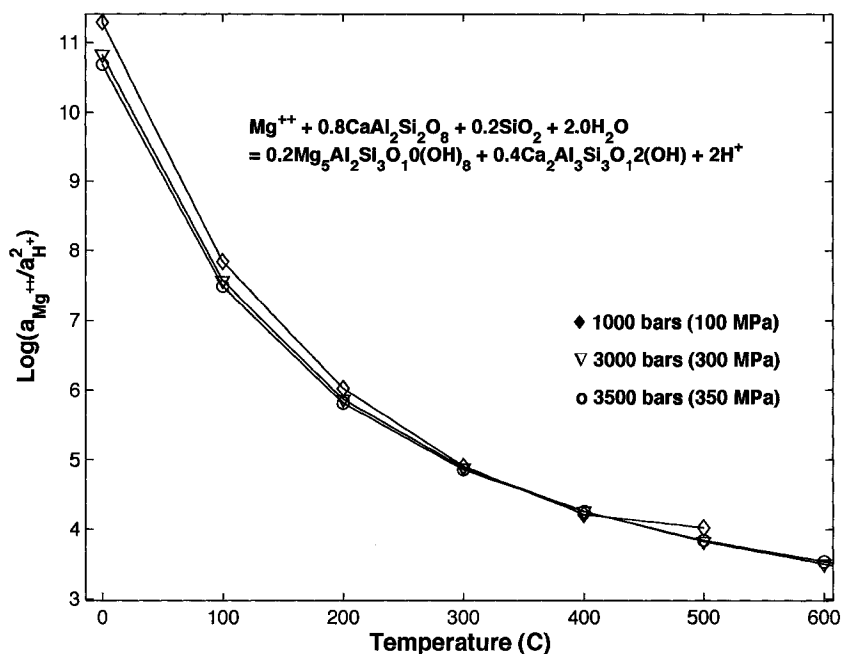


Figure 4.3: SUPCRT calculation of loss of the magnesium cation as a function of temperature and pressure during reaction with mantle rock. The pressures used in this calculation are appropriate for a range of possibilities at the european seafloor, depending on the depth of the ocean. The temperatures also cover a range likely applicable for Europa's oceanic crust, though obviously this is hard to constrain. Nevertheless, even for relatively low crustal temperatures (*e.g.* 100 °C), the magnesium cation is depleted on short geological timescales.

As shown, magnesium in solution exchanges with calcium and other cations during high-temperature, high-pressure reactions. In the presence of significant amounts of sulfur, anhydrite and iron sulfides (*e.g.* pyrite, pyrrhotite) can precipitate, removing the Ca^{2+} and Fe^{2+} from solution. Lower sulfur concentrations, and increased w/r , lead to the formation of magnetite or hematite. The removal of Mg^{2+} consumes OH^- and yields H^+ in solution, causing an initial drop in pH (Seyfried Jr and Mottl, 1982). The subsequent hydrolysis of silicates removes the H^+ , thus causing an increase in pH. However, the second reaction depends on the availability of rock with which to react.

As an added check on the removal of Mg^{2+} , the program SUPCRT (Johnson et al., 1992) was used to theoretically model the consumption of Mg^{2+} in solution as a function of temperature and pressure. Here we were able to test for conditions up to 3500 bars, greater than the highest pressures expected for Europa. The modeled reaction is typical of high-temperature basalt reactions and was taken from Seyfried Jr (1987). The reaction demonstrates magnesium metasomatism by reacting magnesium-rich water with the plagioclase anorthite ($CaAl_2Si_2O_8$). The products, clinocllore ($Mg_5Al_2Si_3O_{10}(OH)_8$) and clinozoisite ($Ca_2Al_3Si_3O_{12}(OH)$) consume magnesium, quartz, and water and cause the pH to drop by releasing protons. The log of the activity quotient is shown on the ordinate and the decrease in Mg^{2+} activity with temperature indicates the removal of the ions from solution, *i.e.* the reaction is moving to the right. Little difference was seen in the results over the range of pressures tested (1000-3500 bars). The numerical results support the experimental observations; high-temperature reaction of seawater with mantle rock on Europa should drawn down the Mg^{2+} concentration.

While temperature is a critical factor, the capacity for hydrothermal circulation to remove Mg^{2+} is also a function of rock availability. The terrestrial seawater concentration of 1.3 grams of Mg^{2+} per kg water is easily depleted, but in the case of Europa we are considering solutions that may have as much as 57 g Mg^{2+} per kg of water. To our knowledge, no experiments with high-Mg solutions and basalt have been published. Therefore we use the water to rock mass ratios (w/r) in the available data (Figure 4.2) to set constraints on the capacity for metasomatism to remove magnesium at high-T and P. Experiments show that removal of Mg^{2+} is efficient and nearly complete for $w/r \sim 125$. For seawater this means that 1 kg of rock can remove ~ 162 grams of Mg^{2+} . This is nearly a factor of three higher than our highest predictions for Mg^{2+} on Europa, thus we conclude that even for very high concentrations of Mg^{2+} , all of the Mg^{2+} will be removed as the water passes through hydrothermal systems on Europa. Removal of Mg^{2+} is efficient regardless of concentration and therefore the limiting factor for Mg^{2+} removal is the fluid flux through the rock.

To estimate the hydrothermal fluid flux on Europa, we scale from the Earth by using the terrestrial ratio of high-temperature axial heat flux to global oceanic heat

| | Earth | Europa |
|---|---------------|--|
| Mg^{2+} input (10^{10} kg yr $^{-1}$) | 13.4 (rivers) | 1.5×10^{-5} (micrometeorites) |
| Mg^{2+} sinks (10^{10} kg yr $^{-1}$) | | |
| Biogenic carbonate | 1.46 | |
| Ion-exchange | <0.97 | |
| Low-T basalt alteration | 0.24 | |
| Hydrothermal loss | 10.7–11.7 | |
| Oceanic heat flux (10^{12} W) | 32 | 0.1-10 |
| Total hydrothermal heat flux (10^{12} W) | 9 ± 2 | 0.01–6.25 |
| Water flux, Axial | | |
| 100% at 350 °C (10^{13} kg yr $^{-1}$) | 3.1-6.1 | 0.02–10 |
| 10% at 350 °C (10^{13} kg yr $^{-1}$) | 0.3-0.6 | |
| 90% at 350 °C (10^{13} kg yr $^{-1}$) | 280-560 | |
| Water flux, Off-axis | | |
| T ~ 5–15°C (10^{13} kg yr $^{-1}$) | 370-1100 | |

Table 4.3: Hydrothermal fluxes and magnesium sources and sinks on Earth and Europa. Data for the Earth are taken from Elderfield and Schultz (1996) and Seyfried Jr (1987). Scaling to Europa is as described in the text.

flux. The global oceanic heat flux on Earth is 3.2×10^{13} W (Stein and Stein, 1994). Of this, some $2(\pm 1) \times 10^{12}$ W is estimated to be from mid-ocean ridges, along the axial regions of seafloor spreading (Elderfield and Schultz, 1996). The heat flux can be converted to a fluid flux by the relation $F = H/\Delta T c_p$, where F is the mass flux (kg s $^{-1}$), H is the heat flux (W), ΔT is the temperature difference between the hydrothermal and ambient water (~ 300 K), and c_p is the heat capacity of the fluid (~ 6 J g $^{-1}$ K $^{-1}$) (Elderfield and Schultz, 1996). For Earth, converting the above heat flux to a flux of water through hydrothermal systems leads to $3(\pm 1.5) \times 10^{13}$ kg of seawater per year. As this water is cycled, essentially all of the magnesium is removed through metasomatism with the underlying rocks.

Taking the ratio of axial heat flux to global heat flux, we can estimate axial fluxes for Europa by using published values for the global flux. This yields a lower limit of $1.31(\pm 0.66) \times 10^{10}$ W and an upper limit of $6.25(\pm 3.13) \times 10^{12}$ W for high-temperature axial flow. The lower limit uses radiogenic heating and the upper limit

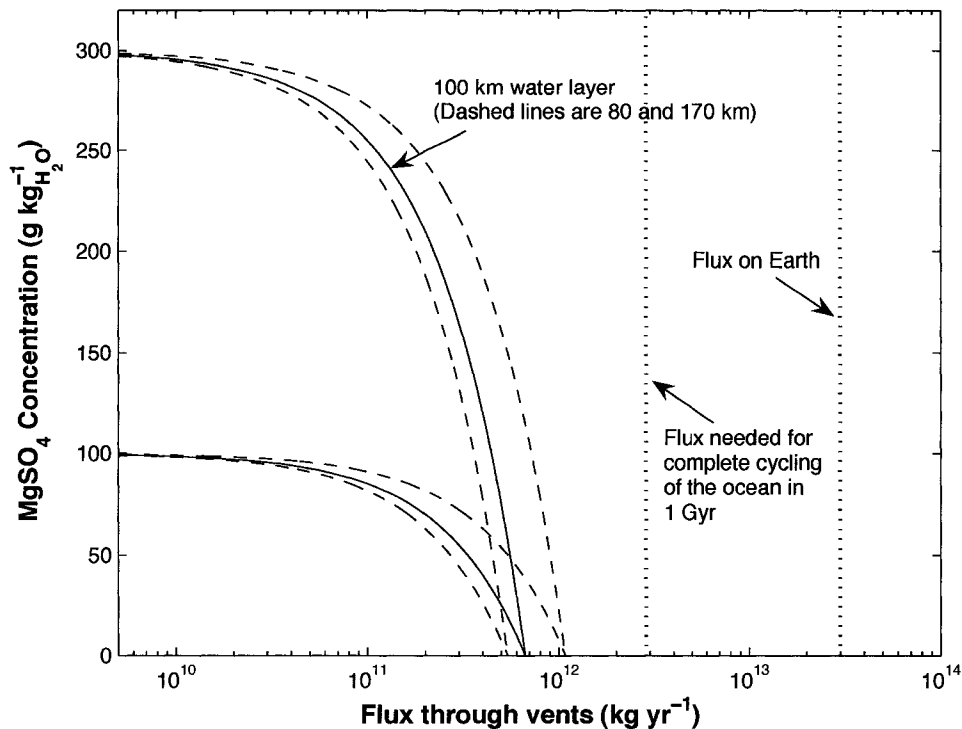


Figure 4.4: Concentration of MgSO_4 in Europa's ocean as a function of seawater flux through hydrothermal vents. The fluid flux estimated for Europa is $2 \times 10^{11} - 1 \times 10^{14} \text{ kg yr}^{-1}$, thus for all but the lowest estimates, Mg^{2+} in the ocean is largely depleted.

uses the convective mantle model of Hussmann and Spohn (2004). Without convection the upper limit is an order of magnitude less for the first ~ 3 Ga of orbital evolution. The fluid flux corresponding to these values are $1.97(\pm 0.98) \times 10^{11} \text{ kg yr}^{-1}$ and $9.37(\pm 4.69) \times 10^{13} \text{ kg yr}^{-1}$. Given the higher pressures on Europa, the heat capacity of the solution is lower and the fluxes will likely be higher than estimated here (Elderfield and Schultz, 1996). Table 4.3 summarizes our knowledge of terrestrial systems and the scaling we have used for Europa.

For a given initial concentration of MgSO_4 in the ocean water, we can calculate the contemporary concentration as a function of the fluid flux through high-temperature axial basalts. In Figure 4.4 we plot this relationship. For a given flux, the resulting oceanic concentration of MgSO_4 is the mass of MgSO_4 in the non-vented fraction

of the ocean diluted over the total mass of water in the ocean. We consider initial MgSO_4 concentrations of 300 and 100 grams per kg of water. Total H_2O layers (ice and ocean thickness) of 80, 100, and 170 km were used so as to cover the range consistent with the 3-layer models of Anderson et al. (1998). The solid black line in each case corresponds to the 100 km ocean and the two dashed lines are for the 80 km and 170 km cases. The dashed line for the 80 km case is below the solid line, while that of the 170 km case is above the solid line.

The plot shows the present day ocean concentration of MgSO_4 for a given vent flux operating over 4.3 Gyr of venting on Europa. Also shown is the flux required to cycle an entire 100 km thick ocean through hydrothermal vents in 1 Gyr. This value was found to be roughly an order of magnitude less than the hydrothermal flux on Earth. The scaling of fluid fluxes to Europa, as calculated above, covers the range $\sim 2 \times 10^{11} - 1 \times 10^{14} \text{ kg yr}^{-1}$. For all but the lowest end of this range, the ocean on Europa is found to be either completely or nearly depleted of MgSO_4 . If the flux over the past 4.3 Gyr has been only $2 \times 10^{11} \text{ kg yr}^{-1}$, then an ocean with an initial concentration of $300 \text{ g MgSO}_4 \text{ kg}_{\text{H}_2\text{O}}^{-1}$, would now have $190\text{--}245 \text{ g MgSO}_4 \text{ kg}_{\text{H}_2\text{O}}^{-1}$, for an ocean thickness of 80–170 km (a 100 km ocean yields a concentration of $208 \text{ g MgSO}_4 \text{ kg}_{\text{H}_2\text{O}}^{-1}$). Similarly, if the initial MgSO_4 concentration was $100 \text{ g MgSO}_4 \text{ kg}_{\text{H}_2\text{O}}^{-1}$, then the contemporary ocean would have $62\text{--}81 \text{ g MgSO}_4 \text{ kg}_{\text{H}_2\text{O}}^{-1}$ for an ocean thickness of 80–170 km (a 100 km ocean yields a concentration of $70 \text{ g MgSO}_4 \text{ kg}_{\text{H}_2\text{O}}^{-1}$). If the flux is just a factor of a few larger than the low end flux estimate, the MgSO_4 concentration reaches zero. In order for the contemporary ocean of Europa to have large concentrations of Mg^{2+} , the average hydrothermal flux over the past 4.3 Gyr must have been lower than $\sim 3 \times 10^{11} \text{ kg yr}^{-1}$.

4.3.2 Candidate Cations?

The calculations and data presented in the previous sections make a strong case for a Mg^{2+} depleted euroman ocean, unless the mantle and ocean floor of Europa is much less active than numerical models predict (Hussmann and Spohn, 2004). This contradicts previously published models for Europa's ocean chemistry (Kargel et al.,

2000; Fanale et al., 2001; Zolotov and Shock, 2001). It also poses a problem for the magnetometer constraint: how is high conductivity achieved if there is very little Mg^{2+} ?

Several other cations likely fill the void left by magnesium. Sodium, the dominant cation in Earth's ocean may well be the dominant cation on Europa and there is considerable observational evidence to suggest that Europa's ocean is losing sodium ions to space. The presence of a thin, extended sodium atmosphere around Europa is consistent within an endogenous source (Leblanc et al., 2002; Brown and Hill, 1996; Johnson, 2000). The observed atmospheric loss rate of Na^+ at Europa is approximately an order of magnitude larger than the source term expected from Io (Leblanc et al., 2002). This is consistent with Na^+ supplied from a subsurface ocean.

Calcium is typically exchanged with magnesium during metasomatism, but the ultimate geological fate of calcium is highly dependent on the temperature and rock type. Coupled with this is the precipitation of highly insoluble species, like anhydrite, and calcium consuming species like calcium carbonate. Calcium will certainly play a role in the ionic chemistry of Europa, but the abundance of calcium in solution is a complex function of the temperature, pH, and mineralogy of Europa's ocean and seafloor.

4.3.3 Abundant Anions?

The solar abundance of chlorine may be insufficient to yield a highly saline, thick ocean on Europa. The Mg/Cl ratio of 197 (Table 4.2) means that roughly 3×10^{19} kg of Cl should be available, but an ocean with ~ 300 grams of NaCl salt per kg of water would require 5×10^{20} kg of Cl, over an order of magnitude more than what is geologically available.

Calculations in Chapter 8 show that sulfate delivery from the surface of Europa to the sub-surface ocean will likely yield high concentrations of sulfate in the European ocean. This is independent of any geologically leached sulfur. Figure 8.2 shows moles of various compounds, including sulfate, reaching the ocean as a function of delivery period. The availability of sulfate is not likely to be a limiting factor for the salinity

or conductivity of the european ocean. Saturation and precipitation of minerals like anhydrite and gypsum is to be expected, even for low concentrations of calcium.

Cycling of sulfate through the hydrothermal vents yields sulfide, but the oxidant flux from the ice shell will then oxidize the sulfide to sulfate. Unlike magnesium, the cycling of sulfur through the vents does not yield a dramatic loss of the element itself. Instead, the redox state of the element is changed, creating a geochemical energy source of potential utility for an ocean ecosystem.

Along with sulfate, carbonate will be dissolved in Europa's ocean (Chapter 8). The exact form of the dissolved carbon will depend on the pH, but as with Earth's ocean this will lead to a balance of CO_2 , H_2CO_3 , HCO_3^- and CO_3^{2-} . Along with the primordially available carbon, the micrometeorite flux generates a source term of carbon equivalent to $\sim 10^4$ – 10^5 kg yr⁻¹ of total dissolved carbon in the ocean. While sulfate is almost certainly the dominant anion, carbonate is also available.

4.4 Surface Observations

Early results from the *Galileo* Near Infrared Mapping Spectrometer (NIMS) observations of the non-icy regions on Europa were interpreted by some workers as evidence of large quantities of hydrated magnesium sulfates (McCord et al., 1999). More recent work has argued for roughly equivalent mixtures of $MgSO_4 \cdot XH_2O$, $Na_2SO_4 \cdot XH_2O$, and $H_2SO_4 \cdot XH_2O$ (Orlando et al., 2005; Spencer et al., 2006a), with high hydration levels and the possible addition of minerals such as sodium bicarbonate (Dalton et al., 2005).

Carlson et al. (1999b, 2002) have long argued for the role of H_2SO_4 hydrate on Europa. Given the geochemical constraints on Mg^{2+} discussed in this work, we find the sulfuric acid hypothesis to be favorable. Indeed, recent analysis of high-spatial resolution NIMS spectra indicates that the endogenous claim for the non-icy material may be flawed (Carlson et al., 2005).

4.5 Consistency with Magnetometer Data

The high amplitude constraint set by the magnetometer data necessitates a highly saline ocean with a thin ice shell (Hand and Chyba, 2007). The geochemical results presented here indicate that it is hard, if not impossible, to have large quantities of Mg^{2+} in solution on Europa. Achieving high conductivity will then require a mixture of salts in Europa's ocean. Additionally, the ions of sulfuric acid may contribute to the conductivity. The surface observations mentioned above make a strong case for radiolytically produced H_2SO_4 and if this compound is introduced into the ocean it will yield H^+ and sulfate. In Figure 4.5 the conductivity versus concentration relationship for sulfuric acid is plotted along with the data shown in Chapter 3. The sulfuric acid data are from Weast and Astle (1981) and from technical specifications for instruments listed at <http://www.smartmeasurement.com>. Future work aims to explore the conductivity of mixed salt and sulfuric acid solutions.

4.6 Conclusion

The paradox of Europa's ocean chemistry is that models for the origin and formation of the ocean lead to an ocean rich in $MgSO_4$ (Kargel et al., 2000; Fanale et al., 2001; Zolotov and Shock, 2001), but terrestrial ocean chemistry has shown us that magnesium will not stay in solution in significant quantities if the ocean water is in contact with mantle rock (Bischoff and Dickson, 1975; Mottl and Holland, 1978; Seyfried Jr, 1987; Elderfield and Schultz, 1996).

Coupled with this is the fact that the magnetometer results necessitate a highly-saline liquid water layer in order to satisfy the amplitude constraints (Chapter 3). The NIMS observations of Europa's surface indicate that magnesium is likely present, but the magnetometer results could well be satisfied by a mixture of dissolved cations and anions.

To conclude we offer an alternative extraction model to that proposed by Zolotov and Shock (2001). The K_{1a} model in that work used the K_1 extraction and then reduced the abundance of salts based on several assumptions. Here we take a similar

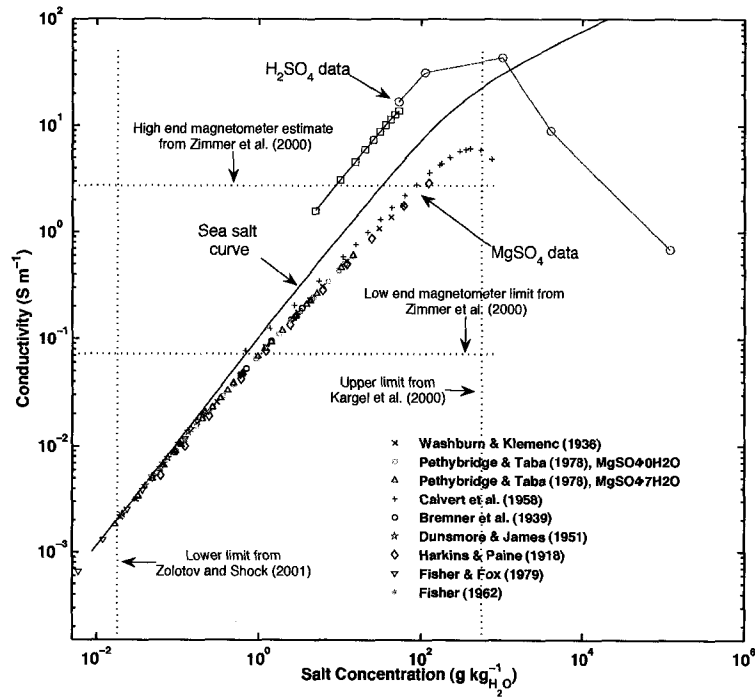


Figure 4.5: The conductivity versus concentration plot of Chapter 3 is shown again, here with the addition of data for conductivity of sulfuric acid as a function of concentration in solution. Though H_2SO_4 generally has a higher conductivity than most salts, for a given concentration, it too reaches a conductivity limit of a few tens of $S\ m^{-1}$. This does not alter our previous work, however it bears mentioning that such high concentrations of H_2SO_4 would imply a sulfuric acid dominated ocean, not a liquid water ocean.

approach, but we increase the abundance of several cations and anions based on comparable assumptions. The final solution has a total salt concentration of 101.95 g per kg of water, yielding a conductivity of $\sim 10 \text{ S m}^{-1}$. The individual ions were calculated as follows. We used the K_1 model extraction results, but instead of lowering the potassium concentration to match the observed Na/K ratio of 25 (Brown, 2001), we increased the sodium concentration to attain Na/K = 25. The total sodium and potassium in solution was found to be $40 \text{ g kg}_{H_2O}^{-1}$ and $1.6 \text{ g kg}_{H_2O}^{-1}$, respectively. This is approximately four times the concentration of sodium and potassium in the terrestrial ocean. Such concentrations are comparable to terrestrial soda lakes and geothermal springs (Arnorsson et al., 1978; Jellison et al., 1999; Mwaura, 1999). As in the K_{1a} model, we decreased the sulfate and calcium concentrations in our model so as to achieve gypsum saturation at $-0.3 \text{ }^\circ\text{C}$. These concentrations were 2.804 and $0.3863 \text{ g kg}_{H_2O}^{-1}$ respectively, identical to Zolotov and Shock (2001). The magnesium concentration was left at its K_1 value of $0.32 \text{ g kg}_{H_2O}^{-1}$. Unlike the K_{1a} model, we accounted for carbon by using the result from the K_1 model, yielding a total dissolved carbon content of $9.5 \text{ g kg}_{H_2O}^{-1}$. Potassium was also present at its K_1 abundance of $0.34 \text{ g kg}_{H_2O}^{-1}$. Finally, to achieve charge balance, we increased the chlorine content to $2.44 \text{ g kg}_{H_2O}^{-1}$, a factor of 3.3 above its K_1 concentration, but a factor of 7.8 less than the concentration found in Earth's ocean. The net effect of this simple model is that we have achieved a highly-saline, very conductive, ocean using many of the same assumptions employed by Zolotov and Shock (2001). Our model is consistent with hydrothermal removal of magnesium, the empirical constraints of sodium salts on the surface (Dalton et al., 2005), a sodium cloud around Europa (Brown, 2001), and the need for a highly-conducting subsurface layer (Zimmer et al., 2000; Schilling et al., 2004; Hand and Chyba, 2007).

Chapter 5

Laboratory simulation of the surface electron irradiation environment of Europa

Chemistry on the icy surface of Europa is heavily influenced by the 7.9×10^{10} keV $\text{cm}^{-2} \text{s}^{-1}$ incident particle flux resulting from the Jovian magnetic field. The majority (>75%) of this energy is in the form of high energy (<10 MeV) electrons. We have constructed a 10^{-8} torr vacuum chamber equipped with a 100 keV electron gun and He-compressor cryostat in order to simulate the electron irradiation environment of Europa.

5.1 Laboratory studies of electron radiolysis

For our simulation of the surface radiation environment, we are largely replicating the trailing hemisphere, electron dominated, processes. The role of protons and ions has been examined in some detail (Moore et al., 1991; Moore and Khanna, 1991; Johnson and Jesser, 1997; Ip et al., 1998; Moore and Hudson, 1998, 2000) as has the role of UV irradiation on ices (Bernstein et al., 1999; Allamandola et al., 1988; Bernstein et al., 1995; Johnson et al., 2004). Little work has been done on the role of high energy electrons under european conditions (Johnson et al., 2004).

In addition to trailing hemisphere radiolytic processes, the electron irradiation environment is also of interest for the near-surface, *i.e.* slightly deeper into the surface, ice chemistry. On average, the incident ions and photons have stopping depths in the range of 0.04-10 μm (for ice of unit density). Electrons, on the other hand, typically reach depths of 0.62 mm (Cooper et al., 2001). The most energetic electrons (~ 50 MeV) are estimated to have an average range of approximately 20 cm while ions of similar energy would have stopping depths of one to two orders of magnitude less (Cooper et al., 2001). The radiolytic chemistry below a few tens of microns, therefore, can largely be attributed to the high energy electrons.

5.2 Experimental set-up

5.2.1 Laboratory hardware

We have constructed a high-vacuum, stainless steel chamber capable of replicating the temperatures and pressures of planetary and astrophysical ices. Mounted onto the chamber is a He-cryostat with a range down to a few Kelvin. A Varian 300 l/s turbo-pump, backed by an oil-free Alcatel fore-pump, produces pressures of $\sim 5 \times 10^{-9}$ torr. Ice films of diameter ~ 0.8 cm and a few microns in thickness are grown by vapor-deposition on a gold mirror mounted on the cryostat's cold finger. An external manifold allows for mixing of volatiles prior to deposition. For the results presented here, however, all ices are neat H_2O . To ensure purity of our ices, nanopore de-ionized water was heated and quenched at least three times to remove dissolved gases before mounting onto the manifold in preparation for deposition.

A 100 keV electron gun mounted on the chamber, perpendicular to the plane of the ice film, provides high-energy electron irradiation of the ice sample. A Faraday cup on a rotation stage within the chamber allows for monitoring of the electron beam current directly above the ice sample. For the results presented here, electron energies of 4 - 20 keV, and beam currents of 10's to 1000's of nA were used.

A Fourier-transform infrared spectrometer (FTIR) is used for transmission spectroscopy of the sample before, during, and after irradiation. The ice-coated mirror is

illuminated by the FTIR at 22° angle of incidence. Refracted radiation passes into the ice and is reflected by the gold surface, giving a double pass through the ice film. Spectra with 4 cm⁻¹ resolution and 1024 co-added spectra are collected continuously, with a ~9-minute integration period for each spectra. Figure 5.3 provides a diagram of the complete experimental set-up.

For all experiments, three spectra were collected prior to ice deposition and prior to irradiation. The average of the either the pre-deposition or pre-irradiation spectra was then used for calculating absorbance,

$$\text{Abs} = -\log_{10} (I_{\text{Sample}}/I_{\text{Baseline}}), \quad (5.1)$$

where I_{Sample} and I_{Baseline} are the spectral intensities of the sample and reference baseline. In all results presented here the average of the pre-irradiation spectra was used for the absorbance baseline. Using the pre-irradiation average allowed for removal of the broad H₂O peak at ~3200 cm⁻¹ that dominates the region near the H₂O₂ 2850 cm⁻¹ band.

During deposition film thickness was determined by monitoring the optical depth at 3500 cm⁻¹, and also by measuring fringes using laser interference transmission through the ice sample. The absorbance, A , at 3500 cm⁻¹ measured relative to the pre-deposition spectra yields the film thickness via the relation,

$$d = \frac{\tau}{[4\pi k/\lambda]} \quad (5.2)$$

where the bracketed quantity is the absorption coefficient and k is the temperature-dependent imaginary component of the index of refraction at wavelength λ (Hudgins et al., 1993). The optical depth of the film, τ , is given by,

$$\tau = \frac{\ln(10)}{2} \cdot \text{Abs} \cdot \cos(\phi), \quad (5.3)$$

where ϕ is the angle of refraction in the film. Interference fringing of a 6328 Å laser transmitted through the ice film allowed for an additional check on film thickness (Sill et al., 1980). Each fringe of the interference sinusoid corresponds to a half wavelength

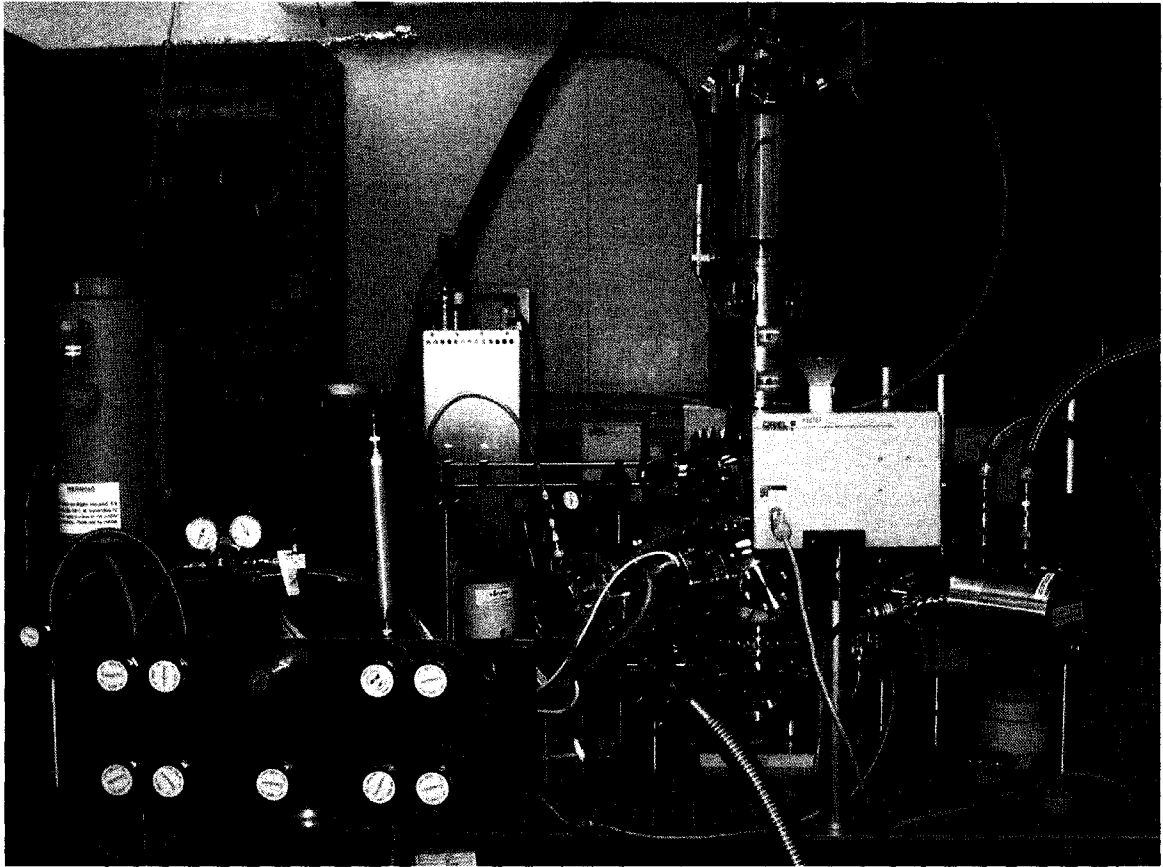


Figure 5.1: Image of the laboratory set-up showing the vacuum chamber, cryostat, and electron gun along with the gas mixing manifold (bottom left) used to prepare mixtures of volatiles for growth of thin ice films on the gold mirror at the end of the cryostat cold finger.

thickness, or $\sim 0.3 \mu\text{m}$. By counting fringes during deposition we were able to gauge our film thickness.

Ice films were grown to a thickness comparable to, but greater than, the projected range of the energetic electron. Johnson (1990) provides an approximation for the range, $R(E)$, as a function of electron energy in keV,

$$R(E) \approx R_\rho E^\alpha. \quad (5.4)$$

The exponent α is empirically determined to be 1.76 and for unit density material

(*e.g.* ice, $\rho \sim 1 \text{ g cm}^{-3}$), $R_\rho = R_1 = 0.046 \text{ }\mu\text{m}$. Irradiating films slightly thicker than $R(E)$ ensures that essentially all of the energy from the electron beam is deposited into the ice film.

Species ejected from the film during irradiation or evolved from the film during warming were detected *in-situ* with a MKSTM quadrupole mass-spectrometer, residual gas-analyzer. This instrument detects volatile species over a 1-300 a.m.u. range.

5.2.2 Software for data analysis

All computational methods, techniques, and algorithms for processing data from the Fourier-transform infrared spectrometer (FTIR), residual gas analyzer (RGA), and matrix-assisted laser desorption/ionization (MALDI) instruments were written by the author. Programs were written in C with much of it utilizing Matlab for graphical capabilities. The author wrote and developed a series of programs and functions hereafter collectively referred to as the ‘speclib’, or spectral function library.

The speclib library was written to take as input the ‘.mat’ data files from the FTIR, the ‘.WBG’ data files from the RGA, or the text (‘.txt’) files from the MALDI instrument. Key functional capabilities include batch processing of an entire sequence of FTIR spectra taken during an irradiation experiment. With an absorbance denominator spectrum file identified, the code can plot the spectral sequence, integrate a specified band, and plot the integrated band absorption as a function of irradiation dose for the specified experiment.

The spectra, plots, and figures in the following chapters were all generated using functions within the speclib.

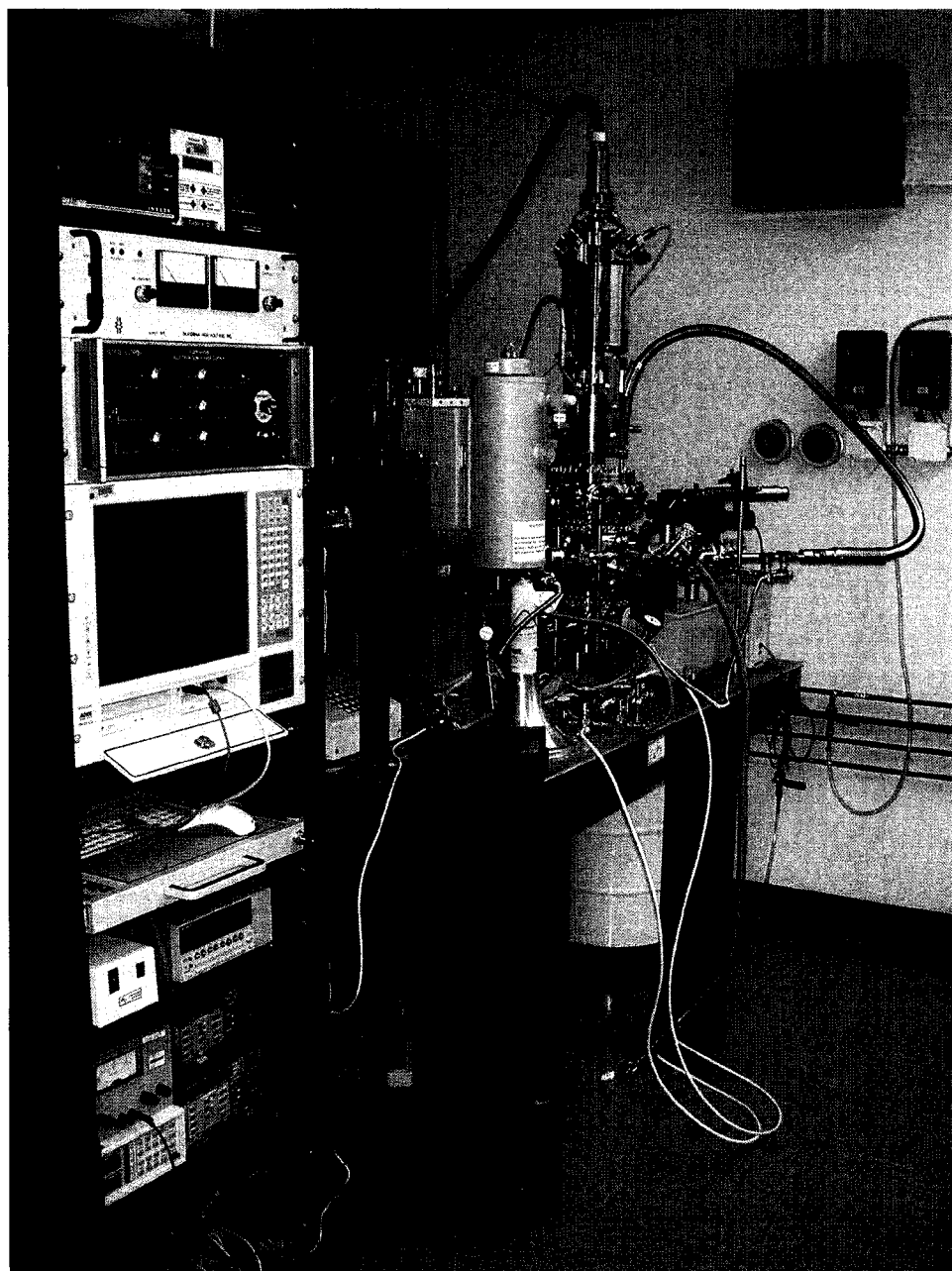


Figure 5.2: Shown here is the vacuum chamber and electron gun along with the rack-mounted computer and controllers for the various instruments. This image was taken prior to construction of the gas manifold and prior to the acquisition of the He-cryostat. The original cryostat, shown here, used liquid nitrogen.

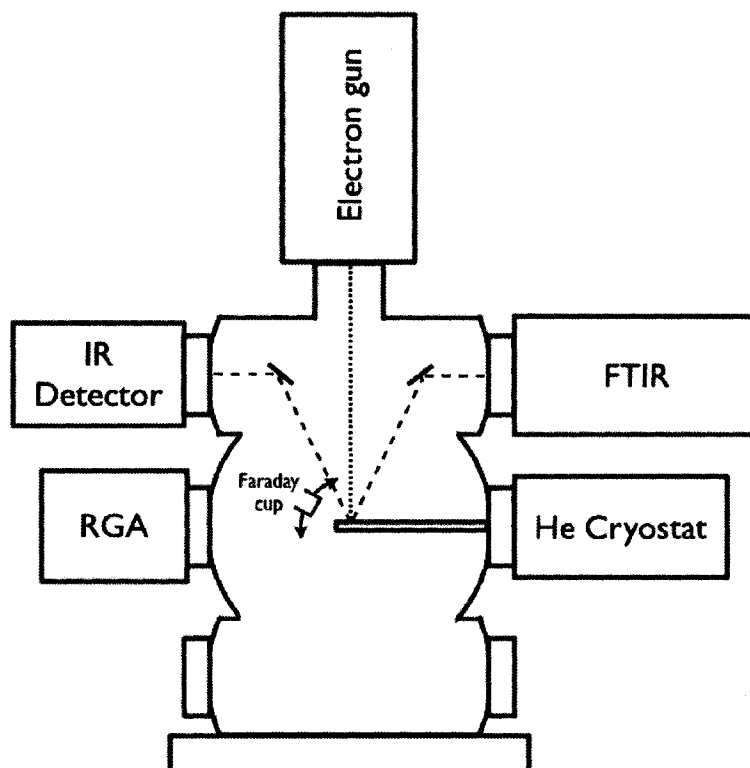


Figure 5.3: Diagram of the laboratory set-up. Ice films are deposited and grown on the end of the cryostat cold-finger and then irradiated with high-energy electrons from the electron gun. In-situ spectral analysis is accomplished in transmission with the Fourier-transform infrared spectrometer (FTIR) and a mass-spectrometer capable of detecting volatile species of 1-300 a.m.u. (RGA). The Faraday cup allows for measurement of the electron beam current throughout the experiment.

Chapter 6

H₂O₂ production by high-energy electrons on icy satellites as a function of surface temperature and depth into the surface

Chemistry on the icy surface of Europa is heavily influenced by the incident energetic particle flux from the Jovian magnetosphere. The majority (>75%) of this energy is in the form of high energy (<10 MeV) electrons. We have simulated the electron irradiation environment of Europa with a vacuum system containing a high-energy electron gun for irradiation of ice samples formed on a gold mirror cooled with a cryostat. Pure water films of $\sim 2\text{--}5\ \mu\text{m}$ thickness were grown at 100 K and then either cooled (to 80 K), warmed (to 120 K) or left at 100 K and subsequently irradiated. The irradiation energy and current was varied between different experiments in order to determine the production and destruction of H₂O₂ as a function of incident energy, dose rate, and temperature. The production of hydrogen peroxide (H₂O₂) was monitored by observation of the $2850\ \text{cm}^{-1}$ ($3.5\ \mu\text{m}$) band. Experimental results are then used to numerically integrate energy deposition, H₂O₂ production, and H₂O₂ destruction as a function of depth into the surface ice of Europa. Steady-state concentrations as a function of depth into the ice are calculated. We find that H₂O₂

materials, specifically O_2 and perhaps CO_2 and SO_2 , may depend in part on H_2O_2 as a necessary precursor in the pathway toward production. Figure 6.1 shows possible pathways toward O_2 as determined by Cooper et al. (2003), all of which have H_2O_2 as a key intermediary. From an astrobiological perspective, H_2O_2 and oxidants derived from H_2O_2 may play a critical role in maintaining biologically useful redox gradients in the subsurface ocean if mechanisms for delivering the surface material to the subsurface are identified.

Laboratory simulation and production of H_2O_2 has been shown with protons, ions, and UV (Moore and Hudson, 2000; Gomis et al., 2004b,a; Loeffler et al., 2006) as with low-energy electrons (Sieger et al., 1998; Pan et al., 2004). Some high-energy electron work has been done, but the low temperatures used during irradiation (12 K) make it hard to justify as a system comparable to the surfaces of icy satellites (50-150K) (Zheng et al., 2006).

Here we specifically focus on electrons with energies > 5 keV and temperatures relevant to Europa and the warmer regions of Enceladus (80-120 K). High-energy electrons dominate the surface irradiation flux (Cooper et al., 2001) and they penetrate deeper into the surface than any other energetic particle. Furthermore, after impact, much of the energy from protons and ions is dissipated as energetic electrons (Johnson, 1990; Mozumder, 1999). For these reasons, understanding the role of high-energy electrons in H_2O_2 production is critical for a comprehensive understanding of the surface oxidants chemistry.

Stopping power is also an important factor and is explored in the work presented here. Figure 6.2 shows a comparison of stopping powers for electrons, protons, and alpha particles. Ions such as S^{n+} and O^{n+} lie in the region above the line for alpha particles. Also shown is a line marking the high-end of the energy spectrum for the incident particle flux at Europa (Cooper et al., 2001; Paranicas et al., 2001). As can be seen, the stopping power for electrons with initial energies ≤ 10 MeV continually increases as the electron loses energy. This means that as the electron penetrates into the surface ice, the bulk of its energy will be deposited in the last $\sim 1/4$ to $1/3$ of its projected range. Translated into H_2O_2 production, this means that much of the energy made available for radiolysis comes toward the end of the electron path.

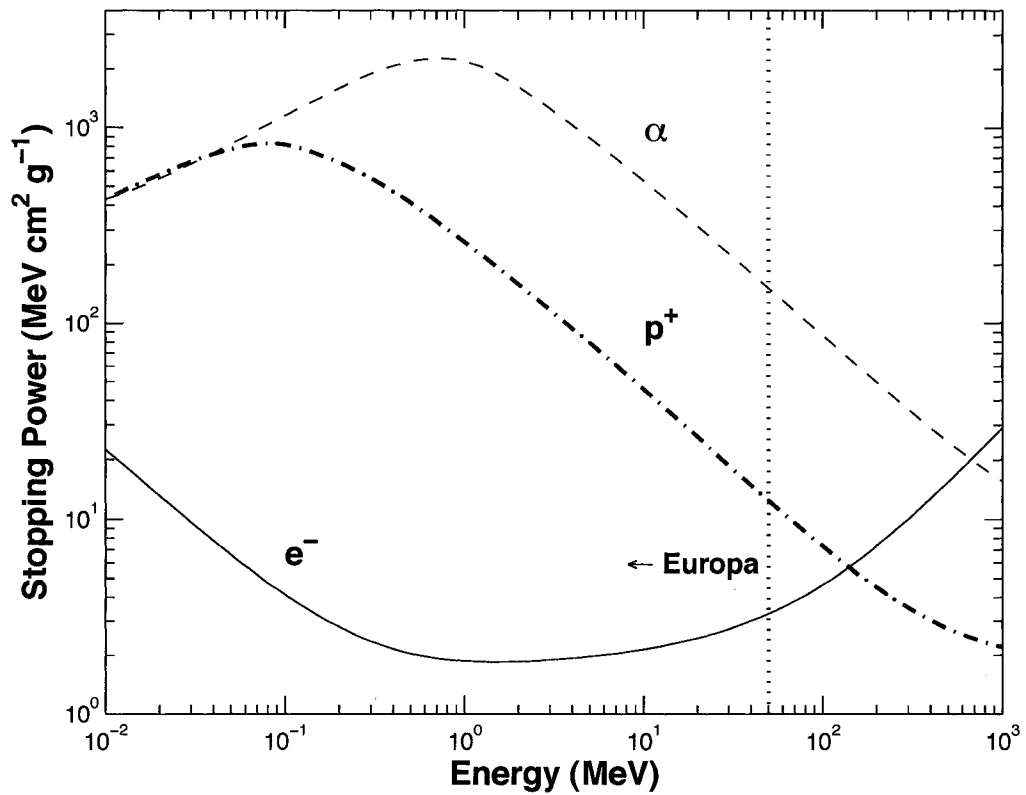


Figure 6.2: Stopping power as a function of energy for electrons, protons, and alpha particles. Show also is a line indicating the upper end of Europa's energy spectrum for incident particles. Higher energy particles (*e.g.* 100 MeV) are certainly present, but the bulk of the flux is <10 MeV (Paranicas et al., 2001). The data used here are from Berger et al. (2005).

Thus, not only do energetic electrons constitute the dominant source of particles at Europa, but they also efficiently deposit their energy at depth, potentially below the destructive influences of micrometeorite impacts and sputtering. Understanding the role of stopping power in H_2O_2 production requires quantifying both the production and destruction cross-sections for H_2O_2 as a function of energy. In this paper we describe our experimental results and numerical fits for these parameters and apply them to a depth profile calculation for steady-state H_2O_2 abundance across a range of energies and over the 2π steradians visible to a given volume element of ice on or below the surface.

6.2 Experiment Details

The laboratory set-up and instruments used for this series of experiments is as described in Section 5.2. Here I provide additional details pertaining to the specifics of H_2O_2 production and analysis.

For our experiments on the temperature dependence of H_2O_2 production all films were deposited at 100 K and then either cooled to 80 K, warmed to 120 K, or kept at 100 K. The films were then irradiated with 10 keV electrons at beam currents of 100 nA. Experiments on H_2O_2 production and variation with dose rate were conducted at 100 K with 10 keV electrons and beam currents ranging from 10 nA to $3 \mu\text{A}$. Finally, experiments examining the relationship between the incident energy of the electrons and H_2O_2 production were performed with 100K films and beam currents of 10-100 nA. The incident electron energies were 8 keV, 10 keV, 12 keV, and 15 keV.

Production of H_2O_2 was measured by observing the change in band area from 2750 cm^{-1} to 2920 cm^{-1} . Depending on the shape of the background water band, a quadratic or linear fit to the spectrum through this region was used to determine the band integration area. Figure 6.3 shows a typical spectrum during irradiation and the quadratic fit (x^2) used to generate the H_2O_2 band area. Also shown is the H_2O_2 data from the *Galileo* Near-Infrared Mapping Spectrometer (NIMS) (Carlson et al., 1999a). Integrated band areas are used in our results in order to easily allow for variations in choice of the strength of band absorption, A . Several values have been published for

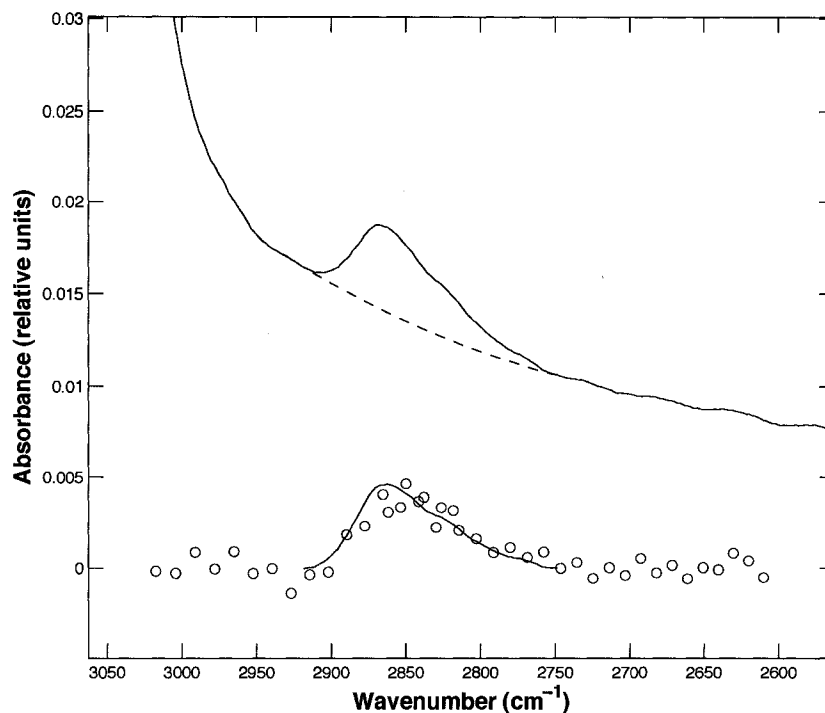


Figure 6.3: The 2850 cm^{-1} band of hydrogen peroxide arises on the shoulder of the broad $\sim 3500\text{ cm}^{-1}$ water band during electron irradiation. Here we have used a quadratic fit to the curvature of the H_2O band in order to extract the H_2O_2 band. Linear fits are used when the background H_2O band is also linear. Shown here is the band with the quadratic fit (upper lines) and the quadratic baseline subtracted H_2O_2 band. Also shown for comparison are the Near-Infrared Mapping Spectrometer (NIMS) data of the H_2O_2 band observed on Europa (Carlson et al., 1999a).

the H_2O_2 line (Moore and Hudson, 2000; Loeffler et al., 2006). Based on the more recent results of Loeffler et al. (2006) and personal communication with Loeffler and Teolis, we choose $A_{80K} = 4.9 \times 10^{-17}$, $A_{100K} = 5.1 \times 10^{-17}$, $A_{120K} = 5.3 \times 10^{-17}$ cm molecule⁻¹ for our 80K, 100K, and 120K films respectively.

6.3 Results

6.3.1 Temperature dependence of H_2O_2 production

Figure 6.4 shows results for variation in H_2O_2 production as a function of temperature. The area of the 2850 cm⁻¹ band, integrated in most cases from 2750 cm⁻¹ – 2920 cm⁻¹, is shown as a function of cumulative dose. Initial net production is seen in the early rise of the band area, after which H_2O_2 production is balanced by H_2O_2 destruction and a steady state plateau is reached. Saturation is reached at $\sim 10^{19}$ eV cm⁻² for the 80 K and 100 K films, but at 120 K it is unclear whether saturation is truly achieved. By $\sim 5 \times 10^{19}$ eV cm² the integrated band area appears to stabilize near ~ 0.03 cm⁻¹ and we use these data points for calculating steady-state H_2O_2 concentration.

For band saturation at each temperature we calculated mean values by using the last twenty integrated band areas. Using the specified band absorption for each temperature we then calculate steady-state H_2O_2 concentrations. At 80 K we find the steady-state column density, $\{H_2O_2\}$, leads to an H_2O_2 concentration of $0.043 \pm 0.002\%$ by number relative to water. At 100 K and 120 K this number falls to $0.029 \pm 0.001\%$ and $0.0063 \pm 0.0006\%$ respectively. The errors on these values represent plus or minus one sigma standard deviation from the mean value.

Assuming that H_2O_2 production is a first-order process, *i.e.* that it is not dependent on the concentration of a previously produced precursor, then the change in the H_2O_2 column density, $\{H_2O_2\}$, with time is the difference between the production of H_2O_2 from irradiated H_2O and the destruction of H_2O_2 by irradiation,

$$\frac{d\{H_2O_2\}}{dt} = \Phi_0 \bar{\sigma}_C \{H_2O\} - \Phi_0 \bar{\sigma}_D \{H_2O_2\}. \quad (6.1)$$

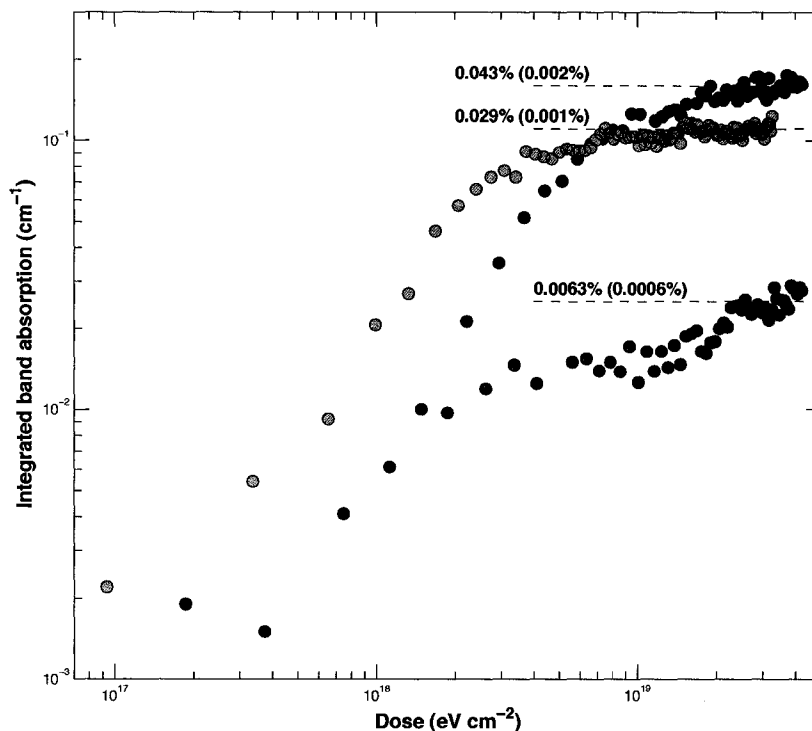


Figure 6.4: Hydrogen peroxide production as a function of temperature. Ices at $T = 80$ K (blue), 100 K (green), and 120 K (red) were irradiated with 10 keV electrons and the growth of the 2850 cm^{-1} band was monitored. Shown to the right of each plateau is the approximate percent by number abundance of H_2O_2 relative to water in the ice film, calculated using the band absorptions $A_{80K} = 4.9 \times 10^{-17}$, $A_{100K} = 5.1 \times 10^{-17}$, $A_{120K} = 5.3 \times 10^{-17}\text{ cm molecule}^{-1}$ (Loeffler et al., 2006; Moore and Hudson, 2000). Errors are given as a deviation of plus or minus one sigma.

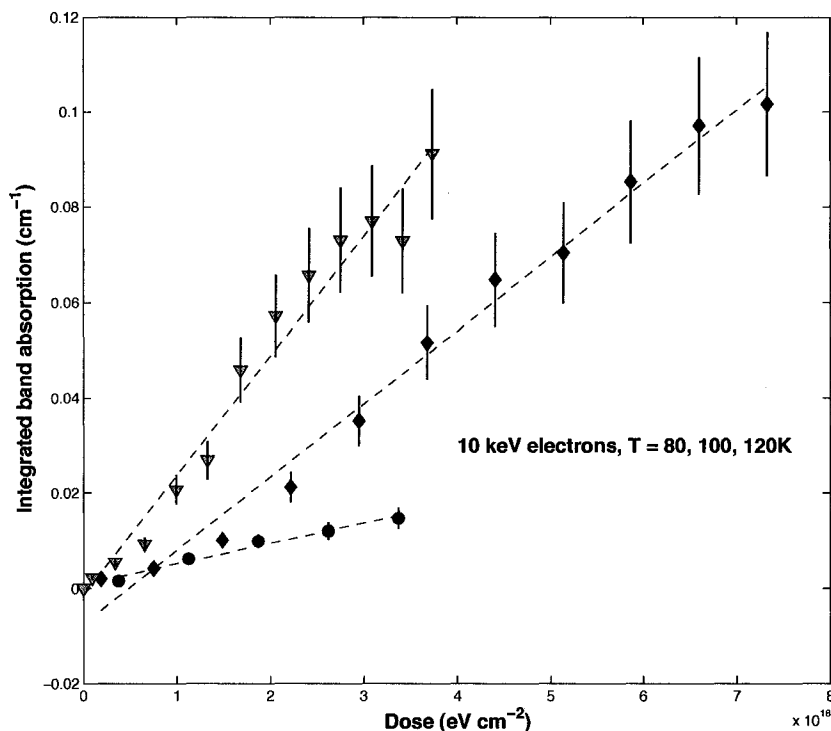


Figure 6.5: The initial rise in H_2O_2 production is used for determining G -values at different temperatures (see text). Linear fits yield the values shown and are given in units of number of molecules produced per 100 eV. Error bars in band area are $\pm 15\%$, most of which is due to uncertainties in integration limits for the initial rise of the 2850 cm^{-1} H_2O_2 band.

Here Φ_0 is the unidirectional flux of electrons ($e^- \text{ cm}^{-2} \text{ s}^{-1}$) and $\bar{\sigma}_C$ and $\bar{\sigma}_D$ are the H_2O_2 creation and destruction cross-sections in cm^2 . The production term for H_2O_2 in Eq. 6.1 can also be written in terms of the G -value, defined as the number of molecules created per unit of absorbed energy (commonly taken as 100 eV): $G[H_2O_2] = \bar{\sigma}_C\{H_2O\}/E_0$. Writing Eq. 6.1 as a function of accumulated dose, D , we find,

$$\frac{d\{H_2O_2\}}{dD} = G - \frac{\bar{\sigma}_d}{E_0}\{H_2O_2\}. \quad (6.2)$$

Here $dD = E_0\Phi_0 dt$, where E_0 is the incident electron energy in eV. The parameter

$\bar{\sigma}_D$ is the density weighted destruction cross-section. Defining $D_0 = E_0/\bar{\sigma}_D$ and integrating Eq. 6.2 then yields,

$$\{H_2O_2\} = GD_0 (1 - e^{-D/D_0}) \quad (6.3)$$

The low beam currents used in our experiments allow us to determine G-values for H_2O_2 production because we can track the rise to steady-state. Figure 6.5 shows linear fits to the low-dose data points, *i.e.* those points corresponding to net H_2O_2 production prior to reaching steady-state. Each spectrum was carefully examined to ensure proper adjustment of integration limits as the 2850 cm^{-1} bands grew with dose. The slope of the linear fit is related to the G-value by a factor of $100/A$, where A is the band absorption strength as defined above. We find $G[H_2O_2]_{80K} = 0.031/100\text{-eV}$, $G[H_2O_2]_{100K} = 0.049/100\text{-eV}$, and $G[H_2O_2]_{120K} = 0.008/100\text{-eV}$. Values for $\bar{\sigma}_D$ are then solved for by using $\{H_2O_2\}_{saturation}$ and $\{H_2O_2\}/dt = 0$ which leads to,

$$\bar{\sigma}_D = \frac{E_0 G}{\{H_2O_2\}}. \quad (6.4)$$

Table 6.1 provides values for these parameters. The errors on integrated band area are small (few percent) compared to the uncertainty on values for A ($\sim 10\%$), thus the errors given for G-values are dominated by that uncertainty. We use an A value uncertainty of $\pm 5 \times 10^{-18}\text{ cm molec}^{-1}$ as per Loeffler et al. (2006).

Loeffler et al. (2006) and Moore and Hudson (2000) have also investigated the temperature dependence of H_2O_2 production. Our results for H_2O_2 saturation are considerably lower than results for 50-100 keV Ar^+ and 100 keV H^+ (Loeffler et al., 2006), and the are lower than most of the results for 0.8 MeV H^+ (Moore and Hudson, 2000). Loeffler et al. (2006) finds steady-state values of $\sim 0.14\%$ by number relative to water for irradiation of 80K ice with protons. Their results for 50-100 keV Ar^+ at 80 K range from $\sim 0.036\text{--}0.15\%$, the low-end of which is comparable to our results for 10 keV electrons at 80–100 K. Moore and Hudson (2000) infer steady state concentrations of $0.07\text{--}0.28\%$ by number abundance, but these values may have been overestimated by nearly a factor of two because they did not use the more recent experimentally

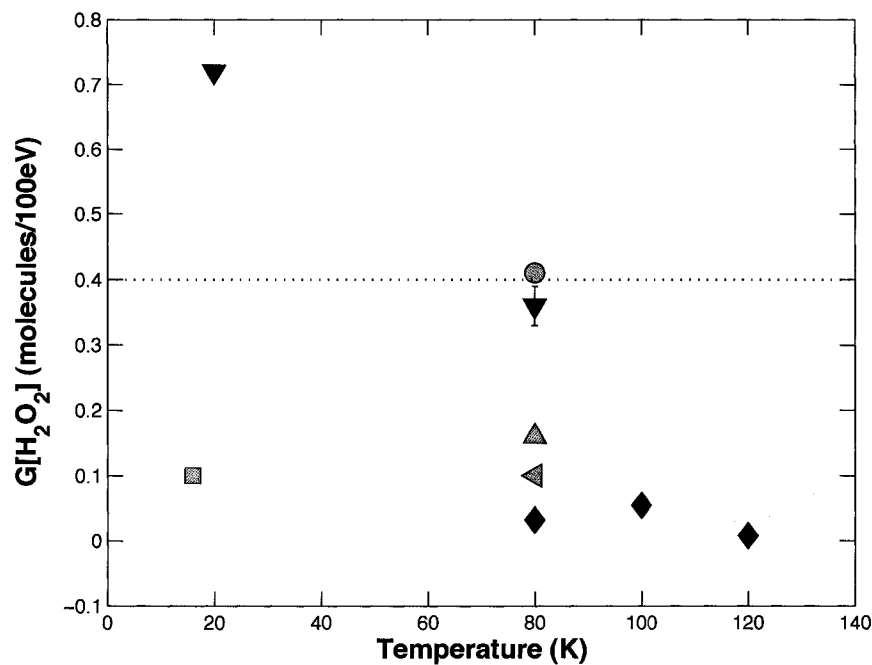


Figure 6.6: Comparison of published G-values for hydrogen peroxide production in ice at various planetary and astrophysical temperatures. The results of this work are shown by the blue diamonds, that of Loeffler et al. (2006) by the inverted red triangles, and that of Moore and Hudson (2000) by the green circle, square, triangle, and sideways triangle. The circle is for results of irradiation in H_2O+O_2 ices, the triangle for O_2 overlaying H_2O , the sideways triangle for CO_2+H_2O ice, and the square is for neat H_2O . The dotted line shows the value of $G[H_2O_2] = 0.4$ used by Carlson et al. (1999a). Our results with high-energy electrons show much lower production rates than that of ions and protons.

| Temp. (K) | Energy (keV) | Current (nA) | G[H ₂ O ₂] (molec./100eV) | $\bar{\sigma}_D$ 10 ⁻¹⁵ cm ² | $\bar{\sigma}_C$ 10 ⁻¹⁹ cm ² |
|--------------|-----------------|-----------------|---|---|---|
| 80 | 10 | 100 | 0.031±0.003 | 0.97 | 3.95 |
| 100 | 10 | 10 | 0.049±0.004 | 2.27 | 6.16 |
| 120 | 10 | 20 | 0.008±0.001 | 1.7 | 1.01 |
| 100 | 6 | 20 | 0.027±0.004 | 1.13 | 5.01 |
| 100 | 7 | 20 | 0.035±0.004 | 1.7 | 5.79 |
| 100 | 8 | 20 | 0.036±0.004 | 2.1 | 5.36 |
| 100 | 10 | 10 | 0.049±0.004 | 2.27 | 6.16 |
| 100 | 12 | 20 | 0.050±0.004 | 3.1 | 5.48 |
| 100 | 10 | 10 | 0.049±0.004 | 2.54 | 6.16 |
| 100 | 10 | 20 | 0.055±0.004 | 3.84 | 7.05 |
| 100 | 10 | 35 | 0.036±0.004 | 1.92 | 4.62 |

Table 6.1: H₂O₂ G-values, density-weighted production cross-sections ($\bar{\sigma}_C$), and density-weighted destruction cross-sections ($\bar{\sigma}_D$), as a function of temperature, electron energy, and electron beam current.

determine A values of Loeffler et al. (2006).

In Figure 6.6 we show the collective work on G-values as a function of temperature. Our work is consistent with much lower production rates at lower temperatures, *e.g.* as shown by Loeffler et al. (2006), however we have not investigated the low temperature range (<50 K) and thus cannot conclude a specific trend with high-energy electrons. Moore and Hudson (2000) find a range of values for G[H₂O₂] at 80 K, each corresponding to a different ice mixture. Their 80 K H₂O+CO₂ results and ~16 K pure H₂O results are comparable to what we find and what Loeffler et al. (2006) find at 120 K.

6.3.2 H₂O₂ production and electron beam current

Europa's flux of 7.9×10^{13} eV cm⁻² s⁻¹ (~ 12.5 μ W cm⁻²) translates to a current of ~ 1.2 nA cm⁻² for 10 keV electrons (Cooper et al., 2001). To compare our laboratory fluxes with those of Europa we examined H₂O₂ production over a range of beam currents at constant electron energy (10 keV) and temperature (100 K).

Our beam is unstable at currents of ~ 1 nA, thus we cannot directly probe the

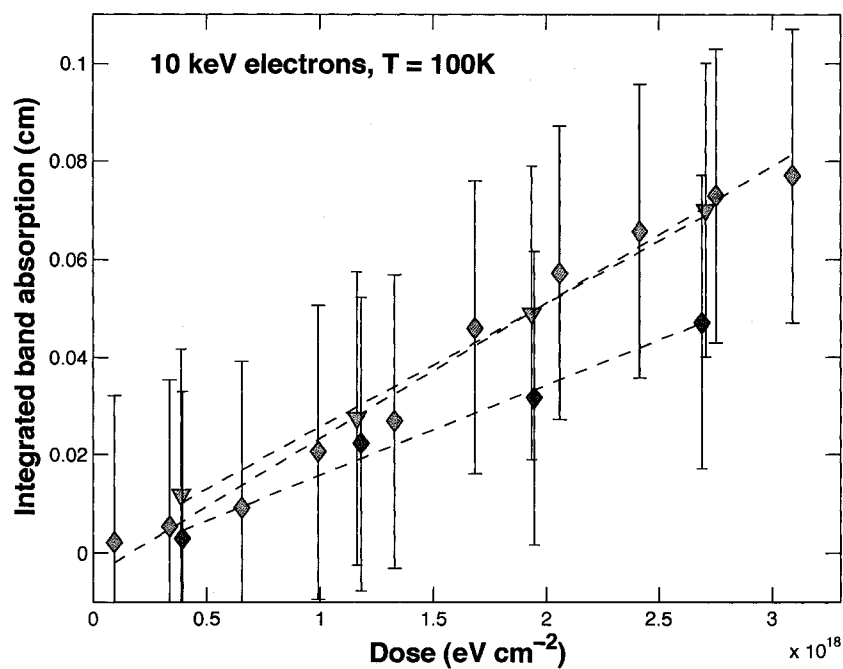


Figure 6.7: Initial production of H_2O_2 at 100 K for 10 keV electrons at several different beam currents. The measured G-values at 10 nA, 20 nA, and ~ 40 nA are all $\sim 0.047/100\text{eV}$. Experiments were also performed with higher currents (*e.g.* hundreds of nA to μA) but production was too rapid to yield reliable measurements of the G-values.

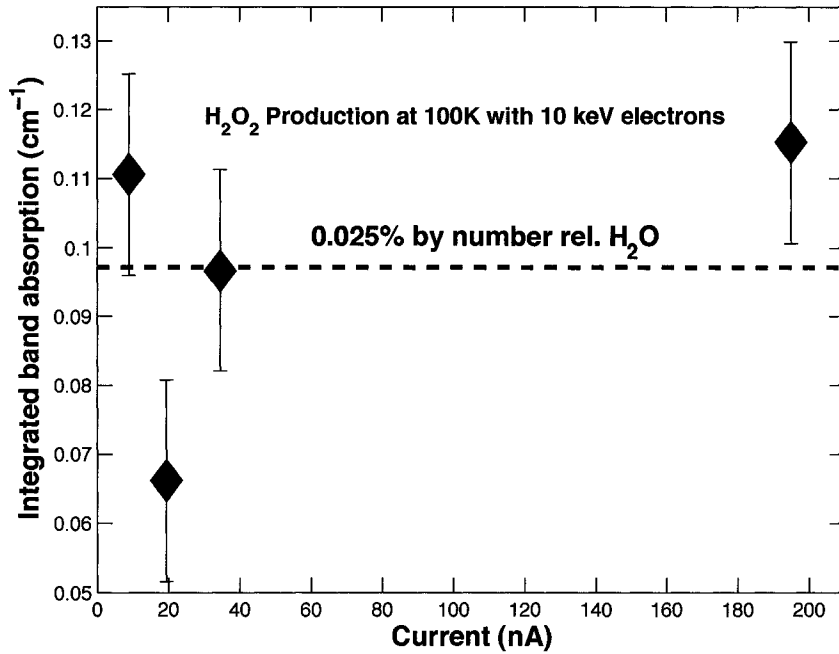


Figure 6.8: H_2O_2 saturation for 10 keV electrons at 100 K over a range of electron beam currents occurs at $\sim 0.025\%$ by number H_2O_2 relative to water.

europian flux at 10 keV. At 10 nA, however, we are able to reliably monitor the current and observe the rise in H_2O_2 . We also ran experiments at 20 nA, 35 nA, 195 nA, and several μA . Results for production and G-values are shown in Figure 6.7.

No significant variation in production rates was observed as beam current was increased. The measured G-values all fall in the range $G[\text{H}_2\text{O}_2] = 0.036\text{--}0.055 \pm 0.004$ per 100 eV with a mean value of $0.047 \pm 0.004/100\text{-eV}$. The consistency of these results gives us confidence that our laboratory results can serve as an accurate indicator of processes on Europa and other icy worlds.

Steady-state H_2O_2 levels were also found to change little over the range of beam currents explored. The mean value was $0.025 \pm 0.004\%$ by number relative to water. Figure 6.8 shows integrated band absorption and resulting saturation levels for variations in beam current.

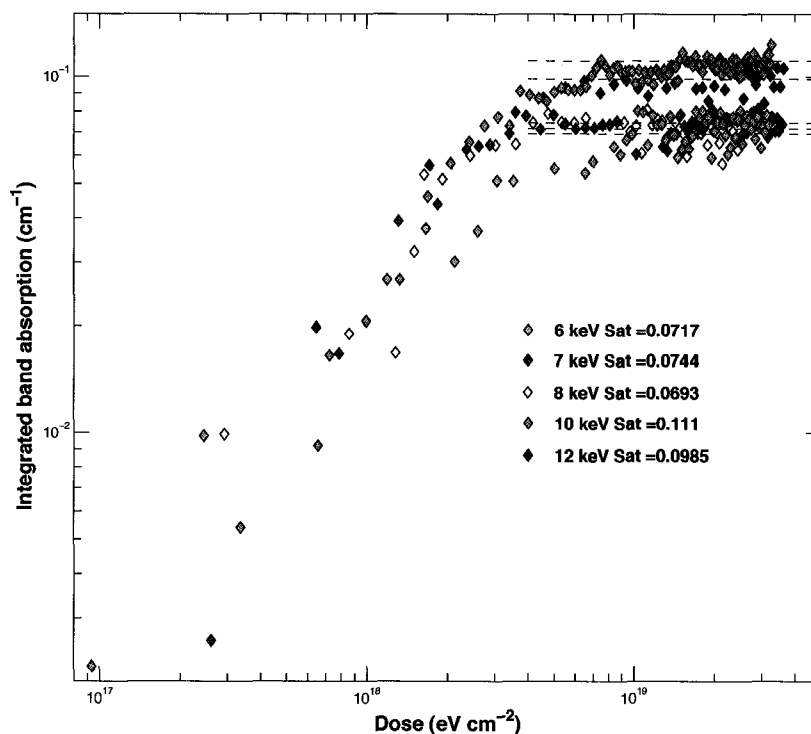


Figure 6.9: Hydrogen peroxide production as a function of incident electron energy. Electrons of 6, 7, 8, 10, and 12 keV were used to irradiate 100 K water ice. All beam currents were in the range of ~ 10 's of nA. Saturation values for integrated beam absorption are shown with dashed lines and are given to the right of each energy value.

6.3.3 H_2O_2 production and electron energy

Ice films at 100 K were irradiated with electrons of energy $E_0 = 6$ keV, 7 keV, 8 keV, 10 keV, and 12 keV. In all cases films were deposited at 100 K and grown to a thickness slightly greater than the projected range, as determined by Eq. 5.4. Results for initial production and saturation, based on integration of the 2850 cm^{-1} band, are shown in Figure 6.9. G-value measurements based on the low-dose initial rise of H_2O_2 are shown in Figure 6.10.

The determination of G-values is useful for understanding production within the

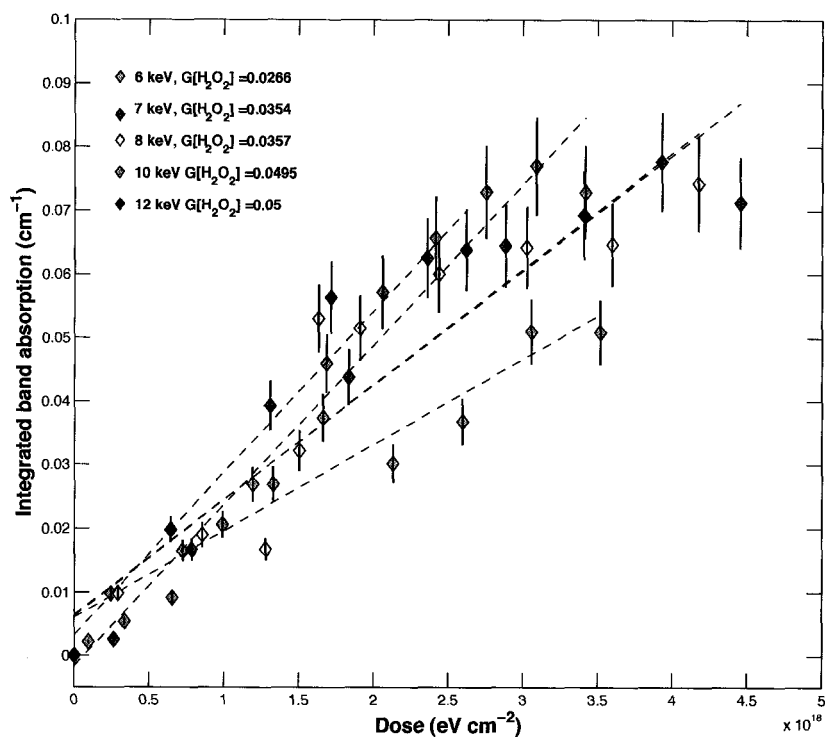


Figure 6.10: Linear fits to initial production rates are used to generate G-values for H_2O_2 at various incident electron energy levels (see text).

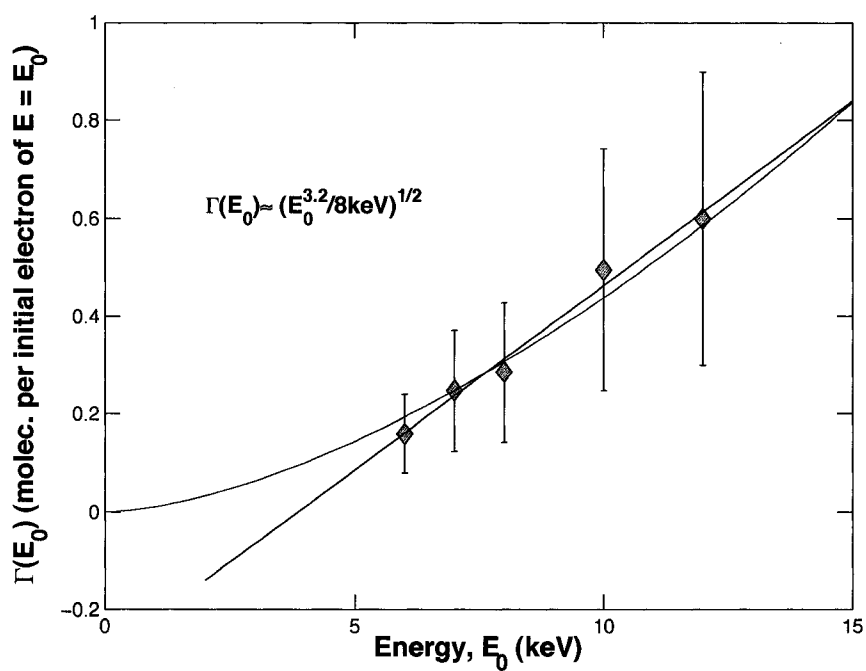


Figure 6.11: The number of molecules of H_2O_2 produced per incident initial electron of energy E_0 is plotted as a function of E_0 , measured in keV.

ice film as a function of energy absorbed, but it provides little insight into the variations of production efficiency for a single electron of energy E_0 as it passes through the ice and imparts an energy dE per unit distance dx . To examine this process we define the parameter Γ as the molecules produced per initial electron and $\gamma = d\Gamma/dE$ as the number of molecules produced per electron per unit energy loss. We can then write Eq. 6.1 as,

$$\frac{d\{H_2O_2\}}{dF} = \Gamma - \sigma_D\{H_2O_2\}, \quad (6.5)$$

where F is the cumulative electron flux, with $dF = \Phi_0 dt$. Integration yields,

$$\{H_2O_2\} = \Gamma F_0 (1 - e^{-F/F_0}) \quad (6.6)$$

where $F_0 = 1/\sigma_D$ and $\Gamma(E_0) = GE_0$. Figure 6.11 shows a plot $\Gamma(E_0)$ vs. E_0 using our laboratory results. A fit of the form,

$$\Gamma(E_0) \approx \left(\frac{E_0^{3.2}}{8\text{keV}} \right)^{1/2} \quad (6.7)$$

is used to find Γ for any energy E_0 with the condition that $\Gamma \rightarrow 0$ at $E_0 = 0$. We use this relationship in Section 6.4.1 to examine production with depth into the ice.

Also of interest for determining the role of initial energy, E_0 , in H_2O_2 steady-state and depth profiles is the effective destruction cross-section, $\sigma_D(E)$, at energy E . This is different from the measured cross-sections, $\bar{\sigma}_D$, which represent the density-weighted average destruction cross-section over the range of the electron, $R(E_0)$, through the ice. The relationship between these two quantities can be expressed as,

$$\bar{\sigma}_D = \frac{\int_0^x \sigma_D(E(x))[H_2O_2]dx}{\int_0^x [H_2O_2]dx} \quad (6.8)$$

where square brackets denote molecular volume density (molec. cm^{-3}). The denominator in Eq. 6.8 integrates to $\{H_2O_2\}$. The measured quantities for $\bar{\sigma}_D$ and $\{H_2O_2\}$

at energies E and $E + \Delta E$ can then be used to solve for σ_D using,

$$\begin{aligned}
 \bar{\sigma}_D(E + \Delta E)\{H_2O_2\}|_{E+\Delta E} - \bar{\sigma}_D(E)\{H_2O_2\}|_E &= \\
 &= \int_0^{x+\Delta E} \sigma_D[H_2O_2]dx - \int_0^x \sigma_D[H_2O_2]dx \\
 &= \sigma_D(E) \int_x^{x+\Delta x} [H_2O_2]dx \\
 &= \sigma_D(E) (\{H_2O_2\}|_{E+\Delta E} - \{H_2O_2\}|_E) \quad (6.9)
 \end{aligned}$$

The σ_D are then calculated using the laboratory results in the following equation,

$$\sigma_D(E) \approx \frac{\bar{\sigma}_D(E + \Delta E)\{H_2O_2\}|_{E+\Delta E} - \bar{\sigma}_D(E)\{H_2O_2\}|_E}{\{H_2O_2\}|_{E+\Delta E} - \{H_2O_2\}|_E} \quad (6.10)$$

Using our experimentally determined values, we find a linear least-squares fit to solution for σ_D yields the general expression,

$$\sigma_D \approx 3.39 \times 10^{-14} E_0 + 4.13 \times 10^{-13} \text{ cm}^2. \quad (6.11)$$

The determination of σ_D as a function of energy allows us to adjust the destruction cross-section for a given electron as it loses energy along its path through the ice. This is an important relationship when considering the depth profile of H_2O_2 production and destruction, as shown in the following section.

6.4 Discussion

6.4.1 H_2O_2 production as a function of depth into ice

We have examined H_2O_2 production as a function of temperature, current, and energy, but ultimately we are interested in the application to the icy satellites. Relating laboratory production of H_2O_2 in thin films to bulk production in the radiolytically

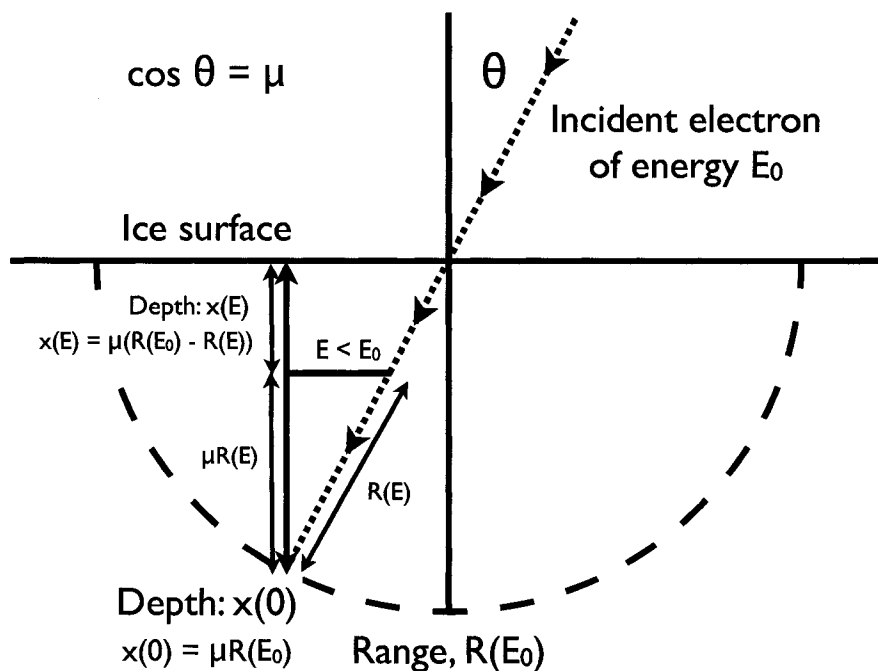


Figure 6.12: The relationship between projected range of an electron with energy E_0 , the depth below the surface to which the electron penetrates, and the depth at which the electron has deposited $E_{dep} = E_0 - E$ of its energy. For radiolytic production and destruction at a given depth below the surface we integrate over 2π steradians and account for the distribution of electrons with energy E_0 imparting energy to a depth x . In each case, the minimum E_0 considered is that for which $\theta = 0$ (*i.e.* incidence is normal to the ice surface).

processed region of moons such as Europa and Enceladus requires understanding H_2O_2 production as a function of depth into the ice. Only by quantifying production and destruction of chemical species with depth into the ice can we begin to understand the bulk radiolytic chemistry.

The production of a given chemical species at depth x in the ice is a function of the flux of electrons integrated over the range of possible energies reaching depth x , times the production rate for the energy deposited, dE , over the range dx . Accounting for electrons incident over 2π steradians, we can express production as a function of

depth as,

$$Q(x) = 2\pi \int_1^0 d\mu \int_0^\infty j(E_0) \gamma(E) S(E) dE_0 \quad (6.12)$$

where $j(E_0)$, $\gamma(E)$, and $S(E)$ are the surface electron flux, the production per unit energy loss, and the stopping power respectively. The parameter μ is the cosine of the incident angle, θ , of the electron at the surface, $\cos \theta = \mu$. Figure 6.12 shows the geometry and definitions relevant to production with depth.

Using data from *Voyager 1* and *Galileo*, Paranicas et al. (2001) described the surface electron flux as seen by Europa via,

$$j(E_0) = j_* E^a \left(1 + \frac{E}{E_*}\right)^{-b}, \quad (6.13)$$

where $j_* = 4.23$, $E_* = 3.11$, $a = -1.58$, $b = 1.86$ and j is given in units of $\text{cm}^{-2} \text{s}^{-1} \text{sr}^{-1} \text{eV}^{-1}$. The energy range examined was $0.01 \text{ MeV} < E_0 < 10 \text{ MeV}$. For a given depth below the surface, x , we need to know the incident energy flux and energy deposited as a function of the initial incident energy, E_0 , and surface flux, $j(E_0)$. The projected range of an electron with energy E_0 is related to the depth reached below the surface by the cosine of the incident angle, μ (Fig. 6.12). As the electron loses energy, the depth for a given energy E , where $E < E_0$, can be found using $x(E) = \mu(R(E_0) - R(E))$. Solving for $E(x)$, an electron of initial energy E_0 will then have an energy at depth x of,

$$E(x) = \left(E_0^\alpha - \frac{x}{\mu R_1}\right)^{1/\alpha} \quad (6.14)$$

where we have used the range relation as described in Section 5.2 to arrive at the final expression. Similarly, differentiation of Eq. 5.4 also leads to the expression,

$$\frac{dR}{R} = \alpha \frac{dE}{E}, \quad (6.15)$$

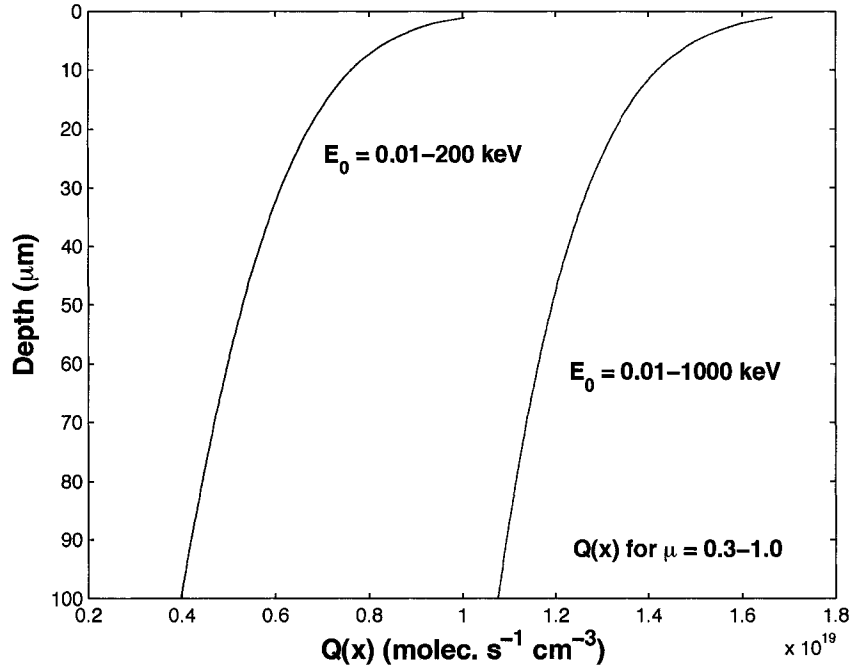


Figure 6.13: Volume production of H_2O_2 as a function of depth below the surface in 100 K ice. At each point x below the surface the production resulting from the contribution of each electron of initial energy E_0 is accounted for and summed over the solid angle range of $\cos\theta = \mu = 0.3-1.0$ and 2π . Results are shown for an initial electron energy spectrum of 0.01–200 keV and 0.01 keV – 1 MeV. Electron fluxes at each energy are calculated using the expression of Paranicas et al. (2001).

allowing us to solve for stopping power, $S(E) \equiv dE/dx$,

$$S(E) \equiv \frac{dE}{dx} = \frac{dE}{dR} = \frac{1}{\alpha R_1 E^{(\alpha-1)}}. \quad (6.16)$$

The above expressions are combined to solve Eq. 6.12 numerically using the experimentally constrained expression for $\gamma(E)$ as derived in Section 6.3.3. The range expression used to derive Eq. 6.14 and 6.16 should only be used for \sim keV electrons, as can be seen in Figure 2.5. Here I solve for $Q(x)$ up to 200 keV and then show that extending the solution up to 1 MeV does not dramatically alter the results. Figure 6.13 show the solution for these two scenarios, integrating from the surface down to

a depth of 100 μm . In both cases at each depth x I have solved for the solid angle solution down to $\mu=0.3$, or an angle of 17.5° up from the surface. Volume production is seen to be in the range of 1×10^{19} molec. $\text{s}^{-1} \text{cm}^{-3}$, with maximum production occurring near the surface and decreasing with depth into the ice. In the 200 keV limit the surface production is found to be 1.49×10^{19} molec. $\text{s}^{-1} \text{cm}^{-3}$ and in the 1 MeV limit it is found to be 2.15×10^{19} molec. $\text{s}^{-1} \text{cm}^{-3}$.

Following the expression for $Q(x)$, we define the destruction rate per unit volume at depth x as,

$$L(x) = 2\pi \int_1^0 d\mu \int_0^\infty j(E_0) \sigma_D(E) dE_0. \quad (6.17)$$

Using our experimentally constrained expression for $\sigma_D(E)$, we solve numerically for $L(E)$. Results are shown in Figure 6.14. As can be seen, the major feature of the solutions is a decrease in volumetric destruction with depth. In both the $Q(x)$ and $L(x)$ solutions the 1 MeV cases yields higher values, but the values are not orders of magnitude higher than the 200 keV case. Thus, while I feel confident that our mathematical expression is valid for E_0 up to 200 keV, my results indicate that the error associated with extending the range to 1 MeV do not greatly alter the results.

Together, the production and destruction rates can be combined to yield the equilibrium density of H_2O_2 at depth x ,

$$[H_2O_2] = \frac{Q(x)}{L(x)}. \quad (6.18)$$

Figure 6.15 shows the results for the steady-state concentration as a function of depth into the ice. Again, we have solve for a 200 keV limit and a 1 MeV limit. A solid angle covering $\mu = 0.3 - 1.0$ was used in each case. As can be seen from these results, I find that concentration increases with depth below the surface. Solving for the total concentration at the surface ($x = 0$) resulting from production and destruction of all electrons in the range 0.01-200 keV and coming from $\mu=0.3-1.0$ over 2π , I find a percent by number abundance for H_2O_2 of 0.37% relative to water. For the 1 MeV case, this number is 0.54% by number relative to water. Interestingly, these numbers are a comparable to, but a few times larger than, empirical results for the abundance

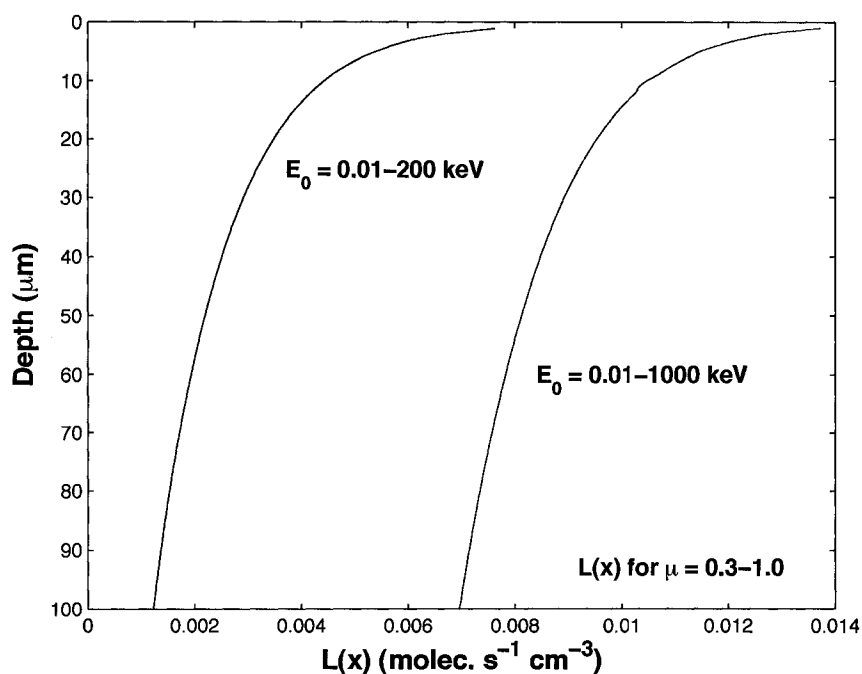


Figure 6.14: Volume destruction of H_2O_2 as a function of integrated contribution from incident electrons over a range of energies and incident angles. As with $Q(x)$, here we consider the energy spectrum of 0.01–200 keV and 0.01 keV – 1 MeV and the solid angle contribution from $\mu = 0.3 - 1.0$. At the surface I find $L = 0.1337 \text{ molec. s}^{-1} \text{cm}^{-3}$ for the 200 keV case and $L = 0.1339 \text{ molec. s}^{-1} \text{cm}^{-3}$ for the 1 MeV limit. With increasing depth destruction decreases, reaching about 5% of its surface value at 100 μm depth.

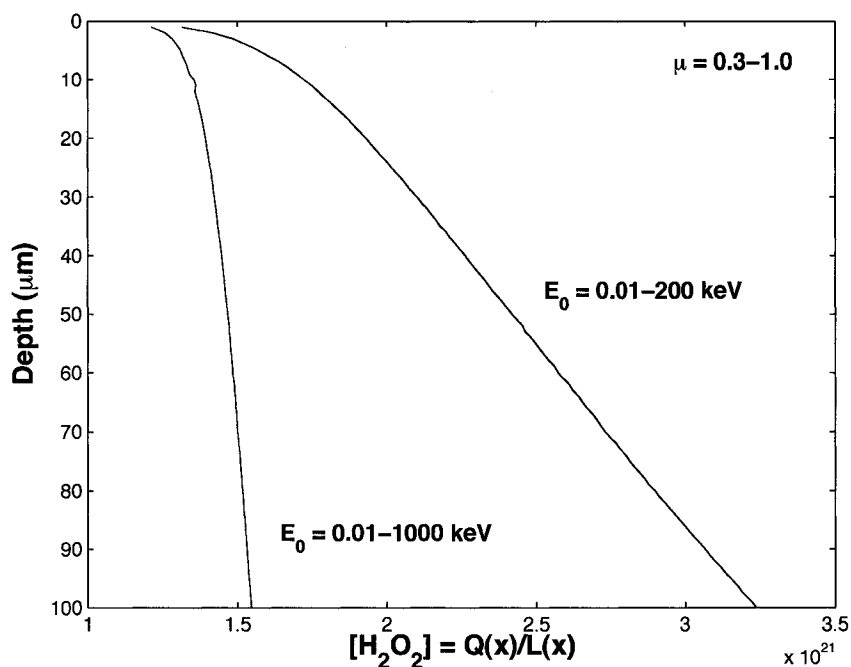


Figure 6.15: Steady-state H_2O_2 concentration (in molecules) as a function of depth below surface. Calculations are based on an incident electron energy spectrum of 0.01-200 keV and 0.01 keV – 1 MeV. Integration over a 2π solid angle for incoming electrons is considered from an angle of 17.5° from the surface plane to the perpendicular. Results indicate an increase in H_2O_2 abundance with depth below the surface. Percent by number abundances for H_2O_2 reach 5–10% at 100 μm depth.

of H_2O_2 on the surface of Europa (Carlson et al., 1999a).

As the steady-state concentration increases with depth, I find that at 100 μm depth the H_2O_2 abundance reaches levels of 5.2% and 10.8% by number relative to water for the 1 MeV and 200 keV limits respectively. These numbers should be treated with caution as they do not account for electrons in the range of ~ 10 MeV and the energy and stopping power calculations for $E_0 > 200$ keV likely included errors. Furthermore our numerical fits for our experimental data are good but should also be treated with caution and extended the data range to higher and lower energies would help build confidence in these fits.

With these caveats in mind however, our results indicate that steady-state H_2O_2 concentrations increase with depth into the surface. Correcting the range expression to account for the NIST results as per Berger et al. (2005) will allow us to more accurately extend our integration to greater depths and to higher energies without the need for more laboratory data.

6.5 Conclusion

6.5.1 Implications for Icy Satellites

The results presented here imply that the NIMS results for H_2O_2 on the surface of Europa represent a lower estimate for what may lie beneath the surface. Sputtering, gardening, and destruction from ion and protons could be responsible for the observed lower surface abundance and these factors will not have large contributions at depth. The high-energy electrons will dominate steady-state H_2O_2 concentrations in these regions.

Critical for understanding the application to icy satellites is a comparison of the H_2O_2 depth profile with surface age and gardening rates. The average surface age, based on crater counts (Zahnle et al., 2003), is between 30-70 Myr. Gardening, from impacts both large and small, is estimated to create a ~ 1.3 m regolith over the course of ~ 10 Myr (Cooper et al., 2001). For the results presented here, in which we have only integrated to 100 μm depth, gardening would mix this layer in ~ 100 years.

Only surfaces younger than this would retain the signature of peroxide production with depth. If we can extend our H_2O_2 depth profile to tens of centimeters to a few meters we should be able to accurately predict the sub-gardening layer H_2O_2 concentration for a given surface age. This is the focus of future work.

The total abundance of H_2O_2 and O_2 will play an important role in oxidizing the subsurface ocean if geological mechanisms are available for delivering the surface material to the subsurface. This could be a key consideration for astrobiology and subsurface habitability (Chyba, 2000; Chyba and Phillips, 2001; Hand et al., 2007).

Finally I note that the increased H_2O_2 concentration must be considered in the context of O_2 formation and the observed steady-state abundance of condensed phase O_2 on the european surface and gas phase O_2 in the european atmosphere (see *e.g.* Chapter 7. As an important precursor for O_2 the H_2O_2 abundance critically feeds into net O_2 production. Understanding this relationship is the subject of ongoing research in our laboratory and several other laboratories, each examining a different, but overlapping, set of irradiation and temperature conditions.

Chapter 7

On the phase and stability of radiolytically produced oxidants¹

The radiolytic production of oxidants on the surface of icy moons such as Europa has been examined theoretically (Cooper et al., 2001; Johnson et al., 2003), in the laboratory (Baragiola et al., 1999; Moore and Hudson, 2000), and through direct observation (Carlson et al., 1999a; Spencer and Calvin, 2002). (For a comprehensive review of all aspects, see Johnson et al. (2004).) The presence of such compounds in the ice may lead to the formation of significant quantities of clathrate hydrates rather than the commonly assumed forms of ice I. Clathrates of oxidants are observed in terrestrial ice sheets and expected elsewhere in the solar system (Blake et al., 1991; Miller, 1961, 1969). Indeed, clathrates in the european ice shell and on the seafloor have been previously examined in some detail (Crawford and Stevenson, 1988; Kargel et al., 2000; Prieto-Ballesteros et al., 2005). Here, however, we consider the contribution from radiolytically produced oxidants. Our purpose is twofold: first, we aim to characterize the ice phases that are likely to exist near the surface and within the ice shell. Second, we hypothesize a possible solution to the puzzling observation of condensed-phase O₂ on the surface of Europa based on an examination of the stability of clathrates near the surface of Europa (Spencer and Calvin, 2002). [Note that much

¹Most of this chapter is published as Hand et al. (2006) with some parts from McKay et al. (2003).

of our argument can also be applied to a similar debate regarding observations of Ganymede (see Johnson and Jessor (1997) and Baragiola et al. (1999)).] Solid O_2 is not stable near the surface of Europa; thus a variety of trapping mechanisms have been invoked to explain the observations (Johnson et al. (2003), and references therein). Here we suggest that clathrates, specifically mixed clathrates hosting O_2 , CO_2 , and SO_2 , could solve this problem.

Our focus on Europa and oxidants is motivated in part by the prospect for finding life on this moon. The habitability of the putative subsurface ocean of Europa may depend on the radiolytic production of oxidants at the surface (Chyba, 2000; Chyba and Phillips, 2001; Cooper et al., 2001). Mechanisms and time scales for the delivery of surface products to the ocean are still highly uncertain, but the geologically young surface of Europa [<250 million years old, and generally considered to be on the order of ~ 50 million years (Zahnle et al., 2003)] gives at least some indication that communication between the surface and subsurface occurs. Thus oxidants produced on the surface and gardened into the near subsurface Phillips et al. (2000); Chyba and Phillips (2001); Cooper et al. (2001) could be mixed into the bulk ice shell and perhaps delivered to the ocean. Here we examine the consequences of transporting such material through the ice shell. Specifically, we analyze the role of O_2 , H_2O_2 , CO_2 , and SO_2 clathrate formation on the bulk physics and chemistry of the ice shell. We also explore, in brief, the fate of clathrates once they reach the subsurface ocean.

7.1 Conditions for clathrate hydrate formation

The formation of clathrate hydrates depends on the temperature and pressure environment, and the properties of the guest molecule (Sloan, 1998). Formation of the hydrogen-bonded hydrate lattice occurs primarily in three different, cubically symmetric structures. Other structures may be possible under conditions yet to be explored. All known forms involve combinations of two or more types of polyhedral cages. Here we discuss structure I (SI) and structure II (SII), as they are host to the compounds of interest in this work (Figure 7.1). Structure H hydrates are typically less stable but can house some alkanes, alkenes, and aromatics. While the terms

‘clathrate’ and ‘hydrate’ are often used interchangeably within the field, hereafter we use the term ‘clathrate’ so as not to confuse the reader with the hydrated material (possibly H_2SO_4 or sulfate salts) discovered on the surface of Europa (McCord et al., 1998a; Carlson et al., 1999b).

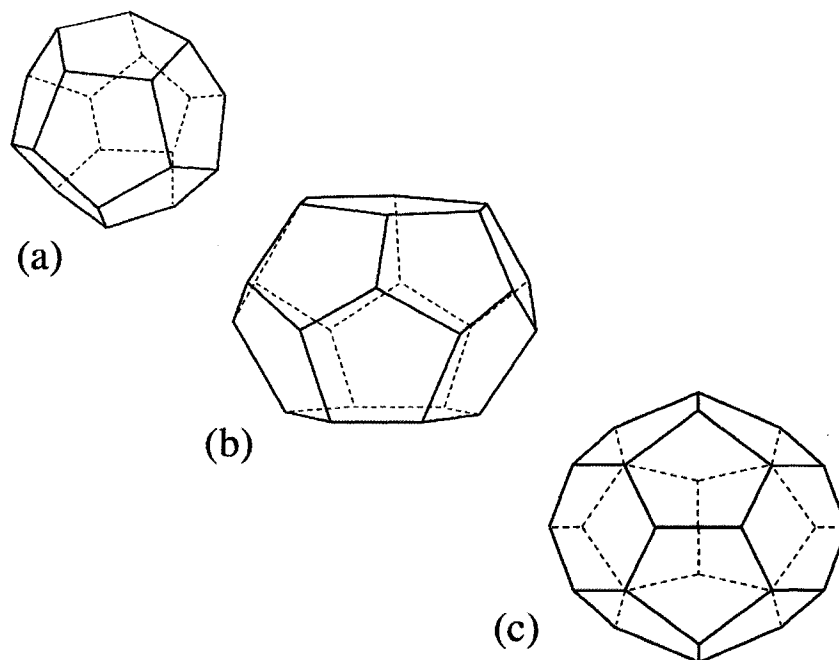


Figure 7.1: Clathrate cages of SI and SII clathrates. Vertices represent water molecules, with oxygen atoms at the center, and the lines represent hydrogen bonds between the H and O atoms of neighboring water molecules. Cage (a) is the pentagonal dodecahedron that forms the small cage of both SI and SII clathrates. Cage (b) is the tetrakaidecahedron that forms the large cage of SI clathrates. Cage (c) is the hexakaidecahedron that forms the large cage of SII clathrates. The average cavity radius for each structure is 3.95 Å, 4.33 Å, and 4.73 Å, respectively (Sloan, 1998). When in SII, the small cage has an average radius of 3.91 Å. Cage forms are modeled after Sloan (1998).

The unit cell of SI clathrate is 12 \AA^3 in volume and consists of two small cages and six large cages for a total of 46 water molecules (Figure 7.1). The SI small cages are 3.95 Å in radius and can house molecules less than 5.1 Å in diameter (Sloan, 1998). The large cages have a radius of 4.3 Å and can hold molecules as large as 5.8

Å in diameter. Typical SI hydrates include methane, carbon dioxide, and hydrogen sulfide. While each unit cell could potentially hold eight host molecules, in reality not all cages are filled; clathrates are non-stoichiometric, *i.e.* the relative proportions of the elements vary. The ratio of cages occupied to the total number of cages is termed the fractional occupancy ratio, and it is largely a function of temperature, pressure, and concentration of the guest molecule.

SII clathrates house oxygen and nitrogen gases as well as a host of larger molecules. The unit cell consists of 136 hydrogen-bonded water molecules arranged in 16 dodecahedral cages and eight hexadecahedral cages (Figure 7.1). The 16 small cages have a radius of 3.91 Å and can hold molecules with diameter less than 5 Å. The eight large cages are 4.73 Å in radius and can hold molecules with diameters of 6.7 Å or less. The SII cubic unit is ~ 17 Å on a side (Kuhs et al., 1997; Sloan, 1998). Figure 7.1 shows all three cage types formed in SI and SII clathrates.

The binding of a given gas molecule into a cage is dependent on the relative size of the molecule and the magnitude of the van der Waals interaction between the host and the surrounding water molecules. Determining the relationship between a gas-phase mixture and its corresponding clathrate mixture depends on the inverse ratio of the dissociation pressures of the pure clathrates (van der Waals and Platteeuw, 1959).

7.2 Clathrate stability

The critical parameter for determining clathrate stability at a given temperature is the dissociation pressure. At the dissociation pressure, ice, gas, and clathrates are in equilibrium. Above this pressure, the clathrate phase is stable, and the ice and gas phases will combine to form the clathrate. Below the dissociation pressure, the clathrate becomes unstable, and only the ice and gas phases are present.

Formation of clathrates in the solid state can be kinetically inhibited by the availability of water molecules to form the cage structure (Barrer and Ruzicka, 1962; Bar-Nun et al., 1987). If the temperature and pressure conditions are satisfied, a gas bubble trapped in ice will form a clathrate layer at the boundary of the bubble.

The impermeability of the clathrate structure, however, can greatly impede further reaction of the gas compound with the ice (Bar-Nun et al., 1987). Diffusion of water through the clathrate may be a rate-limiting factor (Price, 1995), though much work is underway to better understand this process (Salamatin et al., 1998). Interestingly, Barrer and Ruzicka (1962) found that the incorporation of gases into clathrates could be greatly accelerated by shaking an ice crystal and gas mixture with glass beads. This laboratory-observed effect could have a natural analogue in the sputtered and gardened regolith of icy satellites, thus enhancing clathrate formation on such bodies. Recent laboratory work by Grieves and Orlando (2005) suggests that clathrates could be an effective trapping mechanism for O_2 . Their work also supports the claim that radiation could play a role in the formation of the clathrate.

For temperatures above ~ 273 K (at 1 atm), pure liquid water is stable, and a solution is formed with the gas such that the solution is in equilibrium with the dissolved gas. When the concentration of the dissolved gas is beyond the solubility limit for the gas, the solution is said to be supersaturated. If pressure is increased, a point is reached at which water, gas, and clathrate phases are in equilibrium. Under conditions of clathrate stability, excess gas will be partitioned into the clathrate phase, and the clathrate structure will remain stable in liquid water. Note that the stability of methane clathrates in terrestrial oceans is enhanced by the sediments in which they form; only the very localized conditions for solubility need to be exceeded in order for the clathrate to be stable (Buffett, 2000). For a given gas clathrate, there exists a quadruple point (the Q-point) at which all four phases of water-ice-gas-clathrate are in equilibrium. The Q-point can be found by plotting dissociation pressure versus temperature for a given phase boundary. The intersection of the lines for gas-water-clathrate and gas-ice-clathrate represents the Q-point for the system. For the case of oxygen, the Q-point is at a pressure of approximately 11.1 MPa and -1°C (Lipenkov and Istomin, 2001).

For a given gas hydrate, the dissociation pressure scales with temperature as follows (van der Waals and Platteeuw, 1959; Miller, 1961):

$$\log P_d = A + B/T \quad (7.1)$$

Here the dissociation pressure, P_d , is given in MPa and the temperature, T, in Kelvin. The parameters A and B are experimentally determined for a specific system in a given temperature range.

For a given gas mixture, one can calculate the combined dissociation pressure for the system. Having calculated individual dissociation pressures, values for various clathrate gas mixtures can be approximated by assuming that the hydrate behaves as an ideally dilute solution and the fractional occupancy ratio is constant and the same for all gases (Lipenkov and Istomin, 2001). With these assumptions, the mixed gas dissociation pressure can be expressed as:

$$P_{d(max)} = \left[\sum \frac{y_i}{P_{d_i}} \right]^{-1} \quad (7.2)$$

where P_{d_i} is the dissociation pressure, as per Eq. 7.1, for component i , and y_i are the respective relative guest molecule abundances. This expression for the dissociation pressure can now be used in conjunction with Eq. 7.1, and a phase diagram for the mixture can be created for a given set of guest molecules.

We now apply this formalism to the ice shell of Europa. We first examine which guest molecules might be available on the surface, and the relative abundance of such compounds.

7.3 Radiolytic production of oxidants on the eu-ropan surface

The surface ice of Europa is subject to a flux of high-energy ions ($\sim 2 \times 10^{10}$ keV cm^{-2} s^{-1}), electrons ($\sim 6 \times 10^{10}$ keV cm^{-2} s^{-1}), and ultraviolet radiation ($\sim 4 \times 10^{10}$ keV cm^{-2} s^{-1} , for $\lambda < 2800$ Å, energetic enough to break apart water molecules) as a result of being situated deep within the jovian magnetosphere (Cooper et al., 2001). Laboratory simulations have demonstrated that the oxidants observed on the surface of Europa could be directly attributed to the radiolytic chemistry that results from such particles (Moore and Khanna, 1991; Carlson et al., 1999a,b; Moore and Hudson,

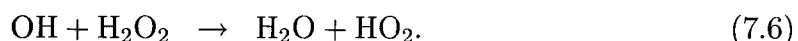
2000). Here we examine each of the observed oxidants in detail to set upper and lower bounds on the relative abundance of each compound on the surface of Europa.

7.3.1 Oxygen

Molecular oxygen is a highly reactive compound in organic chemistry and, as such, represents a potentially useful source of energy to any ecosystem. As a terminal electron acceptor in biochemical reactions, few other compounds offer comparable energetic favorability (Nealson, 1997). The presence of a thin oxygen atmosphere on Europa has been known for some time (Hall et al., 1995), and more recent ground-based observations have reported the presence of condensed O_2 on the surface (Spencer and Calvin, 2002). In addition, data from the *Galileo* Near-Infrared Mapping Spectrometer (NIMS) indicate the presence of hydrogen peroxide (H_2O_2) on the euroman surface (Carlson et al., 1999a). If transported to a subsurface liquid water ocean, the H_2O_2 would decay to O_2 on a geologically short time scale (Chyba, 2000). Therefore, we treat H_2O_2 as equivalent to O_2 when estimating the total abundance of O_2 in the ice shell and ocean. Little is known about H_2O_2 clathrate formation, and so here we make the tentative assumption that the behavior of H_2O_2 clathrate will be comparable to that of oxygen. Ultimately, we show that the H_2O_2 flux is small compared with that of molecular O_2 in the ice, so that H_2O_2 only accounts for a small fraction of the clathrate. In addition, once the peroxide has decayed to oxygen it will not be converted back to peroxide unless it is recycled and exposed to the surface radiation environment. Thus, even if peroxide is not efficiently enclathrated on its initial pass through the ice shell it will later decay to oxygen, which, if reincorporated into the ice shell, will form a clathrate.

Molecular oxygen in the solid phase appears to occur at all longitudes on the surface of Europa (Spencer and Calvin, 2002), whereas H_2O_2 has been observed only on Europa's leading hemisphere (Carlson et al., 1999a; Carlson, 2001). One possibility, consistent with conclusions of this work, is that the solid O_2 pervades the ice crust as an end product of many production and resurfacing cycles, while surficial H_2O_2 may be a more short-lived precursor produced by surface irradiation. The non-detection

of H_2O_2 on the trailing hemisphere may be due to the high radiation noise associated with those measurements or to the more complex chemistry involving the sulfates. Both products are likely part of a radiolytic oxygen cycle that is broadly outlined in Figure 7.2. Destruction of H_2O yields H and OH radicals, which then react along the following pathways (Moore and Hudson, 2000; Cooper et al., 2003):



Formation of O_2 may come directly from the reaction of two trapped O atoms

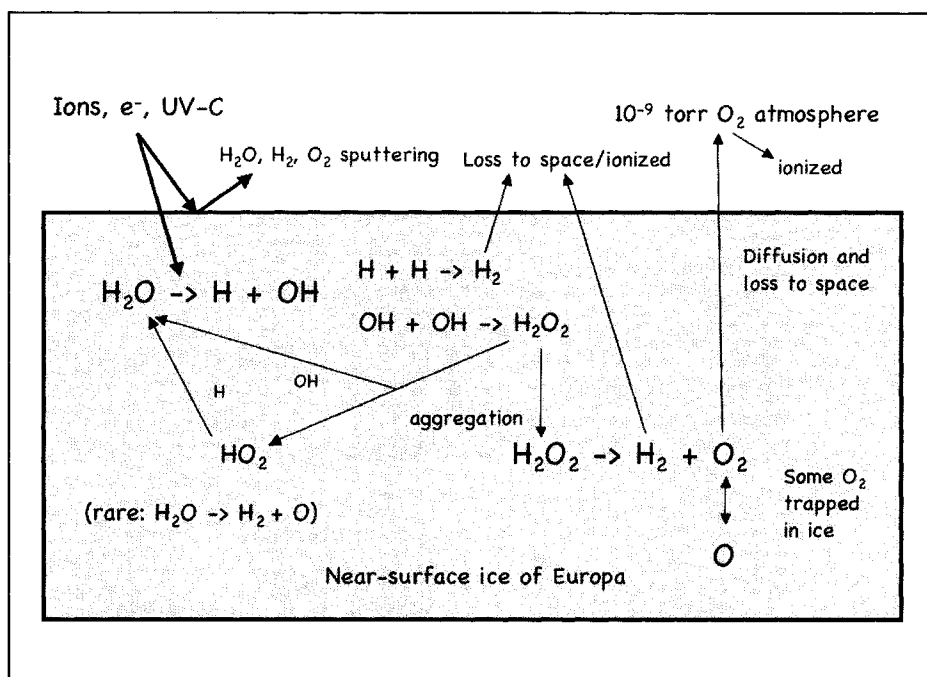
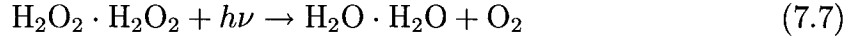
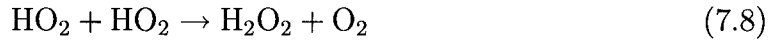


Figure 7.2: A simplified sequence for radiolytic production and destruction of water, H_2O_2 , and molecular oxygen. Some H_2O_2 and O_2 become sequestered below the heavily processed surface.

(Johnson et al., 2003). Alternatively, the photolytic decay of H_2O_2 dimers can lead to O_2 production (Cooper et al., 2003):



Some of the O_2 will be attacked by the H radicals, which leads to hydroperoxy radicals (HO_2). Combination of two such hydroperoxy radicals then leads to the production of H_2O_2 and O_2 (Cooper et al., 2003):



Estimates from the NIMS results put the H_2O_2 surface abundance at 0.13% by number (Carlson et al., 1999a). Based on this number alone as a proxy for O_2 , it has been argued that Europa could have an annual oxygen flux of $10^9 - 10^{12}$ mol from the ice shell to the ocean (Chyba and Hand, 2001). Here, however, we also consider the net radiolytic production of molecular oxygen.

The weak band at 5771 Å observed by Spencer and Calvin (2002) has been attributed to the double excitation of two interacting O_2 molecules in solid (γ -phase) oxygen. As a result of the need for two molecules, one should expect the 5771 Å absorption to follow a quadratic dependence on O_2 concentration. Given the observed band depth ($\delta I/I$) of 0.3% and a γ -phase absorption coefficient of $\alpha = 1.6 \text{ cm}^{-1}$, we calculate the O_2 abundance using:

$$\frac{\delta I}{I} = \left(\frac{2}{3}D\right) (\alpha f^2) \left[\frac{(1+r_0)^2}{(1-r_0)}\right] \quad (7.9)$$

where D represents the surface ice grain diameter [$\sim 80 \mu\text{m}$, obtained here using H_2O grain size maps derived using methods discussed by Carlson et al. (2005)], f is the fractional O_2 density relative to H_2O , and r_0 is the diffuse reflectance. The first quantity on the right-hand side accounts for the average path length through a grain, the second quantity accounts for the resulting absorption, and the final quantity represents the number of scattering (and absorption) events (Hapke, 1993). As a lower limit, we assume the O_2 is embedded in pure, non-absorbing ice grains,

thus maximizing the number of scatterings. With this assumption, it follows that $(1 - r_0) = \delta I/I$, and the above equation can be solved for f , the fractional density of O_2 . We find that in this lower limit case, $f = 1.2\%$.

A more physically realistic estimate must attribute some absorption to impure ice grains, independent of O_2 absorption. For this case, we assume that the O_2 signature is primarily from the bright icy regions and the signal from darker regions is muted by the low number of scattering events. We use the albedo data for the infrared-bright plains (Clark et al., 1998) and assume that the highest albedo value (at $0.66 \mu\text{m}$) corresponds to conservative scattering and unit reflectance. The interpolated reflectance at $0.577 \mu\text{m}$ is then ~ 0.97 so $(1 - r_0) = 0.03 + \delta I/I$, and the fractional density of O_2 is found to be 4.6% .

Combining O_2 and H_2O_2 yields a total equivalent O_2 abundance of no less than 1.3% and perhaps more than 4.7% by number relative to water. While sputtering certainly destroys compounds and causes ions of oxygen and hydrogen to escape, gardening outpaces sputtering (Chyba and Phillips, 2001; Cooper et al., 2001), and over the course of one ice shell resurfacing time scale (50-250 million years) we could reasonably expect at least the upper few meters to have an $O_2+H_2O_2$ abundance similar to that observed for the surface. Indeed, more recent analyses of gardening rates indicate that the upper 1-10 m of ice could be mixed on time scales of ~ 10 million years (Phillips and Chyba, 2001).

Solid O_2 on the surface of Europa is thermodynamically unstable. For the surface temperature range of 70-130 K, the vapor pressure of O_2 falls between 0.007 and 2 MPa. Thus, even in the colder regions, the $\sim 10^{-7}$ Pa europian atmosphere (of primarily O_2) is far too thin to keep the O_2 in solid form. This paradox suggests that either the O_2 in the ice is mechanically trapped or solid O_2 is continuously being produced via radiolysis. It has been proposed that the stability of the observed oxygen on the surface of Ganymede may be related to diurnal temperature cycles (Vidal et al., 1997; Baragiola and Bahr, 1998; Johnson, 1999). Oxygen may condense during the cold nights and then sublime during the warmer daytime temperatures. On Europa, however, this mechanism would not suffice as the night-side of the moon only gets down to ~ 86 K (Johnson et al., 2004). To explain the presence of interacting oxygen

pairs on the icy galilean satellites, Johnson and Jessor (1997) proposed the presence of O₂ microatmospheres in radiation-induced bubbles within the surface ice. However, diffusion of O₂ through normal amorphous or crystalline ice (*i.e.* unirradiated ice) is very fast, and thus the bubble hypothesis has been questioned (Baragiola and Bahr, 1998) [see comment by Johnson (1999) and subsequent reply by Baragiola et al. (1999)]. We address the trapping of O₂ in the near-surface ice in detail in the section on mixed hydrate.

7.3.2 Sulfur dioxide

Sulfur, perhaps both endogenous and exogenous in origin, appears to play a dominant role in the surface chemistry of Europa (McCord et al., 1998b; Carlson et al., 2002). One reservoir for sulfur is that of sulfur dioxide. Using observations from the Hubble Space Telescope (Noll and Weaver, 1995), coupled with absorption measurements (Sack et al., 1992), we estimate the SO₂ abundance in the same way as was shown above for O₂, but here we use a linear dependence instead of quadratic dependence for the absorption. We find an SO₂ number density relative to H₂O of $\sim 0.3\%$. The other predominant forms are likely polymerized sulfur, sulfuric acid hydrate, and hydrated sulfate salts. Here we concern ourselves only with the abundance of SO₂, as this compound is known to form clathrates (Miller, 1961; Sloan, 1998).

While the observed surface abundance for SO₂ is just a few tenths of a percent, leaching and mantle degassing models predict higher levels of SO₂ in the ocean water. Scaling Io's output of SO₂ to Europa, Kargel et al. (2000) find that over the past 4.5 billion years as much as 2×10^{20} kg of SO₂ could have been vented to the ocean. Considering, on the other hand, a carbonaceous chondrite leaching model, they find a comparable value of 4.8×10^{20} kg for SO₂ abundance. By number relative to water this is 0.7-1.7%. Similarly, Crawford and Stevenson (1988) have estimated the SO₂ abundance to be 0.1% by number in ocean. Thus, if resurfacing is driven by water from below erupting to the surface, then these oceanic concentrations could reasonably be expected to set an upper limit for SO₂ that is trapped in the ice and later transformed to SO₂ clathrate.

For the present study, we consider the range of 0.1-1.7% by number relative to water for SO₂ in the ice shell, but use 0.3% as our preferred, and empirically supported, value.

7.3.3 Carbon dioxide

Most models for the formation of Europa assume an origin in the jovian subnebula from material comparable in composition to that of carbonaceous chondrites (Kargel et al., 2000; Zolotov and Shock, 2001), though recent work by Zolotov and Shock (2004) has argued for a composition originating primarily from ordinary chondrites. Assuming only CO₂ derived from leaching of this material, it has been argued that oceanic concentrations could be in the range of roughly 0.02-1.23% by number CO₂ (Crawford and Stevenson, 1988; McCollom, 1999; Kargel et al., 2000). If erupted to the surface, comparable concentrations of solid CO₂ could be expected in the ice shell.

Observations from the *Galileo* NIMS indicate a percent by number abundance for CO₂ of 0.08% (Chyba, 2000). The NIMS data represent only approximately the uppermost millimeter or less of the surface and, consequently, only the most radiation-processed of surface materials. When exposed to high-energy ions and electrons, CO₂ rapidly evolves to CO and O⁺ (Moore and Khanna, 1991). CO is highly volatile and probably will escape into the atmosphere where it can be ionized and swept away by Jupiter's corotating magnetic field. A tenuous CO atmosphere, comparable to or less than that of O₂, could exist on Europa; however, no corresponding carbon lines were seen in the spectra of Hall et al. (1995). The NIMS observations probably represent a lower limit for CO₂ concentration in the ice shell.

CO₂ is found on Europa's leading hemisphere, where the availability of carbon is enhanced by micrometeorite impacts. CO₂ has not been detected on the trailing hemisphere, but the limits are not stringent. The trailing side's exogenous carbon source is primarily in the form of ions trapped in the magnetosphere. Carbon delivery from micrometeoroids is estimated at 1-10 g s⁻¹ over the surface of Europa, though much of this flux is concentrated on the leading hemisphere (Johnson et al., 2004).

For the purpose of estimating clathrate formation and abundance in the ice shell, we conclude that the concentration of CO₂ in the ice shell is likely to fall between the empirically established lower limit of 0.08% and the theoretical modeling result of 1.23% by number abundance relative to water.

7.3.4 Combined oxidant contamination

Using the limits for each oxidant compound discussed above, we find that, at a minimum, the combination of O₂+CO₂+SO₂ (1.3% + 0.08% + 0.3%) will yield a low end oxidant contamination of 1.7% by number relative to water. If the CO₂ abundance is similar to that of SO₂, this number rises to 1.9%. Using the higher estimate for O₂ (4.7%), which is still empirically supported, yields an oxidant contamination of 5.1%. These results for upper limits on CO₂ and SO₂ yield a total oxidant contamination of 7.6% by number relative to water. Thus our predicted range for radiolytically produced oxidant contamination of the surface ice is 1.7-7.6% by number relative to H₂O.

7.4 Temperature and pressure in the european ice shell

Formation of clathrates in ice depends on the temperature and pressure environment within the ice shell. Figure 7.3 shows the dissociation pressure curves for the clathrate phase of the three compounds considered in this work. In Figures 7.4-7.6, we have modeled the temperature and pressure profiles through the ice shell and displayed these curves in relation to that of several different clathrate mixtures. Three shell thicknesses are presented - 5 km, 10 km, and 30 km - and for each shell we have superimposed both a simplified temperature gradient (thermal conductivity constant and a volumetric heating rate of 0) and a more complex temperature gradient consistent with a Maxwell rheology for the ice (Ojakangas and Stevenson, 1989; Chyba et al., 1998). These curves, labeled TF and TM, respectively, are for ice shells models

in which heat is lost through conduction, not convection. Both 130 K and 70 K surface temperature scenarios were modeled, but only the 130 K results are presented in Figures fig:h064a-7.6. In each case the temperature at the base of the ice sheet was assumed to be 273 K. The surface pressure, derived from observed O₂ column densities (Hall et al., 1995), was taken to be 2.2×10^{-7} Pa (Johnson et al., 2004). The pressure at the ice-water interface for the 5-km, 10-km, and 30-km shells was 6.5 MPa, 13 MPa, and 39 MPa, respectively. Here we have used a value of 0.99 g cm^{-3} for the density of the overlying ice. From these profiles the region of clathrate stability is then represented by the area to the right of the ice shell temperature-pressure profile.

7.5 Clathrate hydrates of Oxygen, Carbon Dioxide, and Sulfur Dioxide

Using Eq. 7.1, we calculate dissociation curves for O₂, CO₂, and SO₂. Experimental data for clathrate stability at the low temperatures (70-130 K) and pressures [$\sim 10^{-6}$ Pa ($\sim 10^{-11}$ bar)] expected for the surface of Europa are very limited (Blake et al., 1991), so in each case we combine available data with the low temperature modeling results of (Lunine and Stevenson, 1985), which will allow for a more accurate estimate of the stability of the clathrate phase.

7.5.1 Pure oxygen clathrates in the ice shell

Kuhs et al. (2000) determined the constants A and B in Eq. 7.1 for pure oxygen clathrate over the temperature range 253-273 K and found $A = 4.17$ and $B = -850$. The low temperature thermodynamic model of Lunine and Stevenson (1985) yields the values of $A = 5.20$ and $B = -870$. In Figure 7.3, we show both curves for the temperature range of 70-273 K. At high temperatures, the curve of Kuhs et al. (2000) indicates a dissociation pressure of nearly an order of magnitude lower than that of the curve of Lunine and Stevenson (1985). The theoretical curve fails at higher temperatures, so we use the values of Kuhs et al. (2000) for subsequent calculations. At 100 K, the predicted dissociation pressure is ~ 316 Pa. Within the ice shell, this

corresponds to a depth of approximately 30 cm below the surface. Our conclusion, in agreement with the analysis of Ganymede as discussed in Calvin et al. (1996), is that pure O₂ clathrates would not be stable near the surface. However, given that gardening stirs the upper ~1 m on the time scale of ~ 10⁶ years (Chyba and Phillips, 2001), it follows that dispersed O₂ mixed down below the gardening depth is likely to be in the clathrate phase, especially if gardening enhances clathrate formation (see the section Clathrate stability). In addition, while much of the energy from incident particles is lost in the first few millimeters of ice (Cooper et al., 2001), radiolysis will still form some O₂ at depth, e.g., from deeper interactions of gamma rays produced by electron bremsstrahlung.

As resurfacing processes take place - such as cryovolcanism (Greenberg et al., 1998), impacts (Schenk, 2002), or cycloidal fracturing (Hoppa et al., 1999) - O₂ on the surface may be transported downward through the ice shell. The rise in pressure with depth below the surface ensures that, even as temperature rises, O₂ clathrates remain stable as they are transported downward. The clathrate is stable throughout most of the ice shell in all models of the temperature profile. Curve A in Figure ?? shows the stability of pure O₂ clathrate with respect to the temperature-pressure profile of a 5-km, a 10-km, and a 30-km shell. With a surface temperature of 70 K, the stability of pure O₂ hydrate moves to ~8 μm below the surface. For the case of a 5-km shell with a 70 K surface temperature, O₂ clathrate becomes unstable at a depth of 4.4 km below the surface for the simplified (TF) gradient, and 4.6 km below the surface when Maxwell rheology (TM) is considered. When the surface temperature is increased to 130 K, stability is not reached until ~3.3 m below the surface and is lost at 4.1 km (TF) and 4.4 km (TM) below the surface. At 100 K surface temperature, stability is reached at ~30 cm below the surface but is then lost at a depth of ~4.4 km. Models for the 10-km and 30-km thick ice shells indicate that clathrate will be stable through to the base of the ice shell.

In the pure O₂ case, it is to be expected that SII hydrate forms throughout much of the ice shell and subsequent delivery of molecular oxygen to the ocean is in the form of enclathrated O₂. Would the delivered O₂ clathrate be stable in the aqueous solution of the european ocean? Using Lake Vostok as an analogous system, we note

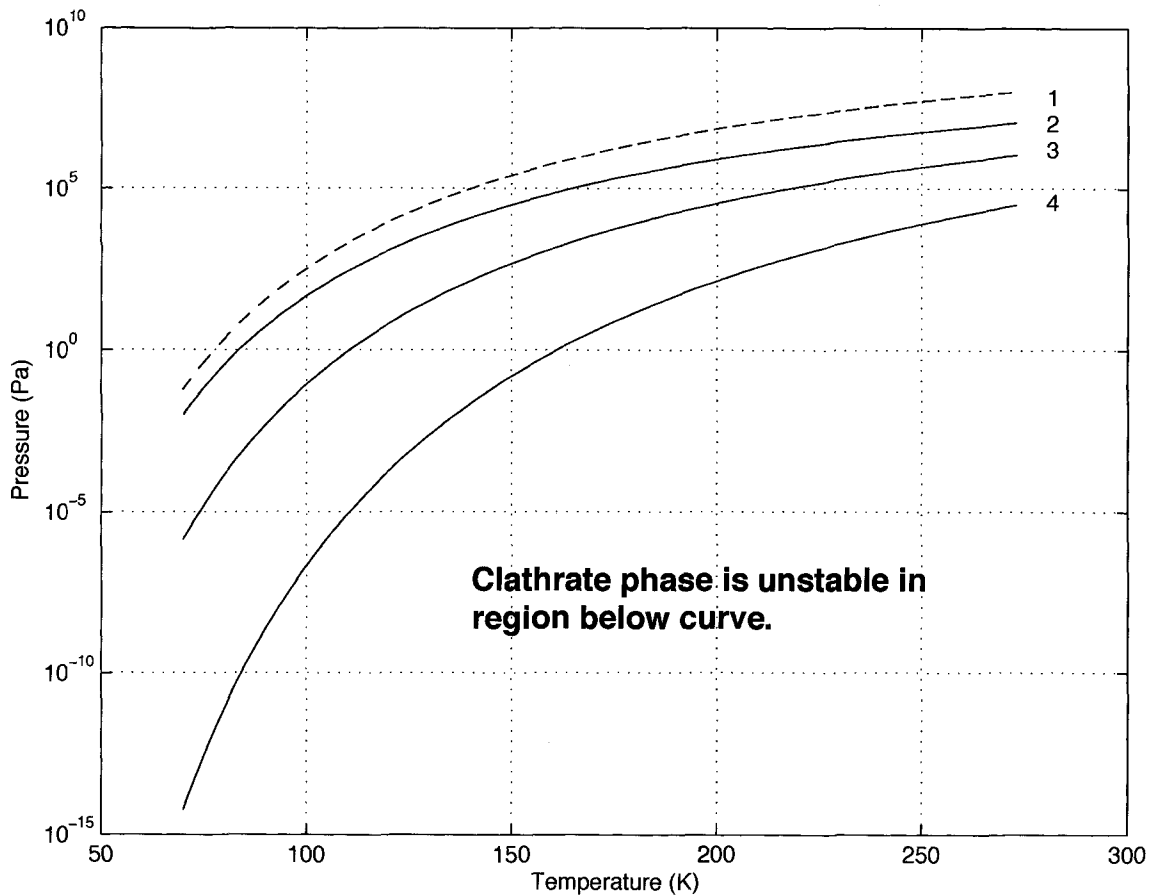


Figure 7.3: Dissociation pressure curves for O_2 , CO_2 , and SO_2 at temperatures expected for the ice shell of Europa. All curves follow the form, $\log P_d = A + B/T$, where P_d is the dissociation pressure in MPa and T is the temperature in Kelvin. Curve 1 is for O_2 and uses values for constants A and B as derived from the theoretical modeling work of Lunine and Stevenson (1985). Curve 2 is for O_2 and uses the empirically determined constants (for 253-273 K) of Kuhs et al. (2000). Curves 3 and 4 are for CO_2 and SO_2 , respectively, and are based on data from Miller (1961) and Miller (1974).

that Lipenkov and Istomin (2001) have calculated an oxygen solubility (mole fraction) of $\sim 7.5 \times 10^{-4}$ for a temperature of 270.15 K and pressures in the range of 35-40 MPa. While such pressures are not expected for the upper ~ 25 km of Europa's hydrosphere, the bulk of the subsurface ocean would be expected to be at or above (greater than) this pressure, and thus we use this value as a rough estimate of average solubility in a european ocean. Note, however, that Lipenkov and Istomin (2001) consider Vostok to be a freshwater lake; the solubility of oxygen in a salty european ocean would be less than that of the freshwater case. This reduced solubility enhances the precipitation of oxygen hydrate. However, ions act to destabilize the clathrate structure (Sloan, 1998), and therefore the net effect is difficult to predict.

Life within the putative european ocean may be oxidant limited (Gaidos et al., 1999), and thus the flux of O_2 is an important consideration for habitability. For an O_2 abundance of 1.3-4.7% through the uppermost 1-10 m of ice, we find that a 50 million year resurfacing time scale yields an annual oxygen flux range of $4.5 \times 10^8 - 1.6 \times 10^{10}$ mol from the ice shell to the ocean. Assuming a 100 km thick ocean, we can then calculate the amount of time needed to reach O_2 saturation if we start with a completely anoxic, freshwater ocean. On the low end (1.3% to a 1 m depth), we find that reaching the O_2 solubility limit would take over 200 billion years. For the high-end estimate, we find that an abundance of 4.7% through the upper 10 m results in O_2 saturation after 7 billion years. If the resurfacing timescale is 10 million years, then saturation is reached after ~ 1.5 billion years. In this case, if there were no sinks, then an additional $\sim 10^{11}$ mol of O_2 hydrate is added to the ocean with each successive recycling period. If the hydrate floats-as would be expected for pure O_2 -then recycling of the shell would likely result in an increasing mass fraction of O_2 hydrate in the ice shell.

Extending this process over long time scales, one could envision a process whereby regions of thicker, deeper ice melt and release O_2 clathrate, which then migrates to thinner regions of the shell and collects as a zone of concentrated hydrate within the ice shell. In terms of chemical potential, such regions would be very attractive for any life forms at the ice-water interface. As shown below, we calculate that oxygen

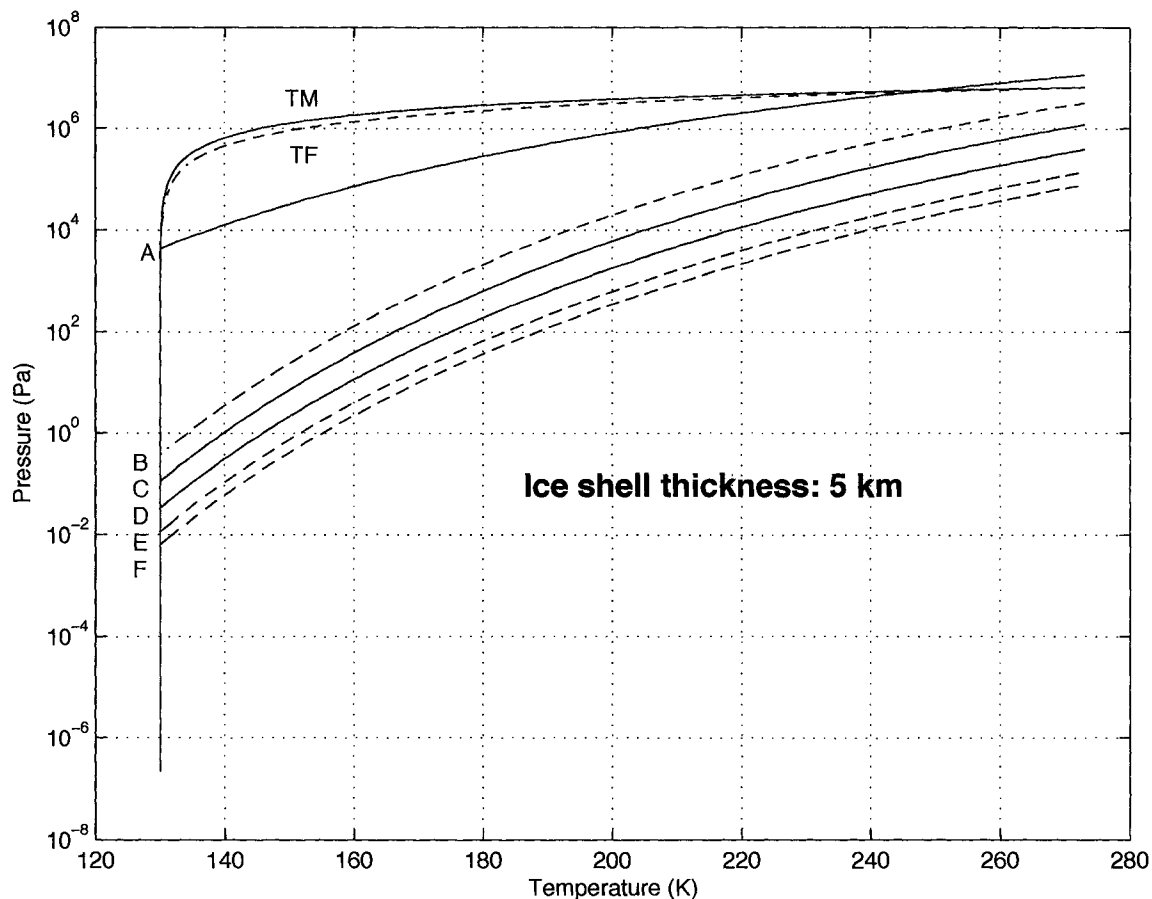


Figure 7.4: Mixed hydrate dissociation pressure curve for combined O_2 , CO_2 , and SO_2 hydrate. Mole fractions used for combined dissociation pressure were taken from european surface abundance measurements and estimates (see text). Percent by number abundances (relative to water) used for each curve are as follows: curve A, $O_2 = 4.0$, $CO_2 = 0.0$, $SO_2 = 0.0$; curve B, $O_2 = 4.7$, $CO_2 = 0.08$, $SO_2 = 0.03$; curve C, $O_2 = 1.3$, $CO_2 = 0.08$, $SO_2 = 0.03$; curve D, $O_2 = 3.0$, $CO_2 = 0.6$, $SO_2 = 0.3$; curve E, $O_2 = 4.7$, $CO_2 = 1.2$, $SO_2 = 1.7$; and curve F, $O_2 = 1.3$, $CO_2 = 1.2$, $SO_2 = 1.7$. Temperature-pressure profiles for three different ice shell thicknesses are presented (5 km, 10 km, and 30 km). For each case, the temperature gradient through the ice shell is modeled by both a simplified solution to Fourier's law (TF) and by a more complex Maxwell rheology (TM). The region below the ice profiles is the region of clathrate stability.

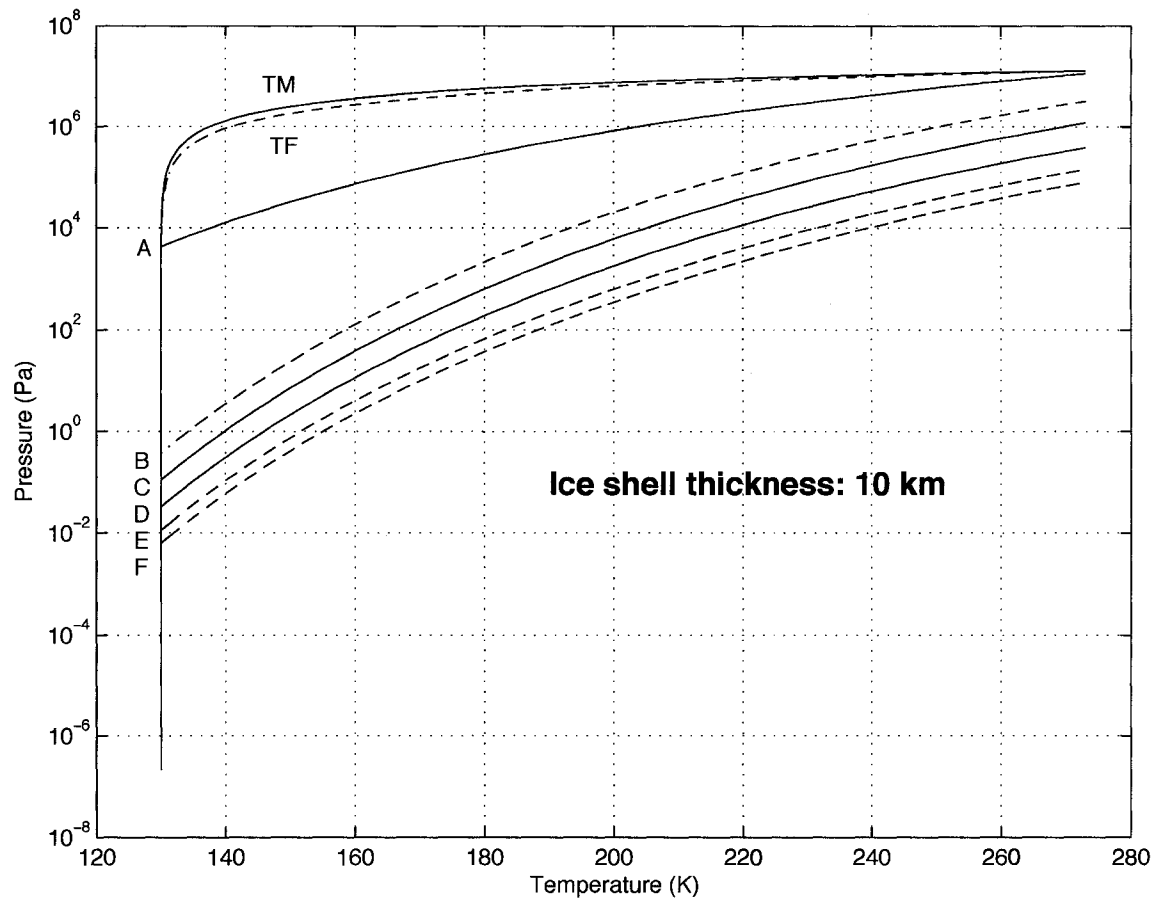


Figure 7.5: Mixed hydrate dissociation pressure curve for a 10 km ice shell on Europa. Details as per caption in Figure 7.4.

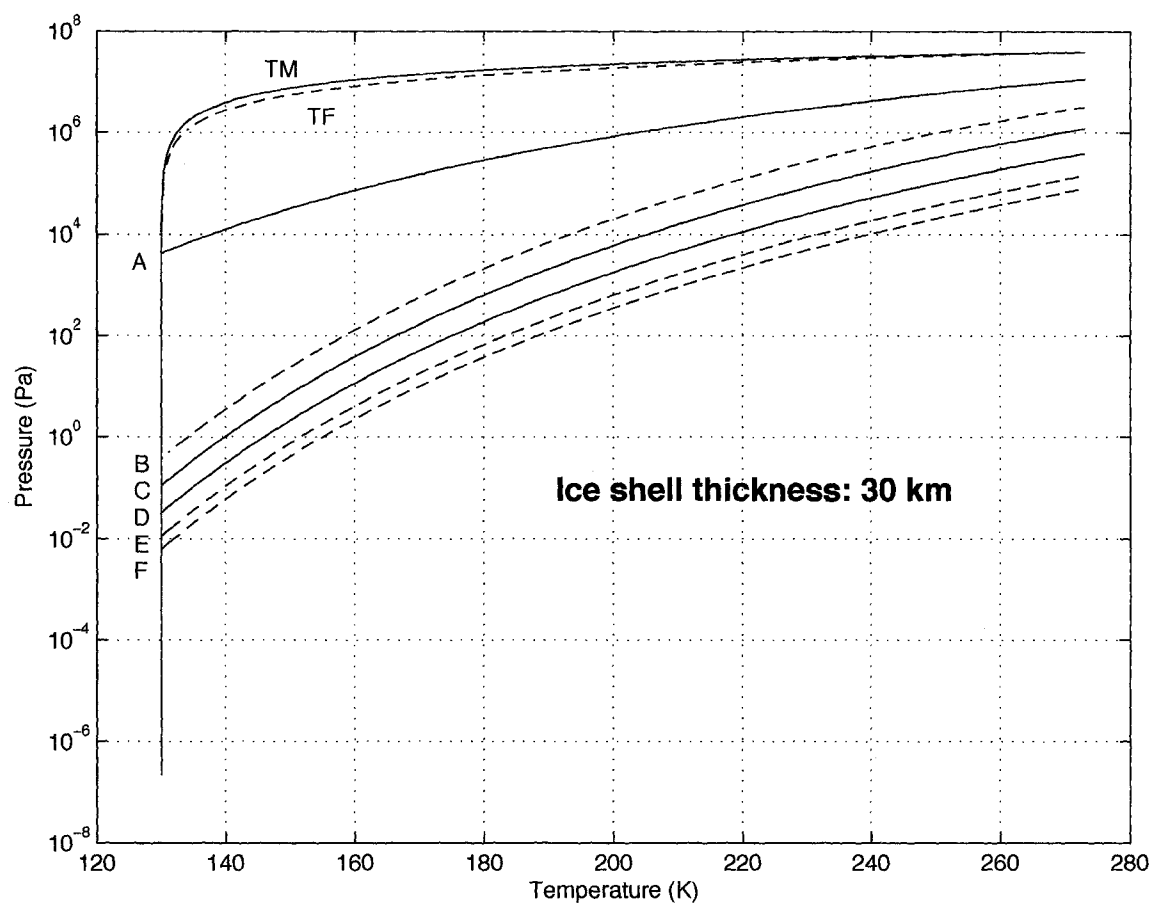


Figure 7.6: Mixed hydrate dissociation pressure curve for a 30 km ice shell on Europa. Details as per caption in Figure 7.4.

clathrate will have a density of 1.01 g cm^3 if 90% of all cages in SII clathrate are occupied. Thus, the pure oxygen clathrate is likely to be heavier than pure ice but lighter than a saltwater ocean solution [$\sim 1.03 \text{ g cm}^3$ for the Earth's ocean (Petrenko and Whitworth, 1999)]. Given the difference between the physical properties of ice and hydrate [*e.g.* very low thermal conductivity of hydrate (Sloan, 1998; Carroll, 2003)], such concentrations of hydrate will have important implications for the ice shell thickness and rheology. Such consequences are examined in more detail in Implications for the ice shell.

7.5.2 Carbon dioxide hydrate

Low temperature experiments by Miller (1961) determined the constants for CO_2 clathrate to be $A = 5.1524$ and $B = -1121.0$ for the temperature range of 175-232 K. The thermodynamic model of Lunine and Stevenson (1985) then predicts that at 100 K, the corresponding dissociation pressure will be $6.04 \times 10^{-2} \text{ Pa}$, a pressure that is reached at a depth of $\sim 47 \mu\text{m}$ below the surface [using a surface pressure of $2.2 \times 10^{-7} \text{ Pa}$ (Hall et al., 1995) and an ice density of 0.990 g cm^3]. The curve of Miller (1961) (shown in Figure 7.3) predicts a dissociation pressure of $8.87 \times 10^{-2} \text{ Pa}$, which corresponds to a depth of $\sim 68 \mu\text{m}$ below the surface. At 70 K and 130 K, the depth below the surface required for stability is $9 \times 10^{-4} \mu\text{m}$ and 2.64 cm, respectively. At 273 K, the dissociation pressure for CO_2 clathrate is $\sim 1.13 \text{ MPa}$, and thus, after nucleation near the surface, a pure CO_2 clathrate will be stable throughout ice shells of thickness 5, 10, and 30 km. Figure 7.3 shows the corresponding curve for CO_2 clathrate stability in the range of 70-273 K.

CO_2 typically forms SI clathrate, though the molecule can easily fit in the large cages of SII clathrate. The ratio of molecular diameter to cavity diameter for CO_2 and an SI small cage is 1.00, which makes CO_2 occupation of the cage without distortion difficult (Sloan, 1998). With a 5% small cage occupancy and a 90% large cage occupancy, we calculate a clathrate density of 1.03 g cm^3 , which is heavier than pure liquid water but comparable to that of salty ocean water. Estimates for CO_2 clathrate

densities over a range of temperature have found that, at lower temperatures, densities can increase by a few percent (Prieto-Ballesteros et al., 2004). Nevertheless, given the uncertainty of the salt content in Europa's putative ocean, it is difficult to predict whether pure CO₂ clathrates would sink to the ocean floor or float and accrete on the bottom of the ice shell.

7.5.3 Sulfur dioxide hydrate

SO₂ was perhaps the first clathrate hydrate ever to be observed, and was reported by Joseph Priestly in the late 1770's (Sloan, 1998). The constants $A = 5.96$ and $B = -1764$ for SO₂ are not well determined for the low temperatures expected on the surface of Europa (Miller, 1961). Nevertheless, Lunine and Stevenson (1985) have predicted a dissociation pressure of 6.65×10^{-7} Pa at 100 K. This is just a factor of ~ 3 larger than the surface pressure on Europa, and thus we expect SO₂ clathrates to be present from the surface to the base of the ice shell.

Clathrates of SO₂ form SI clathrate (Miller, 1961), and while the density of pure SO₂ clathrate has been reported to be as much as 1.4 g cm^3 (Crawford and Stevenson, 1988), we find a more conservative value of 1.13 g cm^3 by assuming zero small cage occupancy and 90% large cage occupancy. This is considerably more than the density of most salty ocean models for Europa (Kargel et al., 2000; Zolotov and Shock, 2001; McKinnon and Zolensky, 2003). Thus, if introduced into the ocean, such clathrates would likely precipitate to the ocean floor if they were not first dissolved into the solution.

7.5.4 Mixed hydrate

Using Eq. 7.2 and the relative abundance concentrations discussed in Radiolytic Production of Oxidants on the European Surface, the dissociation pressure curve for O₂-, CO₂-, and SO₂-contaminated ice on Europa can be calculated. The stability of the mixtures can then be compared with the temperature and pressure profiles for different ice shell thicknesses. Figures 7.4-7.6 shows the resulting plot with several different curves for various permutations of the upper and lower limits for each

molecular species.

The influence of adding a small fraction of CO₂ and SO₂ drastically decreases the dissociation pressure required to enclathrate the mixture with O₂. Despite the fact that the relative mole fractions of CO₂ and SO₂ are much less than that of O₂, the lower dissociation pressures for CO₂ and SO₂ results in an SI hydrate that is dominated by SO₂ occupancy, followed by CO₂ occupancy. For a 5-km shell with a surface temperature of 130 K, it takes only a 20% mixture with SO₂ for a mixed O₂-SO₂ clathrate to become stable at a depth of $\sim 10 \mu\text{m}$. When the mixture is 1:1, the depth below surface for stability is reduced to $\sim 4 \mu\text{m}$. Adding just 8.5% CO₂ or 0.22% SO₂ to O₂ reduces the dissociation pressure enough to allow the clathrate phase to be stable through to the bottom of the 5-km ice shell.

Considering clathrate formation from a mixture, however, may be an erroneous assumption for the surface of Europa. For mixtures in terrestrial systems, where clathrates usually nucleate from liquids or gases, the dissociation pressure and structural preference are a result of the initial mixture. On Europa, radiolysis produces a singular compound within the ice matrix, and such compounds may subsequently aggregate to form bubbles (Johnson and Jesser, 1997). Thus initially one might expect an O₂ bubble to form SII and CO₂ and SO₂ bubbles to form SI. The effect of radiation on clathrate formation has not been well studied in the laboratory environment; thus we are pursuing experiments to analyze these process in the laboratory.

Near the surface, however, neither solid O₂ or pure O₂ clathrate is going to be stable, as was shown in the section on pure oxygen clathrates in the ice shell. Stability of O₂ in the mixed clathrate on the surface of Europa is much greater than the pure O₂ clathrate or the solid-phase O₂. Thus we suggest that radiolytically produced O₂ diffuses through the near surface ice until it either: (a) escapes to the moons surface-bound atmosphere (Shematovich et al., 2005) and ultimately via ionization to the jovian magnetosphere, or (b) is incorporated into the mixed hydrate of CO₂ and SO₂ and is trapped in what is most likely SI clathrate. An interesting consequence of this prediction is that the mixed SI clathrate will predominantly have large cages capable of holding two oxygen molecules. While double occupancy of clathrate cages is inconsistent with the original clathrate theoretical work of van der Waals and

Platteeuw (1959), recent experimental work indicates that double occupancy with some guest molecules, such as O_2 , may occur (Champagnon et al., 1997; Kuhs et al., 1997; Chazallon and Kuhs, 2002). Indeed, the 5771 Å line observed by Spencer and Calvin (2002) could be condensed solid-phase O_2 as described in that work, or as we propose, it may be the result of two enclathrated O_2 molecules occupying the same cage or a clathrate-sealed O_2 microatmosphere-bubble. The interaction of two clathrate-trapped O_2 molecules could be an alternative explanation to the 5771 Å line reported for the presence of solid-phase O_2 on the surface of Europa, Callisto, and Ganymede (Spencer et al., 1995; Spencer and Calvin, 2002). In our model, radiolysis produces SO_2 , CO_2 , and O_2 , after which the SO_2 forms SI clathrate at the surface and CO_2 forms SI clathrate very near the surface. Diffusion of these compounds results in a mixed SO_2 - CO_2 clathrate. Molecular oxygen, which is unstable near the surface, diffuses toward the surface, but if it encounters the clathrate mixture, it too is incorporated into the structure. We note that, as a result of the bonding parameters of the H_2O molecules in the clathrate structure, SII clathrate is intrinsically more stable than SI clathrate (Kuhs et al., 1997). Given the high-energy radiation environment of the near surface of Europa, SII clathrate may be the more stable phase for the SO_2 - CO_2 - O_2 mixture. Alternatively, microatmosphere-bubbles of an O_2 - CO_2 - SO_2 mixture may aggregate and subsequently form a mixed clathrate at the bubble boundary. The low porosity of the clathrate shell could effectively trap the O_2 in the bubble, which would lead to an O_2 - O_2 interaction and photon absorption. However, this scenario would imply gaseous O_2 and thus fails to meet the 1-0 band asymmetry requirement needed to meet the observations (Baragiola et al., 1999).

If conditions for clathrate formation and stability are such that clathrate form in equilibrium with liquid water, then the issue of clathrate density plays an interesting role in where such clathrate will ultimately reside. For a given aqueous solution and clathrate host, one would expect the clathrate crystals to float on the surface or sink to the ocean floor.

Determining the clathrate density is complicated by several factors related to the unique environment of clathrate formation on Europa. First, to determine density, one needs to know which clathrate structure will form, and as mentioned above, it

may not be correct to assume that the $\text{SO}_2\text{-CO}_2\text{-O}_2$ mixture will form SI clathrate. SI clathrates typically have a higher hosting capacity per unit volume, so for a given guest molecule or mixture, formation of SI clathrate will be more dense than that of SII clathrate. For the simple and relatively small hydrate formers discussed here (O_2 , CO_2 , SO_2), both structures are large enough to host the molecules. The small size of O_2 results in additional stability for the SII over the SI form (Sloan, 1998). The SII form has three times the number of small cages per unit volume, so with O_2 occupancy of these cages the structure is stabilized. When mixed with a small amount of CO_2 or SO_2 , however, the SI form becomes the more stable structure.

Density calculations are dependent on the cage structure, the guest molecules, and the fractional occupancy of the guest at a given temperature and pressure. The equation for calculating hydrate density is:

$$\rho = \frac{\frac{N_W}{N_{Ave}} \left[MW_{H_2O} + \sum_{j=1}^C \sum_{i=1}^N y_{ij} \nu_i MW_j \right]}{V_{cell}} \quad (7.10)$$

where N_W is the number of H_2O molecules per cell, N_{Ave} is Avagadro's number, MW_j is the molecular weight of guest j , y is the fractional occupation of cavity i by component j , V is the number of cavities of type I, V_{cell} is the volume of a unit cell, N is the number of cavity types in a unit cell, and C is the number of components in the hydrate phase.

Here we calculate the necessary mixing ratios for O_2+CO_2 and O_2+SO_2 to raise both SI and SII clathrate densities above 1.10 g cm^3 . We choose 1.10 g cm^3 as a reasonable estimate for a substance that would sink in most proposed european saltwater solutions (Kargel et al., 2000; Zolotov and Shock, 2001; McKinnon and Zolensky, 2003). For SI clathrate, an oxygen occupancy of 90% and 10% for the small and large cages, respectively, coupled with a 0% and 80% small and large cage occupancy for SO_2 , yields a clathrate density of 1.16 g cm^3 . By comparison, the density for SII clathrate with the same occupancy is 1.09 g cm^3 . If we replace SO_2 with CO_2 , the SI density is 1.10 g cm^3 , and the SII density is 1.04 g cm^3 . Splitting the large cage occupancy such that 30% of the cages are occupied by CO_2 and 60% by SO_2 , and assuming 100% small cage occupancy by O_2 , gives a density of 1.15 g

cm³. All SI mixtures with a reasonable large cage occupancy of SO₂ or CO₂ result in a density greater than that of most saltwater solutions considered reasonable for Europa (Kargel et al., 2000; Zolotov and Shock, 2001; McKinnon and Zolensky, 2003).

Consequently, as the mixed clathrate is introduced into the liquid water ocean, it is to be expected that the clathrate will precipitate to the seafloor and form a layer of clathrate sediment if no hydrothermal sources are available for reducing the material. This only holds if the mole fractions of CO₂ and SO₂ dissolved in the ocean water is such that clathrate begins to form.

Considering the bulk carbon content of a euroman ocean, Crawford and Stevenson (1988) have used a total CO₂ mass on Europa of $10^{21} - 10^{24}$ g to yield mole fraction concentration levels between 2.6×10^{-4} and 0.21. Factoring in for clathrate buffering, they suggest a CO₂ equilibrium concentration for a 272 K ocean, where $P_{top} = 100$ bar (10 MPa) and $P_{bottom} = 1,000$ bar (100 MPa), of 3×10^{-3} mole fraction. Similarly, given the cosmic abundance of sulfur in relation to rock-forming elements, Crawford and Stevenson (1988) have argued that SO₂ could reach a concentration of $\sim 1 \times 10^{-3}$ mole fraction on Europa. By comparison, the observed surface abundance for these compounds is $\sim 8 \times 10^{-4} - 6 \times 10^{-3}$ mole fraction, which is not too far from the model predictions.

If we assume that the subsurface ocean has reached the above-mentioned concentrations, then any incoming gases-which would already be in mixed clathrate form-would remain in the clathrate phase and precipitate to the ocean floor. Now instead of having an O₂ reservoir at the base of the ice sheet, the available O₂ is trapped in the mixed clathrate with CO₂ and SO₂, and the combination settles on the ocean floor.

Here, however, we reach an interesting problem with regard to the ice shell gas concentration and oceanic gas concentrations. We can assume that the radiolytically produced O₂ (O₂ and H₂O₂) is a net inward flux to the ocean because its source is the intensely irradiated and chemically active surface environment. The case is different for CO₂ and SO₂. If fracturing and eruptions are the primary mechanisms for recycling the ice shell, then ice shell concentrations of these species should closely parallel oceanic concentrations. The only net source of new sulfur and carbon would

be ionogenic sulfur and impact-delivered or solar wind-derived carbon. Interestingly, the near agreement of the observed surface values and the oceanic concentrations needed for clathrate precipitation suggests that, without exogenic sources of S and C, there would be no net mixed clathrate precipitation for a given shell recycling period. Oxygen alone would remain as the net increasing gas and hydrate-forming species. Thus the partitioning of O₂ clathrate in the ice shell and mixed clathrate on the seafloor could be a metric of exogenic sulfur and carbon delivery to Europa. In other words, where the incoming O₂ gets stored - at the base of the ice shell or the base of the ocean - is highly dependent on the incoming flux of other clathrate formers such as carbon and sulfur species.

7.6 Implications for the ice shell

If clathrates play a large role in the ice physics of the european ice shell, then several aspects of the resulting rheology, thermal physics, and electrical chemistry need to be reexamined. Table 7.1 provides a summary of some of these properties. Based on our results, in which we consider only those clathrate guest molecules produced radiolytically at the surface, we expect the bulk ice shell to be mixed with $\sim 1.7-7.6\%$ oxidants by number relative to water. When enclathrated, the cage occupancy and resulting stoichiometry are such that each oxidant molecule requires ~ 6 H₂O molecules (Miller, 1961; Sloan, 1998). This is a conservative estimate as there may be more empty cages that could drive this number higher. At $1.7-7.6\%$ oxidant abundance, the resulting clathrate contribution would fall in the range of $12-53\%$ relative to pure ice. Many of the existing models for the behavior of the european ice shell assume bulk properties comparable to pure water ice. At low levels of clathrate abundance this is a valid assumption; however, once levels get beyond $\sim 10\%$ abundance, as is shown below, the difference in physical properties between clathrates and ice could play a significant role in bulk properties of the ice shell.

Even higher levels of clathrate abundance could easily be reached if clathrates introduced into the ocean are not dissolved but accreted onto the ice shell at the

| <i>Property</i> | <i>Clathrates</i> | <i>Ice (I_h)</i> |
|-------------------------------|---|--|
| Thermal conductivity (263 K) | $0.50 \pm 0.01 \text{ W m}^{-1} \text{ K}^{-1}$ | $2.2 \text{ W m}^{-1} \text{ K}^{-1}$ |
| Thermal expansion coefficient | $44 \pm 9 \times 10^{-6} \text{ K}^{-1}$ | $31 \pm 9 \times 10^{-6} \text{ K}^{-1}$ |
| Young's modulus (at 268 K) | $8.4 \times 10^9 \text{ Pa}$ | $9.5 \times 10^9 \text{ Pa}$ |
| Bulk modulus (272 K) | 5.6 | 8.8 |
| Shear modulus (272 K) | 2.4 | 3.9 |
| Poisson's ratio | 0.33 | 0.33 |
| Dielectric constant (273 K) | ~ 58 | 94 |

Table 7.1: Properties of clathrates and ice. Data are from Sloan (1998), Carroll (2003), and Takeya et al. (2000).

icewater interface. Furthermore, clathrate levels could be considerably higher if endogenous hydrothermal compounds, such as methane, hydrogen sulfide, and carbon dioxide, are incorporated into the ice shell during cryovolcanic events. Compressional events may also serve to concentrate clathrates. Work by Durham et al. (2003) indicates that during deformation of methane hydrate (SI) free water within the hydrate lattice migrates to free surfaces, thus segregating the water ice from the hydrate phase. As the tidal stress and strain deforms the ice shell of Europa, clathrates and ice could become segregated through this process. Such differentiation, taking place over long time scales, could potentially yield a heterogeneous ice shell.

A key consequence of significant clathrate abundance in the ice shell is its role in determining the ice shell thickness. The steady-state thickness of the ice shell on Europa depends on the heat flux through the ice and the temperature difference between the surface and the sub-ice (most likely, liquid water) layer. Here we are considering heat loss only through conduction, not convection. The ice shell thickness grows or shrinks depending on changes in these parameters, and the extent to which the ice shell compensates is directly dependent on the thermal conductivity of the ice. This relationship, known as Fourier's law, is largely analogous to Ohm's law in electronics and is typically expressed as:

$$H = k \left(\frac{\delta T}{\delta z} \right), \quad (7.11)$$

where k is the thermal conductivity. Thermal conductivity, however, is itself a function of temperature:

$$k(T) = \frac{a}{T} + b \quad (7.12)$$

with $a = 651 \text{ W m}^{-1}$ for water ice Ih empirically determined and good for temperatures $>60 \text{ K}$ and b usually taken to be 0 (Petrenko and Whitworth, 1999). Thus for the coldest ices on the surface of Europa ($\sim 70 \text{ K}$), $k = 9.3 \text{ W m}^{-1} \text{ K}^{-1}$, and for the basal ice just above the icewater interface ($\sim 270 \text{ K}$), $k = 2.4 \text{ W m}^{-1} \text{ K}^{-1}$. The heating rate for a given layer within the shell depends on the difference between the heat flow in and out of the shell, combined with the volumetric heating rate (due to tidal heating), q , within the layer itself:

$$\frac{\delta H}{\delta z} + q = \rho C_P \frac{\delta T}{\delta t}, \quad (7.13)$$

where ρ is the density of the material and C_P is the specific heat capacity at constant pressure. At steady state, and with q assumed to be roughly 0, this equation can be solved exactly for the ice shell thickness. In the simplest model, k is chosen at some intermediate value, and the ice layer thickness, h , is then determined by

$$h = k \frac{T_b - T_s}{H} \quad (7.14)$$

where T_b is the temperature at the base of the ice shell and T_s is the temperature at the surface.

Assuming $q \approx 0$, however, is not valid for the case of Europa, where tidal heating occurs within the ice shell. The volumetric heating rate is highly dependent on the ice temperature (Ojakangas and Stevenson, 1989; Chyba et al., 1998):

$$q \propto e^{l(1-T_m/T)} \quad (7.15)$$

where T_m is the melting temperature of the ice and l is equal to 24 at T_m . The net effect is that much of the tidal energy is dissipated near the base of the ice shell. Incorporating $q \neq 0$ and $k \neq \text{constant}$ into our solution yields the following equation

for the ice shell thickness (Chyba et al., 1998):

$$h = \left(\frac{a}{2H^2} \right) \left[-2F \pm (4F^2 + 4H^2 [\ln(T_b/T_s)]^2)^{1/2} \right] \quad (7.16)$$

Here F is the energy flux through the surface. Considering both the simplified model and the more complex rheology model, we examine the effect of clathrates.

Knowledge of the thermal conductivity of clathrates is limited to just a few studies (Sloan, 1998; Carroll, 2003). All studies, however, indicate that the thermal conductivity of clathrates is much less than that of ice and is $\sim 0.5 \text{ W m}^{-1} \text{ K}^{-1}$ (note that reported measurements have been primarily for clathrates of hydrocarbons). The temperature dependence is not well understood, but as a rough estimate we assume that $a = 131.5 \text{ W m}^{-1}$ for clathrates.

Taking the extreme case of a pure clathrate shell, we find that for a given temperature gradient and heat flux, the thickness of the clathrate shell would be reduced by a factor of 3-5 relative to pure ice. For a suggested heat flow of $24\text{-}50 \text{ mW m}^{-1}$ (Squyres et al., 1983; Melosh et al., 2004) and a temperature difference of 170 K, Eq. 7.14 yields an ice shell of $17\text{-}8.2 \text{ km}$ thick or a clathrate shell of only $3.4\text{-}1.7 \text{ km}$ in thickness. With $H = 24 \text{ mW m}^{-1}$ and solving for pure ice, Eq. 7.16 yields a shell thickness $\sim 15 \text{ km}$. For the case of a clathrate shell, the thickness is found to be $\sim 4 \text{ km}$. For $H = 50 \text{ mW m}^{-1}$ the solutions are $\sim 8 \text{ km}$ and $\sim 2 \text{ km}$ for ice and clathrate, respectively. The added insulating capability of the clathrate allows the shell to maintain a much steeper temperature gradient between the liquid water layer and the space environment.

If we consider 10% clathrate abundance and use $k_{ice} = 2.4 \text{ W m}^{-1} \text{ K}^{-1}$ and $k_{clathrate} = 0.5 \text{ W m}^{-1} \text{ K}^{-1}$, we find that the fractional decrease in shell thickness, relative to the pure ice case and using Eq. 7.14, is in the range of 7.9-27.5%. The low-end estimate comes from considering the two different materials conducting in parallel ($k_{Total} = 0.9k_{ice} + 0.1k_{clathrate}$), while the high-end estimate comes from considering the materials conducting in series ($1/k_{Total} = 0.9/k_{ice} + 0.1/k_{clathrate}$). At 50% abundance and 24 mW m^{-1} , the ice shell is reduced to $\sim 6 \text{ km}$ versus $\sim 17 \text{ km}$ for the pure ice case (here we have taken ice and clathrate in series). Physically, the series model is

likely more realistic as this would correspond to a shell with clathrate grains mixed throughout. However, at low clathrate concentrations a complete conductivity path through ice will be easily found, and $k_{Total} \approx k_{ice}$. If layers of clathrate accumulate, the series model for adding the reciprocal of the conductivities is also correct. The parallel configuration would require continuous, direct, independent conduction paths through both materials. As previously mentioned, such differentiation within the shell might be possible, though we see it as unlikely.

Along with the bulk ice shell thickness, the apparent inelasticity of clathrates (Durham et al., 2003) could make convection in a thick shell more difficult. Furthermore, the onset of convection in Europa's ice shell is determined by the Rayleigh number (Turcotte and Schubert, 1982):

$$Ra = \rho g h^3 \alpha \Delta T / (\kappa \eta) \quad (7.17)$$

which, with a thin clathrate shell, would be less likely to surpass the critical Rayleigh number, generally assumed to be in the range of 500-3,500 (Pappalardo et al., 1998). In addition, the morphology of impact craters, used in generating some estimates for the ice shell thickness (Turtle and Pierazzo, 2001; Schenk, 2002), must be reconsidered if our results for clathrates are correct. For instance, calculating the relaxation times for central peaks in large craters would require not only incorporating the clathrate viscosity (poorly constrained), but also the reduced thermal conductivity and increased thermal expansion coefficient. Finally, we note that the dielectric constant of SI and SII hydrates is nearly half that of pure ice (Sloan, 1998) - *i.e.* it is a better insulator - such concentrations could affect Europa's induced magnetic field and possibly influence active remote sensing techniques such as ice-penetrating radio sounding (radar). In the later case, a better insulator permits greater radar penetration (Chyba et al., 1998).

Finally, the above-noted effects on ice shell thickness provide the first suggestion known to us of a significant coupling between irradiation processes of external origin and the internal rheology of an irradiated icy body in a planetary magnetosphere. The $\sim 100 \text{ mW m}^{-2}$ energy flux of incident magnetospheric particles (Cooper et al.,

2001) exceeds the heat fluxes from radiogenic and tidal heating and contributes to clathrate formation via production of mobile volatile gases and possibly through the kinetic effects of sputtering. Europa, we conclude, is potentially a body with both rheological and astrobiological processes driven in part by the extremely high-energy flux of energetic particles from the magnetospheric environment.

7.7 Conclusion

The radiolytic production of O_2 , H_2O_2 , CO_2 , and SO_2 on the surface of Europa likely generates a 1-10 m deep layer of surface ice with an oxidant contribution of 1.7-7.6% by number relative to H_2O . This layer could extend through a larger fraction of the ice shell if resurfacing mechanisms are such that ice processed at the surface is entrained into the bulk ice shell. Compared with oxygen levels found in the Antarctic ice sheet (Lipenkov and Istomin, 2001), we find that the surface ice of Europa may be three to four orders of magnitude more oxidizing. While such compounds could potentially be of use to a subsurface ecosystem, the oxidizing surface may also rapidly destroy any potential chemical or molecular fossils of such organisms.

Molecular oxygen produced via radiolysis at depth (greater than tens of centimeters) could form an SII hydrate. Molecular oxygen produced near the surface will be unstable and migrate upward through the ice where it may encounter a mixed SO_2 - CO_2 clathrate. Similarly, atmospheric O_2 diffusing into the ice may also encounter the mixed clathrate. If O_2 joins the clathrate mixture, it will remain stable in this phase at the surface, and as such, the double occupancy of a clathrate cage by two O_2 molecules could explain the thermodynamically puzzling observation of condensed O_2 on the surface of Europa and other galilean satellites (Baragiola and Bahr, 1998; Johnson, 1999; Spencer and Calvin, 2002). A second possible mechanism for clathrate-enhanced trapping of O_2 is that of a clathrate-sealed gas bubble, though this scenario cannot account for the 5771 Å absorption attributed to solid-phase O_2 .

We also note that the formation of the mixed clathrate could serve as a sink for O_2 in the atmosphere, possibly providing an explanation for the patchiness of Europa's atmospheric oxygen airglow as observed by the Hubble Space Telescope

(McGrath et al., 2004). Laboratory work in progress will hopefully help us unravel the connection between the proposed radiolytic sulfur cycle (Carlson et al., 1999b) and the radiolytic oxygen cycle.

A mixed $\text{SO}_2\text{-CO}_2\text{-O}_2$ clathrate will be stable throughout the ice shell for thicknesses of 5 km and higher. The formation of clathrate from 1.7% to 7.6% by number oxidant abundance implies that clathrate contributions could reach levels of 12-53% by number relative to ice. Such a high concentration of clathrate has significant implications for the flow of heat through the ice shell. We find that for clathrate admixtures in the range of 10-50% by number relative to pure ice, there is a corresponding fractional decrease in the ice shell thickness (relative to pure ice) of $\sim 8\text{-}60\%$. In other words, for a given heat flux through the ice, clathrate-contaminated ice shells are thin in comparison with a pure ice shell. Since the oxidants are produced primarily by surface irradiation, this suggests the new possibility of icy moon rheology driven in part by irradiation, an inescapable environmental process in magnetospheres of large planets with strong magnetic fields.

Oxidants produced on the surface of Europa and trapped as clathrates may represent a reservoir of biologically useful compounds within the ice shell. Such a reservoir could have important implications for habitability of the putative ocean, and the ice shell itself (Chyba and Hand, 2001). Because of uncertainties in ice shell resurfacing time scales and delivery mechanisms, the oxidant flux is difficult to constrain. We find, however, that for a 100 million year resurfacing time scale and a 1.2-4.6% by number O_2 contribution to the upper 1 m of ice, $2 \times 10^8 - 8 \times 10^8 \text{ mol year}^{-1}$ of O_2 is delivered to the ocean. This is comparable to estimates for the delivery of reductants (such as CH_4 and H_2S) expected from activity on the ocean floor (McCollom, 1999).

We note that Raman spectroscopy has been utilized for the study of clathrates in the laboratory and has frequently been considered a useful tool for life detection (Champagnon et al., 1997; Ellery and Wynn-Williams, 2003). Future spacecraft landers equipped with such instrumentation will be of use for understanding both the ice physics and habitability of Europa.

Chapter 8

The surface chemistry of oxidants and reductants on Europa¹

The geographic distribution of surface chemistry on Europa is complicated by the variety of factors affecting different hemispheres of the moon. Due to the small gyroradii of the electrons, the trailing hemisphere experiences the bulk of the irradiation as the magnetic field sweeps past Europa. The leading hemisphere experiences less radiation but undergoes enhanced gardening and delivery of elements from micrometeorite impacts. Exogenous sulfur, carbon, and oxygen are delivered both as high-energy ions and as components of chondritic impact material (Johnson et al., 2004). Endogenous delivery of material from the subsurface may help explain some of the observations (McCord et al., 1998b), but it is difficult to assess endogenous sources. Figure 8.1 summarizes our current understanding of the global distribution of many of the identified compounds and some of the large-scale processes affecting such distributions. This map approximates distributions based on currently available data; some compounds may have much broader distribution, but here we limit ourselves to the available observations. We refer the reader to Carlson (2001); Carlson et al. (2005); Greeley et al. (2004) and Johnson et al. (2004) for more detail.

¹Much of this chapter has been accepted for publication as (Hand et al., 2007).

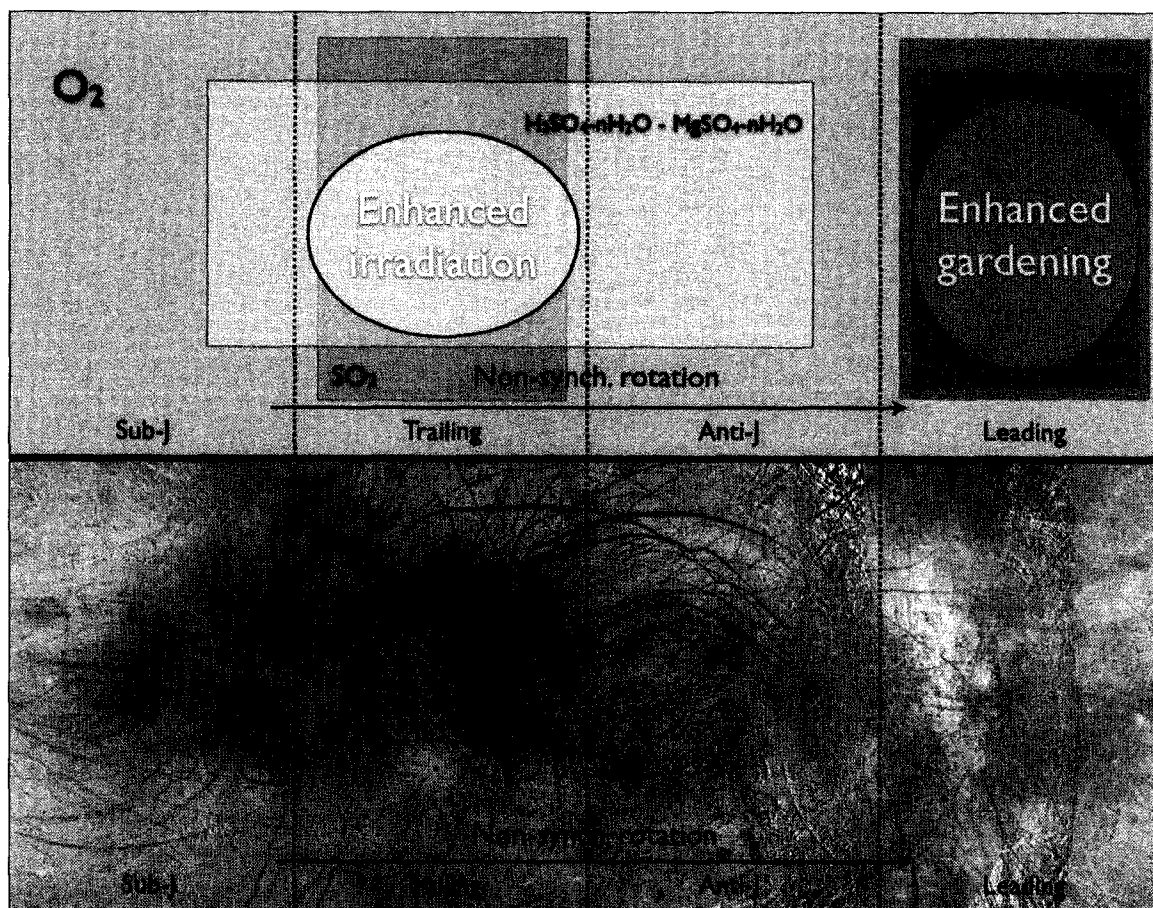


Figure 8.1: Global scale processes affecting the surface of Europa. Sub-J and Anti-J correspond to the sub-jovian and anti-jovian hemispheres. Europa's leading hemisphere experiences enhanced gardening resulting from an increased micrometeorite flux. The trailing hemisphere experiences enhanced irradiation, due to the small gyroradii of the electrons carried by the magnetic field. The direction of (slow) non-synchronous rotation is shown by the arrows. Boxes for distribution of observed chemical compounds are approximate. We note that the sulfur hydrate is found globally, but high concentrations are found in the region outlined.

8.1 Oxidants

The primary observed oxidants on Europa are H_2O_2 , O_2 , SO_2 , CO_2 , and the SO_4^{2-} anion. Observations from the Near Infrared Mapping Spectrometer (NIMS) onboard the *Galileo* spacecraft set the surface abundance of radiolytically produced H_2O_2 at

0.13% by number relative to H₂O (Carlson et al., 1999a). The presence of a thin O₂ atmosphere ($\sim 10^{-14}$ bar) on Europa has long been known (Hall et al., 1995) and more recent work indicates that molecular oxygen is trapped in the surface ice of Europa (Spencer and Calvin, 2002). Hand et al. (2006) have taken a detailed look at the ground based observations of O₂ and concluded that the 0.3% absorption in the 5771 Å band observed by Spencer and Calvin (2002) implies an O₂ abundance of 1.2–4.6% O₂ by number relative to H₂O.

The surface abundance of SO₂ is $\sim 0.3\%$ by number relative to H₂O with a range of 0.1–1.7% constrained by compositional arguments (Hand et al., 2006; Kargel et al., 2000; Crawford and Stevenson, 1988). The dominant reservoir for sulfur on the surface is sulfate, with NIMS observations indicating regions with $\sim 10\%$ sulfate by number relative to H₂O (Carlson et al., 2005).

Carbon dioxide is present on the surface of Europa at an abundance of 0.08% by number relative to H₂O (Chyba, 2000). Given a chondritic origin for Europa, the abundance could be as high as 1.23% (Kargel et al., 2000). Carbon monoxide likely exists as a result of CO₂ radiolysis, but due to low signal to noise with NIMS at the CO 2141 cm⁻¹ band it has not been observed on the surface or in the atmosphere.

The delivery of these oxidants to the sub-surface ocean could drastically alter the oceanic chemistry and, consequently, the habitability of the ocean. The largest uncertainty, however, is the physical mechanism and timescale for delivery. We therefore choose this parameter as a variable and consider the range of delivery rates for these oxidants over a wide range of delivery periods. Here we define the delivery period, τ_d , as the average time it takes for material on the surface of Europa to reach the putative subsurface ocean. In other words, for a given radiolytic product - *e.g.* O₂ - it will take on average τ_d years for that molecule to be transferred to the ocean. Previous work (Chyba, 2000; Chyba and Phillips, 2001) considered τ_d to be roughly equivalent to the observed surface age, τ_{ice} . This may be a fair approximation but other alternatives are possible and for that reason we decouple the two parameters in the work presented here.

In Section 8.4 we explore the relationship between these two quantities and provide some constraints for the delivery period. For the present calculations, however we

make no restrictions on τ_d other than to set an upper limit of 0.5 Gyr. Beyond 0.5 Ga, models for the thermal-orbital evolution of Europa indicate a more tidally active world with a significantly increased heat flux (Hussmann and Spohn, 2004). We assume that an increased heat flux would lead to increased ice shell activity. For this reason we see 0.5 Gyr as a sufficient upper limit for our calculations.

In Figure 8.2 we plot moles of compound delivered per year as a function of delivery period. The total number of moles of each compound is determined by integrating the percent by number abundance constraints through the gardened regolith of the surface. Gardening depths, d_g , are calculated based on Cooper et al. (2001),

$$d_g = 10^{-6} g_0 t (1 + t/t_0)^{-0.55}, \quad (8.1)$$

where $g_0 = 1.2 \mu\text{m yr}^{-1}$ is the initial cumulative growth rate and $t_0 = 1.7 \times 10^5$ yrs is the mixing timescale. For a given delivery period the gardening depth is calculated using $t = \tau_d$ and the resulting total number moles of each compound is found. Though gardening depth is a function of surface age, it is an appropriate integration depth for us to use because resurfacing mechanisms such as cryovolcanism will only serve to increase the depth of the layer of radiolytically processed material. For long delivery periods, the gardening depth is likely a very conservative underestimate for this depth.

The number of moles delivered to the ocean per year, η_i , is then found by dividing the total numbers of moles of compound i by the delivery period,

$$\eta_i = \frac{A d_g \epsilon_i}{\tau_d}. \quad (8.2)$$

Here A is the surface area of Europa and ϵ_i is the concentration of each compound throughout the gardened layer in units of moles per cubic meter.

If the delivery period is comparable to the observed surface age of 30–70 Myr (Zahnle et al., 2003), then the ocean on Europa receives between $8 \times 10^8 - 5 \times 10^9$ moles per year of O_2 . If the delivery period is 10 Myr, the flux lies between $2 \times 10^9 - 9 \times 10^9$ moles per year. Even at $\tau_d = 500$ Myr the flux lies between $3 \times 10^8 - 1 \times 10^9$ moles O_2 per year. These numbers are comparable to the contemporary O_2 flux of 7×10^9

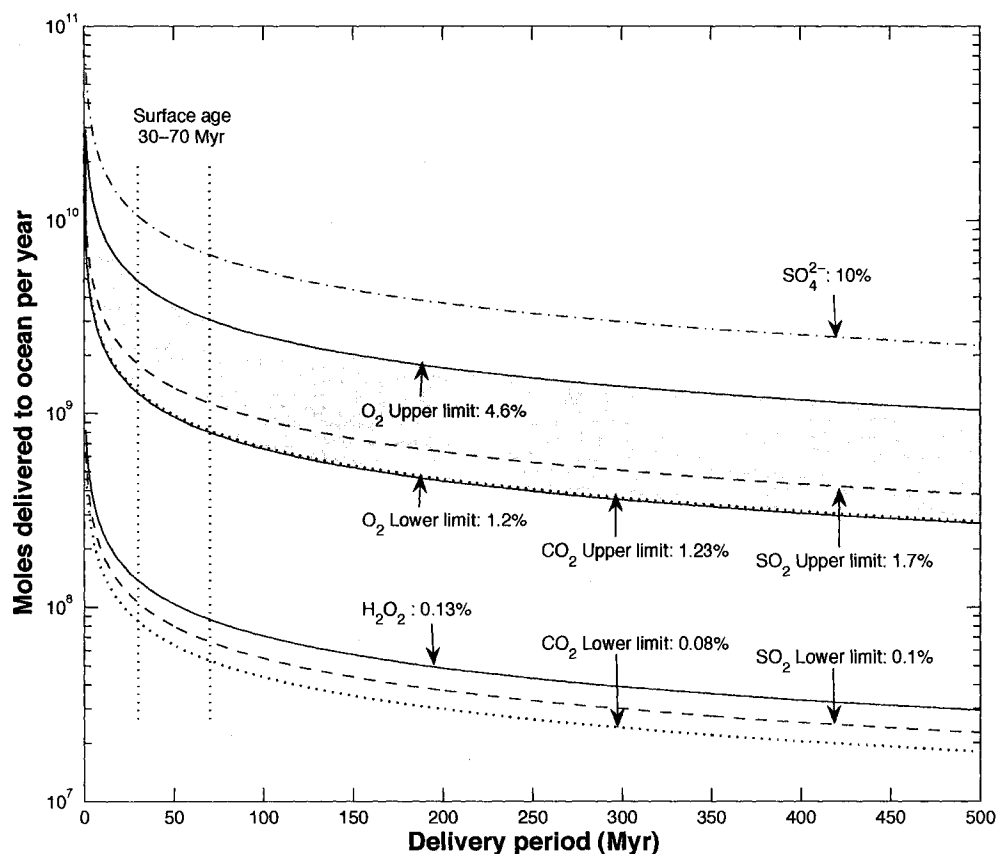


Figure 8.2: Moles per year of radiolytically produced oxidants delivered to the subsurface ocean of Europa. The delivery period, τ_d , is the average time it takes for material on the surface of Europa to reach the ocean. While the surface age falls between 30-70 Myr (Zahnle et al., 2003), the delivery period could be considerably longer depending on ice shell structure and resurfacing mechanisms (see text). The abundances of compounds are given in percent by number abundance relative to water. Upper and lower bounds on abundances are set by empirical constraints or compositional models.

moles yr^{-1} resulting from photolysis in Earth's upper atmosphere. Photosynthesis on Earth, by comparison, yields $\sim 10^{16}$ moles per year (Walker, 1977).

In Figure 8.3 we calculate the integrated molarity of O_2 and H_2O_2 in a 100 km thick global ocean. Our results are for 1 Gyr of integration over the delivery period

– e.g. for $\tau_d = 100$ Myr the ocean would have received the gardened surface reservoir of oxidants ten times. To explore the upper limits on concentration, here we have considered a scenario in which radiolytically produced oxidants are delivered to an ocean with no chemical sinks. Upon delivery to the ocean, these compounds will react with available reductants and we consider this scenario in Figure 8.7 and Section 8.3.

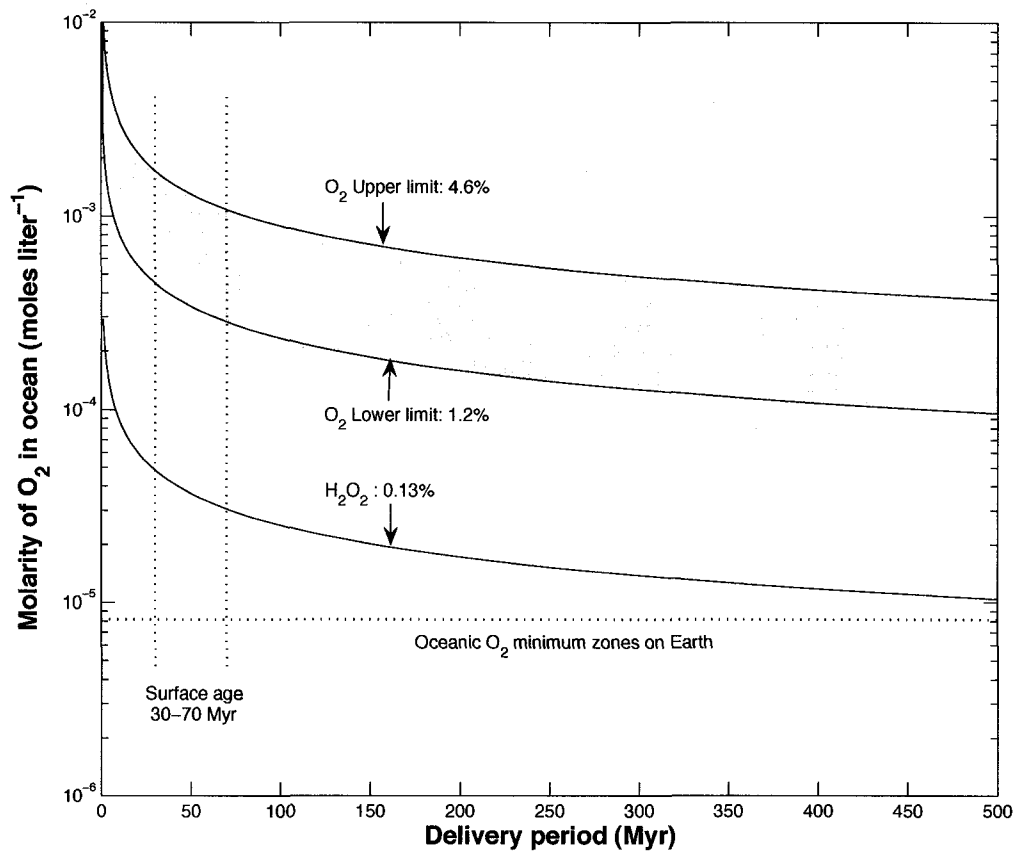


Figure 8.3: Oxygen molarity of a 100 km global ocean on Europa, assuming no oxygen sinks. For a given delivery period the flux is integrated over 1 Gyr.

Shown in Figures 8.3 and 8.7 are limits for dissolved O_2 concentrations needed for some terrestrial oceanic metazoans (Childress, 1968; Childress and Seibel, 1998). The work of Childress (1968) was on the small (35–125 mm in length) crustacean *Gnathopausia ingens*. For all values of the delivery period, O_2 concentrations are at

least an order of magnitude greater than those needed to support complex life forms like *Gnathophausia*. Indeed, delivery of H_2O_2 alone will be sufficient to achieve such concentrations. Oxygen limits for single-celled microorganisms are more difficult to constrain (Sleep, 2005), but are certainly lower than that of metazoans. The solubility of oxygen increases with decreasing water temperature and increasing pressure, thus while regions of our ocean are $\sim 3\%$ supersaturated with O_2 ($\sim 250 \mu\text{M}$), if Europa's ocean is near 0°C and 10–100 MPa, then O_2 saturation will be $\sim 50 \text{ mm}$ (Lipenkov and Istomin, 2001). This is much greater than needed by terrestrial organisms. On Europa, surpassing dissolved O_2 levels comparable to saturation levels for the Earth's ocean occurs for delivery periods less than $\sim 7 \text{ Myr}$ and $\sim 68 \text{ Myr}$, for the low-end and high-end values of surface $\text{O}_2 + \text{H}_2\text{O}_2$, respectively. In other words, for the high-end value, if the delivery period is the same as the surface age, then Europa's ocean could well have enough dissolved oxygen to support any known marine macrofauna.

8.2 Reductants and Radiolysis of $\text{H}_2\text{O} + \text{CO}_2$

Given the highly oxidized nature of the european surface, is it possible to radiolytically produce reduced compounds that could affect ocean chemistry or be of use to a subsurface ecosystem? The evidence for CO_2 on the surface suggests that carbon is available, but what form is that carbon likely to take after years of radiolysis? It has been proposed that radiolytically produced formaldehyde could be a source of carbon for a subsurface ecosystem on Europa (Chyba, 2000; Chyba and Phillips, 2001). Methanol could also be a useful form of carbon and several workers have explored methanol in the context of astrophysical ices (Schutte et al., 1993; Bernstein et al., 1995; Moore et al., 1996). The radiolytic production of H_2CO , CH_3OH and CH_4 from pure $\text{H}_2\text{O} + \text{CO}_2$ mixtures, however, may be a limiting process for the availability of such reductants.

Recent experiments at astrophysical temperatures ($\sim 5\text{--}20 \text{ K}$) have shown that formaldehyde is at best a minor product during ion and UV irradiation of $\text{H}_2\text{O} + \text{CO}_2$ ices (Gerakines et al., 2000; Brucato et al., 1997; Moore and Khanna, 1991). The predominant carbon-bearing products are CO and carbonic acid, H_2CO_3 . Considering

Oxidation states for carbon and sulfur compounds relevant to Europa

| | | | | | | | | | | | | |
|-----------------|--------------------|-----------------|----------------|----|-----------------|--------------------------------|----|----|----|----|----|----|
| CH ₄ | CH ₃ OH | HCHO | | | CO | CO ₂ | | | | | | |
| | H ₂ S | HS ⁻ | S _n | | SO ₂ | H ₂ SO ₄ | | | | | | |
| -6 | -5 | -4 | -3 | -2 | -1 | 0 | +1 | +2 | +3 | +4 | +5 | +6 |

Figure 8.4: Oxidation states of carbon and sulfur compounds relevant to the radiolytic surface chemistry and subsurface aqueous chemistry of Europa.

the progression of oxidation states from methane to carbon dioxide, $\text{CH}_4 \rightarrow \text{CH}_3\text{OH} \rightarrow \text{CH}_2\text{O} \rightarrow \text{HCOO}^- \rightarrow \text{CO}_2$, carbonic acid falls on the far right-hand side with CO_2 and an oxidation state of +4 (See Table 8.4). This is hardly an improvement from the standpoint of chemical disequilibrium and it may have important consequences for the pH of the ocean chemistry. Here we examine the role of high-energy electrons in the radiolytic production of single-carbon species such as H_2CO_3 , H_2CO , CH_3OH , and CH_4 . The configuration of the experiment and vacuum chamber was described in Chapter 5, but in brief we have constructed a 10^{-9} torr vacuum chamber with a He-cryostat cold finger onto which we can deposit thin ice films. A 100 keV electron gun is then used to irradiate the sample while simultaneous acquisition of mid-IR (FTIR) and mass-spectra (RGA) allow monitoring and analysis of the resulting products. In the analysis presented here we examine radiolytic processing of water and carbon dioxide films at temperatures and pressures relevant to Europa. Figure 8.5 shows results from 10 keV electron irradiation of a $\text{H}_2\text{O}+\text{CO}_2$ (2:1) thin ice film. Water vapor and CO_2 gas were co-deposited at 50 K onto a gold mirror. The final thickness of the film was $\sim 1.77 \mu\text{m}$ thick, enough to absorb most of the energy from the 10 keV electrons (see Figure 2.5).

After deposition the film was slowly warmed to 90 K and subsequently irradiated with an electron beam of 100 nA – 3 μA . Spectra were collected at a resolution of 4 cm^{-1} , with each spectrum being the co-added average of 1024 spectra collected over a period of approximately nine minutes. Spectra are presented in units of absorbance,

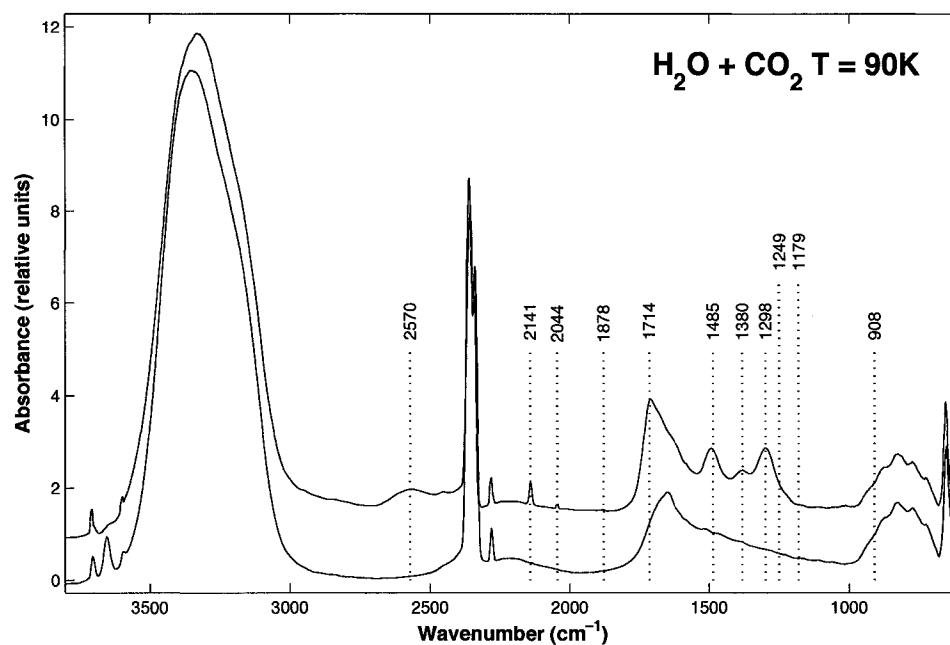


Figure 8.5: Spectra of a 1.77 μm film of [2:1] $\text{H}_2\text{O}:\text{CO}_2$ ice deposited at 50 K and irradiated at 90 K with 10 keV electrons. The bottom spectra shows the film before irradiation and the top spectra shows the film after irradiation. Spectral lines consistent with CO and H_2CO_3 - not H_2CO , CH_3OH , or CH_4 - are observed in the irradiated spectra (See text, Table 8.1).

where an averaged pre-depositional spectra of 3072 spectra has been used in the denominator for calculating absorbance ($Absorbance = -\log_{10}(I_{Irradiated}/I_{Predeposition})$), where I is the intensity of the spectra). When calculating integrated bands for products such as H_2CO_3 we use a pre-irradiation averaged spectra instead of the pre-depositional averaged spectra in the denominator of the absorbance.

The lower line in Figure 8.5 shows the ice film before irradiation and the upper spectra shows the same film after four hours of irradiation. The cumulative dose experienced by the film was $\sim 2 \times 10^{21}$ eV cm^{-2} . As can be seen, the major spectral features to emerge are then strong lines at 2570, 2141, 1714, 1485, 1380, and 1298. The CO_2 bands at 2340 and 2278 persist in the irradiated spectra. Aside from the 2141 band of CO, all of the other bands have been attributed to the formation of H_2CO_3 . Table 8.1 shows published band positions and absorptions for CO_2 , CO, H_2CO_3 , H_2CO , CH_3OH and CH_4 .

Consistent with both the UV and ion laboratory results for astrophysical ices, we find carbonic acid and carbon monoxide to be the primary products of H_2O+CO_2 electron radiolysis of ices at european temperature and pressure. Initially, as shown in Figure 8.6, H_2CO_3 and CO concentrations rise linearly and the CO_2 concentration decreases slightly. Equilibrium is reached at ~ 20 eV/16 amu ($\sim 10^{20}$ eV cm^{-2}), where production and destruction rates become equal and all four components are in steady state (CO_2 , H_2O , CO, and H_2CO_3). The initial H_2CO_3 production rate at 90 K under electron irradiation is $G = 0.020/100$ eV, compared to 0.028 and 0.030 obtained at 18 K for proton radiolysis and UV photolysis, respectively (Gerakines et al., 2000). The carbonic acid destruction cross-section for incident 10 keV electrons is $\sim 10^{-16}$ cm^2 . Using the three H_2CO_3 bands of 2626 cm^{-1} , 1508 cm^{-1} , and 1307 cm^{-1} , with corresponding band strengths of $1.6 \pm 0.08 \times 10^{-17}$, $6.5 \pm 0.6 \times 10^{-17}$, and $1.0 \pm 0.02 \times 10^{-17}$ (Gerakines et al., 2000), we find a total H_2CO_3 production of 3.24×10^{16} molecules per square centimeter. As a fraction of remaining CO_2 , this amounts to a molar ratio of 23.7%. By comparison, the total CO in the ice was 2.78×10^{16} molec cm^{-2} , leading to a CO/ CO_2 molar ratio of 20.4%.

The radiolytic destruction of CO_2 generated 6.22×10^{16} atoms of carbon available for synthesis into other compounds. Some of this carbon escaped into the vacuum

| Compound | Band position (cm ⁻¹) | A (cm molecule ⁻¹) | Reference | |
|--------------------------------------|------------------------------------|--------------------------------|---|--|
| CO ₂ | 2342 | 7.4 × 10 ⁻¹⁷ | Gerakines et al. (2000) Moore and Hudson, 1998 | |
| | 2280 | 7.25 × 10 ⁻¹⁷ | Gerakines et al. (2000) | |
| CO | 2143 | 1.1 × 10 ⁻¹⁷ | Gerakines et al. (2000) | |
| | 2850-2761, O-H str | 9.8 ± 0.4 × 10 ⁻¹⁷ | DelloRusso et al. (1993) Gerakines et al. (2000) Brucato et al., (1997) | |
| H ₂ CO ₃ (18K) | 2576-2626, O-H str | 1.6 ± 0.08 × 10 ⁻¹⁶ | DelloRusso et al. (1993) Gerakines et al. (2000) Brucato et al., (1997) | |
| | 1710-1736, C=O str | 1.1 ± 0.01 × 10 ⁻¹⁶ | DelloRusso et al. (1993) Moore et al. (1991) Brucato et al., (1997) | |
| | 1482-1508, C-OH asym str | 6.5 ± 0.6 × 10 ⁻¹⁷ | DelloRusso et al. (1993) Moore et al. (1991) Brucato et al., (1997) | |
| | 1294-1307, C-OH i.p. bend | 1.0 ± 0.02 × 10 ⁻¹⁶ | DelloRusso et al. (1993) Moore et al. (1991) Brucato et al., (1997) | |
| | 1038-1040, C-OH sym str | 1.4 ± 0.2 × 10 ⁻¹⁸ | DelloRusso et al. (1993) Moore et al. (1991) Brucato et al., (1997) | |
| | 908, C-OH o.p. bend | 5.6 ± 0.8 × 10 ⁻¹⁷ | DelloRusso et al. (1993) Gerakines et al. (2000) | |
| | 811-813, CO ₃ o.p. bend | - | DelloRusso et al. (1993) Brucato et al., (1997) | |
| | 690, CO ₃ i.p. bend | 1.3 ± 0.2 × 10 ⁻¹⁷ | DelloRusso et al. (1993) Gerakines et al. (2000) | |
| | H ₂ CO (20K) | 2886, 2895, C-H str | 2.8 × 10 ⁻¹⁸ | Schutte et al. (1993) Moore et al.* |
| | | 2824, 2827, C-H str | 3.7 × 10 ⁻¹⁸ | Schutte et al. (1993) Moore et al.* |
| 1716-1719 | | 9.6 × 10 ⁻¹⁸ | Schutte et al. (1993) Moore et al. (1991) | |
| 1498 | | 3.9 × 10 ⁻¹⁸ | Schutte et al. (1993) Moore et al. (1991) | |
| 1245 | | 1 × 10 ⁻¹⁸ | Schutte et al. (1993) Moore et al. (1991) | |
| 1176 | | 4.8 × 10 ⁻¹⁹ | Moore et al.* | |
| 1134 | | - | Moore et al. (1991) | |
| CH ₃ OH | 1021 | 1.5 × 10 ⁻¹⁷ | Moore et al. (1991) | |
| CH ₄ | 1302 | 7.2 × 10 ⁻¹⁷ | Moore and Hudson (1998) | |

Table 8.1: Spectral lines for several important single-carbon compounds relevant to Europa. *Indicates bands derived from reference spectra made available by the Cosmic Ice Laboratory at NASA GSFC, <http://www-691.gsfc.nasa.gov/cosmoc.ice.lab>.

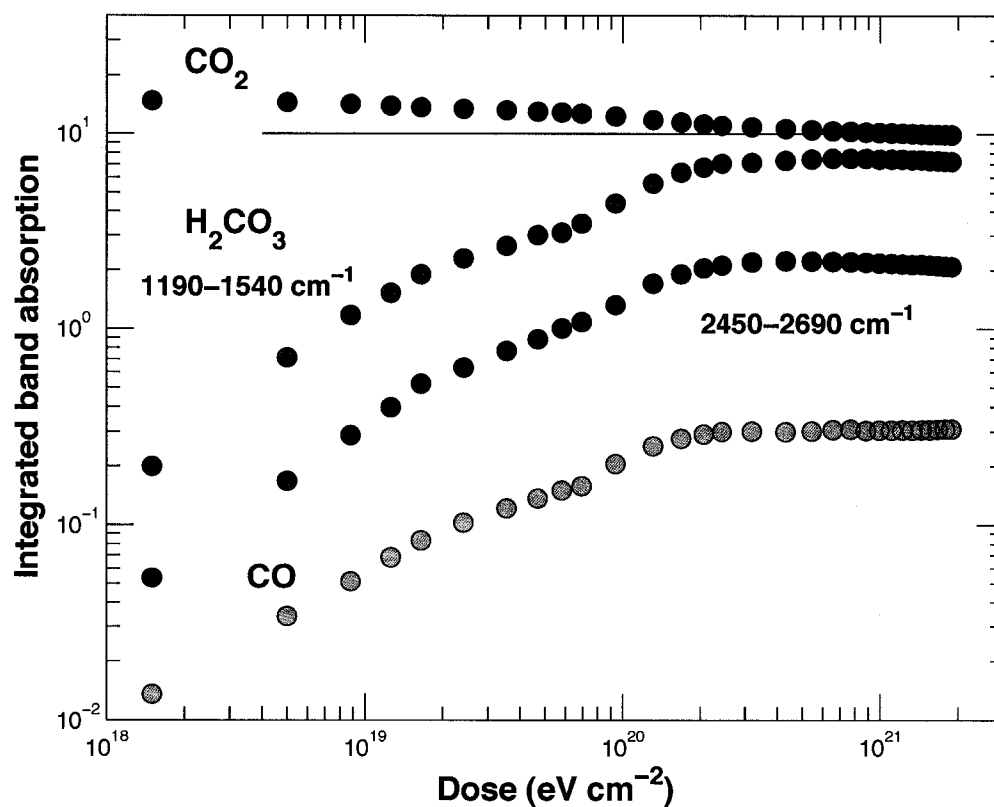


Figure 8.6: Concentrations of CO₂ and radiolytically produced compounds, CO and H₂CO₃, as a function of absorbed dose. Initial production rises linearly with a subsequent plateau as destruction balances production. At ~ 20 eV/16-amu all four components approach equilibrium.

chamber and was lost from the system. Based on our H_2CO_3 and CO production we can account for approximately 97% of the evolved carbon, with roughly equal partitioning into each compound. In an effort to account for the remaining 3%, we found no convincing signature of H_2CO , CH_3OH or CH_4 . In addition, no signature of carbon suboxide (C_3O_2) was found. Interestingly, we do see growth of features at 2044 cm^{-1} and 1878 cm^{-1} , consistent with the production of the CO_3 radical (Moore and Khanna, 1991; Jacox and Milligan, 1971). Lacking band strengths for these features we cannot quantify the carbon sequestered in this compound.

The combined accounting for carbon residing in CO_2 , CO, H_2CO_3 , and possible minor species like CO_3 , lead us to conclude that upper limits for H_2CO , CH_3OH , and CH_4 production are in the range of $\sim 1\%$ of the destroyed carbon or $\sim 0.5\%$ by number of the remaining CO_2 . On the surface of Europa this would be $\sim 4 \times 10^{-4}\%$ H_2CO by number relative to water.

Chyba and Phillips (2001) calculated that the upper 1.3 m of gardened regolith on Europa could contain 5×10^{18} molecules of H_2CO . For a CO_2 percent by number abundance of 0.08% this leads to a 0.16% abundance of H_2CO relative to CO_2 . Our laboratory results show that these numbers are within the bound of our upper limits. The conclusion of Chyba and Phillips (2001) that delivery of radiolytically produced H_2CO could support $\sim 3 \times 10^{23}$ microbial cells is valid to within a factor of three.

Based on our radiolysis results we conclude that the surface of Europa is not likely to be a large source of reductants for the subsurface ocean. Most of the carbon is in the form of the oxidants CO_2 , CO, and H_2CO_3 . An important distinction to make here, however, is that the redox state of the initial carbon compound is a critical factor in the resulting carbon chemistry. Laboratory work by the authors has shown polymerization of short chain alkanes and alkenes in ice and the production of alcohols, methane, and CO_2 (see Chapter 9). Other workers have similarly shown that production of refractory organic material in irradiated ices is possible (Bernstein et al., 1995; Moore and Hudson, 1998). While radiolysis of CO_2 may not lead to large quantities of reduced carbon compounds, exogenous organic material contained within micrometeorites and dust particles could potentially survive radiolysis and be delivered to the ocean in reduced form.

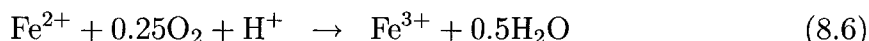
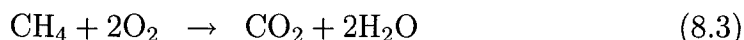
8.3 Abiotic sinks for surface oxidants

In Figures 8.3 and 8.7 we showed that radiolytically produced oxidants could be present in high concentrations in the ocean even if timescales for delivery were much greater than the surface age. Here we consider the role of abiotic sinks within the ocean as a mechanism for drawing down the concentration of oxidants.

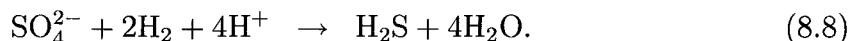
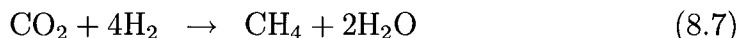
McCollom (1999) has examined the possibility of hydrothermally derived reductants on Europa as a mechanism for driving methanogenesis. In his reduced ocean hydrothermal fluid the reductants CH_4 , H_2 , H_2S , Fe^{2+} are present at 4.9, 12.0, 33.3, and 0.30 mm concentration, respectively. The terrestrial hydrothermal flux is $3(\pm 1.5) \times 10^{13}$ kg of seawater per year (Elderfield and Schultz, 1996), and McCollom (1999) considers the european flux to be $\sim 10^{-3}$ that of the Earth. This leads to delivery fluxes of 1.5×10^8 , 3.6×10^8 , 1.0×10^9 , and 9×10^7 moles per year for CH_4 , H_2 , H_2S , and Fe^{2+} , respectively.

As an added check on these estimates, we calculate a european hydrothermal flux by using the terrestrial oceanic heat flux of 3.2×10^{13} W (Stein and Stein, 1994) and the mid-ocean ridge heat flux of $2 \pm 1 \times 10^{12}$ W (Elderfield and Schultz, 1996), as scaling factors for Europa's hydrothermal fluid flux. For total european ocean heat fluxes ranging between 1.74×10^{11} – 5.1×10^{12} W (corresponding to 6.5–190 mW m^{-2}), we find a fluid flux range of 1.5×10^{11} – 4.8×10^{12} kg yr^{-1} . Using typical terrestrial hydrothermal fluid concentrations for H_2S , CH_4 , and H_2 (Elderfield and Schultz, 1996; Kelley et al., 2001) leads to $\sim 10^9$, $\sim 10^7$, and $\sim 10^8$ moles per year respectively. These are comparable to the values of McCollom (1999).

To build up oxidants in Europa's ocean the annual flux of radiolytically produced oxidants must compensate for the hydrothermally delivered reductants. The reductant-oxidant pairing could be accomplished with the following representative reactions, proceeding abiotically (McCollom and Shock, 1997):



The total O_2 needed to compensate these reactions, based on the reductant fluxes given above, is 2.5×10^9 moles per year. As McCollom (1999) has shown, the temperature and pressure dependence of the above reactions largely determines the reaction thermodynamics. Here we have assumed all reactions move to the right in order to maximize oxidant consumption. The oxidants CO_2 and SO_4^{2-} could also react with available reductants via,



The sinks for the sulfate anion and carbonate anion will include precipitation of anhydrite (CaSO_4) and carbonate (CaCO_3). Both compounds have enhanced solubility at lower temperatures, but we consider precipitation to be complete in order to consume as much of the surface oxidants as possible. Taking the McCollom (1999) hydrothermal flux of 1.5×10^9 moles per year of Ca^{2+} we find that much of the carbon could be consumed via precipitation, but the delivery of sulfate is large enough to accommodate anhydrite precipitation for the full range of delivery periods examined here. In Figure 8.7 we calculate the O_2 molarity of the ocean with the added condition of 2.5×10^9 moles per years of O_2 consumed by hydrothermally delivered reductants. As in Figure 8.3 we have limited our integration to only the past 1 Gyr on Europa. We have treated the H_2O_2 delivery as part of the total O_2 delivery since H_2O_2 decays to O_2 on geologically short timescales ($\tau_{1/2} \sim 10$ yrs). To compensate the reductants with O_2 and H_2O_2 the delivery timescale must be less than 10^7 Myr. For the lower limit of O_2 abundance, the delivery period must be less than 11 Myr.

In both cases, once the net flux of O_2 is positive, then the O_2 concentration rapidly surpasses the terrestrial O_2 minimum zone concentrations. The upper estimate for abundance surpasses O_2 minima zone concentrations when delivery periods are less than 105 Myr. For the lower limit this occurs at 10 Myr. Surpassing O_2 saturation occurs for delivery periods less than 6 Myr and 60 Myr for the lower and upper limits respectively. In other words, if the delivery period is the same as the surface age, then Europa's ocean could well be saturated with oxygen.

In all cases of accounting for sinks we find that the delivery of the sulfate anion will likely serve as the largest oxidant reservoir for aqueous chemistry in the European ocean. Though O_2 and CO_2 could be largely consumed by endogenous reductants, there is a minimum of $\sim 2 \times 10^9$ moles per year of sulfate delivered to the ocean. Achieving sulfate concentrations comparable to those of Earth's ocean (2.86×10^{-2} moles kg^{-1} , Kelley et al. (2001)) requires delivery periods of < 51 Myr. In dissolved form, the SO_4^{2-} and HSO_4^- will buffer the ocean with chemically useful oxidants and it will be sulfate chemistry that dominates the ocean.

8.4 Timescales for Delivery

While radiolytic processing of the upper few millimeters of the surface occurs on short geological timescales ($< 10^2 - 10^3$ yrs, Johnson et al. (2004)), considerable debate exists as to whether or not any of the surface oxidants do indeed reach the putative subsurface ocean. Without such surface-to-subsurface cycling the available free energy will be largely limited to geologically leached or out-gassed oxidants such as CO_2 and SO_4^{2-} (Zolotov and Shock, 2003, 2004). In previous sections we have left the delivery period as a free variable. Here we examine several different factors related to the surface age and resurfacing processes with the aim of providing some constraints on the delivery period of surface material to the sub-surface ocean. We also address specific concerns (Zolotov and Shock, 2004) regarding escape of oxidants to the atmosphere during warm resurfacing events.

The geology of Europa is limited to surface observations and thus remains poorly constrained. There is, at present, no evidence for contemporary resurfacing (Phillips

| Process | Relevant timescale | Reference |
|-------------------------------------|---|-------------------------------|
| Surface age (craters) | 30-70 Myr | Zahnle et al. (2003) |
| Nonsynchronous rotation, t_r | $0.01 < t_r < 0.25$ Myr | Hoppa et al. (1999, 2001) |
| Plume rise | 0.001-0.03 Myr | Barr and Pappalardo (2003) |
| Sodium depletion (1 cm layer)* | 0.3-3.0 Myr | Leblanc et al. (2002) |
| Sputtering erosion | $0.0147 \text{ m Myr}^{-1}$ | Tiscareno and Geissler (2003) |
| Gardening | $\sim 1.2 \text{ m in } 10 \text{ Myr}$ | Cooper et al. (2001) |
| Radiolytic equilibrium (upper 1 mm) | $< 10^2 - 10^3 \text{ yrs}$ | Johnson et al. (2004) |

Table 8.2: Timescales for various processes on Europa. *Sodium escape and depletion from a 1% by number Na ice layer (1% corresponds to ocean water).

et al., 2000). Nevertheless, only $\sim 15\%$ of Europa has been imaged at < 1 km per pixel (Schenk et al., 2004). Without any contemporary activity to which relative ages can be tethered (*e.g.* active plumes or new craters), the only concrete statement that can be made about resurfacing of the ice shell is that ~ 30 -70 Ma much of the surface was renewed (Zahnle et al., 2003).

Two broad classes of ice shell models are put forth in the Europa literature: thin-shell models (~ 5 km thick or less), and thick-shell models (~ 10 -30 km thickness). Recent work based on Galileo magnetometer and gravity data favors thin shells (Hand and Chyba, 2007), but we consider both possibilities here. We examine each model and assess the implications for communication between the surface and the underlying ocean. Our aim is to elucidate processes that may prevent or enhance the delivery of surface material to the sub-surface ocean. In so doing, we assess plausible time scales for various processes. Table 8.2 presents some of the known or modeled timescales for various processes we take to be relevant to resurfacing on Europa.

8.4.1 Thin Shells

With the thin shell model, the dynamics between the surface and subsurface are simplified by the fact that only one layer lies between the surface and the ocean-ice interface. Tectonic fracturing, lineament building and cryovolcanic reworking allow for direct communication between the surface ice and the ocean. Stresses are sufficient for cracks initiated at the base of the ice shell to penetrate to the surface (Crawford

and Stevenson, 1988). Products of the radiolytic chemistry are directly introduced into the ocean. Several geological mechanisms are possible, here we consider two: 1) tectonic events in the ice shell cause resurfacing and allow for delivery of surface material (including possible melt-through events as a subset), and 2) cryovolcanism resurfaces the ice shell from the top down.

In the first case, the surface age (30-70 Myr) is roughly equivalent to the delivery period. As the surface is renewed through extensional processes, surface materials are delivered to the sub-surface through subduction processes. Regions of subduction are still largely unaccounted for on Europa (Prockter and Pappalardo, 2000), but we can at least constrain the delivery period associated with this mechanism were it to be important for resurfacing. Included in this are models that consider direct delivery of material via melt-through events (Greenberg et al., 1999; O'Brien et al., 2002; Thomson and Delaney, 2001). The delivery period in these latter models is the observed surface age of the chaos terrain, which at present is considered comparable to the bulk surface age.

For the case of cryovolcanism, isostatic compensation drives delivery. One millimeter of unit density ice deposited on the surface causes roughly one millimeter of unit density ice to melt from the bottom. This is analogous to snowfall on the Antarctic ice sheet and delivery of melting basal ice to subglacial lakes. The delivery period is regulated by surface deposition, which in turn is directly related to the observed surface age. The period for delivery, however, can be dramatically different from the surface age. For instance, the surface age of the Antarctic ice sheet is essentially zero (new snow and winds cover the surface on the timescale of $\sim 1-10$ years), and yet the bottom of the ice sheet contains material ~ 0.5 Myrs old (Petit et al., 1999). The surface age and the delivery period are off by $\sim 5-6$ orders of magnitude.

On Europa, isostasy would also regulate delivery if surface deposition, *e.g.* cryovolcanism, were the primary resurfacing mechanism. Crater and lineament topography on Europa is on the order of several hundred meters (Schenk, 2002), thus 1 km of global cryovolcanic deposition could serve to erase old features. Lacking direct evidence of contemporary cryovolcanism on Europa, we use the recent *Cassini* observations of the South Polar region of Enceladus (Spencer et al., 2006a) as an upper

limit for what could occur on an active Europa. The south-pole geyser on Enceladus allows $150\text{--}350 \text{ kg s}^{-1}$ of water to escape (Hansen et al., 2006). Kargel (2006) estimates that the actual amount of water ejected could be $\sim 840 \text{ kg s}^{-1}$. The new terrain on Enceladus is restricted to the southern hemisphere, or about a quarter of the moons surface area ($2 \times 10^{11} \text{ m}^2$). We calculate a mass source rate to surface area renewed of $\sim 2.5 \times 10^{-9} \text{ kg m}^{-2} \text{ s}^{-1}$ (here we have taken 500 kg s^{-1} of redeposition). This leads to $80 \mu\text{m yr}^{-1}$ of material on the surface, or 1 km of material deposited every ~ 12.7 Myr. (This is likely a lower limit for deposition as other fractures in the region of the Enceladus tiger stripes may have contributed ejecta to the resurfacing process.) If similar cryovolcanic processes were to take place on Europa during periods of active resurfacing, then through compensation, material deposited on the surface of a 5 km thick shell would require ~ 65 Myr to reach the ice-water interface. An 8 km shell would require ~ 100 Myr for delivery. In all cases, as shown in Figure 8.3, the resulting delivery of O_2 is above that needed to maintain an oceanic O_2 molarity comparable to terrestrial O_2 minima zones. For both the tectonic and cryovolcanic models of a thin-ice shell we find that delivery timescales are short enough to allow for significant oxidant delivery to Europa's ocean.

8.4.2 Thick Shells

Thick shell models introduce a host of complications when trying to relate the observed surface age to the delivery period. It can be argued that the observed surface age of Europa represents the end of a period of increased tidal energy and that we may now be in a period of relative quiescence on Europa, with an ice shell that is continuing to thicken and with little to no new resurfacing for hundreds of millions of years, if not billions of years, to come (Hussmann and Spohn, 2004; Hussmann et al., 2002). In the evolving orbital eccentricity models of Hussmann and Spohn (2004) the thermal history (and future) of Europa is highly dependent on the mechanisms and regions chosen for heat dissipation on Io, Europa, and Ganymede (*e.g.* conduction vs. convection in the mantle and/or ice shell), so predictions are uncertain.

If a thick shell exists, a strong argument can be made that a stagnant ice lid of a

few kilometers thickness overlies a convecting ice shell of tens of kilometers thickness (Pappalardo and Barr, 2004; Barr and Pappalardo, 2003; Barr et al., 2004). In this case, the stagnant lid would not directly communicate with the putative subsurface ocean. The radiolytically-produced oxidants contained in the lid would have to go through a series of coupled geological process before reaching the ocean.

In this model, the observed young surface age of the lid must be explained by resurfacing processes between the lid and the ductile convecting shell. Two arguments can then be made about cycling of the surface material into the ocean, 1) most of the material in the lid stays in the lid, and 2) material in the lid mixes with the convecting shell. If the former case is true, then oxidants produced on the surface will rarely reach the ocean. In the later case, oxidants will eventually reach the ocean via convection processes (Barr and Pappalardo, 2003). The delivery period is then a function of both the observed surface age and cycling processes within the ductile shell.

While a non-mixing stagnant lid cannot be ruled out, several factors make it physically implausible. First and foremost are the mechanical difficulties of creating a surface young in appearance but old in molecular residence time. In other words, the cratering clock needs to be reset without actually recycling material.

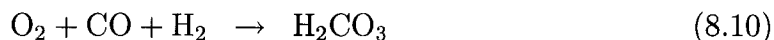
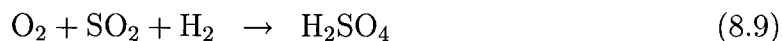
Heating from below can be invoked as a means for relaxing the surface topography and eventually erasing craters (viscoelastic relaxation), but this mechanism would also erase the lineament topography along with the craters. Obviously the latter has not occurred, Europa's surface is saturated with superimposed lineaments.

Erasing craters without cycling surface material could be accomplished by the repeated formation of new lineae. Given enough time and enough fractures, the crater structure will be indistinguishable from other topographic structures. Such activity is at least partially evident in the Tyre impact structure (Moore et al., 2001). This would seem a nice solution were it not for the fact that regions of extensional tectonic activity in the ice shell imply regions of compression or subduction. As discussed above, subduction could be an effective mechanism for delivery, but such regions remain unidentified on Europa.

Strike-slip faults do not necessitate such compression or subduction. Such faults

could serve to partially erase the cratering record. However, some models for double ridge formation via strike-slip faulting argue for frictional heating and thermal upwarping as a means for raising the ridges (Nimmo and Gaidos, 2002). Such heating causes sublimation along the ridges. Ridge sublimation is essentially muted cryovolcanism. On the low end, ridge temperatures of ~ 130 K lead to sublimation and subsequent deposition of $1 \mu\text{m yr}^{-1}$ (Fagents et al., 2000). Higher temperatures (*e.g.* 150 K) raise this rate by nearly three orders of magnitude. Delivery timescales from the surface to the brittle-ductile layer interface for the buried material are then comparable to those described for cryovolcanism, *i.e.* tens of millions of years.

We note that the process of ridge sublimation and subsequent redeposition addresses a concern by Zolotov and Shock (2004) over the fate of radiolytically produced surface oxidants. These workers argued that delivery of oxidants to the ocean would be inhibited by the degassing of ice during warm resurfacing events. We argue that while degassing may occur, most of the oxidants do not escape (Fagents et al., 2000; Carlson et al., 2005). Instead, they are redeposited and trapped in the surface ice. The presence of molecular oxygen in the solid phase on the surface of Europa is itself a puzzle (Baragiola and Bahr, 1998; Johnson, 1999). Recently Hand et al. (2006) have argued that mixed-clathrates of $\text{O}_2\text{-CO}_2\text{-SO}_2$ could solve the trapping problem. While O_2 may be released to the atmosphere, the higher temperatures will also promote the reaction of O_2 to sulfate and carbonate,



These compounds would collect in the ice while H_2O sublimates. Such surface chemistry during warming could in part explain the observations of hydrated sulfate material in the hummocky low-lying matrix terrain of chaos features but not on the surface of intact ‘raft blocks. Carlson et al. (2005) have proposed a similar mechanism to explain the formation of concentrated sulfate hydrate lag deposits on the flanks of double-ridges. While molecular O_2 may evolve out of the ice during warming, some of the O_2 will be sequestered into other oxidants, and O_2 away from the region of

heating may be buried during redeposition of the sublimed material.

Along with the mechanical difficulties, isolation of the lid material is not well supported by the observed surface chemistry. Europa simultaneously experiences a net deposition of sulfur atoms to the surface and a net loss of sodium atoms from the surface (Johnson, 2000; Cooper et al., 2001). The presence of a sodium cloud around Europa was first reported by Brown and Hill (1996) and subsequent observations have helped constrain the net loss of sodium to $\sim 4 - 9 \times 10^6$ atoms $\text{cm}^{-2} \text{s}^{-1}$ (Leblanc et al., 2002). This is significantly larger than the Iogenic flux of $2 - 8 \times 10^5$ atoms $\text{cm}^{-2} \text{s}^{-1}$ (Leblanc et al., 2002). As noted by Leblanc et al. (2002), if the surface ice contained 1% by number sodium, a one-centimeter ice layer would be depleted in less than 1 Myr and a 10 m layer would be depleted in 1 Gyr. Mixing of the surface material with a potentially salt-rich subsurface is an obvious way of providing such a chemical source.

We find it hard to reconcile a young surface age with surface material that does not experience at least some level of subsurface cycling. Material from the surface will eventually be transported to the stagnant lid/ductile shell interface, at which point delivery to the ocean is dependent on convective processes within the ductile shell. Barr and Pappalardo (2003) have estimated vertical velocities for plumes within such a shell to be $\sim 0.1-1$ m yr^{-1} , giving rise/fall times of ~ 1000 to 30,000 years. In other words, if surface material can be transported to the interface between the stagnant lid and ductile shell, then the time for transport to the putative ocean is comparatively short, provided plumes are active in that region of the shell. Transport times through the lid will be comparable to those outlined for the thin shell model, after which transport through the ductile layer will be relatively short.

For both thin and thick shell models, delivery periods are found to lie in the range of 10-100 Myr. Mechanisms may exist that prevent the surface material from reaching the subsurface ocean, but they are hard to justify given the observed surface age. Our results for oxidant delivery indicate that delivery periods of 10-100 Myr result in an oxidant-rich ocean.

8.5 Conclusion

We have shown that even with hydrothermal sinks and long delivery periods, the ocean on Europa is likely to be oxidized. At a minimum, the abundance of sulfate supplied from the surface will likely lead to sulfate buffers in the form of mineral precipitation (*e.g.* anhydrite). Zolotov and Shock (2004) have argued that abiotic reactions would consume radiolytic oxidants, leaving little geochemical energy available for life. We find that for delivery periods of less than ~ 100 Myr the flux of O_2 and H_2O_2 will more than compensate for hydrothermal reductants, given the level of hydrothermal activity predicted by McCollom (1999) and our own scaling of the terrestrial flux to the european system. We also argue that reduction of sulfate - a key metabolic pathway for terrestrial deep ocean ecosystems and one explored by Zolotov and Shock (2004) - would be an obvious niche for European biota and it is one not likely to be limited by the availability of oxidants. The limiting factor for chemical energy on Europa is not oxidants, but rather reductants.

Geology on Europa, however, could impede the delivery of such compounds. But we have shown that even for the most extended of delivery scenarios, oxidant delivery may be sufficient for supporting complex organisms comparable to those found in the oxygen minima zones of the Earth's ocean. In addition, we find that for both thin and thick-shell models it is geologically implausible to isolate this material from the ocean if tectonism and/or cryovolcanism are present on Europa. Nevertheless, one possible interpretation of the observed surface age is that 30-70 Ma Europa experienced resurfacing and since that time Europa has been cooling and the thickness of the ice shell increasing. This may have been the last time surface oxidants were transferred to the sub-surface and Zolotov and Shock (2004) argue that there is no effective mechanism to deliver oxidants to the ocean in the present epoch. This could be the case, but if Europa was active in the past then delivery in the past could serve to maintain chemical disequilibrium through to the present.

Since it appears that the bulk surface age is 30-70 Myr (Zahnle et al., 2003) an interesting question to ask is: how long could O_2 in the ocean persist at biologically useful levels if the last delivery occurred 30-70 Ma and no new material has since

reached the ocean? With 2.5×10^9 moles per year of O_2 consumed by reductants for 30-70 Myr, we find that O_2 levels in Europa's ocean would need to have been $1.1 \times 10^{-4} - 1.4 \times 10^{-4}$ moles per liter in order to achieve contemporary concentrations of 8×10^{-5} moles per liter (comparable to terrestrial O_2 minimum zones and capable of supporting macrofauna). Maintaining an ocean with $1.1 \times 10^{-4} - 1.4 \times 10^{-4}$ moles per liter would have required delivery periods of < 90 Myr. If, however, the delivery period is 30-70 Myr then contemporary O_2 concentrations are between $\sim 10^{-3}$ and $\sim 10^{-4}$ moles per liter.

Nearly all of the Hussmann and Spohn (2004) models indicate that the past ~ 4.5 Gyr of coupled thermal-orbital evolution on Europa have involved substantially more energy than the present epoch. A greater heat flux in the past would have meant a thinner ice shell and potentially shorter delivery periods for surface oxidants.

We have shown that few, if any, reductants are produced through radiolysis of CO_2 with water. If CO_2 is the primary initial form of carbon on Europa, then radiolysis will serve to partition the carbon into reservoirs of CO and H_2CO_3 with an approximate ratio of [5:1:1] for the three species respectively.

Given our calculated abundances for oxidant delivery and our experimental results showing little to no reductant production via CO_2 radiolysis, we conclude that chemical energy derived from redox pairs could be limited by the geological activity of the ocean floor. The availability of reductants is a function of seawater cycling with the mantle and this in turn is a function of tidal dissipation in the mantle. Therefore the partitioning of tidal energy in the ice layer and mantle through time is a critical parameter for discerning the availability of both reductants and oxidants on Europa. Empirical constraints on tidal dissipation in the mantle and of seawater cycling through the oceanic crust could greatly enhance our understanding of the reductants and oxidants available for a putative european biosphere. Along with surface spectroscopy for compositional information, gravity data and altimetry data on a future mission could help resolve these outstanding questions.

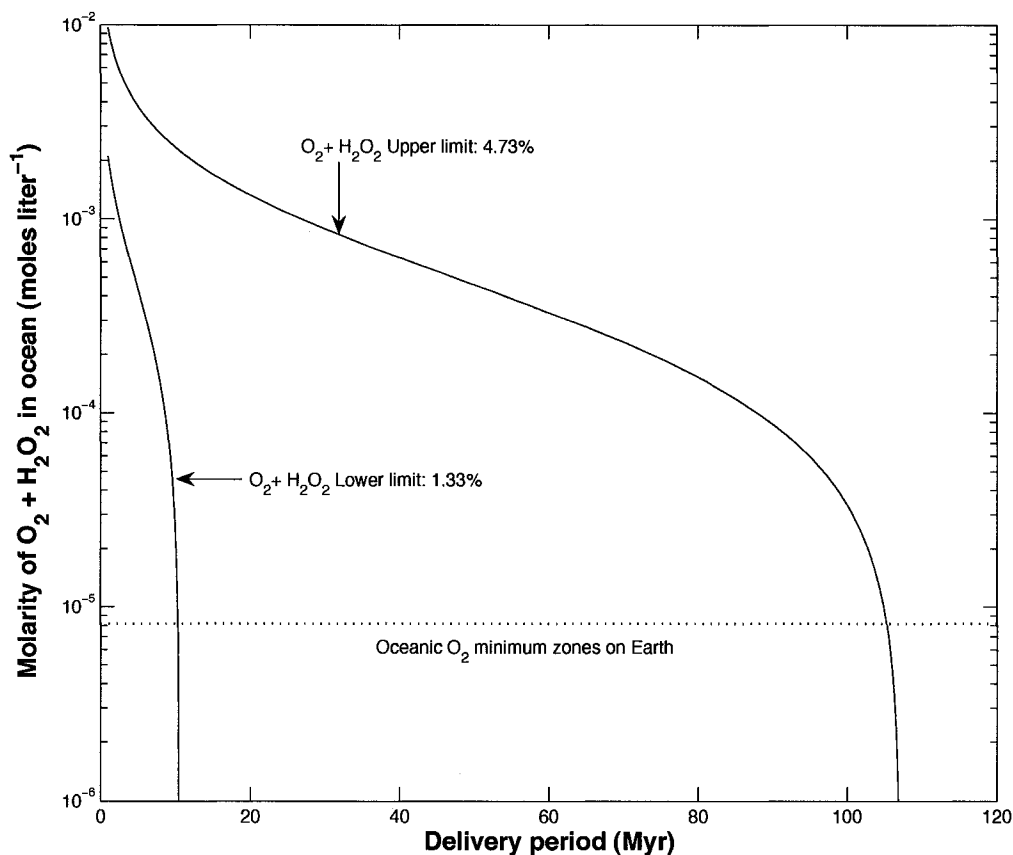


Figure 8.7: Oxygen molarity (with H_2O_2 added) of a 100 km global ocean in which 2.5×10^9 moles per year of O_2 are consumed by the hydrothermally delivered reductants CH_4 , H_2 , and H_2S . Here we show oceanic concentrations that would result from low (1.33% by number abundance relative to H_2O) and high (4.73% by number abundance relative to H_2O) surface concentrations of $O_2 + H_2O_2$. For the high-end, delivery periods as long as 105 Myr will still result in O_2 concentrations that surpass those found in terrestrial O_2 minima zones. For the low-end, the delivery period needs to be 10 Myr or less in order to reach this level. Even with sinks added the oxygen concentration of Europa's ocean can exceed levels comparable to that of the Earth's ocean surface waters ($\sim 250 \mu M$ (Millero, 2005)). If the $O_2 + H_2O_2$ abundance in the surface ice is 4.73% by number relative to H_2O , then ocean concentrations of $250 \mu M$ are exceeded for delivery periods less than ~ 68 Myr. For the lower surface abundance of 1.33% by number relative to H_2O , delivery periods of ~ 7 Myr or less are required to exceed $250 \mu M O_2$.

Chapter 9

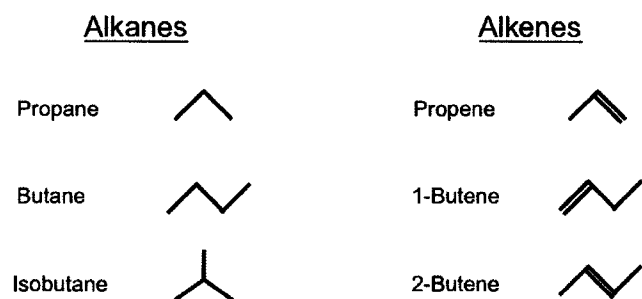
Radiolysis of H₂O + Hydrocarbons

The availability and redox state of carbon on Europa may play a critical role in the habitability of the subsurface ocean. Previously we have examined the abundance of CO₂ and the radiolytic products from CO₂-rich ices. Those results indicated that while carbon may be present in considerable abundance, it is likely in the oxidized forms of CO₂, CO, and H₂CO₃. The only form of carbon observed on Europa is CO₂ (Smythe et al., 1998). Nevertheless, exogenous organics should be delivered to the european surface at a rate of $\sim 40 \text{ g s}^{-1}$ globally (Pierazzo and Chyba, 2002; Johnson et al., 2004). Organics, or at least the C-H bonds at $3.44 \mu\text{m}$, have been detected in the infrared on Callisto, Ganymede, and Enceladus (McCord et al., 1997; Brown et al., 2006). Results from the *Cassini* ion and neutral mass spectrometer (INMS) flyby through the southern hemisphere plumes on Enceladus also indicate organics, specifically methane and trace amounts of propane and acetylene (Waite et al., 2006).

Considerable work has been done on hydrocarbons, methanol, and ammonia in ice (*e.g.* Khare et al. (1989); Moore and Hudson (1998); Bernstein et al. (1995)), but much of that work focused on cometary/astrophysical temperatures ($< 20 \text{ K}$) and UV or ion irradiation. Our work focuses on high energy ($\sim \text{keV}$) electron irradiation of ices in the temperature range appropriate for Europa and for much of Enceladus. Here we report on results from high-energy electron irradiation of thin ice films at $\sim 10^{-8}$ torr and temperatures ranging from 70-100K. Methane and ethane are unstable in solid form on the surface of Europa and for this reason our study of hydrocarbon radiolysis

begins with propane (C₃H₈) and then moves to more complex compounds. Mixtures include water with C₃H₈, C₃H₆, C₄H₁₀ (butane and isobutane), and C₄H₈, (1-butene and cis/trans-2-butene). Figure 9.1 shows the various compounds used for this study and Figure 9.2 shows several reference spectra used for analysis of the irradiation products.

Irradiated Carbon Compounds



Temperature: 80 K, 100 K; Pressure: 10⁻⁸-10⁻⁹ Torr

Figure 9.1: Alkanes and alkenes examined in this work.

In all cases the H₂O+alkane or alkene ice mixtures underwent the following procedure: 1) irradiation, 2) a post-irradiation ‘sitting’ period, during which we looked for changes that may have occurred at the irradiation temperature, 3) warming of the film to 300 K at 1 K per minute, 4) examination of any residue left on the target mirror, and 5) removal of the mirror for further examination of the residue. Mid-infrared spectra and mass spectra were collected throughout. Residues were examined with FTIR and matrix-assisted laser desorption/ionization (MALDI), though no actual matrix was used because desorption of the residue was possible directly off the target mirror.

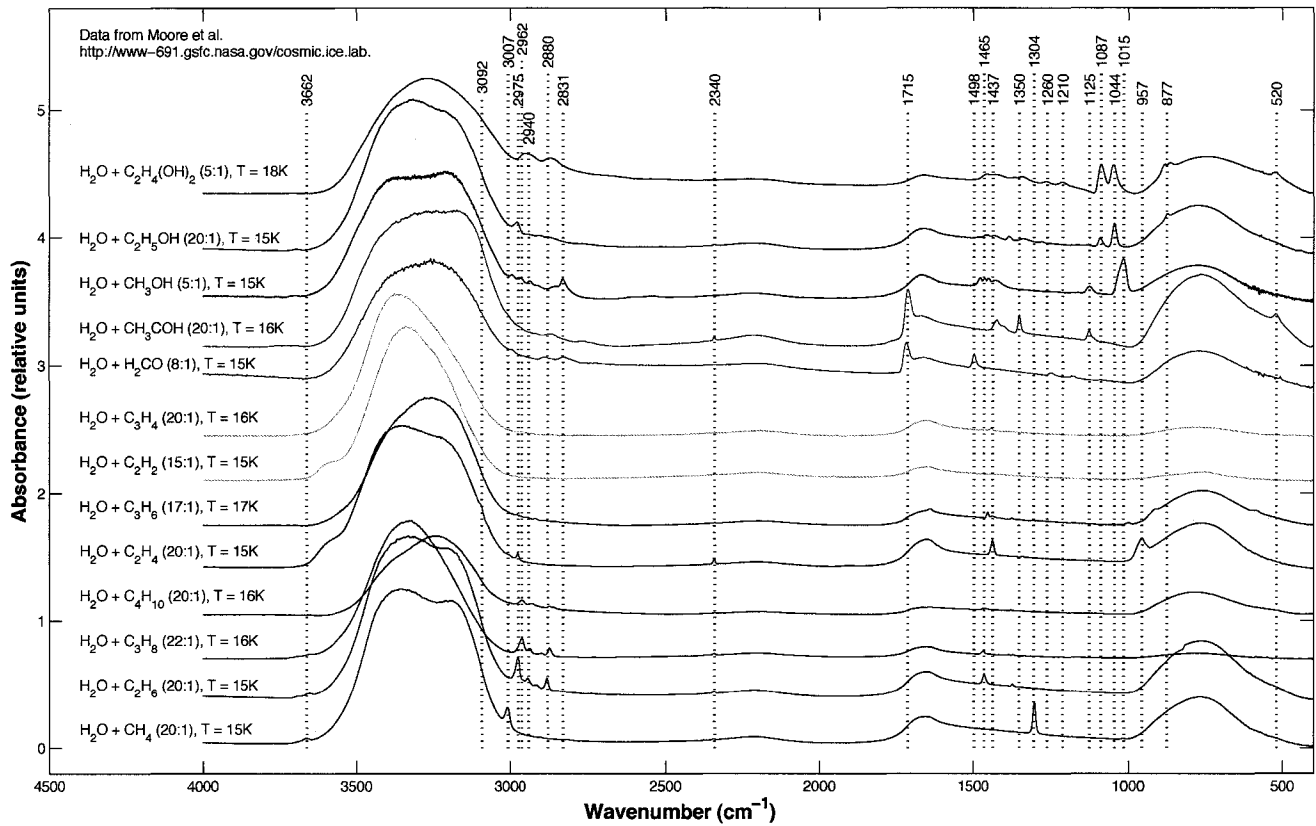


Figure 9.2: Reference spectra for a variety of carbon compounds relevant to this work. The ice mixture, ratio, and temperature are shown to the left of each spectra. The lower spectra in black are alkanes, blue spectra are alkenes, green spectra are alkynes, red spectra are aldehydes, and the upper black spectra are alcohols. Data are from the Cosmic Ices lab of Goddard Space Flight Center, Moore et al., <http://www-691.gsfc.nasa.gov/cosmic.ice.lab>.

Two primary questions were explored. First, what is the steady-state chemical form of the irradiated carbon? Second, what is the fate of the carbon-carbon bonds in our irradiated alkanes and alkenes? We find that while some of the carbon is lost to CO₂ formation, much of the carbon is sequestered into highly refractory, long-chain aliphatic compounds that remain as a thin residue even after the ice film has been raised to standard temperature and pressure (T = 25 °C, 1 atm (760 torr)).

The double bonds of the alkenes in our initial mixtures were rapidly destroyed or converted to single carbon bonds, covalent bonds with hydrogen, bonds with -OH (hydroxyl), bonds with oxygen (C-O), or double bonds with oxygen (carbonyl). Spectra resulting from irradiation of alkane and alkene ices are largely indistinguishable; the initial differences in film composition are destroyed and the resulting mixture includes long-chain, branched aliphatics, aldehydes, ketones, esters, and alcohols. MALDI analysis of the residues indicates some differences between the polymerization patterns of the alkane and alkene films, but further work is necessary to establish the repeatability of these results.

9.1 In-situ analysis of radiolytic evolution

9.1.1 Propane vs. Propene

In Figure 9.3 we show the evolution of a H₂O+C₃H₈ [3:1] mixture irradiated at 80 K with 10 keV electrons at 200 nA. The bottom spectrum shows the ice film after sitting for ~5 hours with no irradiation. The upper three lines show representative spectra after 20 minutes of irradiation, 5 hours of irradiation, and 7 hours of irradiation (moving upward).

The formation of CO₂ and CH₄ was monitored by the rise of the 2340 cm⁻¹ and 1302 cm⁻¹ bands respectively. While the C-H related peaks in the 2800-3000 cm⁻¹ and 1350-1550 cm⁻¹ range decreased as a function of dose, the most striking result of the irradiated propane was the stability of the C-H and C-C bonds. Aside from the loss of carbon to CO₂ and CH₄, the post-irradiation spectra were very similar to the pre-irradiation spectra. The strong peak in the pre-irradiation spectrum at

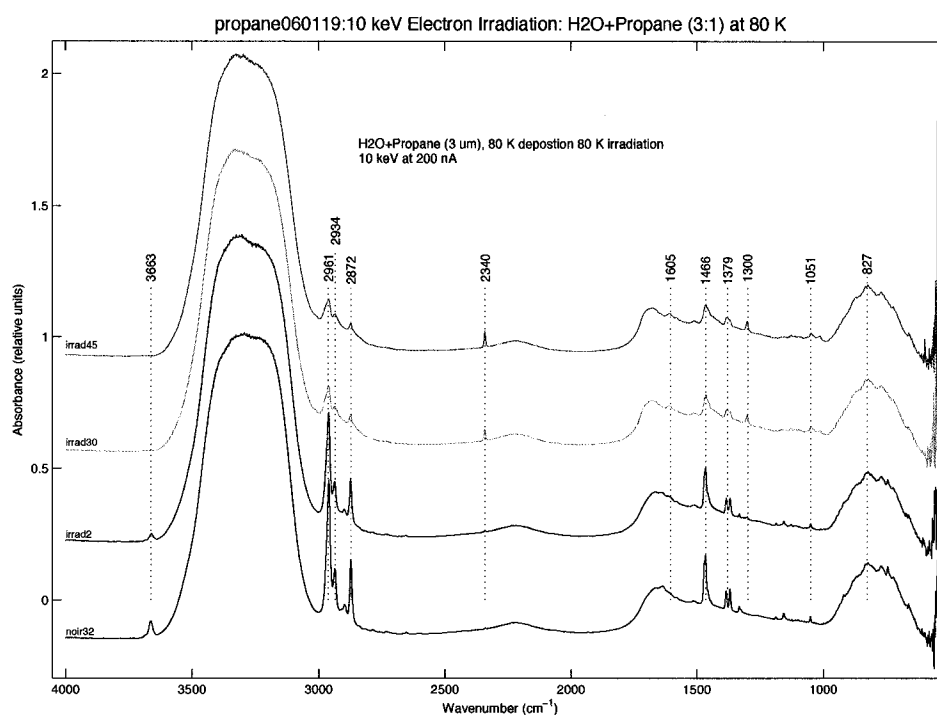


Figure 9.3: Mid-infrared spectra of a propane+water ice mixture (80 K) during irradiation with 10 keV electrons at 200. The bottom spectrum is prior to the onset of irradiation and each sequentially higher spectrum is from a point later in time during irradiation. The top spectrum is after approximately 7 hours of irradiation.

$\sim 2965\text{ cm}^{-1}$ and $\sim 2872\text{ cm}^{-1}$ correspond to the -CH₃ asymmetric and symmetric stretches, respectively. The decrease in these peaks, coupled with the persistence of the -CH₂- asymmetric stretch at $\sim 2934\text{ cm}^{-1}$ and the -CH₂- scissoring at $\sim 1466\text{ cm}^{-1}$, indicate that the short-chain hydrocarbons were being polymerized. This conclusion is supported by the observation of refractory residues left on the gold mirror substrate after warming and sublimation of the H₂O ice, discussed later in this chapter. Also observed, though more subtle and obscured by the broad water band at $\sim 1700\text{ cm}^{-1}$, was the emergence of the carbonyl bond at 1710 cm^{-1} .

In Figure 9.4 we show the change in band area for several of the above-mentioned chemical species and bonds as a function of integrated dose. Each data point represents the integrated area of a given band for an individual spectrum collected during the irradiation process. Baseline fits were either linear or quadratic depending on the position of the band relative to the curvature of the broad water bands.

The two primary species observed evolving from the spectra were carbon dioxide and methane. The rise of methane was rapid but then leveled off with saturation, reached at $\sim 2 \times 10^{20}\text{ eV cm}^{-2}$. Carbon dioxide, on the other hand, continued to rise. After more than seven hours of irradiation no steady-state saturation level for CO₂ was observed.

Two band regions related to C-H and C-C bonding were integrated as clusters. The close proximity and overlapping nature of the bands makes separating individual bands difficult and, for the purpose of understanding dominant processes, unnecessary. The data for the first region, from $2836\text{--}2996\text{ cm}^{-1}$ was integrated using a quadratic fit to the background water band and is shown in red circles. The data for the second region, integrated from $1356\text{--}1510\text{ cm}^{-1}$ with a linear fit, is shown with blue triangles. While both regions decreased in band area, the more rapid drop seen in the first region can, at least in part, be attributed to the reduction in the -CH₃ bands that dominate that region. The band at 2961 cm^{-1} is the -CH₃ asymmetric stretch while that at 2872 cm^{-1} is the symmetric stretch. Between these two bands is the asymmetric stretch of -CH₂- (2934 cm^{-1}). The bands within the second region are largely due to the -CH₂- scissoring at 1466 cm^{-1} and the C(CH₃) symmetric bending at 1379 cm^{-1} . Loss of -CH₃ relative to -CH₂-, as evidenced by the relative decrease in bands

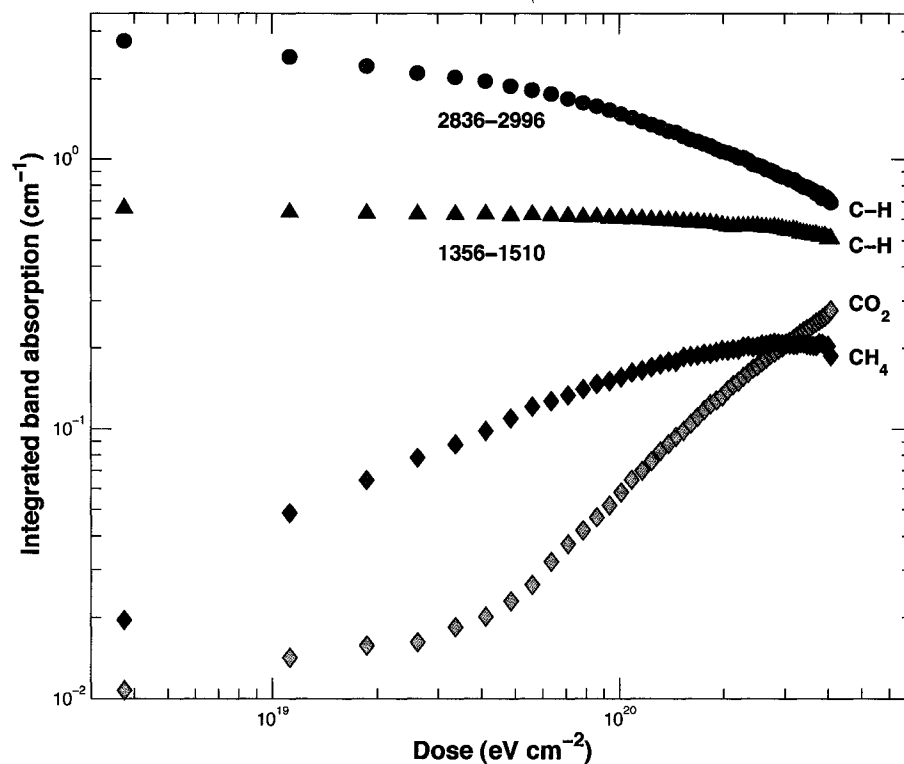


Figure 9.4: Integrated bands vs. Dose for an initial ice mixture of H₂O+C₃H₈. Shown here are the changes in band area for C-H regions, one of which consists principally of the CH₃ stretching modes (2836-2996 cm⁻¹), and one of which is dominated by -CH₂- modes (1356-1510 cm⁻¹). Also shown are the growth in the CO₂ and CH₄ bands. The loss of the CH₃ band while the -CH₂- band remains relatively constant is consistent with the polymerization of the propane. Production of CH₄ consumed most of the initially available carbon and tracked the CH₃ band closely. Methane was a likely product of the cleaved methyl functional group joined with a free H⁺. The production of CO₂ was initially slow but increased rapidly after $\sim 5 \times 10^{19}$ eV cm⁻². This is consistent with the production of a terminal carboxyl precursor followed by cleavage and loss of H⁺ to form CO₂. CO₂ continued to rise throughout the experiment and the area of the -CH₂- region began to decrease steadily. Radiolysis first cleaves the terminal CH₃, producing CH₄. As polymerization proceeded and CH₃ carbons became scarce, the radiolytic energy resulted in destruction of -CH₂- and terminal -COOH.

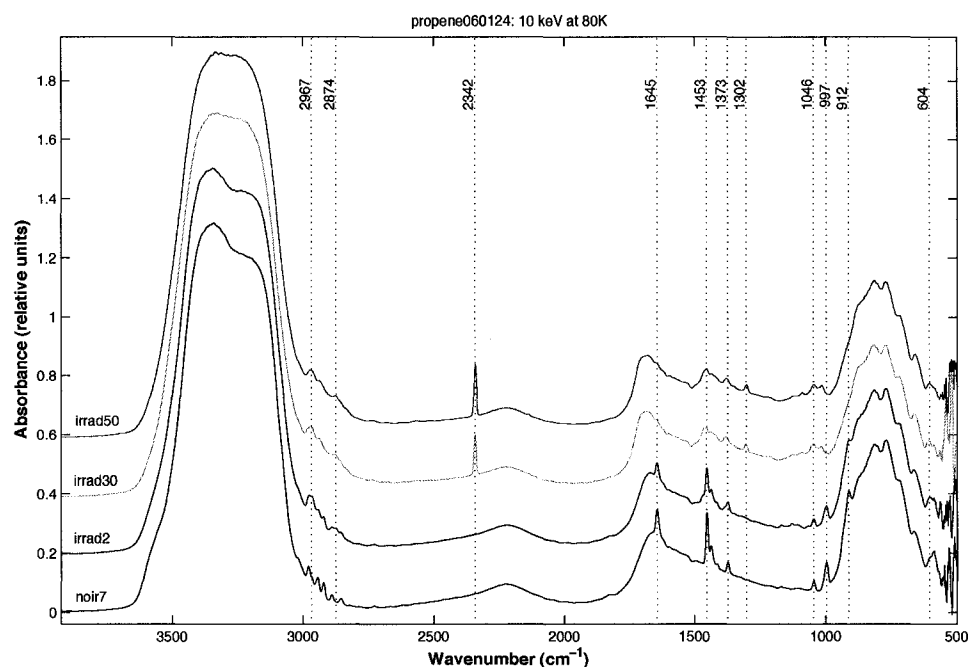


Figure 9.5: Irradiation sequence of a H₂O+propene [3:1] ice mixture. The lowermost spectrum shows the ice film pre-irradiation. Each subsequent higher spectrum is from a point in time later in during the irradiation sequence. Loss of the carbon π bond is readily apparent in the decreasing strength of the peaks at 1645 cm^{-1} and 997 cm^{-1} . As with the propane, we also observe destruction of the $-\text{CH}_3$ band region and production of both CO_2 and methane.

strengths, is consistent with propane polymerization. The minor decrease in area of the 1356-1510 cm^{-1} region with increased dose is consistent with carbon lost to CO_2 and CH_4 while some carbon remains in the long-chain aliphatic compounds resulting from polymerization. The final, post-irradiation spectrum of the H₂O+propane film also shows the small but broad band that emerges between ~ 1000 -1050 cm^{-1} . This band is characteristic of the C-O bond in alcohols and becomes more apparent after warming and loss of H₂O.

Changing one of the carbon-carbon bonds to a double bond, *i.e.* using propene (C_3H_6) instead of propane, altered the initial radiolytic chemistry, but the steady-state composition - at least as observed in the mid-infrared - appeared quite similar to

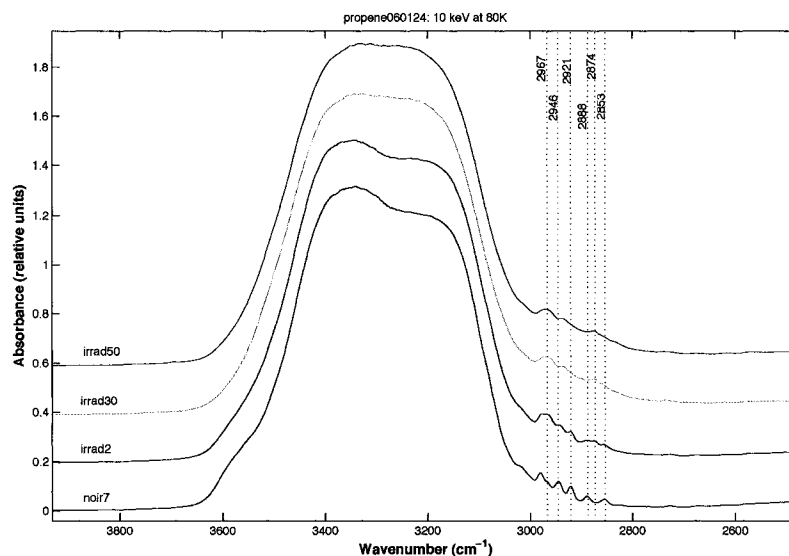


Figure 9.6: Detail of Figure 9.5 showing modification of the -CH₃ dominated region on the shoulder of the broad H₂O \sim 3300 cm⁻¹ band.

its alkane counterpart. Figures 9.5, 9.6, and 9.7 show the irradiation sequence, again moving from the unirradiated 80 K ice (lowermost spectrum) to the spectrum of the ice mixture after \sim 7 hours of irradiation with 10 keV electrons at 200 nA (uppermost spectrum).

Differences between the starting spectra of the propane and propene films include the strong 1645 cm⁻¹ peak (-CH=CH₂), the strong 997 cm⁻¹ peak (CH=CH), and the strong 912 cm⁻¹ peak (-CH=CH₂). None of these bands persisted during radiation. Information about the alkene nature of the initial film was completely absent in the final ice spectra.

The -CH₃ and -CH₂- bands in the 2800-3000 cm⁻¹ region of the propene film were initially more complex due to the additional vibrations of double-bonded =C-H (Figure 9.6). During irradiation, however, the double bond was destroyed and the additional vibrational modes vanished, leaving the aliphatic -CH₃ asymmetric and symmetric stretches, and the asymmetric stretch of -CH₂-. As with the irradiated propane, the relative strength of the 2934 cm⁻¹ -CH₂- band compared to the -CH₃ bands is consistent with polymerization. Figures 9.9, 9.10, and 9.11 show the pre-

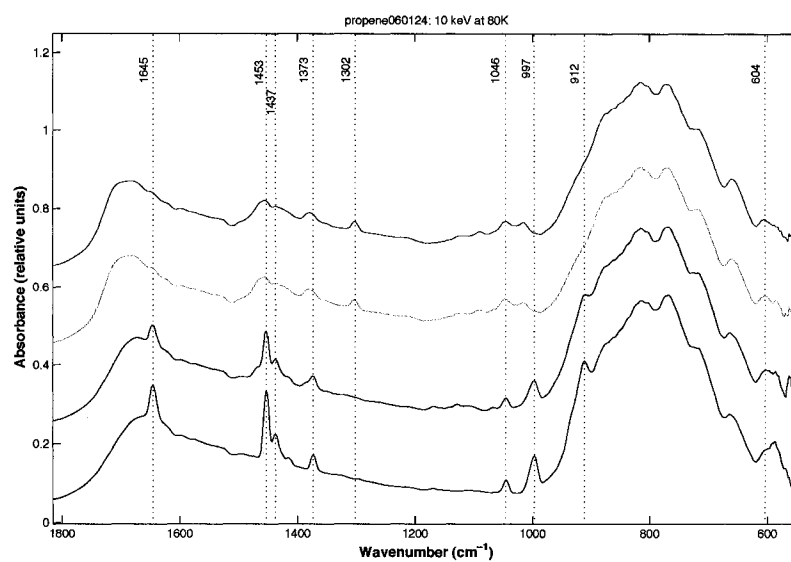


Figure 9.7: Detail of Figure 9.5 showing destruction of the C=C π bonds as the bands at 1645 cm^{-1} and 997 cm^{-1} decrease with increasing dose. Also evident here is the production of methane via the growth of the band at 1302 cm^{-1} and modification of the $-\text{CH}_2-$ and $-\text{CH}_3$ bands in the region of $1400\text{--}1470\text{ cm}^{-1}$.

and post-irradiation spectra for propane and propene together in order to facilitate comparisons.

The change in band strength as a function of dose for the H₂O+C₃H₆ ice film is quantified in Figure 9.8. Integrated band absorptions are shown for CO₂, CH₄, and the two C-H regions discussed above. In addition the C=C bands at 1645 cm⁻¹ and 997 cm⁻¹ are shown, both with linear fits used to extract the band area from the background water profile. At a dose of $\sim 10^{20}$ eV cm⁻² the 997 cm⁻¹ band disappeared and the 1645 cm⁻¹ band diminished to just a small feature on the shoulder of the broad water band at ~ 1680 cm⁻¹ (see Figure 9.7). The double bond of the propene molecule was rapidly destroyed. Interestingly, the 2340 cm⁻¹ band of CO₂ rose rapidly and was larger than the corresponding band in the propane study.

As with the irradiated propane, after a dose of $\sim 10^{19}$, CO₂ production increased concomitantly with CH₄ and continued to increase at the same rate until $\sim 10^{20}$ eV cm⁻² at which point the production rate decreased slightly but continued upward. The C-H regions show the same behavior as observed with propane, though in this case the 2836-2996 cm⁻¹ region shows only a very minor decrease with accumulated dose. Conspicuously absent in both the propane and propene films was any sign of CO at 2140 cm⁻¹. We address this point below in the context of chemical pathways during irradiation.

At a dose of $\sim 10^{20}$ eV cm⁻² each molecule in the ice film has received on average ~ 10 eV. This amounts to roughly 3.2 eV per bond in the H₂O+C₃H₈ film and 3.6 eV per bond in the propene film. These doses are comparable, though roughly a factor of two less than those used in the similar work of Moore and Hudson (1998). Of the carbon bonds initially present in our films (C-C, C-H, and C=C), the most radiation resistant bonds were seen to be those of C-C, followed by C-H and C=O. This stability sequence can be understood through the molecular orbital theory of bond strength. The C=O is stronger than the C=C bond because, according to molecular orbital theory (Winter, 1994), the two additional valence electrons in C=O (10 total) go into an additional σ -bond, giving greater bonding strength (and shorter bond-length, hence the larger wavenumber for the absorption) than the C=C bond with eight valence electrons, four of which are in σ -bonds and four of which are in the

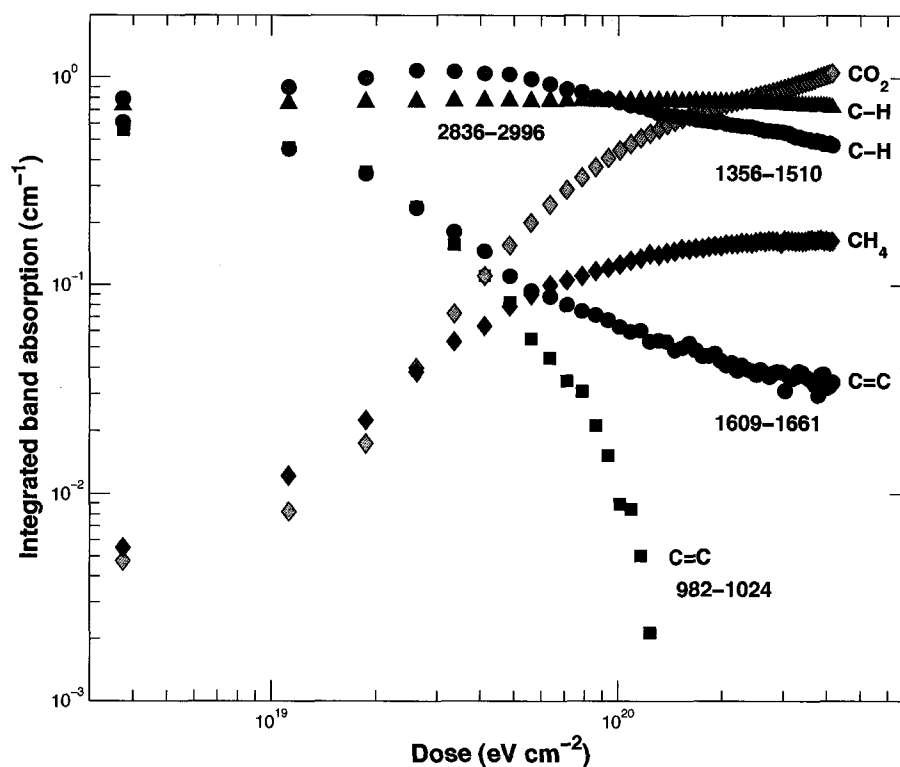


Figure 9.8: Irradiation of an $H_2O + C_3H_6$ ice mixture results in rapid degradation of the C=C bond, as made clear by the decrease in both the 982-1024 cm^{-1} band and the 1609-1661 cm^{-1} bands. As with the alkane mixtures, here we see production of CO_2 and methane coupled with loss of the $-CH_3$ dominated C-H region (1356-1510 cm^{-1}). The 2836-2996 C-H band is stable and is, in part, indicative of polymerization of the short-chain hydrocarbon.

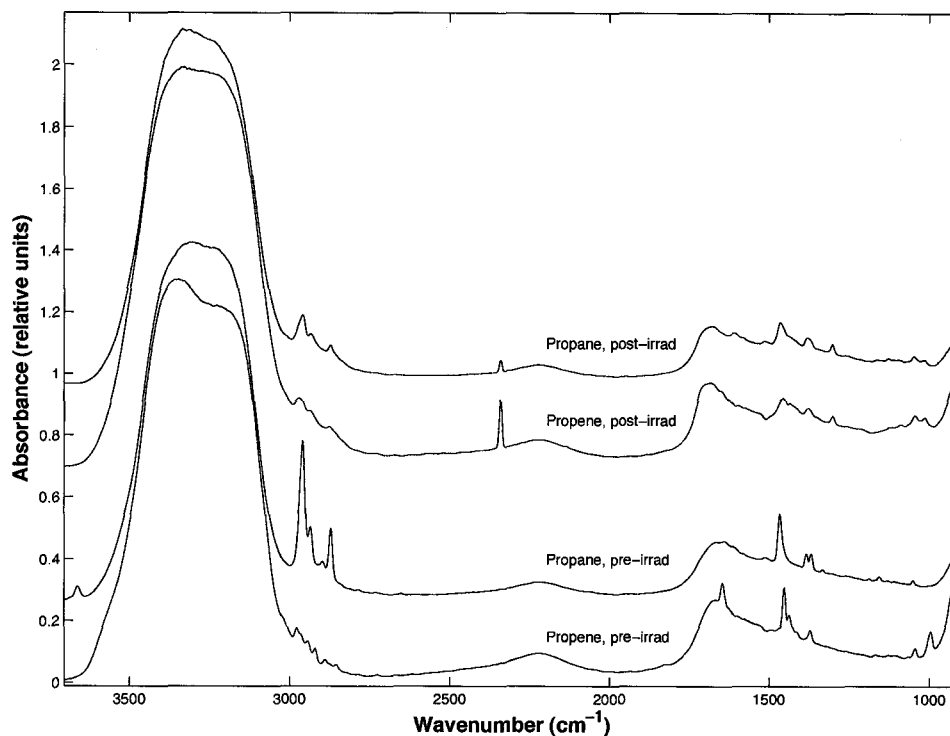


Figure 9.9: Comparison of the propane and propene irradiation results. In blue are spectra from before and after irradiation of a propene-rich ice film. In black are pre- and post-irradiation spectra of a propane-rich ice film. While the initial propene film is easily distinguished from the initial propane film as a result of the C=C vibrational modes at 1645 cm^{-1} and 997 cm^{-1} , after irradiation the films are largely indistinguishable. The additional complexity of the alkene in the ice mixture is lost as a result of exposure to the high-energy electron irradiation.

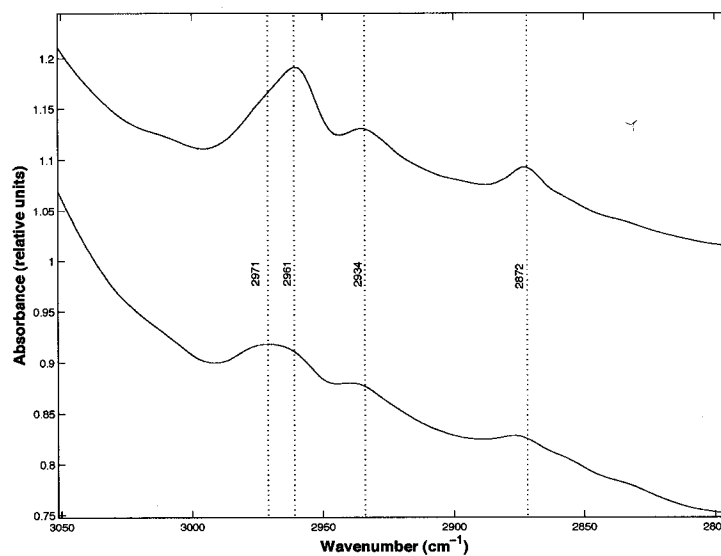


Figure 9.10: Detail of Figure 9.9 showing similarity of propane (black) and propene (blue) ice films after irradiation. While the strength of the -CH₃ band at ~ 2960 remains stronger in the propane ice (upper spectrum), the two spectra show the same C-H bands with similar relative intensities.

| Bond | Bond type | Energy (eV/bond) | Bond length (pm) |
|---|---------------|------------------|------------------|
| C-H | σ | 4.28 | 109 |
| C-C | σ | 3.61 | 154 |
| C=C | $\sigma+\pi$ | 6.36 | 134 |
| C \equiv C | $\sigma+2\pi$ | 8.65 | 120 |
| C-O | σ | 3.71 | 143 |
| C=O | $2\sigma+\pi$ | 8.28 or 7.67 | 120 |
| O=O | | 5.17 | |
| O-H | σ | 3.79 or 4.81 | 96 |
| Typical σ bond: ~ 3.8 eV per bond | | | |
| Typical π bond: ~ 2.7 eV per bond | | | |

Table 9.1: Interatomic bonds and associated parameters for carbon, hydrogen, and oxygen. Data from Darwent (1970), Cottrell (1958), and Winter (1994).

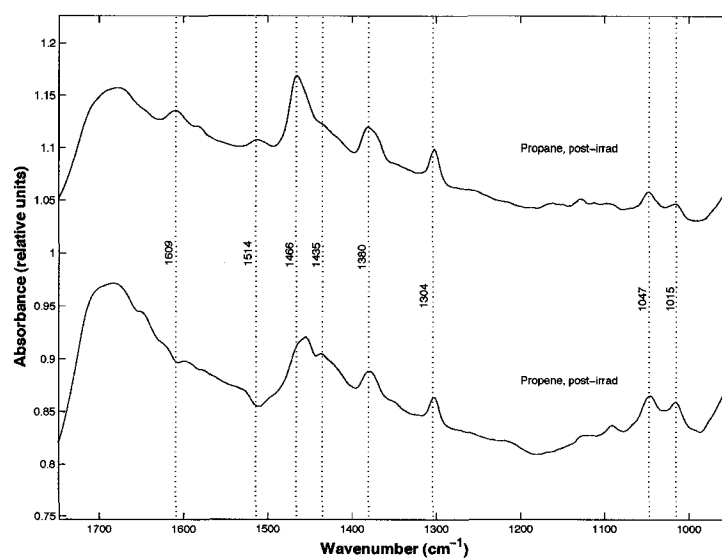


Figure 9.11: Detail of Figure 9.9 showing similarity of propane (black) and propene (blue) ice films after irradiation. Despite the initial added complexity of a C=C bond, the alkene (propene) results in an irradiated spectrum with little difference from that of the alkane (propane).

weaker π -bonds. The π bond of the C=C is destroyed by the electron irradiation and the double bond becomes a single σ bond. In the C=O bond however, the σ bond needs to be broken before the weaker π bonds can be broken. Table 9.1 shows the energy and configuration differences among these bonds.

9.1.2 Four Carbon Compounds

Results for the irradiation of butane, isobutane, and (1,2)-butene did not vary significantly from the changes observed between the three-carbon alkane and alkenes. Radiolysis resulted in rapid degradation of the CH₃ bands but persistence of the CH₂ bands, consistent with polymerization of the starting hydrocarbon. The alkenes were observed to undergo destruction of the C=C bonds. The final products consisted of long chain aliphatics with -OH, C-O, and C=O bonds. CO₂ and CH₄ were also seen to evolve.

Figure 9.12 shows a pair of spectra characteristic of the pre- and post-irradiation sequence for an ice film of H₂O+C₄H₁₀ [2.25:1]. The bands in both spectra are largely indistinguishable from their counterpart in the propane films. This is not surprising given that the bonds and functional groups of the two starting compound are identical. A slight excess of -CH₂- might be expected in the butane film but it was not observed in our spectra. Clearly visible in the irradiated spectrum, in the 1000-1030 cm⁻¹ region, are the C-O bands of alcohols (see Figure 9.2 for reference).

Starting with an ice film containing the branched alkane, isobutane, did little to alter the results. Figure 9.13 shows the irradiation sequence and Figures 9.14 and 9.15 show details of regions of interest. Pure isobutane contains no -CH₂- and very little of that band was observed in the initial film (Figure 9.14). What was seen of that band is mostly due to cracking and modification of some of the isobutane during deposition. The isobutane appeared to have minor alkene contamination, as evidenced by the small bands at 1636 cm⁻¹ and 912 cm⁻¹.

The irradiated isobutane film shows a high -CH₂-/-CH₃ ratio, again a strong indication of hydrocarbon polymerization. Coupled with this are the CO₂, CH₄, C=O, and C-O bonds characteristic of all the irradiated hydrocarbons. Figure 9.15

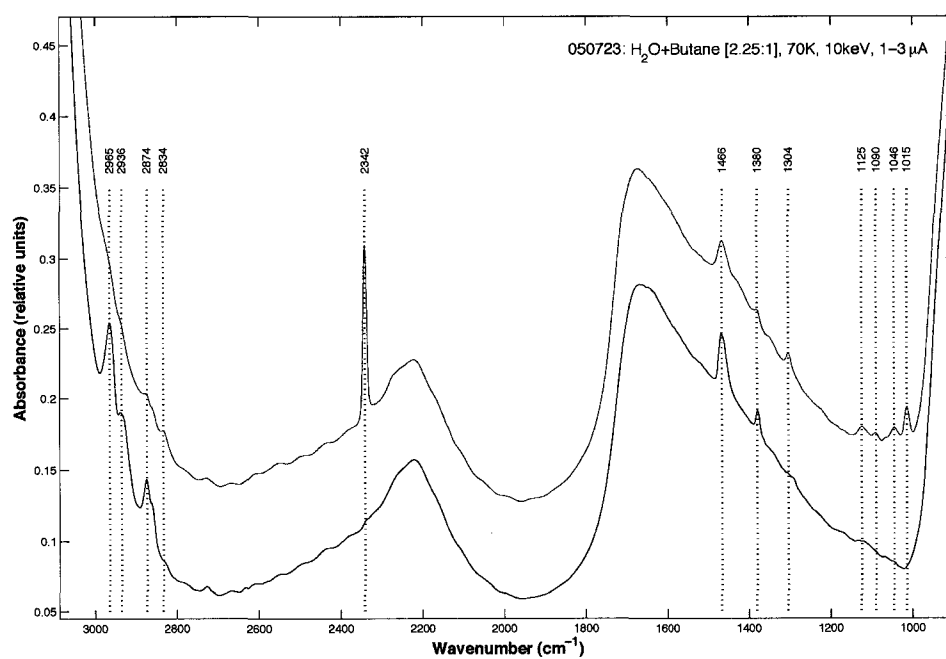


Figure 9.12: Pre- and post-irradiation spectra of H₂O+butane film, 500-4000 cm⁻¹. The film was irradiated at 70 K with 10 keV electrons and a beam current of 1-3 μA. Bands relevant to production and destruction process are shown.

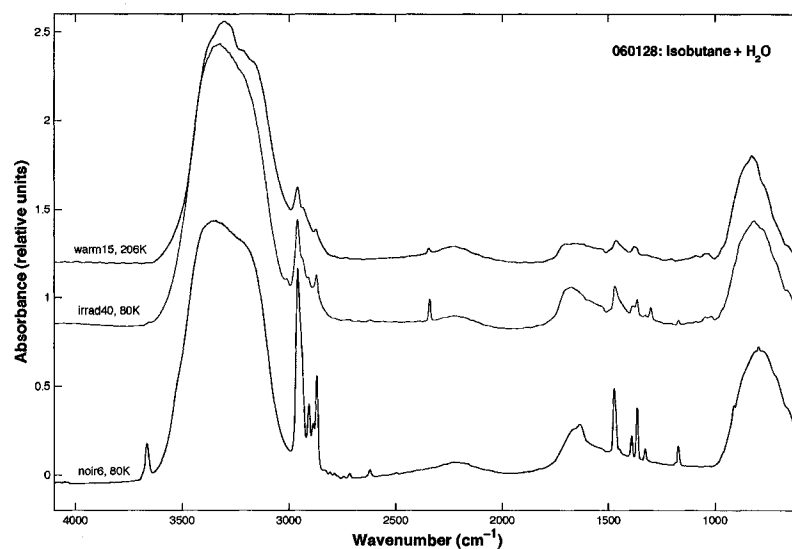


Figure 9.13: Spectra of H₂O+isobutane film, 500-4000 cm⁻¹. The black spectrum was taken prior to the onset of irradiation, the red spectrum was taken after approximately eight hours of irradiation, and the blue spectrum was taken during warming at a temperature of 206 K.

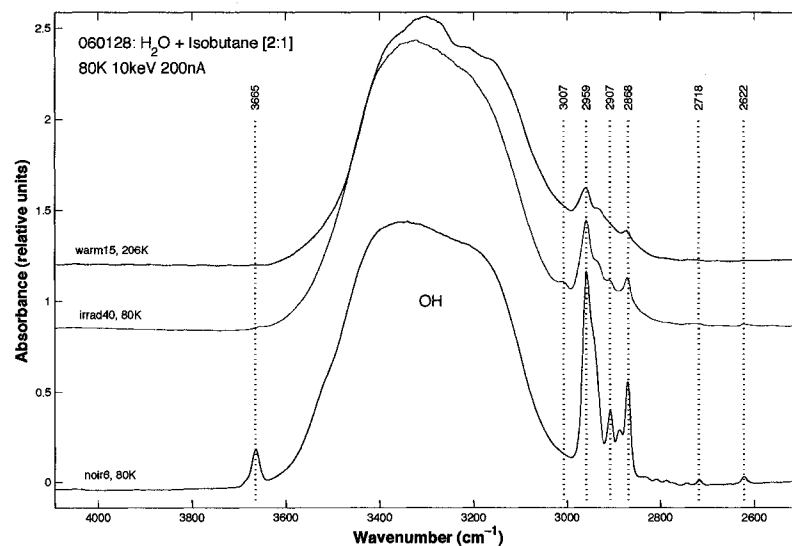


Figure 9.14: Spectra of H₂O+isobutane film, detail of Figure 9.13, 2600-4000 cm⁻¹.

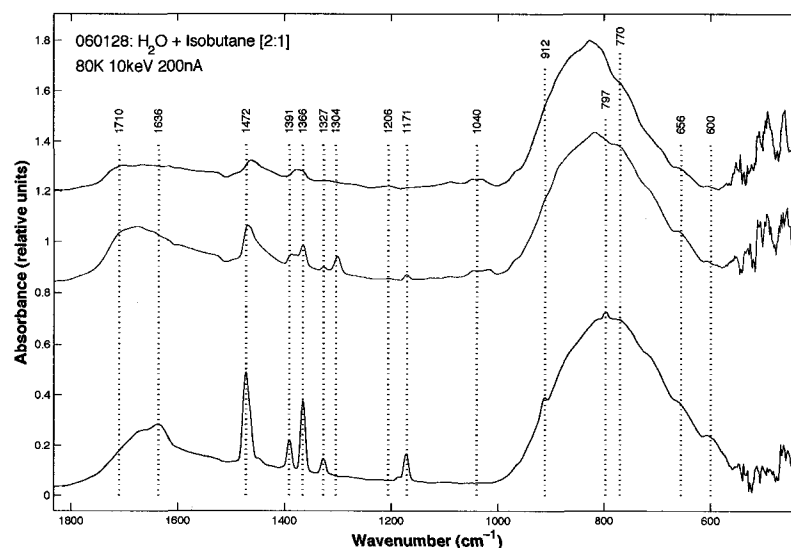


Figure 9.15: Spectra of H₂O+isobutane film, detail of Figure 9.13, 500-1800 cm⁻¹.

shows results down to ~ 500 cm⁻¹ and none of the strong bands expected for aromatics are seen. This is especially significant for the case of isobutane. With the straight chain hydrocarbons no aromatic bands were seen and we suspected that perhaps trapping in the ice matrix limited mobility, bending, and linking of the hydrocarbon units, inhibiting the formation of aromatic rings. The branched structure of isobutane should have addressed some of these concerns and yet we still saw no definitive sign of aromatics in the spectra. These points are addressed in greater detail at the end of this chapter.

The four-carbon alkenes, 1-butene and 2-butene, were irradiated at 80 K with 10 keV electrons. Figures 9.16, 9.17, and 9.18 show a representative 1-butene spectrum prior to irradiation (lower) and after approximately seven hours of irradiation (upper spectrum). Again, little difference was seen between the spectra of the irradiated film containing these hydrocarbons and the previously discussed hydrocarbons. Some residual C=C bonds persisted, but the final spectrum was dominated by the signature of the aliphatics with aldehydes, ketones, and alcohols. Integrated band areas are shown for several key bonds in Figure 9.19. The latent rise of CO₂ relative to CH₄

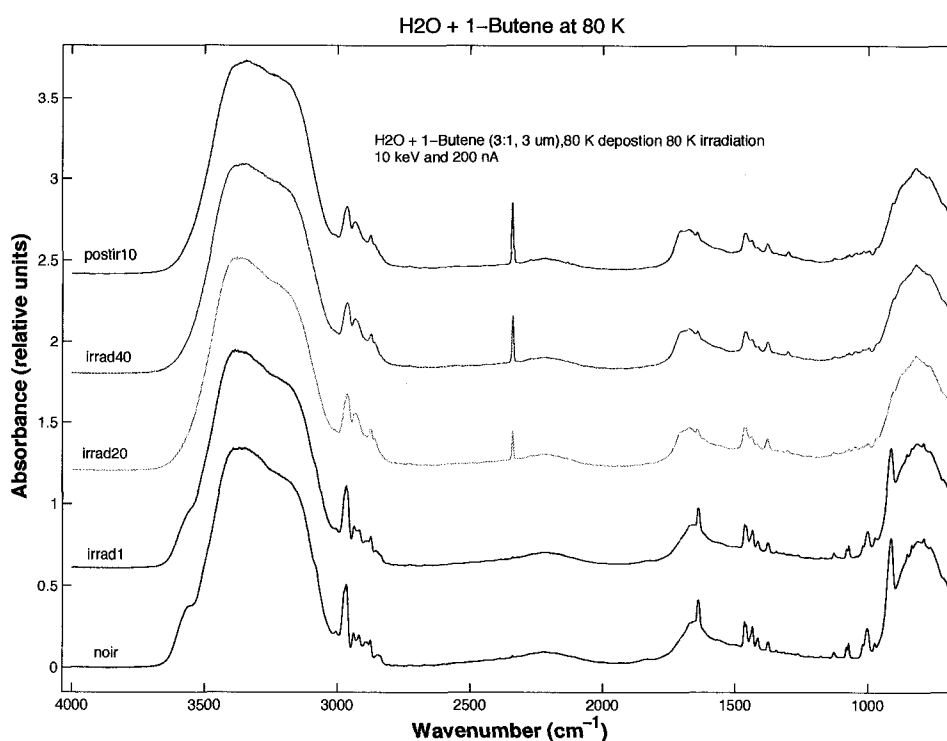


Figure 9.16: Spectra of H₂O + 1-butene during irradiation. The bottom spectra (black) shows the ice film before irradiation. The progression of the spectra upwards show the evolution of the ice film during irradiation. The uppermost spectra (red) shows the film after sitting for more than an hour after irradiation. Production of CO₂ is apparent at the 2340 cm⁻¹.

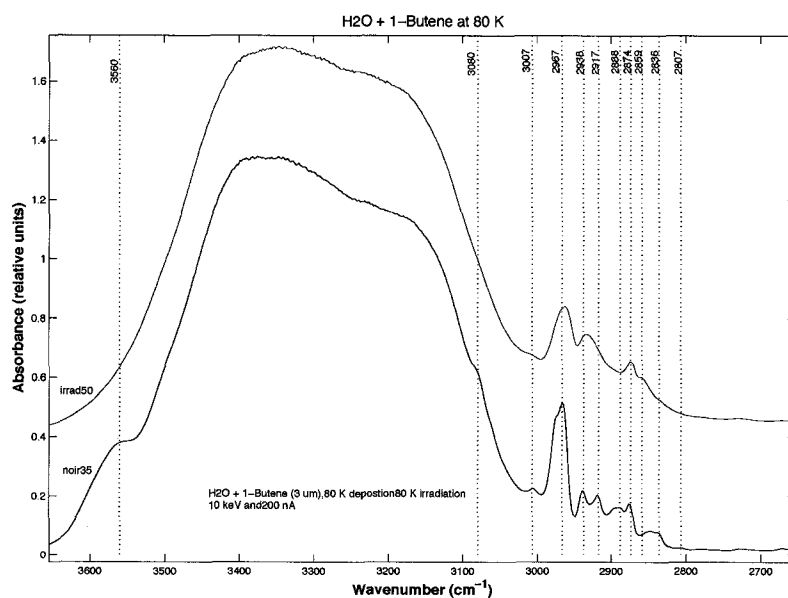


Figure 9.17: Spectra of H₂O + 1-butene pre- and post-irradiation, detail of Figure 9.16, 2700-3600 cm⁻¹. In the upper spectrum, showing irradiated ice, the relative band height of the -CH₃ symmetric stretch has been greatly diminished while the -CH₂- str remains relatively constant, if not increasing some. This is similar to what was seen with the three-carbon compounds and is indicative of polymerization of the short chain hydrocarbons.

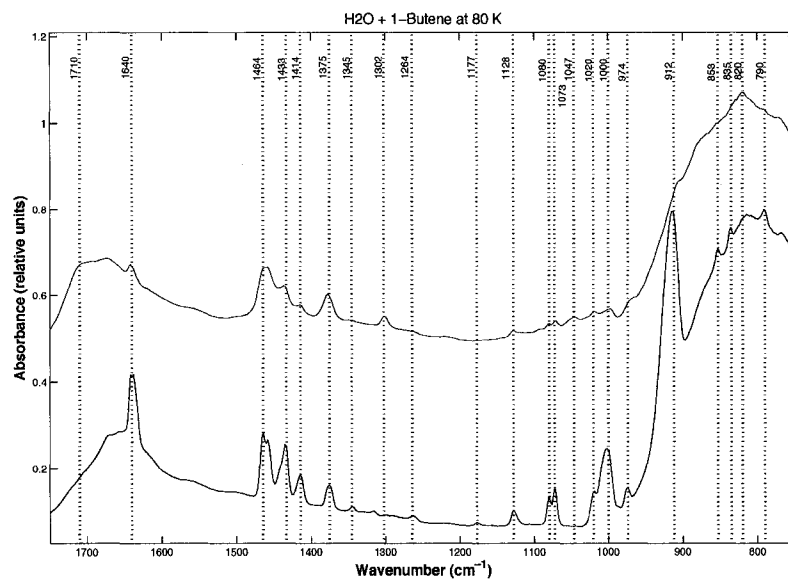


Figure 9.18: Spectra of H₂O + 1-butene pre- and post-irradiation, detail of Figure 9.16, 600-1700 cm⁻¹. In this region the loss of the C=C bond is confirmed through observation of six different bands, centered at 1640, 1414, 1080, 1073, 1000, and 912 cm⁻¹. Similarly, the loss of -CH₃ can be seen by the change in the 1433 cm⁻¹ band. Methane production can be seen by the band rising at 1302 cm⁻¹. Particularly visible in these before and after spectra is the appearance of the shoulder at 1710 cm⁻¹, indicative of carbonyl bonds (C=O) on the long-chain aliphatic hydrocarbons.

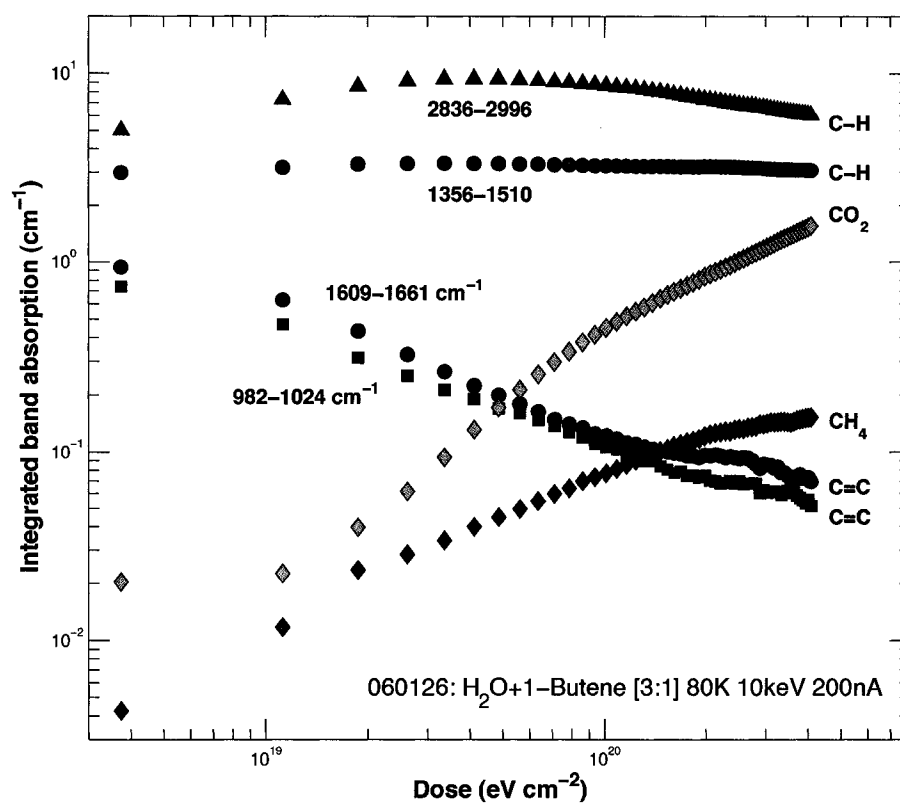


Figure 9.19: Integrated bands vs. Dose, H₂O + 1-Butene film. As in Figures 9.4 and 9.8, destruction of bonds and synthesis of new products was tracked by integrating band areas and observing the changes as a function of dose. Results for propene and 1-butene are very similar.

suggests that methane be a precursor to full oxidation of the carbon. The 982-1024 cm^{-1} band of the 1-butene film did not decrease as rapidly as seen in the propene film, but the 1609-1661 cm^{-1} region showed very similar behavior when compared to propene. Methane production reached saturation at a band area of $\sim 0.1-0.2 cm^{-1}$. Carbon dioxide production never reached saturation.

9.2 Hydrocarbon residue analysis

Analysis of the residues remaining on the gold substrate, after warming and sublimation of the water ice and other volatiles, is interesting for two primary reasons. First, we can better understand the spectral signature of such materials observed remotely on other worlds, such as Ganymede, Callisto, and Enceladus (Brown et al., 2006; McCord et al., 1997). Second, the radiolytic production of such compounds on worlds like Europa could have important consequences for the ocean chemistry, and habitability, if such surface materials reach the subsurface ocean (see Chapter 8 for more detail on delivery to the sub-surface).

Caution is necessary, of course, because the final residue does not perfectly represent the compounds produced in-situ during irradiation. Warming from ~ 70 K to ~ 300 K results in the loss of many compounds that would not escape on icy worlds. Indeed, these materials may also be delivered to the sub-surface ocean on worlds like Europa. The loss of volatiles and warming also likely modifies the compounds left on the substrate.

To assess the smaller molecules lost during warming, mass spectral data from the residual gas analyzer (RGA) was collected throughout all irradiation and warming sequences. In Figure 9.20 the data from the isobutane experiment are shown. This spectrum was created by integrating species collected throughout the warming process from 80 K to 300 K at 1 K per minute. A background spectrum was collected while the ice film sat at 80 K prior to irradiation. This spectrum was then subtracted from the integrated warming spectrum. The water peaks at 17 and 18 m/z dominate the spectrum, followed by the peak at 44 m/z due largely to carbon dioxide and propane. The peaks at 57 and 58 are from butane and ketones (*e.g.* acetone CH_3CH_2HCO).

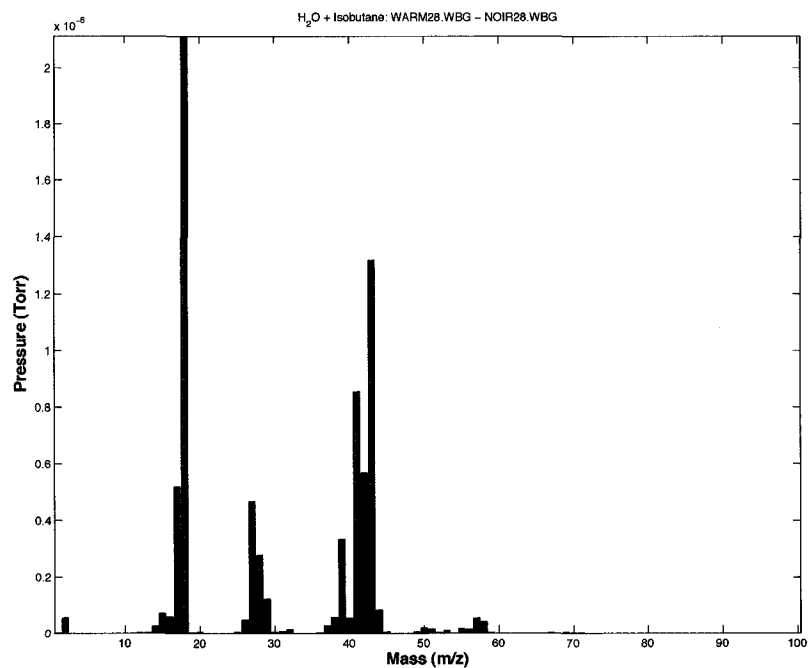


Figure 9.20: Data from the residual gas analyzer (RGA) integrated over the warming process from 80-300 K. The three large clusters of peaks are from H_2O (18), CO (28), and CO_2 + a hydrocarbon fraction (44, *e.g.* C_3H_8). The CO, not seen in the infrared, is derived from CO_2 .

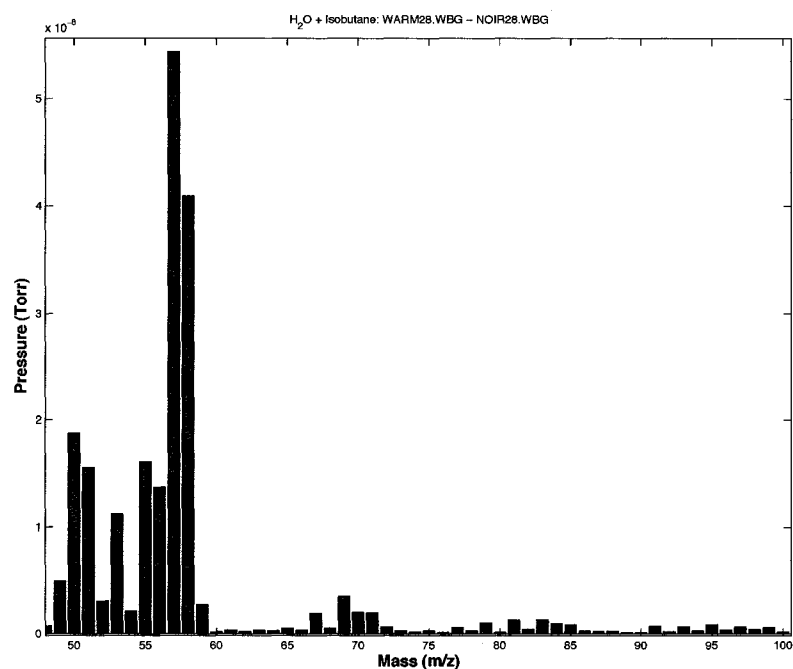


Figure 9.21: Detail of data from Figure 9.20, showing the m/z range from 50-100. The butane, and likely aldehyde and alcohol, fraction is seen at m/z of 57 and 58. Clusters at higher m/z are primarily due to polymerization via addition of methyl or formyl radicals.

In Figure 9.21 the region from 50-100 m/z is shown in greater detail. Though only trace species were observed in this region, evidence for polymerization to compounds such as butanal (m/z = 72) and pentanal (m/z = 86) can be seen in the peak clusters around these regions.

The temperature at which various species evolve from the film is of particular interest in the context of loss from the surface of Europa and the possible remote detection by instruments onboard a spacecraft orbiter. While it seems unlikely that sufficient quantities would reach the altitude of orbit (~ 100 - 200 km) for the case of the relatively massive Europa, detection of organics in the plume of Enceladus do serve as an intriguing proof of concept (Waite et al., 2006). In Figure 9.22 the time-series evolution of the lighter volatiles from the film during warming is plotted. As shown, many species exhibit a spike of release in the range of ~ 105 K. This is well within the range for Europa's daytime equatorial surface temperatures (Spencer et al., 1999), indicating that perhaps such species could be remotely detected if the molecules were to reach the altitude of the spacecraft. More discussion on science from orbit is given in Chapter 11.

After warming, residues were found on the target mirrors of all samples. Figure 9.23 shows the gold mirror substrate removed from the vacuum chamber and cryostat. Figure 9.24 shows microscopic images of the residues. The circular structures seen in the alkene residues are suggestive of bubbles or membranes. Aliphatic compounds have been shown to form vesicles after synthesis through ultra-violet irradiation (Dworkin et al., 2001), a result of interest for prebiotic chemistry. Future work will focus on isolating the aliphatic component from these residues.

Using a laboratory FTIR we collected spectra of the residues at room temperature and pressure. As can be seen from Figures 9.25 and 9.26 the largest differences between these spectra and the in-situ spectra are the distinct O-H peaks at 3400 cm^{-1} and 1060 cm^{-1} . These peaks were obscured by the O-H of the water in the ice spectra, but here one can clearly see that this functional group is an important component of the resulting aliphatic mixture. With much of the water signature removed, the organic signature is very strong. There are eight major bands that characterize all of the residue spectra. These are: 1) the broad -OH at $\sim 3400\text{ cm}^{-1}$, 2) the ~ 2960

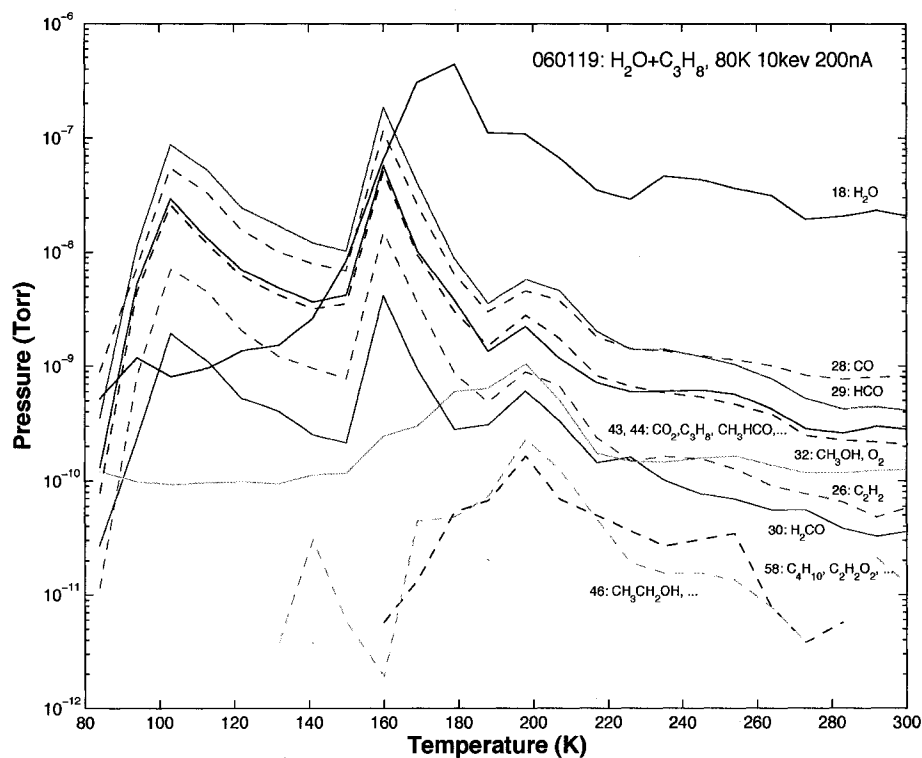


Figure 9.22: Results from the residual gas analyzer (RGA) collected during warming of an irradiated propane and water ice film. Irradiation temperature was 80 K and the electrons used were 10 keV with a 200 nA beam current. Each line corresponds to the partial pressure of the gas phase for the mass-to-charge ratios (m/z) indicated. Next to each m/z are candidate species for the detected ions. Black line (18), H₂O; Red dash (28), CO; Purple line (29), HCO; Blue line and dash (43, 44), CO₂, C₃H₈, CH₃HCO; Green line (32), CH₃OH, O₂; Purple dash (26), C₂H₂; Red line (30), H₂CO; Black dash (58), C₄H₁₀, C₂H₂O₂; Green dash (46), CH₃CH₂OH.

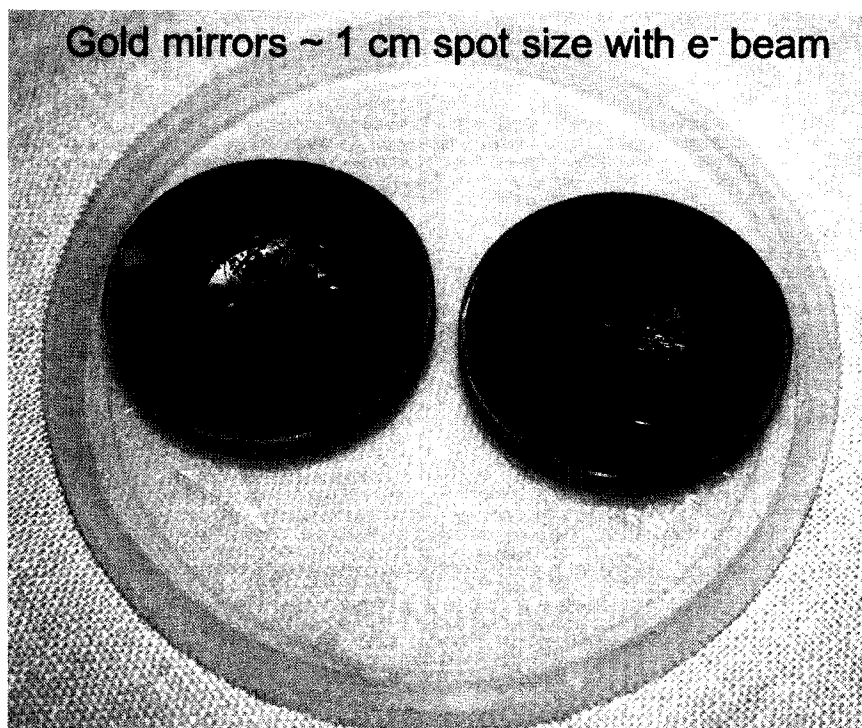


Figure 9.23: Hydrocarbon residues on the gold mirror substrate. The faint residues apparent here are left behind after warming of irradiated H₂O+hydrocarbon ices. After irradiation and warming, the vacuum chamber is repressurized and the cryostat cold-finger removed so that the gold mirror can be retrieved for further laboratory analysis. We estimate the residue mass to be <math>< \mu\text{g}</math>, making traditional GCMS and other techniques difficult and susceptible to confusion with trace contaminants.

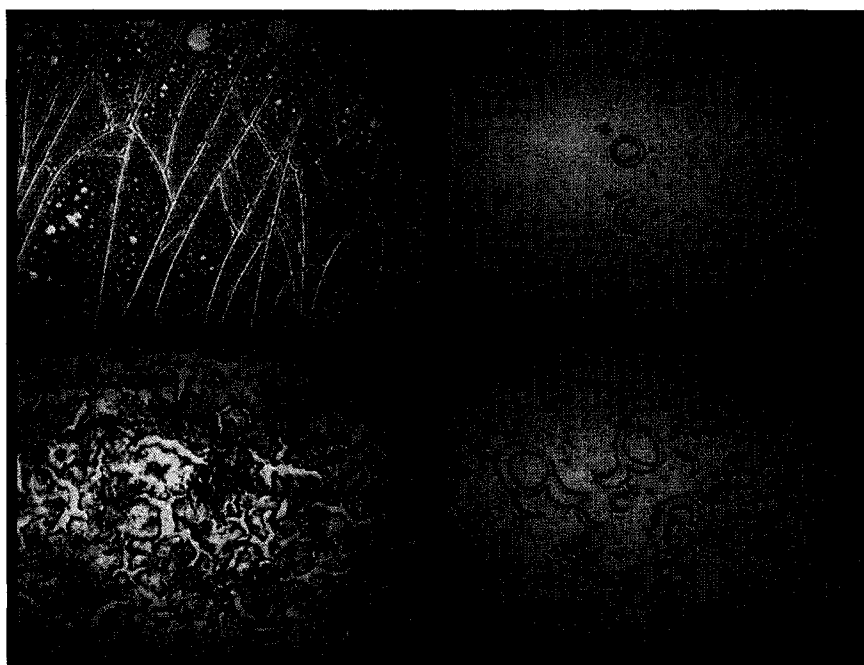


Figure 9.24: The hydrocarbon residues of Figure 9.23 are shown here under a microscope. The width of each image is approximately 850 μm (see scale bar in lower left). The curious hydrocarbon structures were unexpected and may be of interest in the context of vesicle formation from amphiphiles formed during irradiation (Dworkin et al., 2001). Our ongoing analysis is looking into this possibility by rehydrating some of the residue material and isolating any aliphatic component.

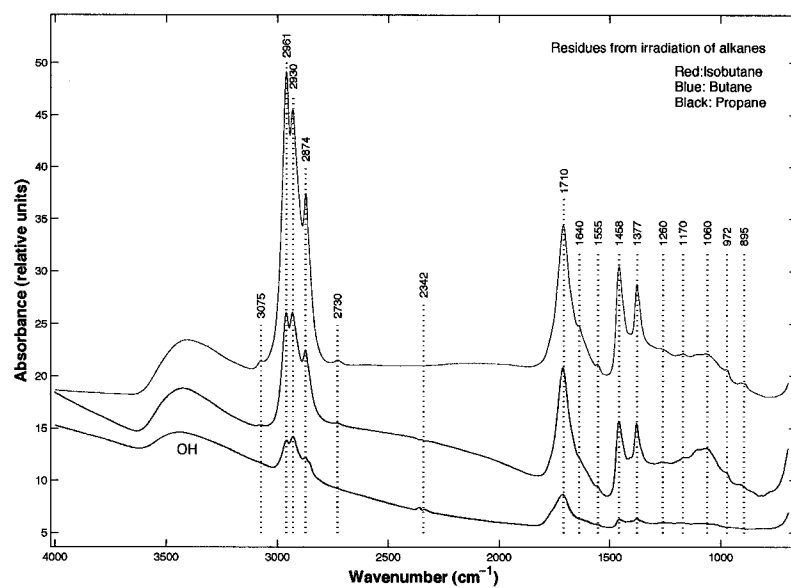


Figure 9.25: Spectra from residues resulting from electron irradiation of $H_2O +$ alkane ices. The similarity of bands observed in these spectra indicate that the chemical composition of the residues is quite similar.

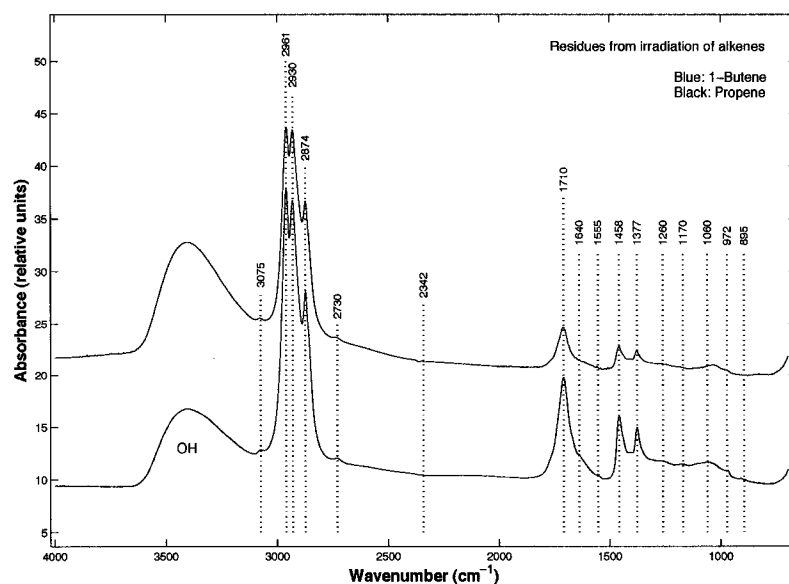


Figure 9.26: Spectra from residues resulting from electron irradiation of H₂O+ alkene ices. The similarity of bands observed in these spectra indicate that the chemical composition of the residues is quite similar. In addition, little difference can be seen between these spectra and those of the alkane residues in Figure 9.25.

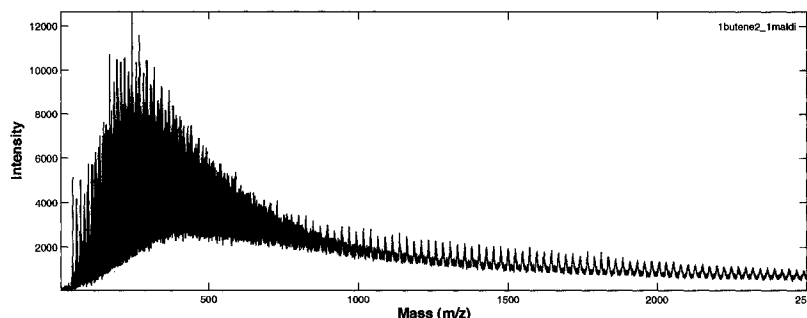


Figure 9.27: Matrix-assisted laser desorption/ionization (MALDI) spectrum of a hydrocarbon residue produced during irradiation of an 80 K H₂O+C₄H₈ ice with 10 keV electrons. A custom MALDI mount was constructed for our gold mirrors so that the films could be analyzed directly without dissolution and coupling with a matrix (*i.e.* our analysis is LDI). Shown here is the entire spectrum up to 2500 m/z. The strongest peak within the broad distribution <1000 m/z is at 241.8 m/z. Beyond m/z of 1000, the peaks are real but their periodicity is still not well understood.

cm⁻¹ asymmetric stretch of -CH₃, 3) the ~2930 cm⁻¹ asymmetric stretch of -CH₂-, 4) the symmetric stretch of -CH₃ at ~2874 cm⁻¹, 5) the C=O carbonyl band at ~1710 cm⁻¹, 6) the -CH₂- scissor at ~1458 cm⁻¹, 7) the symmetric bend of C(CH₃)₃ at ~1377 cm⁻¹, and 8) the broad C-O alcohol band centered at approximately 1060 cm⁻¹. The combination of all these bands indicates that the residues are dominated by long chain aliphatic hydrocarbons, with a mixture of aldehydes, ketones, and alcohols.

To better understand the size and mass of the compounds in the residue, matrix-assisted laser desorption/ionization (MALDI) was utilized. Our samples, however, were not first dissolved into a matrix. A custom plate for the MALDI instrument was constructed such that the gold mirrors from our experiments could be introduced into the MALDI instrument directly. This eliminated the need for removing the small residue sample from the mirror and prevented us from having to take many steps that could have introduced considerable contamination. The end result is that the compounds in our residues were directly desorbed and ionized without the aid of a matrix compound.

The MALDI was operated in linear mode with polarity positive and an accelerating voltage of 20 kV. The laser was cycled at 20 Hz and each spectrum is the result of

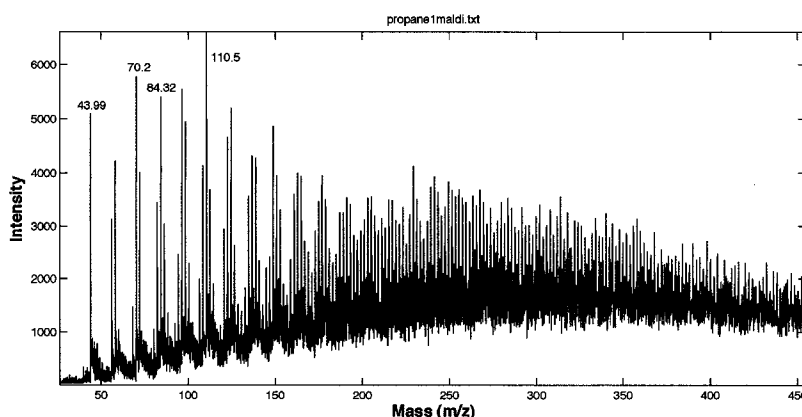


Figure 9.28: MALDI spectrum of hydrocarbon residue after irradiation of an 80 K propane+water ice with 10 keV electrons. Shown here is the low end ($m/z < 500$) of the MALDI spectrum, highlighting the peaks at ~ 44 , 70, 84, and 110 m/z . The peak at 44 is propane (C_3H_8), the peak at 70 is likely a pentane fraction (C_5H_{10}), 84 is likely a hexane fraction (C_6H_{12}), and 110 is likely an octane fraction (C_8H_{14}). Beyond 110 the distinct peaks are harder to resolve.

100 laser pulses. The default calibration, *i.e.* that for α -cyano-4-hydroxycinnamic acid, was used throughout. Given the non-uniform thickness and distribution of the residues, the intensity of the laser was adjusted as needed in order to produce spectra with good signal to noise.

MALDI results show polymerization of the starting hydrocarbon material, yielding aliphatics with $m/z > 2500$. The process of polymerization produces systematic peaks consistent with the addition of the hydrocarbon subunits and functional groups such as C=O and -OH. Beyond m/z of 1000, the periodicity in the peaks appears with a $\Delta m/z \sim 24$. This could be cracking of a terminal $C\equiv C$, but the lack of alkyne bonds in the infrared spectra would imply that the triple bond would be formed during desorption by the laser. Another possibility is the loss of an $-CH_2HCO$ radical attached to a carbonyl, followed by hydroxyl substitution and conversion of the carbonyl to a hydroxyl. In either case, the high m/z values observed for all residues indicates polymerization and production of compounds 1-2 orders of magnitude more massive than the original hydrocarbons. While the production of such material is

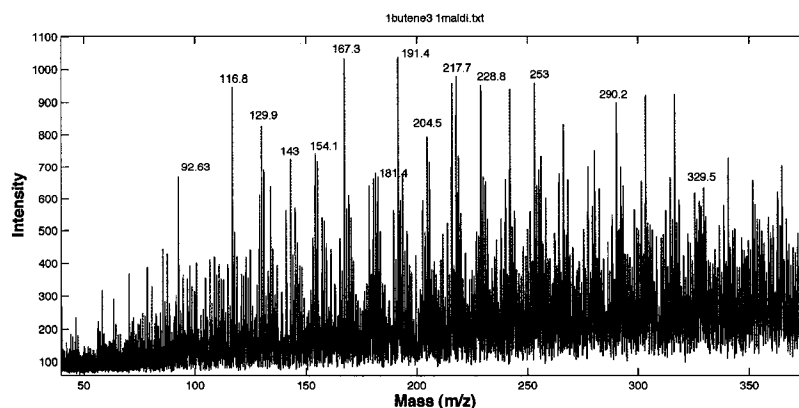


Figure 9.29: MALDI spectrum of hydrocarbon residue after irradiation of an 80 K H₂O+ 1-butene ice with 10 keV electrons. The peak at $m/z = 92.63$ may be glycerol (C₃H₅(OH)₃), while the peak at $m/z = 116.8$ may be isopropyl propionate (C₆H₁₂O₂). Subsequent peaks a likely products of methyl or formyl radical polymerization ($\Delta m/z = 13, 14$).

not necessarily unexpected given the long history of work on tholins and astrophysical ices (*e.g.* see Khare and Sagan (1973), Sagan and Khare (1979), Moore et al. (1983), Strazzulla et al. (1983), Khare et al. (1989), and Bernstein et al. (1995)), the results presented here are unique to the temperature, pressure and dominant form of radiation found on Europa.

At the lower m/z end of the MALDI spectra, a $\Delta m/z \sim 14$ is observed, likely due to cracking and loss of a methyl group (-CH₃) or conversion of an aldehyde to a terminal methyl group (*i.e.* -HCO is replaced by -CH₃). The center of the broad m/z distribution observed in most samples is at an m/z of approximately 241. This could be indicative of compounds such as the carboxylic acid *n*-pentadecanoic acid (C₁₅H₃₀O₂) or the alcohol *n*-hexadecanol (C₁₆H₃₄O).

Figure 9.28 shows the lower m/z region from a propane residue. The peak at 44 is likely a propane fraction (C₃H₈), the peak at 58 a butane fraction, the peak at 70 a pentane fraction (C₅H₁₂), at 84 a hexane fraction (C₆H₁₂), and at 110 an octane fraction (C₈H₁₄). These peaks are also in part due to the corresponding aldehydes, *e.g.* butanal, pentanal, etc.

Beyond an m/z of 200 clusters of peaks are lost in the distribution. A similar

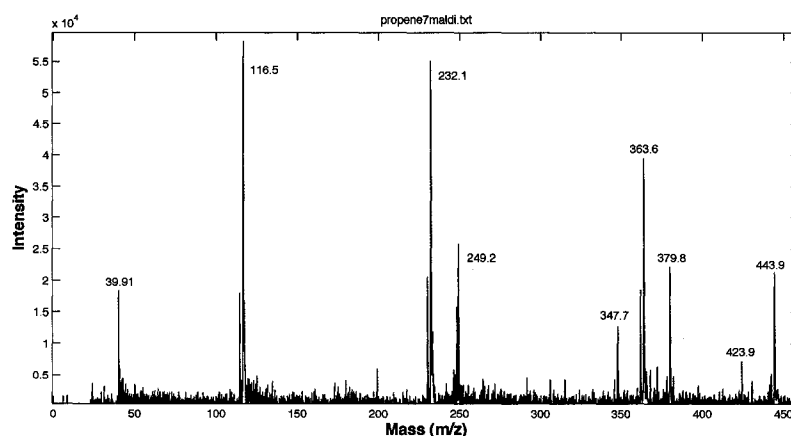


Figure 9.30: MALDI spectrum of hydrocarbon residue after irradiation of an 80 K H₂O + propene ice with 10 keV electrons. Unlike the H₂O+propane residue, the H₂O + propene residue shows a very select pattern of hydrocarbon fractions at highly specific m/z values. We have identified these as $m/z = 116$ subunits of (iso)propyl propionate (C₆H₁₂O₂). No significant species were detected beyond m/z of 450.

spectrum is shown in Figure 9.29. Here the peak at $m/z \sim 92$ may indicate glycerol (C₃H₅(OH)₃) and the peak at $m/z \sim 116$ that of (iso)propyl propionate (C₆H₁₂O₂), or possibly fumaric acid (C₄H₄O₄), though significant amounts of the latter would necessitate a stronger C=C signature in the infrared than what is observed in our results.

The (iso)propyl propionate unit (also referred to as propionic acid, *n*-propyl ester, or sometimes as its very close relative ethyl butyrate) appears again in the MALDI results for the propene residue (Figure 9.30). Here, however, a very distinct polymerization pattern emerges. The $m/z \sim 116$ subunit repeats at 232 and 348. No strong signals were seen beyond the peak at $m/z \sim 444$. The peaks at 363.6 and 379.8 are 16 and 32 m/z off of the propyl propionate trimer respectively, indicating the addition of hydroxyl groups to the molecule. The peaks at 423.9 and 443.9 do not fit the polymer sequence, instead these may be the *n*-octacosanoic acid (C₂₈H₅₆O₂) at 424 and 1,2,3-propanetricarboxylic acid, 2-hydroxy-, trihexyl ester (C₂₄H₄₄O₇) at 444. Many combinations are of course possible.

| | Approximate band center (cm ⁻¹) | | | | | | | | | | | |
|-------------------------|---|------|------|------|------|------|------|------|------|------|------|------|
| | 3007 | 2960 | 2936 | 2907 | 2868 | 2834 | 2340 | 1710 | 1640 | 1464 | 1433 | 1414 |
| Pre-irradiation | | | | | | | | | | | | |
| Propane | | X | X | X | X | | | | | X | | X |
| Propene | | X | X | X | X | | | | X | X | X | |
| Butane | | X | X | | X | | | | | X | | |
| Isobutane | | X | X | X | X | | | | | X | X | X |
| 1-Butene | X | X | X | X | X | X | | | X | X | X | X |
| Post-irradiation | | | | | | | | | | | | |
| Propane | | X | X | | X | | X | X | | X | X | |
| Propene | | X | X | | X | | X | X | | X | X | |
| Butane | | X | X | | X | X | X | X | | X | X | X |
| Isobutane | X | X | X | X | X | | X | X | | X | X | X |
| 1-Butene | | X | X | | X | | X | X | | X | X | |
| Residue | | | | | | | | | | | | |
| Propane | | X | X | | X | | | X | X | X | | |
| Propene | | X | X | | X | | | X | | X | | |
| Butane | | X | X | | X | | | X | | X | | |
| Isobutane | | X | X | | X | | | X | X | X | | |
| 1-Butene | | X | X | | X | | | X | X | X | | |

Table 9.2: Infrared bands observed in hydrocarbon ice film mixtures during various stages of the experiments. An X indicates the presence of the band.

9.3 Conclusion

A summary of the bonds, both major and minor, observed throughout the various stages of the hydrocarbon+water experiments is provided in Tables 9.2 and 9.3. Regardless of the starting hydrocarbon, both the final irradiated ice mixtures and the residue mixtures appear very similar in the infrared. The dominant products are found to be aliphatic aldehydes, alcohols, ketones and esters. Results from MALDI analysis show distinct ester polymerization in the propene residue, but if this process was occurring in the other films, the signature was lost within the broad peak of hydrocarbons produced at $m/z < 500$.

Moore and Hudson (1998) quantified the various compounds produced during their ion-irradiation experiments involving water and hydrocarbons. While we observe many of the same infrared bands, we do not attempt such specific quantification because: 1) CO₂ continues to be produced even after $\sim 5 \times 10^{20}$ eV cm⁻², indicating that we are not at steady-state for carbon chemistry, and 2) the residue that remains after warming indicates that some of the observed bands are likely due to long-chain aliphatics, not just the shorter compounds quantified by Moore and Hudson (1998).

| | | Approximate band center (cm ⁻¹) | | | | | | | | | | | | |
|-------------------------|--|---|------|------|------|------|------|------|------|-----|-----|-----|-----|-----|
| | | 1375 | 1345 | 1302 | 1175 | 1125 | 1090 | 1046 | 1015 | 912 | 820 | 790 | 656 | 600 |
| Pre-irradiation | | | | | | | | | | | | | | |
| Propane | | X | X | | | | | | | | X | X | X | |
| Propene | | X | | | | | | X | X | X | X | X | X | X |
| Butane | | X | | | | | | | X | X | X | X | X | X |
| Isobutane | | X | X | | X | | | | | X | X | X | X | X |
| 1-Butene | | X | X | | X | X | X | | X | X | X | X | X | X |
| Post-irradiation | | | | | | | | | | | | | | |
| Propane | | X | | X | | X | X | X | X | | X | X | X | |
| Propene | | X | | X | | X | X | X | X | | X | X | X | X |
| Butane | | X | X | X | | X | X | X | X | | X | X | X | X |
| Isobutane | | X | X | X | X | X | X | X | X | | X | X | X | X |
| 1-Butene | | X | | X | | X | X | X | X | | X | X | X | X |
| Residue | | | | | | | | | | | | | | |
| Propane | | X | | | X | | X | X | X | | | | | |
| Propene | | X | | | X | | X | X | X | | | | | |
| Butane | | X | | | X | | X | X | X | | | | | |
| Isobutane | | X | | | X | | X | X | X | | | | | |
| 1-Butene | | X | | | X | | X | X | X | | | | | |

Table 9.3: (cont.) Infrared bands observed in hydrocarbon ice film mixtures during various stages of the experiments. An X indicates the presence of the band.

Methanol, ethanol, formaldehyde, and short aliphatics (e.g. Figure 9.2) are part of our final mixture, but it is unlikely that they account for all of the newly synthesized compounds.

Several compounds are of interest precisely because of their absence. Our results show little evidence for production of CO, aromatics, or polyoxymethylene (POMs). Carbon monoxide was observed in H₂O+CO₂ irradiation experiments (Chapter 8), but it was largely absent from the FTIR spectra involving hydrocarbon irradiation. Loss of CO to the vacuum chamber cannot account for the difference as the CO₂ experiments were performed at 90 K and most of the work presented here was for 80 K films, *i.e.* CO was less volatile in the hydrocarbon experiments. The production of CO₂ never reached saturation and tracking CO₂ was possible throughout all stages of all experiments. Production of CO must result from radiolysis of CO₂ as per the experiments in Chapter 8, but CO never accumulates in the hydrocarbon-rich ices.

We propose that the availability of hydrogen within the ice causes all CO to rapidly

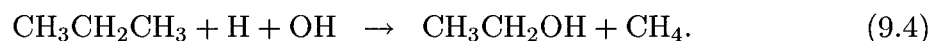
synthesize the formyl radical (HCO), followed by synthesis of formaldehyde (H₂CO),



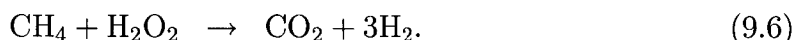
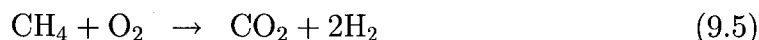
This is consistent with the results of Moore and Hudson (1998), but they observed CO formation in their infrared spectra. Most of their experiments, however, were at a much lower temperature (< 20 K) and started with a higher H₂O/hydrocarbon ratio than our experiments, *i.e.* the availability of hydrogen was likely greater in our work, consistent with CO scavenging of H.

The relationships between the growth and destruction of the bands represented in Figures 9.4, 9.8 and 9.19 reveal information about chemical pathways and synthesis. Methane production occurs with the onset of irradiation, but in all cases the CO₂ band does not increase significantly until a dose of $\sim 2 - 4 \times 10^{19}$ eV cm⁻² is reached. For the alkanes, methane production was more efficient but steady-state for methane in all cases was achieved at $\sim 4 \times 10^{20}$ eV cm⁻², with an integrated band area of approximately 0.2 cm⁻¹. Using the integrated band absorbance value from Moore and Hudson (1998), $A = 6.63 \times 10^{-18}$ cm molec⁻¹, we find a methane column density of 3×10^{16} molecules cm⁻². Given the behavior of the bands, methane may serve as a precursor for CO₂ production, which could then lead to CO and synthesis of HCO.

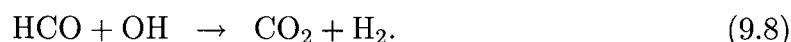
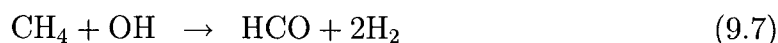
The simultaneous decrease in the 2836-2996 cm⁻¹ C-H region while the methane band increases (*e.g.* Figure 9.4) indicates that loss of the terminal methyl is a likely step toward methane production. As an example, irradiation of H₂O yields H and the hydroxyl radical, which can then produce ethanol and methane if propane is available,



Methane may then be oxidized directly by O₂ or H₂O₂ formed during radiolysis,

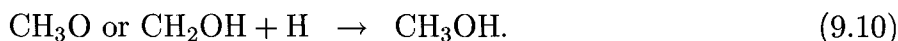
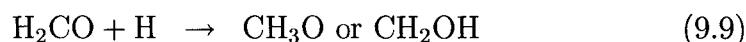


Carbon dioxide may also be formed by subsequent attacks of the OH radical yielding formyl intermediaries which then yield CO₂,

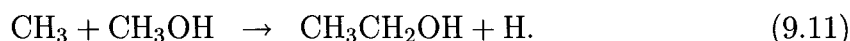


The production of CO₂ from a methane precursor is consistent with our results for integrated bands strength of all the hydrocabons used in our study. Carbon monoxide, however, likely forms from breaking the C=O of CO₂ (Brucato et al., 1997). With hydrogen readily available, however, the C-O is quickly converted to HCO and then H₂CO. The production of CO, and H₂CO₃ for that matter (as discussed in Chapter 8), requires a low ratio of H₂/C. In all of our hydrocarbon experiments, the H₂/C ratio was ~ 2.3, whereas the experiments with CO₂ were with H₂/C ~ 2. The relative ratio of H₂ to CO₂ in the CO₂ experiments was 2, but for the initial conditions in our hydrocarbon experiments [H₂]/[CO₂] ~ 4.7 (here the available carbon was converted to CO₂, but the reaction is limited by the availability of oxygen). The significance of these ratios for the organic chemistry in the atmosphere of the early Earth has been well studied (*e.g.* Chyba and Sagan (1992), Chyba (1991), and Chyba and Hand (2006) for a recent treatment). In the gas phase, [H₂]/[CO₂] ~ 3 yields optimal, *i.e.* maximum, production of organic compounds of prebiological interest (*e.g.* formaldehyde). Lower ratios lead to too much oxidation and higher ratios, specifically > 5, lead to an overabundance of hydrogen. The excess hydrogen inhibits formation of C-C, C-O, and C=O bonds needed for prebiotic compounds. Our ice phase experiments straddle this range and interestingly we observe results similar to those of the gas phase experiments.

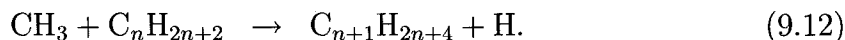
The methyl radical and formyl radical are the key subunits of synthesis and polymerization in our irradiated hydrocarbon ice films. Following Hudson and Moore (1999), production of methanol can proceed from formaldehyde,



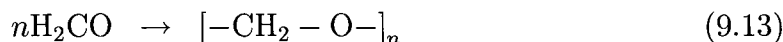
Longer aliphatic alcohols can then be generated by addition of a methyl radical cleaved from a hydrocarbon or from CH₄,



This reaction pathway competes with direct polymerization of the hydrocarbons (Moore and Hudson, 1998),



Both our RGA and MALDI results show that polymerization occurred primarily through the addition of methyl radicals or larger hydrocarbon radicals (*e.g.* propyl and butyl). We do not see clear evidence of aldehyde polymerization to polyoxymethylenes (POMs). Had such polymerization occurred we should have seen the $\Delta m/z \sim 30$ cracking patterns associated with such compounds. Bernstein et al. (1995) reported POM production via,



but they note, with reference to Schutte et al. (1993a,b), that aldehyde polymerization occurs during warming only if some ammonia is present. Lacking ammonia in our films, this pathway was likely inhibited. Instead, we saw the propyl propionate polymerization. The ratio of C, H, and O for POMs is [1:2:1] whereas for the propyl propionate polymer the ratio is [3:6:1]. In other words, we produce a polymer with three times less oxygen than that of Schutte et al. (1993a) and Bernstein et al. (1995).

Carbon dioxide is the most probable reservoir for the excess oxygen and the differences may be largely due to the difference in temperature (*i.e.* astrophysical vs. icy satellite) between these experiments.

Finally, also conspicuously absent in our results is evidence for aromatic hydrocarbons, specifically the polyaromatic hydrocarbons (PAHs) that appear to dominate interstellar organic chemistry (Allamandola et al., 1987, 1988; Bernstein et al., 1999). Were such compounds present in our irradiated films we should have seen strong lines characteristic of these species in the range of 700-800 cm⁻¹ (Allamandola et al., 1989; Langhoff, 1996; Smith, 1999; Socrates, 2001). No such lines were seen in either the post-irradiated ices or the post-warming residues from our experiments. Some of the spectral features used for identification of PAHs by Bernstein et al. (1999) were present in our spectra but we cannot convincingly claim PAH production without the longer wavelength bands, and those were absent from our spectra.

The closest we come to convincingly producing aromatic compounds is our propyl propionate polymers. This is perhaps not surprising. Despite the widespread evidence for interstellar PAHs (Allamandola et al., 1987, 1989), production of PAHs from short hydrocarbons in interstellar ices is still not well-understood. Many of the proposed chemical pathways utilize an acetylene precursor (Allamandola et al., 1989; Bauschlicher Jr and Ricca, 2000). Other pathways start with simple PAHs from which more complex PAHs are generated (Bernstein et al., 2001; Gudipati and Allamandola, 2003). Acetylene is not a compound not readily found in our results.

Perhaps colder, more energetic astrophysical environments are conducive to the formation of acetylene, and consequently better environments for PAH production. For Europa, however, our results show that PAHs are not to be expected in abundance in the radiolytic organic chemistry driven by energetic electrons in reaction with water and alkanes or alkenes. The possible detection of acetylene in the plume of Enceladus is intriguing (Waite et al., 2006), and if future data corroborate that result, then PAH production at Enceladus may indeed proceed in some of the ways proposed (Allamandola et al., 1989; Bauschlicher Jr and Ricca, 2000).

Chapter 10

Radiolysis of NH₃-rich ices

Nitrogen has not been observed on Europa, but spectral evidence for a C≡N containing compound on the surface of Callisto and Ganymede has been reported (McCord et al., 1997). The temperatures and pressures on Europa during formation would not have been sufficient for retaining N₂ or NH₃ in great abundance (Fanale, 1986). Radiolysis of ammonia-rich ices is therefore not motivated by empirical constraints but rather by the need to understand the predominant chemical form in which nitrogen could be retained on the surface of Europa. Synthesis of complex nitrogen compounds are also of particular interest in the context of prebiotic chemistry. Radiolytically driven synthesis of prebiotic compounds on the surface of Europa and other icy satellites could be important for the origin of life in such worlds (Khare et al., 1989; Levy et al., 2000; Dworkin et al., 2001).

10.1 In-situ analysis of radiolytic evolution

Experiments with H₂O+CO₂+NH₃ at 100 K yielded no interesting results. This was likely due to the high temperature; little condensation of CO₂ on the gold substrate was observed during deposition of the film and therefore little interaction between the available carbon and nitrogen was possible. Figure 10.1 shows pre- and post-irradiation spectra for the H₂O+CO₂+NH₃ [5:1:1] film irradiated with 10 keV electrons at 200 nA. Electron radiolysis resulted in escape of carbon and nitrogen, as can

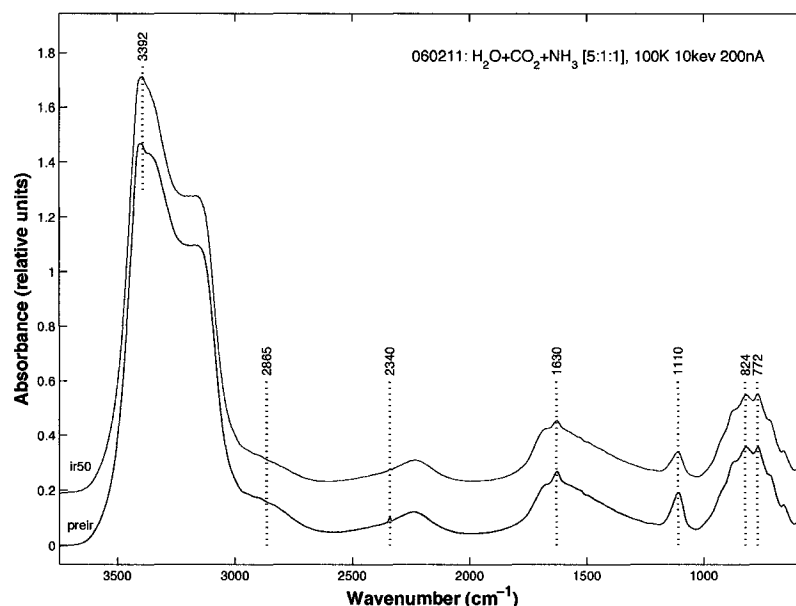


Figure 10.1: Pre- and post-irradiation spectra for a H₂O+CO₂+NH₃ [5:1:1] film irradiated at 100 K with 10 keV electrons at 200 nA. The pre-irradiation spectrum is shown in blue and the post-irradiation spectrum is shown in red. The small peak at 2340 cm⁻¹ indicates that little CO₂ was retained in the initial film. This was likely a limiting factor for radiolytic chemistry. The ammonia peaks at 1630 cm⁻¹ and 1110 cm⁻¹ decrease with dose, consistent with loss of nitrogen and hydrogen to the vacuum chamber.

be seen by the decrease in the 2340 cm⁻¹ CO₂ band and the decrease in the 1630 cm⁻¹ and 1110 cm⁻¹ ammonia bands. No new products were seen to form in the film.

Subsequent experiments replaced CO₂ with propane or propene in the initial film mixture. At 100 K problems involving retention of propane in the initial film were observed. Deposition temperatures were decreased to 70 K and the resulting films showed strong hydrocarbon peaks (~2960 cm⁻¹, 1450 cm⁻¹, and 1370 cm⁻¹) as well as the associated ammonia peaks (~1630 cm⁻¹, ~1110 cm⁻¹). The 1630 cm⁻¹ band is attributed to the ν_4 N-H deformation of NH₃ and the 1110 cm⁻¹ band is from the ν_2 NH₃ umbrella vibration (Brucato et al., 2006; Moore et al., 2007). The bottom, black spectrum of Figure 10.2 shows the initial film and the peaks of the ammonia,

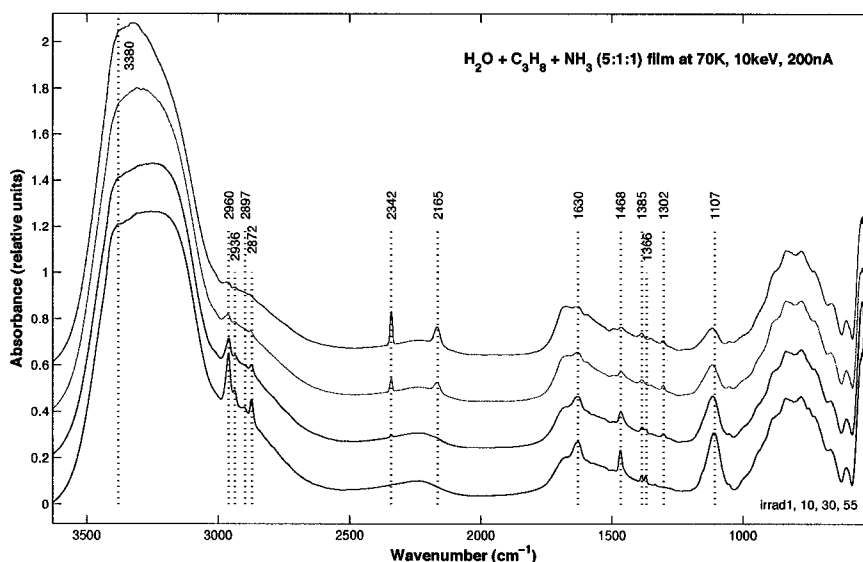


Figure 10.2: Irradiation sequence of a H₂O+NH₃+C₃H₈ [5:1:1] ice mixture with 10 keV electrons at 70K. The lower-most spectrum is prior to irradiation and each subsequent spectrum up is from a point later in time during the irradiation sequence.

propane, and water mixture. Comparison with the initial spectra for H₂O + propane experiments shows many overlapping bands.

As with hydrocarbon irradiation (Chapter 9) loss of bands in the -CH₃ dominated C-H region at ~ 2900 cm⁻¹ was observed as was production of CO₂ (2340 cm⁻¹) and methane (1302 cm⁻¹). In the ~ 2900 cm⁻¹ region, the post-irradiation spectrum of H₂O+C₃H₈+NH₃ (Figure 10.2) is hard to distinguish from that of H₂O+C₃H₈ (Figure 9.3). The strongest bands in both spectra emerge at 2964, 2934, and 2872 cm⁻¹. The 3380 cm⁻¹ NH₃ band is weak and largely obscured by the broad water feature. The 3181 cm⁻¹ ν_2 symmetric stretch of NH₂, and the N-H stretches of NH₄⁺ at 3206 and 3074 cm⁻¹, would also be weak compared to the water line (Brucato et al., 2006).

The strong ammonia bands at 1630 cm⁻¹ and 1110 cm⁻¹ decreased but did not vanish during irradiation. The only new product undoubtedly observed, other than CO₂ and CH₄, was that of the OCN⁻ ion at 2165 cm⁻¹ (Hudson et al., 2001). A strong case for synthesis of formamide (HCONH₂) can be made by the observation

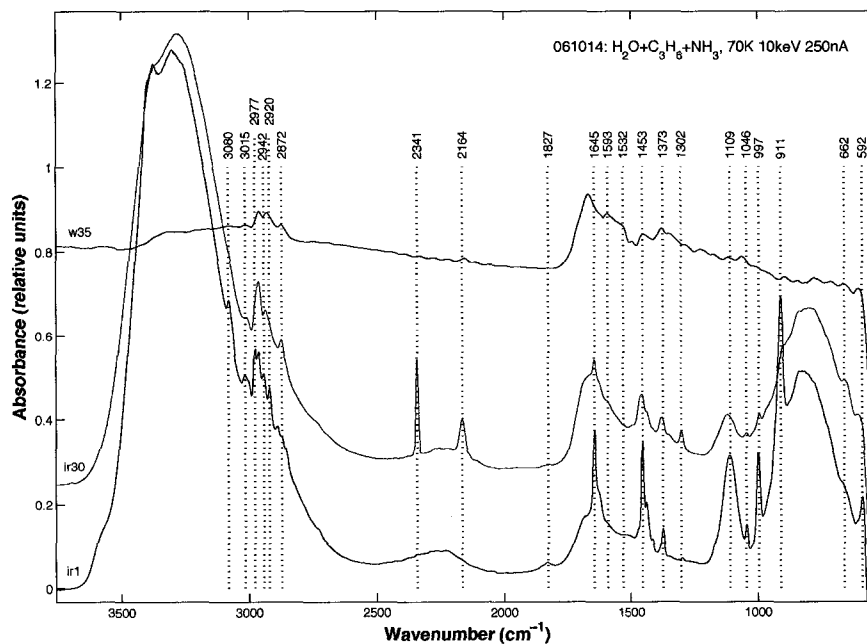


Figure 10.3: Irradiation sequence of a H₂O+NH₃+C₃H₈ [2:1:1] ice mixture with 10 keV electrons at 70 K. The lower-most spectrum is prior to irradiation and each subsequent spectrum up is from a point later in time during the irradiation sequence.

of the bands near 2881 cm⁻¹ (ν_3 CH stretch), 1708 cm⁻¹ (ν_4 CO stretch), 1631 cm⁻¹ (ν_5 NH₂ scissoring), 1388 cm⁻¹ (ν_6 CH scissoring), and 1328 cm⁻¹ (ν_7 CN stretch). These are bands for formamide at 20 K as reported by Brucato et al. (2006).

The NH₃ ν_2 band at 1107 cm⁻¹ persists throughout the irradiation sequence, indicating retention and stability of the ammonia. No signature of the ammonium ion (NH₄⁺) was observed at 1506 cm⁻¹ (Moore et al., 2007). Had the formation of ammonia hydrates occurred (*e.g.* the monohydrate NH₃·H₂O or hemihydrate 2NH₃·H₂O) a shift toward slightly longer wavelengths (1102 cm⁻¹ and 1084 cm⁻¹ respectively) should have been observed (Moore et al., 2007). Instead, we observed a decrease in total band area with only a slight shift of the band peak toward shorter wavelengths. The destruction of this band, and its relationship to other bands in the spectrum, was examined in greater detail during irradiation of H₂O + C₃H₆ + NH₃ mixtures.

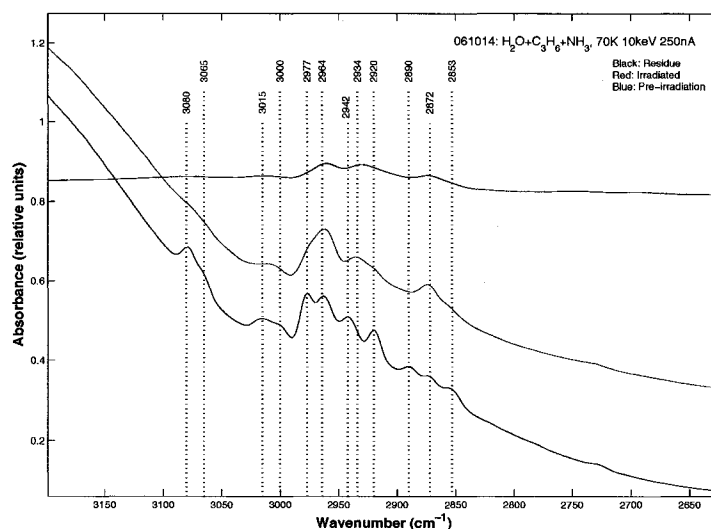


Figure 10.4: Detail of Figure 10.3 highlighting changes in the C-H and N-H rich region on the shoulder of the broad water band at $\sim 3300\text{ cm}^{-1}$.

The transition to hydrate phases likely occurred during warming as the film passed through the 130-150 K temperature range.

Switching from an alkane (propane) to an alkene (propene) in the water and ammonia mixture was of interest for several reasons. Foremost, we were interested in any differences between the products of the alkane versus alkene films. Second, while destruction of the C=C bond was rapid in the H₂O + hydrocarbon films, the carbonyl bond was seen as a new and stable product. Would the C=N also result as a new and stable product during irradiation? Results from the alkane film indicate no, but by starting with an alkene we were able to further investigate this question. Our spectra indicate that the C=N is not a product of either alkane or alkene irradiation in combination with ammonia and water. Aside from single bonds, the only bonds observed to be stable throughout irradiation were the C=O and the C≡N bonds.

The irradiation sequence for H₂O + C₃H₆ + NH₃ is shown in Figure 10.3. The initial spectrum (in blue), shows many of the same bands observed in the initial H₂O + C₃H₆ spectrum of Figure 9.5. In this experiment the ratio of water to ammonia and propene was reduced to two (*i.e.* [2:1:1]) with the hope of enhancing reactions

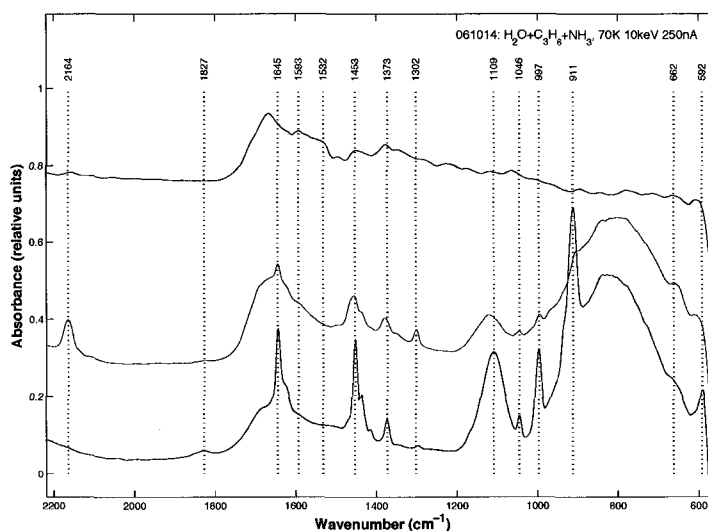


Figure 10.5: Detail of Figure 10.3 showing modification of ammonia and hydrocarbon bands in the 600-2200 cm^{-1} region. Production of methane (1302 cm^{-1}) and the OCN^- ion (2164 cm^{-1}) was readily observed. Destruction of C=C and NH_3 was also seen. New products include formamide and isonitriles. No C=N containing compounds were seen in the ice.

between carbon and nitrogen.

During irradiation of the film (shown in red) production of CO_2 and the OCN^- ion was observed. The double bonds of the alkene were destroyed, as evidenced by the loss of peaks at 1645, 1433, and 911 cm^{-1} . With the [2:1:1] composition, the ν_1 and ν_3 band of NH_3 at 3380 cm^{-1} (Moore et al., 2007) was initially observed, but during irradiation this distinct peak was reduced to a subtle shoulder on the edge of the broad $\sim 3300 \text{ cm}^{-1}$ band.

After irradiation, a very weak band could be seen in the ammonia-rich spectrum at $\sim 3080 \text{ cm}^{-1}$, a band attributed to the N-H stretch of NH_4^+ or to HCN (Brucato et al., 2006). Figure 10.4 shows this region in detail. Aside from the two weak features at 3380 cm^{-1} and 3080 cm^{-1} , it would be very hard to infer the presence of any ammonia or nitrogen chemistry in the irradiated film if the spectrometer was not capable of collecting data at longer wavelengths. For this reason, remote sensing techniques must utilize longer wavelengths if we are to understand nitrogen chemistry

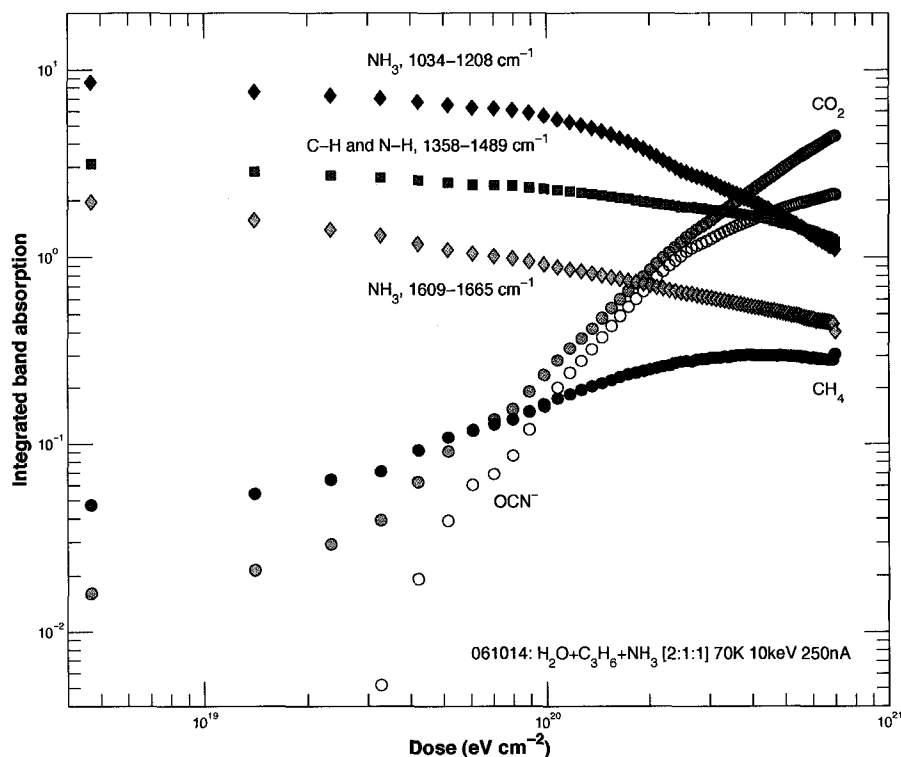


Figure 10.6: Integrated band absorption versus dose for an irradiated H₂O + NH₃ + C₃H₆ ice mixture at 70 K. The production of the OCN⁻ ion requires carbon and nitrogen made available through the destruction of the hydrocarbons and ammonia within the film. Only methane was seen to reach steady-state.

on icy satellites.

In the region from 600-2200 cm⁻¹ (Figure 10.5) the production of OCN⁻ and CH₄, along with the destruction of C=C was observed. The carbonyl band was observed at ~1710 on the edge of the 1650 cm⁻¹ water feature. No other new bands were observed. In particular, no band was observed at 2254 cm⁻¹. This band would have been a strong indicator of C=N bonds, as seen in HNCO (Lowenthal et al., 2002). A weak peak at 1325 cm⁻¹, seen between the methane band and the 1373 cm⁻¹ C(CH₃) band, could have been a contribution from C=N, but without the 2254 cm⁻¹ band, the evidence is weak. We conclude that no C=N bonds are present.

The behavior of several key bands and regions of interest was monitored as a function of irradiation dose. Results for the integrated band absorption are shown in Figure 10.6. The strong N-H bands from 1609-1665 cm⁻¹ and 1034-1208 cm⁻¹ were seen to decrease by a factor of ~ 8 over the course of the total dose of $\sim 8 \times 10^{20}$ eV cm⁻². The former band decreased slightly less than the latter and this was likely due to the added C-H and C=O contribution to that region. In neither case was steady-state reached. Indeed, while the slope of the 1609-1665 cm⁻¹ band remained constant with dose, the 1034-1208 cm⁻¹ band showed a change to a steeper destruction rate at a dose of roughly 10^{20} eV cm⁻². The reason for this change in slope was not apparent from the integrated band data. The OCN⁻ ion appears at a dose of $\sim 3 \times 10^{19}$ eV cm⁻² and rises steeply with CO₂. The reaction to form OCN⁻ may be limited by the availability of carbon until this point, after which it becomes an efficient pathway for consuming nitrogen. This would explain the increased NH₃ destruction along with the appearance of OCN⁻ only after significant growth in the CO₂ and CH₄ bands was seen. Pathways for OCN⁻ production are discussed in greater detail later in this chapter.

The residual gas analyzer was used to investigate volatile compounds released from the irradiated films during warming to 300 K. Figure 10.7 shows the mass spectrum integrated over the warming period for a H₂O+NH₃+C₃H₆ ice film. Warming proceeded from 70 K to 300 K at 1 K per minute. A background spectrum, collected prior to irradiation, was subtracted from the spectrum taken during warming.

The cluster of peaks around m/z of 18 is from water and associated ions. At $m/z = 27$ lies a strong peak from HCN. Part of this peak was likely due to CO and N₂ but the lack of a strong peak at $m/z = 28$ supports the case for HCN.

Unlike the hydrocarbon RGA results, here we saw only a very weak peak at $m/z = 44$ and instead strong peaks at $m/z = 41$ and 39 dominated. These peaks were likely due to the OCN⁻ ion and to synthesized nitriles such as isocyanomethane (C-N \equiv C) and acetonitrile (C-C \equiv N). The peak at 39 is a related ion, HCNC.

At larger m/z , a cluster of peaks around $m/z = 56$ was seen. Much of this was likely due to the nitrile of propane (isocyanopropane, C-C-C \equiv N). Hydrocarbons without nitrogen, such as propenal may have also contributed to this peak. The

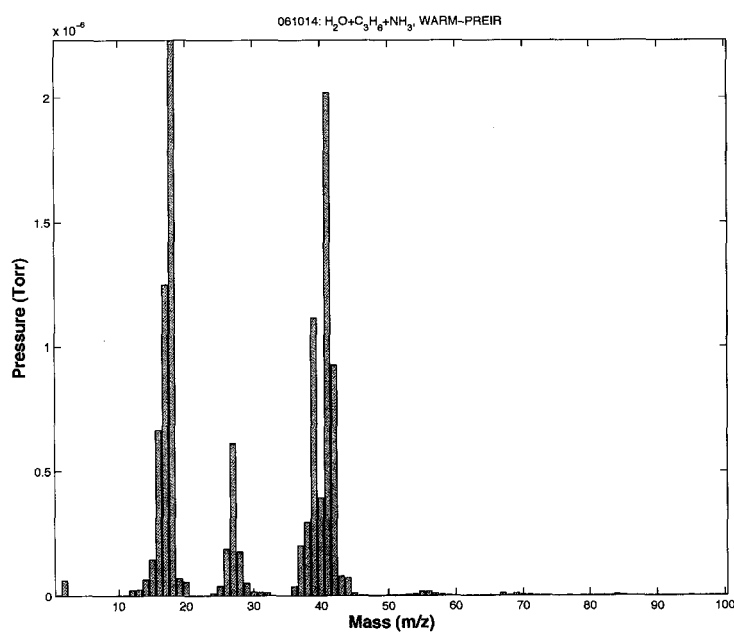


Figure 10.7: RGA results integrated over the warming period from 70-300 K after irradiation of a H₂O+NH₃+C₃H₆ ice film.

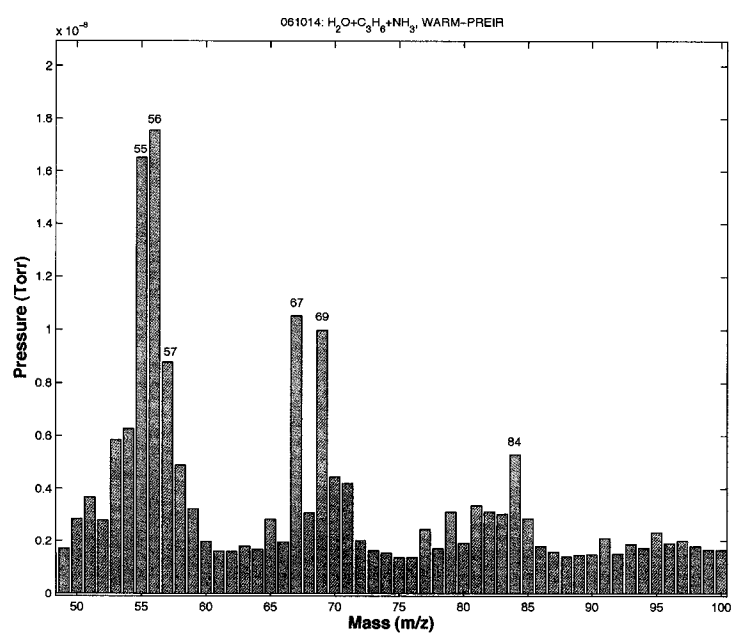


Figure 10.8: Same as spectrum in Figure 10.7, but with detail on the m/z region of 50-100.

infrared signature of this alkene could have been within the band at $\sim 1645\text{ cm}^{-1}$; completely ruling out alkenes that survived irradiation was complicated by the C=C band overlap with the N-H vibrations.

For the heaviest ions, those at $m/z = 67, 69,$ and 84 (Figure 10.8), several complex nitriles serve as candidates. For the peak at 84 , formamide with a cyanomethyl-group is consistent with both the RGA and FTIR data. Similarly, 2-cyanoacetamide contains similar bonds (though it hosts an NH₂ group, unlike cyanomethylformamide) and yields an m/z of 84 . Loss of an NH, NH₂, or NH₃ would then yield the peaks at 67 and 69 .

Bernstein et al. (1995) reported synthesis of hexamethylenetetramine (HMT, or C₆H₁₂N₄) resulting from their GCMS analysis of residues resulting from UV-photolysis of H₂O + CH₃OH + CO + NH₃ ice. Our infrared results and our RGA data could support the conclusion that HMT is synthesized in our electron irradiated films, but the data is not conclusive. The HMT standard presented by Bernstein et al. (1995) shows peaks at $m/z = 42, 69, 71, 85, 112,$ and 140 . Our data only go up to m/z of 100 , but the peaks we observe at $42, 69,$ and 84 are consistent with HMT. The results of Bernstein et al. (1995) are from the entire residue eluted through the GCMS, whereas our RGA results only detect the volatile fragments escaping the gold substrate during warming. It is possible that HMT was synthesized in the residue and that we detected HMT fragments cracking from the warming film. To date, however, the only mass spectral data we have for the NH₃ films is the volatile fraction from the RGA. Future GCMS work with our residues will hopefully clarify the nature of these larger products.

10.2 Residue analysis

The residues remaining on the gold substrate were analyzed with the FTIR at 300 K while still inside the vacuum chamber. The pressure inside the chamber was $\sim 10^{-7}$ torr in all cases. Figure 10.9 shows three spectra of three different residues. The uppermost spectrum is from the irradiated H₂O+C₃H₆+NH₃ film and the lower two spectra are from irradiated H₂O+C₃H₈+NH₃ films. For the film with propene, an

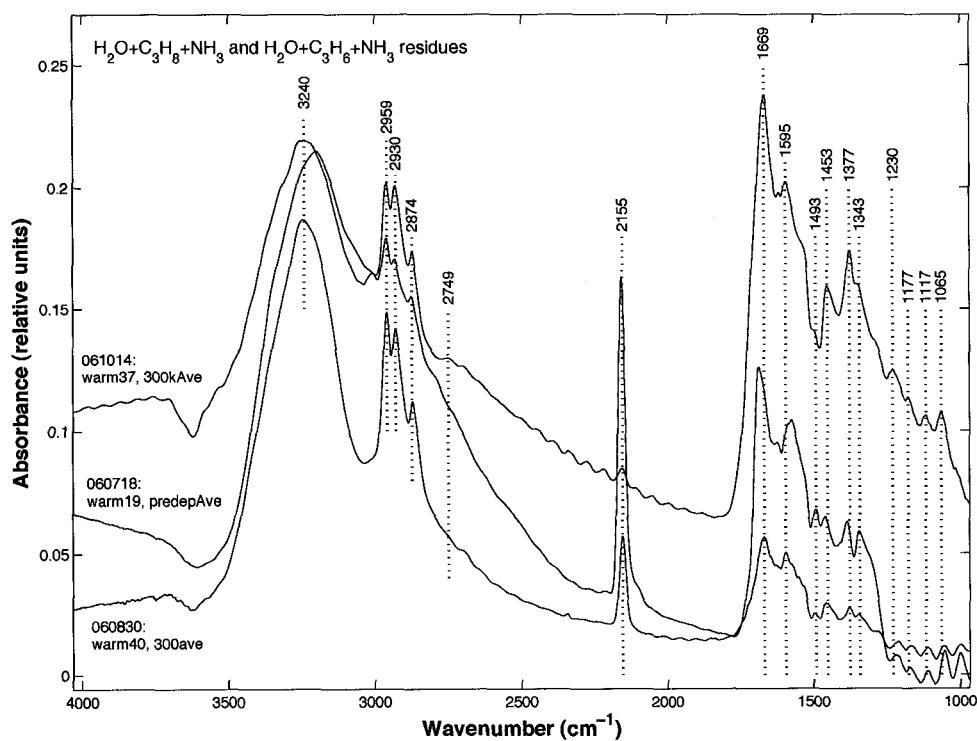


Figure 10.9: Infrared spectrum of the H₂O+NH₃+C₃H₈ ice residue after much of the water has been lost during warming. This spectrum is at T \approx 250K and while much of the water is gone, some hydrated features still complicate the spectrum in the 3300 cm⁻¹ and 1500 cm⁻¹ regions. Nevertheless, strong C-H, C \equiv N, and NH₂ features are seen at 2900, 2155, and the 1400-1700 cm⁻¹ regions.

averaged spectrum taken at 300 K prior to the beginning of the experiment was used for calculating absorbance. This was also true for the lowermost spectrum involving a propane-rich ice. For the center spectrum an average spectrum taken at 80 K prior to deposition was used for calculating absorbance. This was necessary because spectra at 300 K were not captured before cooling of the cryostat. Nevertheless, all three spectra show strong bands in many of the same positions.

The broad band centered at 3240 cm⁻¹ is primarily the O-H stretch but given the long-ward shift in wavelength relative to the hydrocarbon residues, significant N-H stretch may be hidden within this region. The three bands at 2959, 2930, and 2874 cm⁻¹ are the -CH₃, -CH₂, and -CH₃ vibrational modes as observed in the hydrocarbon residues of Chapter 9. The strong and narrow band at 2155 is due to the C≡N stretch (Khare et al., 1994), a likely byproduct of the OCN⁻ ion reacting with hydrocarbons and possibly forming an HCN polymer during warming. Bernstein et al. (1997) examined nitriles in order to better understand this band in astrochemical environments. Given the position of the band we observed, and the assignments provided by those workers, we conclude that the C≡N stretch in our residues is likely due to *n*-butylisocyanide (CH₂(CH₂)₃NC) or a related isonitrile. Though *n*-butylisocyanide is not volatile at standard temperature and pressure, synthesis of this compound is consistent with the *m/z* fragments detected during warming with the RGA. Specifically the peak at *m/z* = 69 corresponds to loss of a methyl group from *n*-butylisocyanide, and the peaks at *m/z* = 55 and 41 correspond to the loss of a second and third methyl group.

At 1669 cm⁻¹ is a band that Khare et al. (1994) attributed to C=N stretching or NH₂ bending, but which Bernstein et al. (1995) attributed to a C=O related amide. We do not see the 1710 cm⁻¹ band typical of the carbonyl bond observed in our hydrocarbon residues. Given the relatively broad nature of the peak, we attribute the 1669 cm⁻¹ band to contributions from the C=O, C=N, and NH₂. This C=N bond must have formed during warming as FTIR evidence for this band was absent. The 1595 cm⁻¹ band is consistent with NH₂ scissoring (Khare et al., 1994; Bernstein et al., 1995).

Interestingly, Khare et al. (1994) attributes the 1493 cm⁻¹ band, seen with a

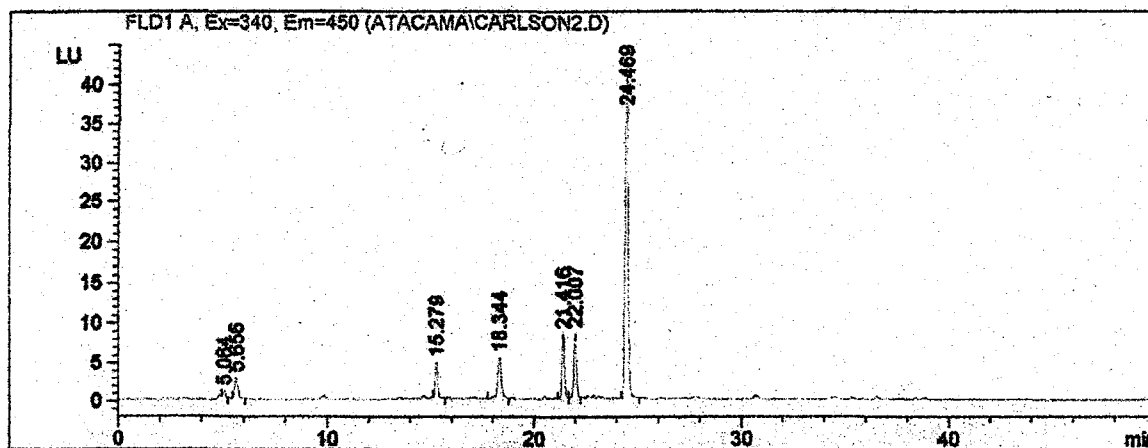


Figure 10.10: HPLC analysis of the H₂O+NH₃+C₃H₈ residue. The double peaks of D- and L-alanine can be seen at 21 and 22 minutes, respectively. Such a racemic mixture is a good indication that contamination was not the source of the alanine.

weak but definite signature in our spectra, to the benzene ring. We are reluctant to conclude the presence of aromatics given the lack of the associated longer wavelength bands. The region $<1000\text{ cm}^{-1}$ is not shown in these spectra because no strong bands were seen and the signal to noise of the spectra was bad.

Most of the remaining strong bands can be attributed to C-H, C-C, and C-O related bands (*e.g.* 1453, 1377, 1343, 1177, 1065, cm^{-1}). Overlap with N-H bend and NH₂ rocking may occur in the bands at 1343 cm^{-1} and 1177 cm^{-1} , respectively. Similarly, the broad region from 900-1150 cm^{-1} , and containing the peak marked here at 1117 cm^{-1} , may be due in part to C-N stretch as well as the C-O vibrations seen in the hydrocarbon residues. Bernstein et al. (1995) note that the $\sim 1230\text{ cm}^{-1}$ band is either C-N stretch or C-O stretch. Taken together, the above combination of bands leads to a nitrile-rich residue with possible HCN-polymers.

After removal of the H₂O+NH₃+C₃H₈ residue from the vacuum chamber the sample was analyzed for amino acids via high-performance liquid chromatography (HPLC). This work was done in the laboratory of Dr. Alexandre Tsapin at the Jet Propulsion Laboratory. The procedure for hydrolysis, labeling, and elution through the column was similar to that of Bernstein et al. (2002). Results are shown in Figure 10.10 and allow for a tentative identification of racemic alanine production. The peaks

at 5 minutes are due to dextro-rotary (D-) and laevo-rotary (L-) aspartic acid. The peaks at 15 and 18 minutes may be serine and glycine respectively.

At 21 and 22 minutes we saw the double peaks of D- and L-alanine respectively. The matching heights makes a strong case for racemic, non-biological production. If handling of the gold mirror post-irradiation resulted in contamination, we would have seen only the L-alanine since this is the chiral form employed in biology. It is possible that contamination of the mirror occurred prior to attaching it to the cryostat and introducing the mirror into the chamber. Radiolysis may have then created a racemic mixture from biologically derived alanine. But we took caution to be sure that all mirrors were introduced into the chamber in a pristine state. Were we not careful and clean during this process, results for all experiments would have been affected. In this particular case, (*i.e.* the mirror on which the residue in Figure 10.10 formed), the mirror had been in the chamber for several previous films and had thus experienced considerable exposure to irradiation, vacuum, and cryogenic temperatures. In other words, had contamination occurred prior to introducing the mirror, the material would have likely 'burned' away during irradiation and warming, or we would have seen the products in our FTIR or RGA data.

Despite confidence in the cleanliness of our techniques, the singular peak at 15 minutes poses some questions. If this peak was indeed serine resulting from radiolysis, then we should also have seen a double peak here, since this too is a chiral amino acid. While the racemic alanine and aspartic acid make a case for *in-situ* radiolytic production, the possible serine peak calls into question that conclusion.

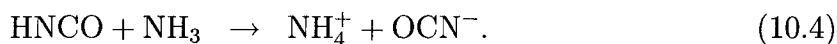
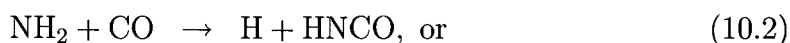
Subsequent experiments have attempted to replicate these results, but to date we have not been convincingly successful. At present we are working to reproduce these results and further refine our HPLC protocol so as to better constraint the possible amino acid component of our radiolysis experiments. A confirmation of amino acid production under Europa-like conditions would be important for advancing both our understanding of prebiotic chemistry in general, and for understanding the chemical environment and possible origin of life on Europa. While Bernstein et al. (2002) and others have shown amino acid production under similar conditions, the initial composition of our films (water + propane or propene + ammonia) is less complex;

they started with methanol and HCN as well as H₂O and NH₃. Other workers, specifically Ponnampertuma et al. (1963), produced the nucleic acid base adenine with pulsed, 4.5 MeV electrons in a simple mixture of H₂O + CH₄ + NH₃. That work, however was in gas phase and at temperatures and pressures specific to early Earth. The work presented here is potentially the first production of amino acids using energetic electrons in simple ice mixtures at 70-100 K; conditions specifically relevant to the surface of Europa.

10.3 Conclusion

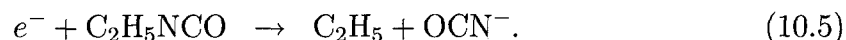
The most interesting *in-situ* feature of the irradiated H₂O+ hydrocarbon + ammonia ice films is the cyanate ion, OCN⁻ at 2165 cm⁻¹. Considerable debate persisted in the literature regarding the nature of this feature, originally denoted as the ‘XCN’ band (Bernstein et al., 1997; Strazzulla and Palumbo, 1998), but the work of Hudson et al. (2001) made a convincing advance toward the OCN⁻ assignment.

Hudson et al. (2001) proposed an OCN⁻ formation pathway that utilizes CO as a precursor,



We do not observe CO accumulation in our films, nor do we see the strong peak at 2254 cm⁻¹ that would be characteristic of the ν_2 (C=N asym. stretch) of isocyanic acid, HNCO (Lowenthal et al., 2002). This is consistent with the above pathway in that CO and HNCO are consumed. The production of the ammonium ion NH₄⁺ should have been observed, but it is difficult to confirm with the FTIR spectra. The N-H stretches of NH₄⁺ at 3206 and 3074 cm⁻¹ are clouded by the water band and the N-H symmetric bending at 1478 cm⁻¹ is obscured by the -CH₂- scissoring at 1453 cm⁻¹.

Alternatively, as discussed by Hudson et al. (2001), OCN⁻ is easily produced upon irradiation of ethyl isocyanate via,



Those workers found similar results during photolysis of formamide and related compounds. In our film, we observed the initial water, hydrocarbon and ammonia evolving to products like formamide, thus making the above pathway plausible for the observed OCN⁻ feature.

The behavior of the band strengths with dose, as shown in Figure 10.6, indicates OCN⁻ emerging only after significant production of CO₂ and CH₄. Again, this is consistent with the above pathways because CO₂ serves as a precursor for CO. The formyl radical, HCO, as discussed in Chapter 9 may also serve as a precursor for HNCO in the above pathway.

The production of formamide and nitriles is well supported by the combination of observed FTIR bands and mass spectral data. These compounds are of particular interest for prebiotic chemistry. The capacity for hydrolysis of HCN-oligimers to form amino acids and nucleic acid bases has been an area of much experimentation since the work of Oró (1960). Concentration and stability of HCN, however, proved to be a critical limiting factor when moving from the controlled laboratory settings to the natural environment. In dilute aqueous solutions hydrolysis of HCN leads first to formamide and then to formic acid. Only at high concentrations will HCN lead to the synthesis of nucleobases and amino acids. Formamide is also directly useful for synthesis of prebiotic compounds (Ochiai et al., 1968; Philipp and Seliger, 1977), and it has the added benefit of being a good solvent in which to synthesize nucleosides, peptides, and even adenosine-triphosphate (ATP) (Benner et al., 2004). In water these compounds would hydrolyze to ammonia and acids, but in formamide they are stable.

Miyakawa et al. (2002) explored the possibility of ice and eutectic freezing as a means for concentrating HCN and formamide to promote synthesis of prebiotic compounds. They found that such processes could have provided important niches for

polymerization. Miller had the great foresight to prepare, and then freeze (at -20 °C and -78 °C), solutions of ammonium cyanide in 1972. The analysis, performed 25 years later (Levy et al., 2000), revealed production of adenine, guanine, and several amino acids, including glycine and alanine. These results, when combined with our radiolytic synthesis of formamide and nitriles from water, ammonia, and short-chain hydrocarbons, support the conclusion that the surface and ice shell of Europa may have played a significant role in providing the sub-surface ocean with the building blocks for life. Radiolytic products, produced on the surface but then buried in the ice shell, may have been concentrated in seismic cracks or fractures where synthesis of peptides and other large molecules could have taken place before mixing into the vast body of liquid water below. It is interesting to note that formamide as a solution has a density of 1.13 g cm⁻³ and therefore may be buoyant relative to a salty ocean. Depending on mechanisms for the delivery of compounds from the surface, the ice-water interface on Europa could have been, and may still be, a very interesting environment for prebiotic chemistry.

Chapter 11

Biomarkers of the european near-surface environment

If life exists within the Europa's sub-surface ocean and is brought to the surface through cryovolcanism or other geological mechanisms, then a structural, molecular, and/or chemical biomarker could potentially be detectable from an orbiting or landed spacecraft on Europa.

Here we describe laboratory investigation of a relatively simple analog for biomarker investigation on Europa. Viable spores of *Bacillus pumilus* were introduced into the vacuum chamber and irradiated with high-energy electrons under conditions comparable to the surface of Europa. The resulting products indicate what known, terrestrial microbes might look like were they to be exposed to the european surface. As is shown, both infrared spectroscopic and mass spectroscopic techniques provide useful, but certainly not conclusive data for life detection, especially when compared to the complex abiotic organic chemistry observed in the previous experiments.

These results are also interesting in the context of contamination. While much of our work is motivated by the prospect of discovering signs of indigenous life on Europa, any future spacecraft will be plagued with the potential for sending back a false-positive. In other words, the spacecraft may detect life from Earth that inadvertently hitched a ride on the spacecraft. Our results provide a metric against which to test terrestrial contamination at Europa.

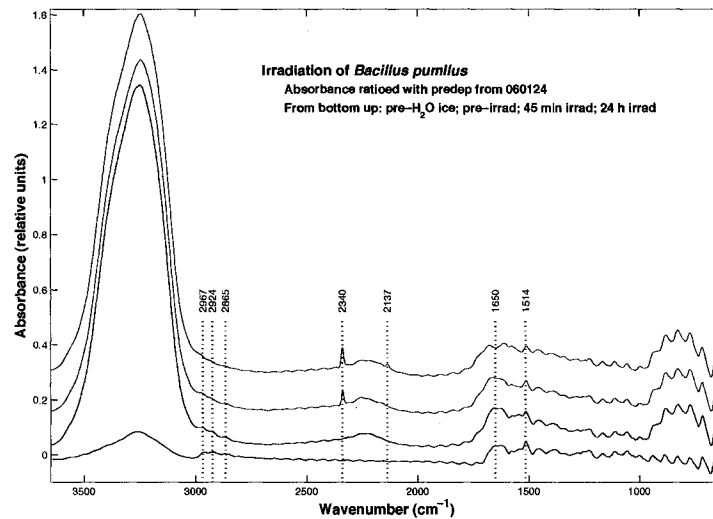


Figure 11.1: Irradiation sequence of *Bacillus pumilus* spores in ice at 100 K. Electrons of 20 keV at 500 nA were used to penetrate the sample completely.

Building on the results from these initial experiments we suggest some additional laboratory work and instrumentation possibilities for biosignature detection both from an orbiting spacecraft and from a lander. We have constructed a new vacuum chamber specifically designed to better address these biosignature questions. This chamber allows us to irradiate many independent targets without opening and closing the chamber. This provides for much better experimental controls. Results from this new chamber are forthcoming.

11.1 Irradiation of *Bacillus pumilus* spores

Spores of *Bacillus pumilus*, a bacterial species commonly found in soils and plants, were selected for use in these initial experiments because of their relevance to spacecraft sterility and planetary protection. La Duc et al. (2003) studied the Mars *Odyssey* spacecraft and found *Bacillus pumilus* to be one of the most abundant viable organisms on the spacecraft after cleaning the spacecraft with H_2O_2 , exposure to intense UV, and baking of the craft to high temperatures. From the standpoint of selecting

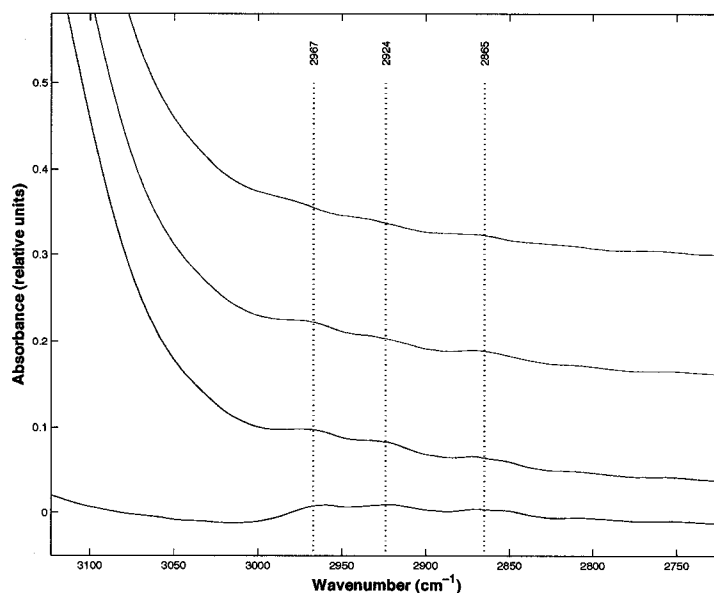


Figure 11.2: Detail of the spectra presented in Figure 11.1, highlighting the region of strong C-H vibrational modes. Irradiation of the bacterial spores results in diminished C-H band strength. No spectral lines in this region of the spectral sequence could be distinguished as being of biological origin when compared with the abiotic results from Chapters 9 and 10.

an organism that may share qualities with indigenous european organisms, the salt-loving *Halophiles* would perhaps have been a more suitable choice and we intend to irradiate those microbes in subsequent studies. The fact that *Bacillus pumilus* can tolerate H_2O_2 cleaning and UV-irradiation lead us to believe that this organism may be one of the better candidates for retaining a chemical of molecular biosignature detectable post-electron irradiation with our FTIR, RGA, or MALDI. Ongoing work by La Duc et al. (2003) and Dickinson et al. (2004) also helps provide a standard against which we can compare our results.

Figure 11.1 shows a sequence of FTIR spectra following the modification of *Bacillus pumilus* spores irradiated with 20 keV electrons at 500 nA. The spores could not be vapor deposited as with previous experiments. Instead, we had to swab a uniform residue onto the gold mirror substrate prior to closing and pumping out the vacuum

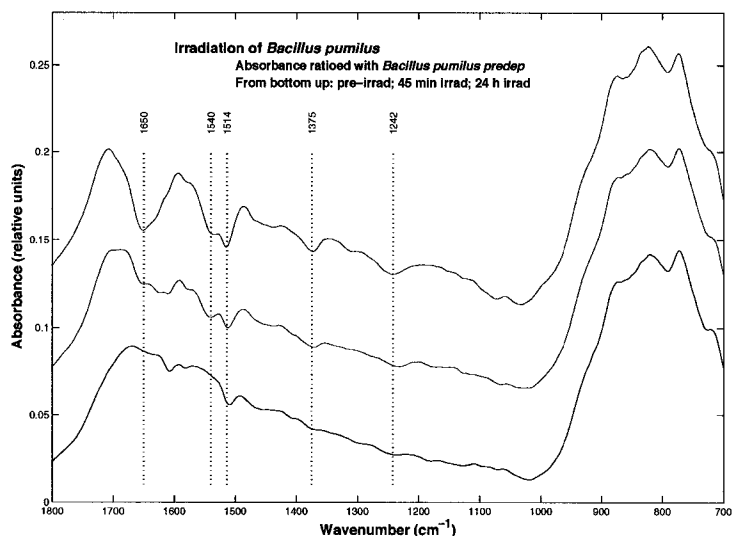


Figure 11.3: Destruction of amide bonds during irradiation is shown by the decrease in absorption of bands in the $1200\text{--}1700\text{ cm}^{-1}$ region. The three spectra shown here are the same as the upper three spectra in Figure 11.1, but a pre-depositional spectrum with the bacterial residue in place was used for calculating absorbance. For this reason, the irradiated spectra show loss and destruction of bands, *e.g.* the amide I and II bands at 1650 , 1540 , and 1514 cm^{-1} . The uppermost spectrum, taken after 24 hours of irradiation, shows a large decrease in all of these bands.

chamber. Having done this, we then cooled the chamber to 100 K and deposited a thin film ($\sim 2\text{ }\mu\text{m}$) of water ice on top of the spore residue.

The procedure of having to swab the spores directly onto the mirror made it impossible for us to collect reference spectra prior to deposition. Whenever the chamber is opened and the gold mirror replaced, realignment must be done with the FTIR. Slight differences in alignment lead to canceling errors when using spectra from different runs as background spectra for other runs. With no other option for this experiment, we used an averaged pre-depositional spectra from an earlier experiment to serve as our denominator file when calculating absorbance. For this reason, the spectra in Figures 11.1, 11.2, and 11.3 show signs of imperfect cancelation, *e.g.* in the region $<1200\text{ cm}^{-1}$ where spurious oscillations can be seen.

Nevertheless, four large changes are easily observed. First, the strength of the

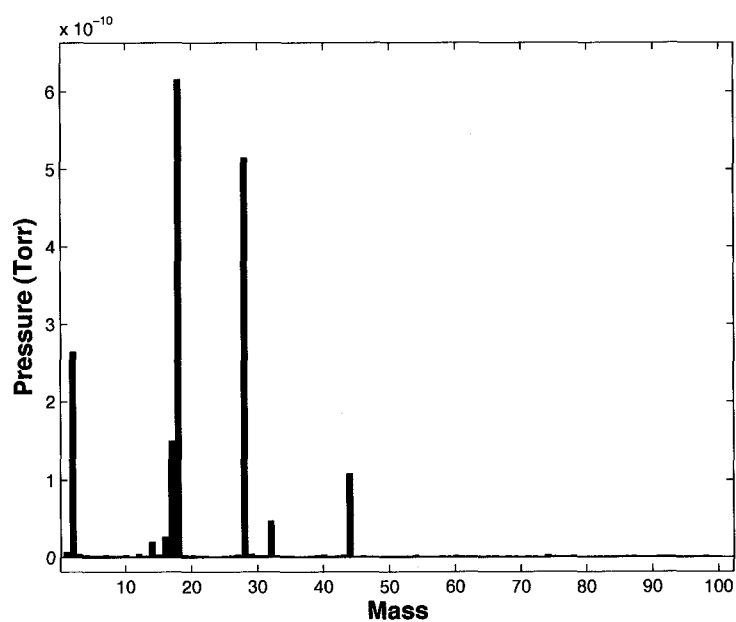


Figure 11.4: RGA mass spectrum taken during the irradiation process. Nothing of unique biological significance was released from the film. The major peaks correspond to hydrogen, water, CO and N_2 , O_2 , and CO_2 . Alkanes and alcohols may be present at $m/z = 32$ and 44 , *e.g.* CH_3OH and C_3H_8 .

C-H bands in the region of 2900 cm^{-1} decrease as the sample is irradiated. Figure 11.2 highlights this region. The bottom, black spectrum shows the initial *Bacillus pumilus* film and the blue spectrum shows the *Bacillus pumilus* film covered with a thin water ice film (made obvious by the broad peaks at $\sim 3300\text{ cm}^{-1}$ and $\sim 800\text{ cm}^{-1}$). The lower red spectrum shows the film after 45 minutes of irradiation and the upper spectrum shows a full day of irradiation. After 24 hours, or a dose of $\sim 5 \times 10^{21}\text{ eV cm}^2$, the C-H bands are barely resolvable from the large background water band.

The 2340 cm^{-1} and 2140 cm^{-1} bands for CO_2 and CO, respectively, increased as a function of dose. This is not surprising given the loss of C-H bonds, but the distinct signature of CO is interesting in light of the absence of this band during the $\text{H}_2\text{O} + \text{hydrocarbon}$ and $\text{H}_2\text{O} + \text{hydrocarbon} + \text{NH}_3$ irradiation experiments. The implication here, based on the chemical pathways discussed in Chapters 9 and 10, is that CO is not being rapidly consumed during synthesis of aliphatics and nitriles. Indeed, in this experiment, the chemical structures of biomolecules likely saturate the production of new aliphatics and nitriles, leading to destruction and net accumulation of CO in the film.

In the $1000\text{-}1750\text{ cm}^{-1}$ region (Figure 11.3) details are difficult to resolve, but a decrease in the strength of the bands at ~ 1650 and $\sim 1514\text{ cm}^{-1}$ was observed. Though the 1650 cm^{-1} band overlaps some of the same region attributed to the ν_4 , 1645 cm^{-1} band of NH_3 (Moore et al., 2007) in our ammonia experiments, the slightly shorter wavelength observed here is consistent with the N-H and carbonyl vibrational modes in the amide I of protein α -helical structures (Maquelin et al., 2002). The amide bond, and the associated vibrational excitations, specifically refers to the C-N linkage between amino acids and the interaction with the C=O and N-H on either side of that bond.

In the FTIR literature on microbes, the 1514 cm^{-1} band is sometimes denoted the ‘tyrosine’ band, as it is a hallmark of the presence of that amino acid in proteins (Naumann et al., 1996; Maquelin et al., 2002). The band sits next to, and in conjunction with, the amide II band at $1520\text{-}1550\text{ cm}^{-1}$ characteristic of the C-N stretch and C-N-H bend in the peptide structures of proteins. The observed decrease in band strength in our experiments indicates destruction and loss of proteins. The resulting

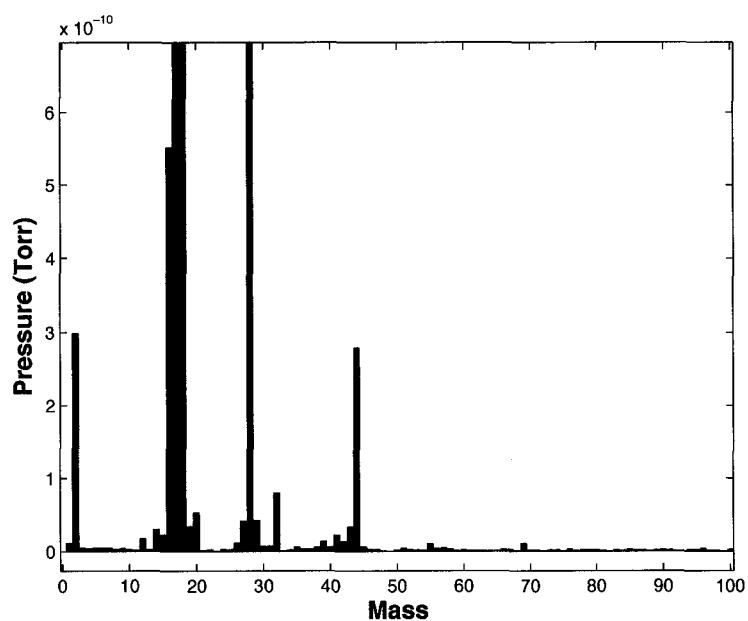


Figure 11.5: After irradiation, the *B. pumilus* sample was warmed at a rate of 1 K per minute. This RGA spectrum is from an ~ 8 minute integrated period during warming from ~ 120 K to ~ 130 K. While peaks at $m/z = 55$ and 69 now become detectable, the dominant peaks are still those associated with the gases listed in Figure 11.4. This pattern of peaks cannot be easily distinguished from the abiotic RGA results of Chapters 9 and 10.

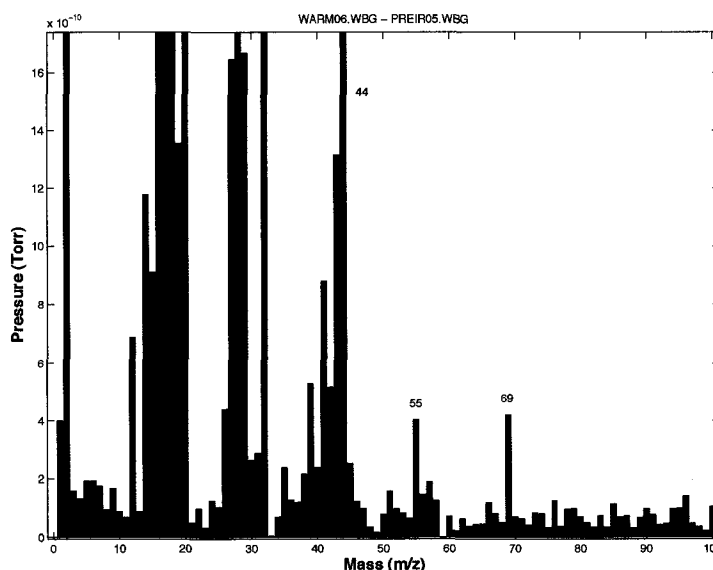


Figure 11.6: RGA mass spectrum of an irradiated ice film containing *Bacillus pumilus* spores. Here we have integrated the spectrum over the course of the entire warming period as the film is raised from 100 K to 300 K at 1 K per minute. Having integrated the detection for such a long period and by incorporating warmer temperatures, new peaks can be seen. Peaks at 55 a.m.u. and 69 a.m.u. are likely hydrocarbons and nitriles, not unlike those seen in Chapter 10.

nitrogen may be sequestered as ammonia in the ice film, but growth of the relevant bands at 1630 and 1110 cm^{-1} was not confirmed.

The RGA results collected during the irradiation process, as shown in Figure 11.4, indicate that much of the nitrogen was likely lost as N_2 . The peaks at $m/z = 28$ and $m/z = 14$ are strong indicators of this conclusion, though CO likely contributes in part to the strength of the $m/z = 28$ peak. Also seen in this spectrum is loss of CO_2 , O_2 , H_2O , and H. No mass fractions larger than $m/z = 44$ were seen. Nothing in this spectrum reveals a signature unique to the presence of biological material in the film.

As perhaps a more interesting analogy to the scenario of detecting a biosignature with a mass spectrometer on board an orbiting spacecraft (*e.g.* the *Cassini* INMS), in Figure 11.5 we show an RGA spectrum collected over an eight minute period during warming of the irradiated *Bacillus pumilus* film from ~ 120 -130 K. Using our

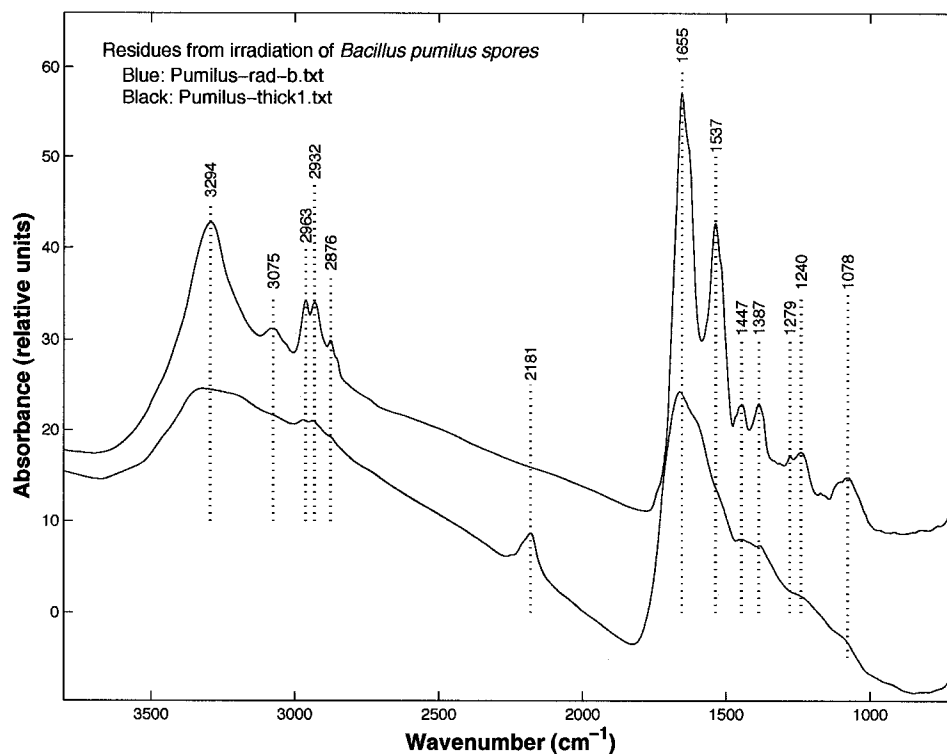


Figure 11.7: FTIR spectrum of *B. pumilus* residue after irradiation and removal from the vacuum chamber. The C-H bands show a similar match to the abiotic residues but the amide I, II, and A bands of proteins are shifted relative to comparable bands in abiotic residues. Such bands may serve as spectroscopic biosignatures on the irradiated surface of Europa. Also seen was a nitrile signature at 2181 cm^{-1} . This band has no well characterized spectral match in the microbial FTIR literature, and thus needs further study.

vacuum chamber environment, this is about as close as we can get to approximating the scenario of an instrument like the INMS flying through a plume, such as that observed on Enceladus (Spencer et al., 2006b; Waite et al., 2006).

In addition to the peaks of Figure 11.4, peaks at $m/z = 55$ and 69 were observed. Compared with the RGA results for the products of $H_2O + C_3H_6 + NH_3$ irradiation (Figure 10.7), it is clear that these peaks are not unique to biological material. In that analysis the same peaks were attributed to hydrocarbons and nitriles. These compounds were also likely produced, and subsequently released, in the case of irradiated *Bacillus pumilus*.

Potentially significant, however, is the isolated strength of both the $m/z = 55$ and 69 peaks. Unlike the abiotic experiments with water, hydrocarbons, and ammonia, here we see two very distinct peaks with neighboring peaks that are relatively weak by comparison. Results for the abiotic experiments showed small, but significant clusters around these peaks. The observed m/z pattern is not uniquely characteristic of biomolecules, but the distinct peaks are interesting. Some workers have argued that the pattern of distinct peaks versus broad distributions will serve as a mass spectral biosignature, distinguishing biological processes (distinct peaks) from abiotic process (broad distributions) (McKay, 2004). Certainly this may be a useful piece of the life-detection puzzle, but our results indicate that when radiolytic processes are involved, a great deal of caution is warranted. This issue is addressed in greater detail later in this chapter.

With the warming process complete, and the ice layer and water removed through sublimation, the chamber was then opened and the mirror containing the *Bacillus pumilus* spores removed. Laboratory FTIR and MALDI, at standard temperature and pressure, were then used to further analyze the residue remaining on the gold mirror.

The most striking result of the FTIR analysis was the similarity of the *Bacillus pumilus* residue spectra to those of the residues formed by irradiating water, hydrocarbons, and ammonia. The form and pattern of relative peak heights was largely the same. Figure 11.7 shows two spectra from two different regions of the irradiated portion of the *Bacillus pumilus* mirror. Many of the spectral features can be matched

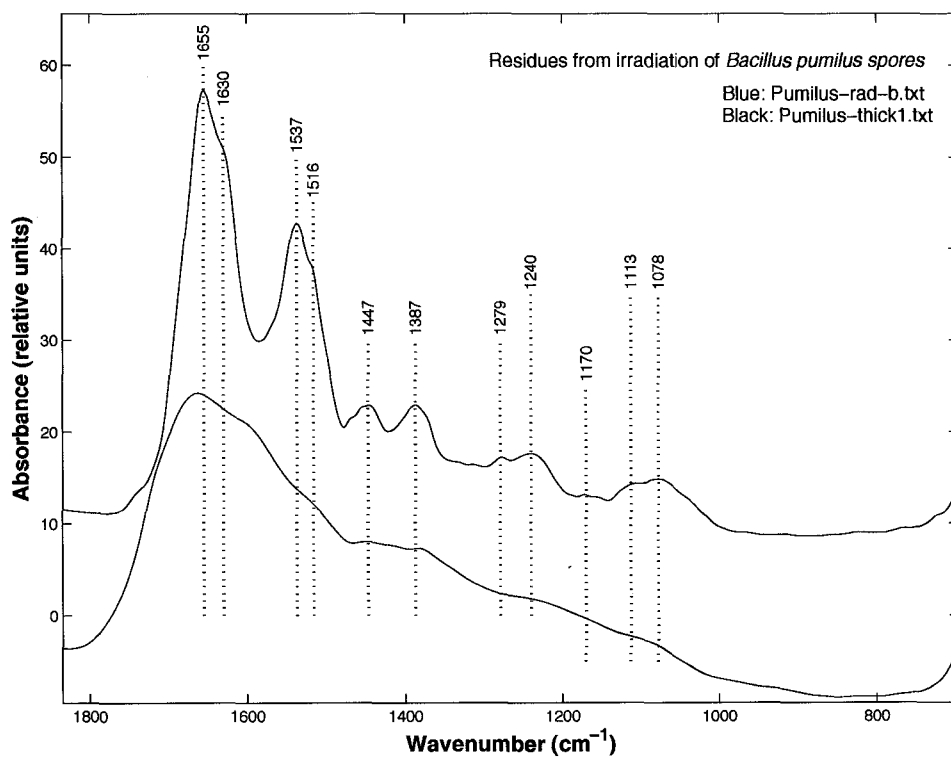


Figure 11.8: FTIR spectrum (800-1800 cm^{-1}) of *B. pumilus* residue after irradiation and removal from the vacuum chamber. The amide and phosphodiester bonds in this spectrum may serve as a useful, post-irradiation, spectral biosignature (see text).

to similar lines seen in the residues from the abiotic irradiation experiments (*e.g.* Figure 10.9).

The C-H bands at 2963, 2932, and 2876 cm^{-1} match almost perfectly, both in position and relative peak heights, to those in the NH_3 ice residue. The broad peak at 3294 cm^{-1} in the bacterial residue, however, was shifted to a shorter wavelength than the NH_3 residue. In both cases, the peak is largely due to O-H, as was seen in the hydrocarbon residues. The hydrocarbon residues, however, all showed this peak at $\sim 3400 \text{ cm}^{-1}$. The 3240 cm^{-1} peak in the NH_3 residue is shifted as a result of N-H stretch in the nitriles of the residue. For the *Bacillus pumilus* residue, this peak was at 3294 cm^{-1} and was largely due to the amide A stretching mode of N-H in proteins (Naumann et al., 1996; Maquelin et al., 2002).

The amide bands seen to decrease during irradiation were easily seen with the post-irradiation FTIR (Figure 11.8). The amide I band of α -helical structures in proteins, resulting from the carbonyl bond in the right-handed spiral of the helical structure, was seen at 1655 cm^{-1} . The comparable band in the abiotic residue was seen at 1669 cm^{-1} . The shift seen in the abiotic residue was likely the result of the variety of bonds to which the carbonyls in that residue were attached. As an example, the carbonyl band of formaldehyde, and as seen in the hydrocarbon residues, was positioned at 1710 cm^{-1} . The NH_3 residue likely consists of carbonyls with a greater diversity of secondary bonds, thereby shifting the peak toward the C-C=O carbonyl at 1710 cm^{-1} , as opposed to that of the amide bond (N-C=O) at 1655 cm^{-1} . Also contributing to this difference was the amide I band of the β -pleated sheet structures in proteins. This band, at 1637 cm^{-1} (Naumann et al., 1996), is also due to the carbonyl stretch interacting with the amide N-H, but in this case the strands of linked amino acids form a sheet by hydrogen bonding with neighboring strands. The change in molecular geometry shifts the amide I in β -sheets to the longer wavelength. This band was seen on the shoulder of the α -helix amide I band.

The amide II band, attributed to N-H bending coupled to the C-N stretch (Hayashi and Mukamel, 2007), was seen 1537 cm^{-1} in the *Bacillus pumilus* residue. Its dopelganger in the abiotic residue was seen at 1595 cm^{-1} and was largely due to NH_2 scissoring, though a contribution from uncoordinated amide bonds (*e.g.* from alanine

if it was indeed synthesized) is possible.

As with the C-H bands at ~ 2900 , the two peaks at 1447 cm^{-1} and 1387 cm^{-1} in the bacterial residue match quite closely to those seen at 1453 cm^{-1} and 1377 cm^{-1} in both the NH_3 residue and the hydrocarbon residues. No shift in band positions was seen across these spectra.

Moving to even longer wavelengths, a pair of strong broad bands were seen that have no direct pairing with the bands in the NH_3 residue. Centered at 1240 cm^{-1} in the bacterial residue is a band corresponding to the asymmetric stretch of the P=O bond in a phosphodiester, $>\text{PO}_2^-$, linkage (Maquelin et al., 2002). The phosphodiester bond is responsible for connecting the nucleotides of RNA and DNA. The diesters of ATP occur at slightly shorter wavelengths, $\sim 1260\text{ cm}^{-1}$, compared to what we observed (Liu et al., 2005).

The second broad band, centered at 1078 cm^{-1} , also corresponds to the phosphodiester bond, but in this case the band results from the symmetric stretch of P=O (Choo-Smith et al., 2001; Maquelin et al., 2002).

Not surprisingly, spectra from our abiotic residues failed to show these bands. Perhaps if our initial mixtures had included phosphate we would have synthesized the phosphodiester. This is an experiment for future work. The bands observed in the ammonia residue show some overlap with the phosphodiester bands, but they constitute an array of weaker, separate bands resulting from C-O, C-C, and NH_2 . It is easy to distinguish the strong, broad phosphodiester bands from these smaller peaks.

Lastly, we move to the $2100\text{-}2200\text{ cm}^{-1}$ region to address a $\text{C}\equiv\text{N}$ band. In one of the irradiated *Bacillus pumilus* residue spectra a strong peak was observed at 2181 cm^{-1} (Figure 11.7). This peak was shifted significantly from the 2155 cm^{-1} isonitrile peak observed in the NH_3 residue. Additionally, this band is not addressed, nor is it seen, in the literature we have examined for FTIR analysis of microbes (see, for instance, Naumann et al. (1996) and other chapters within the same volume). The 2181 cm^{-1} band was not seen in our *in-situ* spectra, Figure 11.1, but again it is important to mention the limitation of our laboratory set-up for collecting good *in-situ* background spectra. It is also possible that the CO observed in those spectra

reacted with nitrogen-containing compounds in the film to form nitriles with the 2181 cm^{-1} band.

The work of Bernstein et al. (1997) lists 3-aminocrotonitrile $[(\text{CH}_3)(\text{NH}_2)\text{CCHCN}]$ as having a $\text{C}\equiv\text{N}$ stretching feature at 2192 cm^{-1} with a full-width, half-maximum of 28 cm^{-1} . Also identified was a band at 2172 cm^{-1} (FWHM of 19 cm^{-1}) corresponding to the $\text{C}\equiv\text{N}$ of methylisocynoacetate $[\text{CH}_3\text{OC}(=\text{O})\text{CH}_2\text{NC}]$. The position and shape of the band we observed in the *Bacillus pumilus* residue fits the wider, 2192 cm^{-1} band better, but given the offset it is likely that the nitrile we synthesized is a similar but distinct compound from the ones examined by Bernstein et al. (1997). Moore et al. (1983) observed a feature at 2180 cm^{-1} after irradiating various mixtures of $\text{H}_2\text{O} + \text{N}_2 + \text{CO}$ or CO_2 with protons. The feature was left unidentified in that work. Palumbo et al. (2000) also report this feature resulting from ion irradiation of $\text{N}_2 + \text{CO}$ mixtures. These workers attribute the band to a $-\text{C}\equiv\text{N}$ but provide no additional detail.

It is important to note that Cruikshank et al. (1991) reported on a 2.2 μm ($\sim 4500 \text{ cm}^{-1}$) $\text{C}\equiv\text{N}$ band seen in outer solar system objects, but we have not yet observed that feature in our laboratory spectra and thus we cannot yet connect it to the $\text{C}\equiv\text{N}$ we see at 2155 cm^{-1} and 2181 cm^{-1} . The $\text{C}\equiv\text{N}$ feature on Ganymede and Callisto, as reported by McCord et al. (1997), occurred at 4.57 μm ($\sim 2188 \text{ cm}^{-1}$). This is intriguingly close to the feature we observe in the *Bacillus pumilus* residue.

In summary, it seems that the band positions associated with C-H in *Bacillus pumilus* spores cannot, after irradiation with energetic electrons, be easily differentiated from comparable bands seen in abiotic residues. The prevalence of proteins in terrestrial organisms, however, may provide an interesting clue toward the biogenic nature of the initial material. The highly-ordered arrangement of amide bonds in α -helical structures and β -pleated sheets was found to provide a systematic, and potentially detectable, shift in N-H and C=O features when compared to similar bands in residues of an abiotic origin. To establish these lines as viable spectral biomarkers we will need to run these experiments to steady-state to see if the amide bonds survive larger doses. More complex initial compositions for the abiotic films are also required.

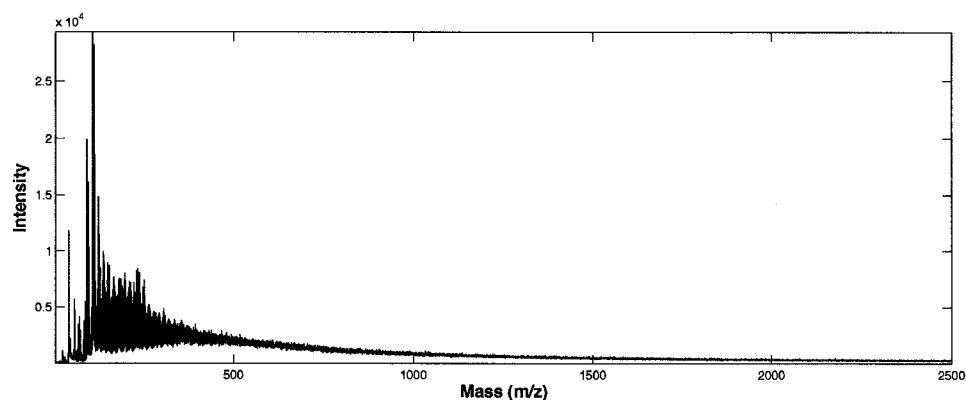


Figure 11.9: MALDI spectrum of *B. pumilus* residue taken from the non-irradiated annular region surrounding the spot irradiated with 20 keV electrons. This portion of the film likely still experienced some radiolytic processing, either directly or with secondary products in the film (*e.g.* OH and H₂O₂). It is not a perfect control. No obvious products were seen at $m/z > 1000$, but a series of peaks at $m/z < 500$ allows for useful comparison to the irradiated sample.

In particular, phosphorous should be added to the mixture in order to test the uniqueness of the phosphodiester bonds to biology. Finally, the radiolytic production of a nitrile was observed and was not found to match infrared bands commonly identified in the FTIR literature on microbes. Such a band could serve as a useful spectral signpost for radiolytically processed biological material. More work must be done in order to better understand this synthesis pathway and to understand the radiolytic stability of various nitriles.

Matrix-assisted laser desorption/ionization (MALDI) was used to investigate the large, refractory compounds within the residue. The technique used was the same as described in Chapter 9. The gold mirrors from the vacuum chamber were directly introduced into the MALDI instrument and analysis of the residue was done without a matrix.

While the irradiation chamber set-up did not allow for the processing of multiple samples at one time, thereby limiting the experimental controls we could perform, we were able to perform controls by analyzing different portions of the same residue with the MALDI instrument. The initial, pre-irradiation *Bacillus pumilus* film covered

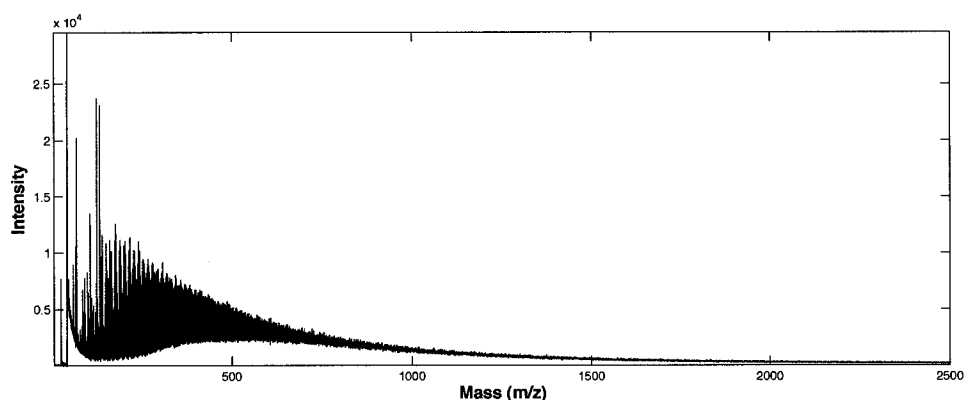


Figure 11.10: MALDI spectrum of *B. pumilus* residue after irradiation and removal from the vacuum chamber. No products were seen beyond $m/z > 1000$. When compared to the spectrum in Figure 11.9, however, we observe a distribution of peaks below $m/z < 500$ that appears ‘smeared’ by radiolytic processing. The peak distribution became more Gaussian in form and several of the strong, distinct peaks in Figure 11.9 were destroyed or greatly reduced in size.

the entire area of the gold mirror exposed by the cryostat fixture. The electron beam, however, was adjusted to only target the central ~ 1 cm circle of this region. Upon removal of the mirror from the chamber, an un-irradiated ring could be seen around the central electron beam spot. The MALDI instrument allows high spatial resolution sampling of the target with the laser. Using this to our advantage, we were able to analyze both irradiated and non-irradiated portions of the same *Bacillus pumilus* residue. This procedure was by no means perfect, certainly the non-irradiated region likely experienced some irradiation and was also subject to oxidants and other compounds synthesized in the film during irradiation of the central portion of the film. Nevertheless, the two regions allowed for useful comparison.

Figures 11.9 and 11.10 show MALDI spectra from m/z of 0 to 2500 for the non-irradiated region and the irradiated region respectively. In both spectra no peaks were seen beyond m/z of 1000. This was likely a limitation of our technique, and specifically a limitation of working without a matrix. Previous work with *Bacillus pumilus* (Dickinson et al., 2004), and with bacteria in general (Lay, 2001), has shown characteristic peaks well out to $m/z \sim 35,000$. Nevertheless, those workers also cite

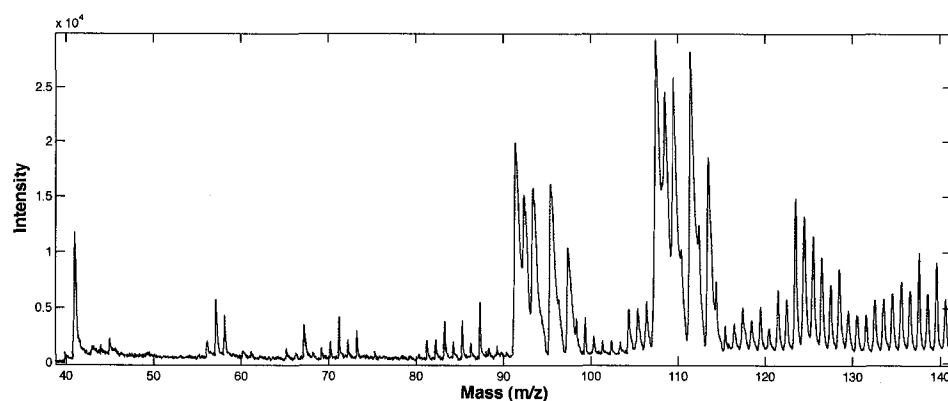


Figure 11.11: MALDI spectrum of *B. pumilus* residue after removal from the vacuum chamber. This spectrum is from an area of no irradiation. Shown here is a detail of the $m/z = 40-140$ region from the spectrum shown in Figure 11.9.

important peaks in the m/z range of 700-2500, and yet we observed nothing in this region. Rectifying the differences in technique between our work and that of Dickinson et al. (2004) is an important component of the next stage of our work on this topic.

Despite the lack of high m/z peaks in our spectra, several interesting observations were made at $m/z < 300$. Shown in Figure 11.11 is a spectrum of the non-irradiated sample with a detail of the large peaks observed in the spectrum from Figure 11.9. Two clusters of peaks were observed in the range of $90 < m/z < 100$ and $107 < m/z < 115$. These may well be fragments of larger proteins or carbohydrates but it was not possible to identify the origin of these peaks without larger m/z results. A comparison with a similar range in the spectrum of the irradiated *Bacillus pumilus* revealed several interesting features. The peaks observed in the non-irradiated sample were not observed in the irradiated sample. Instead, as shown in Figure 11.12, we observed a few smaller peaks at m/z of 104.4, 105.4, 123.5, and 131.6. Beyond these peaks the data showed systematic clusters at intervals of $\Delta m/z \sim 12-14$, consistent with loss of a methyl group, as observed in the MALDI analysis of the hydrocarbon residues. In other words, the MALDI results for the irradiated *Bacillus pumilus* looked quite similar to the many of the results from the hydrocarbon residues.

The MALDI data presented here were largely a technological and instrumentation test, *i.e.* that we could perform this kind of analysis on our samples. Much work

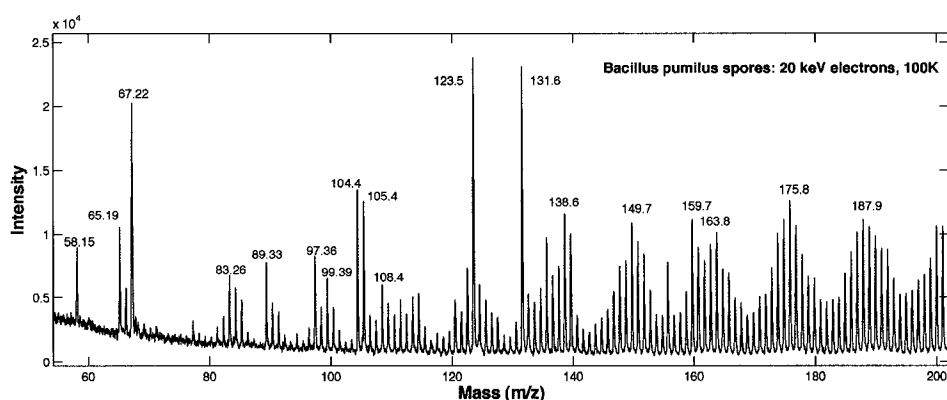


Figure 11.12: MALDI spectrum of *B. pumilus* residue after irradiation and removal from the vacuum chamber. This is a detail of the $m/z = 60$ -200 region from the spectrum show in Figure 11.10.

remains to be done in order to improve the efficacy our data and the degree to which we can compare that data with results from other experiments. With those caveats, however, we were intrigued with the results from the data we were able to collect. Radiolysis of the bacterial spores results in the production of many new fragments and smaller compounds that appear to at least partially hide a MALDI biosignature. The irradiated spores yield a spectrum that is hard to distinguish from the abiotically produced residues of Chapter 9. As a technique for life detection, such mass spectral analysis would be ambiguous. Our hope is that by extending this analysis to much larger m/z we may observe spectral features that could aid in distinguishing a biogenic signature from an abiotic signature.

11.2 Implications for the search for life on Europa

Does the surface of Europa harbor a biosignature of sub-surface life? This is a critical question for our near-future exploration of Europa, which will largely be limited to observations of the surface or near-surface ice. While answering this question could be greatly facilitated by presence of a spacecraft lander, remote sensing with an orbiter could reveal important lines of evidence, allowing us to build a very compelling case

for life. At one extreme is direct observation of morphological fossils with high-resolution imagery. At the other extreme is detection of complex organic chemistry, a tantalizing find but far from a convincing detection of life.

The prospect of a habitable, or inhabited, Europa underscores the need to understand abiological organic chemistry driven by radiolytic processes. The work presented in this thesis has explored this relationship in considerable depth. Abiotic organic chemistry driven by radiolysis can produce patterns in mass spectroscopy data that could potentially be misinterpreted as biosignatures. Infrared spectroscopy provided some important clues about what might constitute a spectral biosignature. The highly order nature of proteins and nucleic acids yields strong infrared bands significantly offset from comparable vibrations in abiotic mixtures. The amide bands in proteins and phosphodiester bands in nucleic acids could be important clues on Europa, if life on Europa were to utilize a biochemistry similar to that of terrestrial organisms

Tracking the spatial distribution of hydrocarbon, amide, and phosphodiester bands across fractures and lineaments on Europa could allow for differentiating between endogenous organic chemistry in the subsurface and organic chemistry driven by surface radiolysis. The asymmetries of the various processes on Europa (Figure 8.1) may be a useful aid for deconvolving biosignatures on Europa from abiotic chemistry.

It is important that the youngest terrains be targeted as these areas will contain the greatest amount of spectral information about the sub-surface material. Radiolysis acts on geologically short timescales and erases many of the more subtle spectral features. Young terrains on the leading hemisphere of Europa are likely the best areas to minimize the radiation exposure, however the leading hemisphere will also be the region of maximum exogenous organic delivery. The presence or absence of aromatic material on the surface of icy satellites may help distinguish between exogenous carbon (*e.g.* micrometeorites) and radiolytically processed material. Biology, of course, complicates matters. Future laboratory work by the author will aim at exploring the spectral signatures of biological aromatics and polyaromatic hydrocarbons (PAHs).

The combined compositional and surface age mapping as described above could

yield a strong, compelling - though unlikely conclusive - case for an inhabited subsurface ocean. To be convinced of life, we will almost certainly have to see it in its full form. Imagery in the visible, be it of macroscopic fossils or microscopic microbes will be critical. The many biomarkers used to trace the history of life here on Earth can certainly help guide us, but those biomarkers work for Earth because we know life exists here on Earth. Found elsewhere in the solar system, such biomarkers would be remarkable indeed, but their biogenicity would be heavily debated until we found the synthesizing culprit.

Critical to our capability to search for life beyond Earth is the development of a better understanding of how to detect the life we know exists here on Earth. Remote sensing techniques are largely limited to the spectral signatures of photosynthesis, *i.e.* the spectral lines of chlorophyll A and B. Such lines could be useful for Mars, but on Europa photosynthesis is likely limited by the thickness of the ice shell.

Other pigments and compounds of life here on Earth should be explored in the context of their capacity to be detected by orbiting spacecraft. In particular, do the sulfur-based systems of hydrothermal vent ecosystem have unique pigments or biomolecules that could be detected from space? Perhaps hemoglobin would be an interesting molecule to study, given its importance for redox chemistry in complex terrestrial organism? Such spectral signatures, and non-photosynthetically biased ecosystems, could serve as the best analog for what we might utilize as a biosignature when we search for life from orbit around Europa.

Finally, it is important to note that the detection of life from orbit, by a robotic spacecraft designed for the Jovian system, is not unprecedented. Sagan et al. (1993) turned the instruments of the *Galileo* spacecraft back on Earth during the 1990 gravity assist fly-by and detected several signs of life, including an atmosphere out of chemical thermodynamic equilibrium and continents rich with photosynthetic pigments. While traditional, massive, and very capable satellites in orbit around the Earth had obviously been sending back data about life on Earth for decades, the results from the *Galileo* fly-by were unique in that the design spacecraft was such that all of the engineering constraints (*e.g.* payload mass, data rate, etc.) were satisfied for Jupiter and the instruments onboard were not designed with life detection in mind.

The results of the *Galileo* experiment were a good proof-of-concept: we are technologically capable of detecting an inhabited planet. Granted, it was our own planet and the surface is teeming with life. Nevertheless, Sagan et al. (1993) were wise to advise that in the analysis of their data, 'life is the hypothesis of last resort'. We would do well to abide these words as we move forward with our exploration of the solar system. The scientific and technical challenges posed by the prospect of detecting life on Europa, or any world beyond Earth for that matter, is great. But the question, of whether or not we are alone in the universe, is a question worthy of such a great challenge.

Bibliography

- Addison, J., 1969. Electrical Properties of Saline Ice. *Journal of Applied Physics* 40 (8), 3105–3114.
- Allamandola, L., Sandford, S., Valero, G., 1988. Photochemical and thermal evolution of interstellar/precometary ice analogs. *Icarus* 76, 225–252.
- Allamandola, L., Sandford, S., Wopenka, B., 1987. Interstellar Polycyclic Aromatic Hydrocarbons and Carbon in Interplanetary Dust Particles and Meteorites. *Science* 237 (4810), 56.
- Allamandola, L., Tielens, G., Barker, J., 1989. Interstellar polycyclic aromatic hydrocarbons - The infrared emission bands, the excitation/emission mechanism, and the astrophysical implications. *Astrophysical Journal Supplement Series* 71, 733–775.
- Allen, D., Seyfried, W., 2004. Serpentinization and heat generation: constraints from Lost City and Rainbow hydrothermal systems. *Geochimica et Cosmochimica Acta* 68 (6), 1347–1354.
- Anderko, A., Lencka, M., 1997. Computation of Electrical Conductivity of Multicomponent Aqueous Systems in Wide Concentration and Temperature Ranges. *Ind. Eng. Chem. Res* 36 (5), 1932–1943.
- Anderson, J., et al., 1998. Europa's Differentiated Internal Structure: Inferences from Four Galileo Encounters. *Science* 281 (5385), 2019–2022.
- Arnorsson, S., Groenvold, K., Sigurdsson, S., 1978. Aquifer chemistry of four high-temperature geothermal systems in Iceland. *Geochim. Cosmochim. Acta* 42 (5).

- Bagenal, F., Dowling, T., McKinnon, W., 2004. *Jupiter: The Planet, Satellites and Magnetosphere*. Cambridge University Press.
- Bar-Nun, A., Dror, J., Kochavi, E., Laufer, D., 1987. Amorphous water ice and its ability to trap gases. *Physical Review B* 35 (5), 2427–2435.
- Baragiola, R., Atteberry, C., Bahr, D., Peters, M., 1999. Reply: Laboratory studies of the optical properties and stability of oxygen on Ganymede. *Journal of Geophysical Research* 104 (E6), 14183–14187.
- Baragiola, R., Bahr, D., 1998. Laboratory studies of the optical properties and stability of oxygen on Ganymede. *Journal of Geophysical Research* 103 (E11), 25865–25872.
- Barlow, P., 2003. *Ground Water in Freshwater-saltwater Environments of the Atlantic Coast*. US Dept. of the Interior, US Geological Survey.
- Barr, A., Pappalardo, R., 2003. Numerical Simulations of Non-Newtonian Convection in Ice: Application to Europa. 34th Annual Lunar and Planetary Science Conference, March 17-21, 2003, League City, Texas, abstract no. 1477.
- Barr, A., Pappalardo, R., Zhong, S., 2004. Convective instability in ice I with non-Newtonian rheology: Application to the icy Galilean satellites. *J. Geophys. Res* 109.
- Barrer, R., Ruzicka, D., 1962. Non-Stoichiometric Clathrate Compounds of Water. Part 2. Formation and Properties of Double Hydrates. *Trans. Faraday Society* 58, 2262–2271.
- Bauschlicher Jr, C., Ricca, A., 2000. Mechanisms for polycyclic aromatic hydrocarbon (PAH) growth. *Chem. Phys. Lett* 326, 283–287.
- Benner, S., Ricardo, A., Carrigan, M., 2004. Is there a common chemical model for life in the universe? *Curr. Opin. Chem. Biol* 8 (6), 672–689.

- Berger, M., Coursey, J., Zucker, M., Chang, J., 2005. ESTAR, PSTAR, and ASTAR: Computer programs for calculating stopping-power and range tables for electrons, protons, and helium ions. Version 1.2.3. National Institute of Standards and Technology, Gaithersberg, MD. [Online] Available at <http://physics.nist.gov/Star>.
- Bernstein, M., Dworkin, J., Sandford, S., Allamandola, L., 2001. Ultraviolet irradiation of naphthalene in H₂O ice: Implications for meteorites and biogenesis. *Meteor. Planet. Sci* 36, 351–358.
- Bernstein, M., Dworkin, J., Sandford, S., Cooper, G., Allamandola, L., 2002. Racemic amino acids from the ultraviolet photolysis of interstellar ice analogues. *Nature* 416 (6879), 401–403.
- Bernstein, M., Sandford, S., Allamandola, L., 1997. The Infrared Spectra of Nitriles and Related Compounds Frozen in Ar and H₂O. *Astrophysical Journal* 476, 932–942.
- Bernstein, M., Sandford, S., Allamandola, L., Chang, S., Scharberg, M., 1995. Organic Compounds Produced by Photolysis of Realistic Interstellar and Cometary Ice Analogs Containing Methanol. *The Astrophysical Journal* 454, 327.
- Bernstein, M., Sandford, S., Allamandola, L., Gillette, J., Clemett, S., Zare, R., 1999. UV Irradiation of Polycyclic Aromatic Hydrocarbons in Ices: Production of Alcohols, Quinones, and Ethers. *Science* 283 (5405), 1135–1138.
- Bischoff, J., Dickson, F., 1975. Seawater-basalt interaction at 200 °C and 500 bars: Implications for origin of sea-floor heavy-metal deposits and regulation of seawater chemistry. *Earth and Planetary Science Letters* 25 (3), 385–397.
- Blake, D., Allamandola, L., Sandford, S., Hudgins, D., Freund, F., 1991. Clathrate hydrate formation in amorphous cometary ice analogs in vacuo. *Science* 254 (5031), 548.
- Bremner, R., Thompson, T., Utterback, C., 1939. Electrical Conductances of Pure and Mixed Salt Solutions in the Temperature Range 0° to 25°. *Journal of the American Chemical Society* 61 (5), 1219–1223.

- Brown, M., 2001. Potassium in Europa's Atmosphere. *Icarus* 151 (2), 190–195.
- Brown, M., Hill, R., 1996. Discovery of an extended sodium atmosphere around Europa. *Nature* 380 (6571), 229–231.
- Brown, R., Clark, R., Buratti, B., Cruikshank, D., Barnes, J., Mastrapa, R., Bauer, J., Newman, S., Momary, T., Baines, K., et al., 2006. Composition and Physical Properties of Enceladus' Surface. *Science* 311 (5766), 1425–1428.
- Brucato, J., Palumbo, M., Strazzulla, G., 1997. Carbonic Acid by Ion Implantation in Water/Carbon Dioxide Ice Mixtures. *Icarus* 125 (1), 135–144.
- Brucato, J., Strazzulla, G., Baratta, G., Rotundi, A., Colangeli, L., 2006. Cryogenic Synthesis of Molecules of Astrobiological Interest: Catalytic Role of Cosmic Dust Analogues. *Origins of Life and Evolution of Biospheres* 36 (5), 451–457.
- Buffett, B., 2000. Clathrate hydrates. *Annual Review of Earth and Planetary Sciences* 28 (1), 477–507.
- Cagniard, L., 1953. Basic theory of the magneto-telluric method of geophysical prospecting. *Geophysics* 18 (3), 605–635.
- Calvert, R., Cornelius, J., Griffiths, V., Stock, D., 1958. The Determination of the Electrical Conductivities of Some Concentrated Electrolyte Solutions Using a Transformer Bridge. *The Journal of Physical Chemistry* 62 (1), 47–53.
- Calvin, W., Johnson, R., Spencer, J., 1996. O₂ on Ganymede: Spectral characteristics and plasma formation mechanisms. *Geophysical Research Letters* 23 (6), 673–676.
- Campbell, M., Ulrichs, J., 1969. Electrical properties of rocks and their significance for lunar radar observations. *J. Geophys. Res* 74, 5867–5881.
- Carlson, R., 2001. Spatial Distribution of Carbon Dioxide, Hydrogen Peroxide, and Sulfuric Acid on Europa. American Astronomical Society, DPS Meeting #33, #47.02; *Bulletin of the American Astronomical Society* 33, 1125.

- Carlson, R., Anderson, M., Johnson, R., Schulman, M., Yavrouian, A., 2002. Sulfuric acid production on Europa: the radiolysis of sulfur in water ice. *Icarus* 157 (2), 456–463.
- Carlson, R., Anderson, M., Johnson, R., Smythe, W., Hendrix, A., Barth, C., Soderblom, L., Hansen, G., McCord, T., Dalton, J., et al., 1999a. Hydrogen Peroxide on the Surface of Europa. *Science* 283 (5410), 2062–2064.
- Carlson, R., Anderson, M., Mehlman, R., Johnson, R., 2005. Distribution of hydrate on Europa: Further evidence for sulfuric acid hydrate. *Icarus* 177 (2), 461–471.
- Carlson, R., Johnson, R., Anderson, M., 1999b. Sulfuric Acid on Europa and the Radiolytic Sulfur Cycle. *Science* 286 (5437), 97–99.
- Carr, M., Belton, M., Chapman, C., Davies, M., Geissler, P., Greenberg, R., McEwen, A., Tufts, B., Greeley, R., Sullivan, R., et al., 1998. Evidence for a subsurface ocean on Europa. *Nature* 391 (6665), 363–5.
- Carroll, J., 2003. *Natural Gas Hydrates: A Guide for Engineers*. Gulf Professional Publishing.
- Cassen, P., Peale, S., Reynolds, R., 1980. Tidal dissipation in Europa - A correction. *Geophysical Research Letters* 7, 987–988.
- Cassen, P., Reynolds, R., Peale, S., 1979. Is there liquid water on Europa? *Geophysical Research Letters* 6, 731–734.
- CDC-EPA, 1999. *Health Effects from Exposure to Sulfate in Drinking Water Workshop*. Centers for Disease Control & US Environmental Protection Agency, Office of Water, Atlanta.
- Champagnon, B., Panczer, G., Chazallon, B., Arnaud, L., Duval, P., Lipenkov, V., 1997. Nitrogen and Oxygen Guest Molecules in Clathrate Hydrates: Different Sites Revealed by Spectroscopy Raman. *Journal of Raman Spectroscopy* 28, 711–715.

- Chazallon, B., Kuhs, W., 2002. In situ structural properties of N-, O-, and air-clathrates by neutron diffraction. *The Journal of Chemical Physics* 117, 308.
- Choo-Smith, L., Maquelin, K., van Vreeswijk, T., Bruining, H., Puppels, G., Thi, N., Kirschner, C., Naumann, D., Ami, D., Villa, A., et al., 2001. Investigating Microbial (Micro)colony Heterogeneity by Vibrational Spectroscopy. *Applied and Environmental Microbiology* 67 (4), 1461–1469.
- Chyba, C., 1991. Extraterrestrial organic molecules, the heavy bombardment, and the terrestrial origin of life. Ph.D. thesis, Cornell University.
- Chyba, C., 2000. Energy for microbial life on Europa. *Nature* 403 (6768), 381–2.
- Chyba, C., Hand, K., 2001. Planetary Science: Life Without Photosynthesis. *Science* 292 (5424), 2026–2027.
- Chyba, C., Hand, K., 2005. Astrobiology: The Study of the Living Universe. *Annual Review of Astronomy and Astrophysics* 43, 31–74.
- Chyba, C., Hand, K., 2006. Comets and Prebiotic Organic Molecules on Early Earth. In: Thomas, P., Hicks, R., Chyba, C., McKay, C. (Eds.), *Comets and the Origin and Evolution of Life*, 2nd Edition. Springer, *Advances in Astrobiology and Biogeophysics*, pp. 169–206.
- Chyba, C., McDonald, G., 1995. The Origin of Life in the Solar System: Current Issues. *Annual Review of Earth and Planetary Sciences* 23 (1), 215–249.
- Chyba, C., Ostro, S., Edwards, B., 1998. Radar detectability of a subsurface ocean on Europa. *Icarus* 134 (2), 292–302.
- Chyba, C., Phillips, C., 2001. Possible ecosystems and the search for life on Europa. *Proc. National Acad. Sciences* 98 (3), 801–803.
- Chyba, C., Sagan, C., 1992. Endogenous production, exogenous delivery and impact-shock synthesis of organic molecules: an inventory for the origins of life. *Nature* 355 (6356), 125–132.

- Clark, B., Helfenstein, P., Veverka, J., Ockert-Bell, M., Sullivan, R., Geissler, P., Phillips, C., McEwen, A., Greeley, R., Neukum, G., et al., 1998. Multispectral Terrain Analysis of Europa from Galileo Images. *Icarus* 135 (1), 95–106.
- Connerney, J., Acuna, M., Ness, N., Satoh, T., 1998. New models of Jupiter's magnetic field constrained by the Io flux tube footprint. *Journal of Geophysical Research* 103 (A6), 11929–11940.
- Cooper, J., Johnson, R., Mauk, B., Garrett, H., Gehrels, N., 2001. Energetic Ion and Electron Irradiation of the Icy Galilean Satellites. *Icarus* 149, 133–159.
- Cooper, P., Johnson, R., Quickenden, T., 2003. Hydrogen peroxide dimers and the production of O₂ in icy satellite surfaces. *Icarus* 166 (2), 444–446.
- Cottrell, T., 1958. *The Strengths of Chemical Bonds*, 2nd Edition. Butterworths, London.
- Crawford, G., Stevenson, D., 1988. Gas-driven water volcanism in the resurfacing of Europa. *Icarus* 73, 66–79.
- Cruikshank, D., Allamandola, L., Hartmann, W., Tholen, D., Brown, R., Matthews, C., Bell, J., 1991. Solid C triple bond N bearing material on outer solar system bodies. *Icarus* 94, 345–53.
- Dalton, J., Mogul, R., Kagawa, H., Chan, S., Jamieson, C., 2003. Near-infrared detection of potential evidence for microscopic organisms on Europa. *Astrobiology* 3 (3), 505–29.
- Dalton, J., Prieto-Ballesteros, O., Kargel, J., Jamieson, C., Jolivet, J., Quinn, R., 2005. Spectral comparison of heavily hydrated salts with disrupted terrains on Europa. *Icarus* 177 (2), 472–490.
- Darwent, B., 1970. Bond dissociation energies in simple molecules (Bond dissociation energies in simple inorganic compounds). National Standard Reference Data System.

- Denny, M., 1993. *Air and Water: The Biology and Physics of Life's Media*. Princeton University Press.
- Dickinson, D., La Duc, M., Satomi, M., Winefordner, J., Powell, D., Venkateswaran, K., 2004. MALDI-TOFMS compared with other polyphasic taxonomy approaches for the identification and classification of *Bacillus pumilus* spores. *Journal of Microbiological Methods* 58 (1), 1–12.
- Dunsmore, H., James, J., 1951. The electrolytic dissociation of magnesium sulphate and lanthanum ferricyanide in mixed solvents. *Journal of the Chemical Society*.
- Durham, W., Kirby, S., Stern, L., Zhang, W., 2003. The strength and rheology of methane clathrate hydrate. *J. Geophys. Res* 108 (2182), 1–11.
- Dworkin, J., Deamer, D., Sandford, S., Allamandola, L., 2001. Special Feature: Self-assembling amphiphilic molecules: Synthesis in simulated interstellar/precometary ices. *Proceedings of the National Academy of Sciences* 98 (3), 815.
- Elderfield, H., Schultz, A., 1996. Mid-ocean ridge hydrothermal fluxes and the chemical composition of the ocean. *Annual Review of Earth and Planetary Sciences* 24 (1), 191–224.
- Ellery, A., Wynn-Williams, D., 2003. Methodologies and Techniques for Detecting Extraterrestrial (Microbial) Life. *Astrobiology* 3, 565–579.
- EPA, 2004. *The 2004 Edition of the Drinking Water Standards and Health Advisories*. Office of Water, United States Environmental Protection Agency, Washington, DC.
- ESB-NAS, 1972. *Water Quality Criteria*. National Academy of Sciences & National Academy of Engineering, Washington, DC.
- Fagents, S., Greeley, R., Sullivan, R., Pappalardo, R., Prockter, L., 2000. Cryomagnetic Mechanisms for the Formation of Rhadamanthys Linea, Triple Band Margins, and Other Low-Albedo Features on Europa. *Icarus* 144 (1), 54–88.
- Fahie, J., 1903. *Galileo, His Life and Work*. James Pott & Company, New York.

- Fanale, F., 1986. Planetary volatile history - principles and practice. In: Kivelson, M. (Ed.), *The solar system: Observations and interpretations*. Vol. 4. Englewood Cliffs, NJ, Prentice-Hall (Rubey), pp. 135–175.
- Fanale, F., Li, Y., De Carlo, E., Farley, C., Sharma, S., Horton, K., Granahan, J., 2001. An experimental estimate of Europa's 'ocean' composition-independent of *Galileo* orbital remote sensing. *Journal of Geophysical Research-Planets* 106 (E7).
- Fisher, F., 1962. The effect of pressure on the equilibrium of magnesium sulfate. *The Journal of Physical Chemistry* 66 (9), 1607–1611.
- Fisher, F., Fox, A., 1979. Divalent sulfate ion pairs in aqueous solutions at pressures up to 2000 atm. *Journal of Solution Chemistry* 8 (4), 309–328.
- Gaidos, E., Neelson, K., Kirschvink, J., 1999. Life in Ice-Covered Oceans. *Science* 284 (5420), 1631–1633.
- Galileo, G., Drake, S., 1957. *Discoveries and opinions of Galileo* (Translated, with Introduction and Notes, by S. Drake). Anchor Books, Doubleday, New York.
- Gerakines, P., Moore, M., Hudson, R., 2000. Carbonic acid production in H₂O: CO₂ ices. *Astron. Astrophys* 357, 793–800.
- Geymonat, L., 1965. *Galileo Galilei: a biography and inquiry into his philosophy of science*. New York, McGraw-Hill, 260.
- Gomis, O., Leto, G., Strazzulla, G., 2004a. Hydrogen peroxide production by ion irradiation of thin water ice films. *A&A* 420, 405–410.
- Gomis, O., Satorre, M., Strazzulla, G., Leto, G., 2004b. Hydrogen peroxide formation by ion implantation in water ice and its relevance to the Galilean satellites. *Planetary and Space Science* 52 (5), 371–378.
- Goodman, J., Collins, G., Marshall, J., Pierrehumbert, R., 2004. Hydrothermal plume dynamics on Europa: Implications for chaos formation. *Journal of Geophysical Research* 109 (3), DOI 10.1029/2003JE002073.

- Greeley, R., Chyba, C., Head III, J., McCord, T., McKinnon, W., Pappalardo, R., Figueredo, P., 2004. Geology of Europa. In: Bagenal, F., Dowling, T., McKinnon, W. (Eds.), *Jupiter. The planet, satellites and magnetosphere*, 1st Edition. Cambridge University Press, Ch. 15, pp. 329–362.
- Greenberg, R., Geissler, P., Hoppa, G., Tufts, B., 2002. Tidal-tectonic processes and their implications for the character of Europa's icy crust. *Reviews of Geophysics* 40 (2), 1034–1038.
- Greenberg, R., Geissler, P., Hoppa, G., Tufts, B., Durda, D., Pappalardo, R., Head, J., Greeley, R., Sullivan, R., Carr, M., 1998. Tectonic processes on Europa: Tidal stresses, mechanical response, and visible features. *Icarus* 135 (1), 64–78.
- Greenberg, R., Hoppa, G., Tufts, B., Geissler, P., Riley, J., Kadel, S., 1999. Chaos on Europa. *Icarus* 141 (2), 263–286.
- Grieves, G., Orlando, T., 2005. The importance of pores in the electron stimulated production of D₂ and O₂ in low temperature ice. *Surface Sci* 593, 180–186.
- Gudipati, M., Allamandola, L., 2003. Facile Generation and Storage of Polycyclic Aromatic Hydrocarbon Ions in Astrophysical Ices. *The Astrophysical Journal* 596 (2), L195–L198.
- Guillot, T., Stevenson, D., Hubbard, W., Saumon, D., 2004. The interior of Jupiter. In: Bagenal, F., Dowling, T., McKinnon, W. (Eds.), *Jupiter. The planet, satellites and magnetosphere*, 1st Edition. Cambridge University Press, pp. 35–57.
- Haida, O., Matsuo, T., Suga, H., Seki, S., 1974. Calorimetric study of the glassy state. X. Enthalpy relaxation at the glass-transition temperature of hexagonal ice. *J. Chem. Thermodyn* 6 (9), 815–825.
- Hall, D., Strobel, D., Feldman, P., McGrath, M., Weaver, H., 1995. Detection of an oxygen atmosphere on Jupiter's moon Europa. *Nature* 373 (6516), 677–679.
- Hand, K., Carlson, R., Chyba, C., 2007. Energy, chemical disequilibrium, and geological constraints Europa. *Astrobiology X* (X), X–X.

- Hand, K., Chyba, C., 2007. Empirical constraints on the salinity of the european ocean and implications for a thin ice shell. *Icarus* 189 (2), 424–438.
- Hand, K., Chyba, C., Carlson, R., Cooper, J., 2006. Clathrate Hydrates of Oxidants in the Ice Shell of Europa. *Astrobiology* 6 (3), 463–482.
- Hansen, C., Esposito, L., Stewart, A., Colwell, J., Hendrix, A., Pryor, W., Shemansky, D., West, R., 2006. Enceladus' water vapor plume. *Science* 311 (5766), 1422–1425.
- Hapke, B., 1993. *Theory of Reflectance and Emittance Spectroscopy*. Cambridge University Press New York, NY, USA.
- Harkins, W., Paine, H., 1919. Intermediate and complex ions. V. The solubility product and activity of the ions in bi-bivalent salts. 1. *Journal of the American Chemical Society* 41 (8), 1155–1168.
- Hayashi, T., Mukamel, S., 2007. Vibrational-Exciton Couplings for the Amide I, II, III, and A Modes of Peptides. *J. Phys. Chem. B* 10.1021/jp070369b (x), xxx.
- Hogenboom, D., Kargel, J., Ganasan, J., Lee, L., 1995. Magnesium sulfate-water to 400 MPa using a novel piezometer: Densities, phase equilibria, and planetological implications. *Icarus* 115, 258–277.
- Holland, H., 1984. *The Chemical Evolution of the Atmosphere and Oceans*. Princeton University Press.
- Hoppa, G., Randall Tufts, B., Greenberg, R., Hurford, T., O'Brien, D., Geissler, P., 2001. Europa's Rate of Rotation Derived from the Tectonic Sequence in the Astypalaea Region. *Icarus* 153 (1), 208–213.
- Hoppa, G., Tufts, B., Greenberg, R., Geissler, P., 1999. Formation of Cycloidal Features on Europa. *Science* 285 (5435), 1899–1902.
- Hudgins, D., Sandford, S., Allamandola, L., Tielens, A., 1993. Mid- and far-infrared spectroscopy of ices – Optical constants and integrated absorbances. *The Astrophysical Journal Supplement Series* 86, 713–870.

- Hudson, R., Moore, M., 1999. Laboratory Studies of the Formation of Methanol and Other Organic Molecules by Water + Carbon Monoxide Radiolysis: Relevance to Comets, Icy Satellites, and Interstellar Ices. *Icarus* 140 (2), 451–461.
- Hudson, R., Moore, M., Gerakines, P., 2001. The Formation of Cyanate Ion (OCN-) in Interstellar Ice Analogs. *The Astrophysical Journal* 550 (2), 1140–1150.
- Hussmann, H., Spohn, T., 2004. Thermal-orbital evolution of Io and Europa. *Icarus* 171 (2), 391–410.
- Hussmann, H., Spohn, T., Wiczerkowski, K., 2002. Thermal Equilibrium States of Europa's Ice Shell: Implications for Internal Ocean Thickness and Surface Heat Flow. *Icarus* 156 (1), 143–151.
- Ip, W., Williams, D., McEntire, R., Mauk, B., 1998. Ion sputtering and surface erosion at Europa. *Geophysical Research Letters* 25 (6), 829–832.
- Jacox, M., Milligan, D., 1971. Infrared Spectrum and Structure of the Species CO₃. *Journal of Chemical Physics* 54 (3), 919–926.
- Janecky, D., Seyfried Jr, W., 1986. Hydrothermal serpentinization of peridotite within the oceanic crust: Experimental investigations of mineralogy and major element chemistry. *Geochimica et Cosmochimica Acta* 50 (7), 1357–1378.
- Jellison, R., Macintyre, S., Millero, F., 1999. Density and conductivity properties of Na - CO₃ - Cl - SO₄ brine from Mono Lake, California, USA. *International Journal of Salt Lake Research* 8 (1), 41–53.
- Johnson, J., Oelkers, E., Helgeson, H., 1992. SUPCRT92: a software package for calculating the standard molal thermodynamic properties of minerals, gases, aqueous species, and reactions from 1 to 5000 bar and 0 to 1000 °C. *Computers & Geosciences* 18 (7), 899–947.
- Johnson, R., 1990. *Energetic Charged-Particle Interactions with Atmospheres and Surfaces*. Springer-Verlag, New York.

- Johnson, R., 1999. Comment on 'Laboratory studies of the optical properties and stability of oxygen on Ganymede' by Raul A. Baragiola and David A. Bahr. *Journal of Geophysical Research* 104 (E6), 14179–14182.
- Johnson, R., 2000. Sodium at Europa. *Icarus* 143 (2), 429–433.
- Johnson, R., Carlson, R., Cooper, J., Paranicas, C., Moore, M., Wong, M., 2004. Radiation effects on the surfaces of the Galilean satellites. In: Bagenal, F., Dowling, T., McKinnon, W. (Eds.), *Jupiter. The planet, satellites and magnetosphere*, 1st Edition. Cambridge University Press, pp. 485–512.
- Johnson, R., Jesser, W., 1997. O₂/O₃ microatmospheres in the surface of Ganymede. *Astrophys. J* 480, L79–L82.
- Johnson, R., Killen, R., Waite, J., Lewis, W., 1998. Europa's surface composition and sputter-produced ionosphere. *Geophysical Research Letters* 25 (17), 3257–3260.
- Johnson, R., Quickenden, T., Cooper, P., McKinley, A., Freeman, C., 2003. The Production of Oxidants in Europa's Surface. *Astrobiology* 3 (4), 823–850.
- Jones, B., Grant, W., Duckworth, A., Owenson, G., 1998. Microbial diversity of soda lakes. *Extremophiles* 2 (3), 191–200.
- Kargel, J., 1991. Brine volcanism and the interior structures of asteroids and icy satellites. *Icarus* 94, 368–390.
- Kargel, J., 2006. Enceladus: Cosmic Gymnast, Volatile Miniworld. *Science* 311 (5766), 1389–1391.
- Kargel, J., Kaye, J., Head, J., Marion, G., Sassen, R., Crowley, J., Ballesteros, O., Grant, S., Hogenboom, D., 2000. Europa's Crust and Ocean: Origin, Composition, and the Prospects for Life. *Icarus* 148 (1), 226–265.
- Kasting, J., Whitmire, D., Reynolds, R., 1993. Habitable zones around main sequence stars. *Icarus* 101 (1), 108–28.

- Kelley, D., Karson, J., Blackman, D., Früh-Green, G., Butterfield, D., Lilley, M., Olson, E., Schrenk, M., Roe, K., Lebon, G., et al., 2001. An off-axis hydrothermal vent field near the Mid-Atlantic Ridge at 30 N. *Nature* 412 (6843), 145–149.
- Khare, B., Sagan, C., 1973. Red clouds in reducing atmospheres. *Icarus* 20 (3), 311–321.
- Khare, B., Sagan, C., Thompson, W., Arakawa, E., Meisse, C., Tuminello, P., 1994. Optical properties of poly-HCN and their astronomical applications. *Canadian Journal of Chemistry* 72 (3), 678–694.
- Khare, B., Thompson, W., Chyba, C., Arakawa, E., Sagan, C., 1989. Organic solids produced from simple C/H/O/N ices by charged particles: applications to the outer solar system. *Adv Space Res* 9 (2), 41–53.
- Khurana, K., Kivelson, M., Russell, C., 1997. Interaction of Io with its torus: Does Io have an internal magnetic field? *Geophys. Res. Lett* 24, 2391–2394.
- Khurana, K., Kivelson, M., Stevenson, D., Schubert, G., Russell, C., Walker, R., Polanskey, C., 1998. Induced magnetic fields as evidence for subsurface oceans in Europa and Callisto. *Nature* 395 (6704), 749–751.
- Khurana, K., Kivelson, M., Vasyliunas, V., Krupp, N., Woch, J., Lagg, A., Mauk, B., Kurth, W., 2004. The configuration of Jupiter's magnetosphere. In: Bagenal, F., Dowling, T., McKinnon, W. (Eds.), *Jupiter. The planet, satellites and magnetosphere*, 1st Edition. Cambridge University Press, pp. 594–616.
- Kivelson, M., Khurana, K., Bennett, L., Joy, S., Russell, C., Walker, R., Zimmer, C., Stevenson, D., Polanskey, C., 1999. Europa and Callisto- Induced or intrinsic fields in a periodically varying plasma environment. *Journal of Geophysical Research* 104 (A3), 4609–4626.
- Kivelson, M., Khurana, K., Joy, S., Russell, C., Southwood, D., Walker, R., Polanskey, C., 1997. Europa's Magnetic Signature: Report from Galileo's Pass on 19 December 1996. *Science* 276 (5316), 1239–1241.

- Kivelson, M., Khurana, K., Russell, C., Volwerk, M., Walker, R., Zimmer, C., 2000. Galileo Magnetometer Measurements: A Stronger Case for a Subsurface Ocean at Europa. *Science* 289 (5483), 1340–1343.
- Kuhs, W., Chazallon, B., Radaelli, P., Pauer, F., 1997. Cage Occupancy and Compressibility of Deuterated N₂-Clathrate Hydrate by Neutron Diffraction. *Journal of Inclusion Phenomena and Macrocyclic Chemistry* 29 (1), 65–77.
- Kuhs, W., Klapproth, A., Chazallon, B., 2000. Chemical physics of air clathrate hydrates. *Physics of Ice Core Records*, T. Hondoh (Ed.), Hokkaido University, 373–392.
- Kuskov, O., Kronrod, V., 2005. Internal structure of Europa and Callisto. *Icarus* 177 (2), 550–569.
- La Duc, M., Nicholson, W., Kern, R., Venkateswaran, K., 2003. Microbial characterization of the Mars Odyssey spacecraft and its encapsulation facility. *Environmental Microbiology* 5 (10), 977–985.
- Langhoff, S., 1996. Theoretical Infrared Spectra for Polycyclic Aromatic Hydrocarbon Neutrals, Cations, and Anions. *J. Phys. Chem* 100, 2819–2841.
- Lay, J., 2001. MALDI-TOF mass spectrometry of bacteria. *Mass Spectrometry Reviews* 20 (4), 172–194.
- Leblanc, F., Johnson, R., Brown, M., 2002. Europa's Sodium Atmosphere: An Ocean Source? *Icarus* 159 (1), 132–144.
- Levy, M., Miller, S., Brinton, K., Bada, J., 2000. Prebiotic Synthesis of Adenine and Amino Acids Under Europa-like Conditions. *Icarus* 145 (2), 609–613.
- Lipenkov, V., Istomin, V., 2001. On the stability of air clathrate-hydrate crystals in subglacial Lake Vostok, Antarctica. *Mater. Glyatsiol. Issled* 91, 1–30.
- Liu, M., Krasteva, M., Barth, A., 2005. Interactions of Phosphate Groups of ATP and Aspartyl Phosphate with the Sarcoplasmic Reticulum Ca²⁺-ATP-ase: An FTIR Study. *Biophysical Journal* 89 (6), 4352–4363.

- Lodders, K., Fegley, B., 1998. *The Planetary Scientist's Companion*. Oxford University Press US.
- Loeffler, M., Raut, U., Vidal, R., Baragiola, R., Carlson, R., 2006. Synthesis of hydrogen peroxide in water ice by ion irradiation. *Icarus* 180 (1), 265–273.
- Lowell, R., DuBose, M., 2005. Hydrothermal systems on Europa. *Geophysical research letters* 32 (5), 5202–5202.
- Lowenthal, M., Khanna, R., Moore, M., 2002. Infrared spectrum of solid isocyanic acid (HNCO): vibrational assignments and integrated band intensities. *Spectrochim. Acta A* 58, 73–78.
- Lunine, J., Stevenson, D., 1985. Thermodynamics of clathrate hydrate at low and high pressures with application to the outer solar system. *Astrophysical Journal Supplement Series* 58 (3), 493–531.
- Maquelin, K., Kirschner, C., Choo-Smith, L., van den Braak, N., Endtz, H., Naumann, D., Puppels, G., 2002. Identification of medically relevant microorganisms by vibrational spectroscopy. *Journal of Microbiological Methods* 51 (3), 255–271.
- Mather, J., Fixsen, D., Shafer, R., Mosier, C., Wilkinson, D., 1999. Calibrator Design for the COBE Far-Infrared Absolute Spectrophotometer (FIRAS). *The Astrophysical Journal* 512 (2), 511–520.
- McCollom, T., 1999. Methanogenesis as a potential source of chemical energy for primary biomass production by autotrophic organisms in hydrothermal systems on Europa. *Journal of Geophysical Research* 104 (E12), 30729–30742.
- McCollom, T., Shock, E., 1997. Geochemical constraints on chemolithoautotrophic metabolism by microorganisms in seafloor hydrothermal systems. *Geochim Cosmochim Acta* 61 (20), 4375–91.
- McCord, T., Carlson, R., Smythe, W., Hansen, G., Clark, R., Hibbitts, C., Fanale, F., Granahan, J., Segura, M., Matson, D., et al., 1997. Organics and other molecules in the surfaces of Callisto and Ganymede. *Science* 278 (5336), 271–275.

- McCord, T., Hansen, G., Fanale, F., Carlson, R., Matson, D., Johnson, T., Smythe, W., Crowley, J., Martin, P., Ocampo, A., et al., 1998a. Salts on Europa's Surface Detected by Galileo's Near Infrared Mapping Spectrometer. *Science* 280 (5367), 1242–1245.
- McCord, T., Hansen, G., Fanale, F., Hibbitts, C., Matson, D., Johnson, T., Carlson, R., Smythe, W., Martin, P., 1999. Hydrated salt minerals on Europa's surface from the Galileo near-infrared mapping spectrometer (NIMS) investigation. *Journal of Geophysical Research* 104 (E5), 11827–11852.
- McCord, T., Hansen, G., Martin, P., Hibbitts, C., 1998b. Non-water-ice constituents in the surface material of the icy Galilean satellites from the Galileo near-infrared mapping spectrometer investigation. *Journal of Geophysical Research* 103 (E4), 8603–8626.
- McGrath, M., Lellouch, E., Strobel, D., Feldman, P., Johnson, R., 2004. Satellite atmospheres. *Jupiter The Planet, Satellites and Magnetosphere*, 457–484.
- McKay, C., 2004. What Is Life-and How Do We Search for It in Other Worlds? *PLoS Biol* 2 (9), e302.
- McKay, C., Hand, K., Doran, P., Andersen, D., Priscu, J., 2003. Clathrate formation and the fate of noble and biologically useful gases in Lake Vostok, Antarctica. *Geophys. Res. Lett* 30, 1702.
- McKinnon, W., Zolensky, M., 2003. Sulfate Content of Europa's Ocean and Shell: Evolutionary Considerations and Some Geological and Astrobiological Implications. *Astrobiology* 3 (4), 879–897.
- Melosh, H., Ekholm, A., Showman, A., Lorenz, R., 2004. The temperature of Europa's subsurface water ocean. *Icarus* 168 (2), 498–502.
- Miller, S., 1961. The Occurrence of Gas Hydrates in the Solar System. *Proceedings of the National Academy of Sciences* 47 (11), 1798–1808.
- Miller, S., 1969. Clathrate Hydrates of Air in Antarctic Ice. *Science* 165 (3892), 489.

- Miller, S., 1974. The nature and occurrence of clathrate hydrates. *Natural Gases in Marine Sediments*, 151–177.
- Millero, F., 2005. *Chemical Oceanography (Marine Science Series)*, 3rd Edition. CRC Press, Inc., New York, NY.
- Miyakawa, S., Cleaves, H., Miller, S., 2002. The cold origin of life: B. Implications based on pyrimidines and purines produced from frozen ammonium cyanide solutions. *Orig. Life Evol. Biosph* 32, 209–218.
- Monnard, P., Apel, C., Kanavarioti, A., Deamer, D., 2002. Influence of ionic inorganic solutes on self-assembly and polymerization processes related to early forms of life: implications for a prebiotic aqueous medium. *Astrobiology* 2 (2), 213–219.
- Moore, J., Asphaug, E., Belton, M., Bierhaus, B., Breneman, H., Brooks, S., Chapman, C., Chuang, F., Collins, G., Giese, B., et al., 2001. Impact Features on Europa: Results of the Galileo Europa Mission (GEM). *Icarus* 151 (1), 93–111.
- Moore, J., Reid, A., Kipfstuhl, J., 1994. Microstructure and electrical properties of marine ice and its relationship to meteoric ice and sea ice. *J. Geophys. Res.*, 5171–5180.
- Moore, M., Donn, B., Khanna, R., Ahearn, M., 1983. Studies of proton-irradiated cometary-type ice mixtures. *Icarus* 54, 388–405.
- Moore, M., Ferrante, R., Hudson, R., Stone, J., 2007. Ammonia–water ice laboratory studies relevant to outer Solar System surfaces. *Icarus* 190 (1), 260–273.
- Moore, M., Hudson, R., 1998. Infrared study of ion-irradiated water-ice mixtures with hydrocarbons relevant to comets. *Icarus* 135 (2), 518–527.
- Moore, M., Hudson, R., 2000. IR detection of H₂O₂ at 80 K in ion-irradiated laboratory ices relevant to Europa. *Icarus* 145 (1), 282–288.
- Moore, M., Khanna, R., 1991. Infrared and mass spectral studies of proton irradiated H₂O+ CO₂ ice: evidence for carbonic acid. *Spectrochim. Acta* 47, 255–262.

- Moore, M., Khanna, R., Donn, B., 1991. Studies of proton irradiated H₂O+ CO₂ and H₂O + CO ices and analysis of synthesized molecules. *Journal of Geophysical Research* 96, 17.
- Moore, W., 2006. Thermal equilibrium in Europa's ice shell. *Icarus* 180 (1), 141–146.
- Mottl, M., Holland, H., 1978. Chemical exchange during hydrothermal alteration of basalt by seawater–I. Experimental results for major and minor components of seawater. *Geochimica et Cosmochimica Acta* 42 (8), 1103–1115.
- Mottl, M., Wheat, C., 1994. Hydrothermal circulation through mid-ocean ridge flanks: Fluxes of heat and magnesium. *Geochimica et Cosmochimica Acta* 58 (10), 2225–2237.
- Mozumder, A., 1999. *Fundamentals of radiation chemistry*. Academic Press, San Diego.
- Mwaura, F., 1999. A spatio-chemical survey of hydrogeothermal springs in Lake Elementaita, Kenya. *International Journal of Salt Lake Research* 8 (2), 127–138.
- Naumann, D., Schultz, C., Helm, D., 1996. What can infrared spectroscopy tell us about the structure and composition of intact bacterial cells? In: Mantsch, H., Chapman, D. (Eds.), *Infrared Spectroscopy of Biomolecules*. Wiley-Liss: New York, pp. 279–310.
- Nealson, K., 1997. The limits of life on Earth and searching for life on Mars. *J Geophys Res* 102 (E10), 23–675.
- Nimmo, F., Gaidos, E., 2002. Strike-slip motion and double ridge formation on Europa. *J. Geophys. Res* 107 (10.1029).
- Nisbet, E., Sleep, N., 2001. The habitat and nature of early life. *Nature* 409, 1083–1091.
- Noll, K., Weaver, H., 1995. The albedo spectrum of Europa from 2200 Å to 3300 Å. *Journal of Geophysical Research* 100, 19057–19059.

- NRC, 2003. *New Frontiers in the Solar System an Integrated Exploration Strategy*. National Academies Press.
- O'Brien, D., Geissler, P., Greenberg, R., 2002. A melt-through model for chaos formation on Europa. *Icarus* 156 (1), 152–161.
- Ochiai, M., Marumoto, R., Kobayashi, S., Shimazu, H., Morita, K., 1968. A Facile One-Step Synthesis of Adenine. *Tetrahedron* 24, 5731–5737.
- Ojakangas, G., Stevenson, D., 1989. Thermal state of an ice shell on Europa. *Icarus* 81 (1), 220–241.
- Oren, A., 1994. The ecology of the extremely halophilic archaea. *FEMS Microbiology Reviews* 13 (4), 415–440.
- Oren, A., 2001. The bioenergetic basis for the decrease in metabolic diversity at increasing salt concentrations: implications for the functioning of salt lake ecosystems. *Hydrobiologia* 466 (1), 61–72.
- Oren, A., 2002. Diversity of halophilic microorganisms: Environments, phylogeny, physiology, and applications. *Journal of Industrial Microbiology and Biotechnology* 28 (1), 56–63.
- Orlando, T., McCord, T., Grieves, G., 2005. The chemical nature of Europa surface material and the relation to a subsurface ocean. *Icarus* 177 (2), 528–533.
- Oró, J., 1960. Synthesis of adenine from ammonium cyanide. *Biochem. Biophys. Res. Commun* 2, 407–412.
- Palumbo, M., Strazzulla, G., Pendleton, Y., Tielens, A., 2000. R-O-C≡N Species Produced by Ion Irradiation of Ice Mixtures: Comparison with Astronomical Observations. *The Astrophysical Journal* 534 (2), 801–808.
- Pan, X., Bass, A., Jay-Gerin, J., Sanche, L., 2004. A mechanism for the production of hydrogen peroxide and the hydroperoxyl radical on icy satellites by low-energy electrons. *Icarus* 172 (2), 521–525.

- Pappalardo, R., Barr, A., 2004. The origin of domes on Europa: The role of thermally induced compositional diapirism. *Geophys. Res. Lett* 31 (10.1029).
- Pappalardo, R., Belton, M., Breneman, H., Carr, M., Chapman, C., Collins, G., Denk, T., Fagents, S., Geissler, P., Giese, B., et al., 1999. Does Europa have a subsurface ocean? Evaluation of the geological evidence. *Journal of Geophysical Research-Planets* 104 (E10).
- Pappalardo, R., Head, J., Greeley, R., Sullivan, R., Pilcher, C., Schubert, G., Moore, W., Carr, M., Moore, J., Belton, M., et al., 1998. Geological evidence for solid-state convection in Europa's ice shell. *Nature* 391 (6665), 365–368.
- Paranicas, C., Carlson, R., Johnson, R., 2001. Electron bombardment of Europa. *Geophysical Research Letters* 28 (4), 673–676.
- Parkinson, W., 1983. *Introduction to Geomagnetism*. Scottish Academic Press.
- Pethybridge, A., Taba, S., 1977. Precise conductimetric studies on aqueous solutions of 2:2 electrolytes. Interpretation of new data in terms of the current theories of Pitt and Fuoss. *Faraday Discuss. Chem. Soc* 64, 274–284.
- Petit, J., Jouzel, J., Raynaud, D., Barkov, N., Barnola, J., Basile, I., Bender, M., Chappellaz, J., Davis, M., Delaygue, G., et al., 1999. Climate and atmospheric history of the past 420,000 years from the Vostok ice core, Antarctica. *Nature* 399, 429–436.
- Petrenko, V., Whitworth, R., 1999. *Physics of Ice*. Oxford University Press, New York.
- Philipp, M., Seliger, H., 1977. Spontaneous phosphorylation of nucleosides in formamideAmmonium phosphate mixtures. *Naturwissenschaften* 64 (5), 273–273.
- Phillips, C., Chyba, C., 2001. Impact Gardening Rates on Europa: Comparison with Sputtering. 32nd Annual Lunar and Planetary Science Conference, March 12-16, 2001, Houston, Texas, Abstract No. 2111.

- Phillips, C., McEwen, A., Hoppa, G., Fagents, S., Greeley, R., Klemaszewski, J., Pappalardo, R., Klaasen, K., Breneman, H., 2000. The search for current geologic activity on Europa. *Journal of Geophysical Research* 105 (E9), 22579–22598.
- Pierazzo, E., Chyba, C., 2002. Cometary Delivery of Biogenic Elements to Europa. *Icarus* 157 (1), 120–127.
- Poisson, A., 1980. Conductivity/salinity/temperature relationship of diluted and concentrated standard seawater. *Oceanic Engineering, IEEE Journal of* 5 (1), 41–50.
- Ponnamperuma, C., Lemmon, R., Mariner, R., Calvin, M., 1963. Formation of Adenine by Electron Irradiation of Methane, Ammonia, and Water. *Proceedings of the National Academy of Sciences* 49 (5), 737–740.
- Price, A., 1962. The Theory of Magnetotelluric Methods When the Source Field Is Considered. *Journal of Geophysical Research*.
- Price, P., 1995. Kinetics of Conversion of Air Bubbles to Air-Hydrate Crystals in Antarctic Ice. *Science* 267, 1802–1804.
- Prieto-Ballesteros, O., Kargel, J., Fernández-Sampedro, M., Hogenboom, D., 2004. Evaluation of the Possible Presence of CO₂-Clathrates in Europa's Icy Shell or Seafloor. 35th Lunar and Planetary Science Conference, March 15-19, 2004, League City, Texas, Abstract No. 1748.
- Prieto-Ballesteros, O., Kargel, J., Fernandez-Sampedro, M., Selsis, F., Martinez, E., Hogenboom, D., 2005. Evaluation of the possible presence of clathrate hydrates in Europa's icy shell or seafloor. *Icarus* 177 (2), 491–505.
- Prockter, L., Pappalardo, R., 2000. Folds on Europa: Implications for Crustal Cycling and Accommodation of Extension. *Science* 289 (5481), 941–943.
- Quist, A., Marshall, W., 1968. Electrical conductances of aqueous sodium chloride solutions from 0 to 800. degree. and at pressures to 4000 bars. *The Journal of Physical Chemistry* 72 (2), 684–703.

- Reynolds, R., Squyres, S., Colburn, D., McKay, C., 1983. On the habitability of Europa. *Icarus* 56, 246–254.
- Rothschild, L., Mancinelli, R., 2001. Life in extreme environments. *Nature* 409, 1092–1101.
- Sack, N., Johnson, R., Boring, J., Baragiola, R., 1992. The effect of magnetospheric ion bombardment on the reflectance of Europa's surface. *Icarus* 100 (2), 534–540.
- Sagan, C., Khare, B., 1979. Tholins - Organic chemistry of interstellar grains and gas. *Nature* 277 (5692), 102–107.
- Sagan, C., Thompson, W., Carlson, R., Gurnett, D., Hord, C., 1993. A search for life on Earth from the Galileo spacecraft. *Nature* 365 (6448), 715–721.
- Sakai, H., Tsutsumi, M., Kishima, N., 1979. Experimental peridotite-seawater reaction at 300 C and 1000 bars. *Geol. Soc. Amer. Abstr. Prog.* 11, 509.
- Salamatina, A., Hondoh, T., Uchida, T., Lipenkov, V., 1998. Post-nucleation conversion of an air bubble to clathrate air-hydrate crystal in ice. *Journal of Crystal Growth* 193 (1), 197–218.
- Saur, J., Strobel, D., Neubauer, F., 1998. Interaction of the Jovian magnetosphere with Europa- Constraints on the neutral atmosphere. *Journal of Geophysical Research* 103 (E9), 19,947–19,962.
- Schenk, P., 2002. Thickness constraints on the icy shells of the galilean satellites from a comparison of crater shapes. *Nature* 417 (6887), 419–421.
- Schenk, P., Chapman, C., Zahnle, K., Moore, J., 2004. Ages and interiors: the cratering record of the galilean satellites. In: Bagenal, F., Dowling, T., McKinnon, W. (Eds.), *Jupiter. The planet, satellites and magnetosphere*, 1st Edition. Cambridge University Press, Ch. 15, pp. 427–456.
- Schilling, N., Khurana, K., Kivelson, M., 2004. Limits on an intrinsic dipole moment in Europa. *J. Geophys. Res* 109 (E5), 5006–5006.

- Schilling, N., Neubauer, F., 2005. Time varying interaction of Europa's atmosphere and its conducting ocean with the Jovian Magnetosphere. American Geophysical Union, Fall Meeting 2005, Abstract #SH43A-1156.
- Schutte, W., Allamandola, L., Sandford, S., 1993a. An experimental study of the organic molecules produced in cometary and interstellar ice analogs by thermal formaldehyde reactions. *Icarus* 104, 118–37.
- Schutte, W., Allamandola, L., Sandford, S., 1993b. Formaldehyde and organic molecule production in astrophysical ices at cryogenic temperatures. *Science* 259 (5098), 1143.
- Seyfried Jr, W., 1987. Experimental and theoretical constraints on hydrothermal alteration processes at mid-ocean ridges. *Ann. Rev. Earth and Planetary Science* 15, 317–35.
- Seyfried Jr, W., Mottl, M., 1982. Hydrothermal alteration of basalt by seawater under seawater-dominated conditions. *Geochimica et Cosmochimica Acta* 46 (6), 985–1002.
- Shematovich, V., Johnson, R., Cooper, J., Wong, M., 2005. Surface-bounded atmosphere of Europa. *Icarus* 173 (2), 480–498.
- Sieger, M., Simpson, W., Orlando, T., 1998. Production of O₂ on icy satellites by electronic excitation of low-temperature water ice. *Nature* 394 (6693), 554–6.
- Sill, G., Fink, U., Ferraro, J., 1980. Absorption coefficients of solid NH₃ from 50 to 7000 per cm. *Optical Society of America, Journal* 70, 724–739.
- Sloan, E., 1998. *Clathrate Hydrates of Natural Gases*. Marcel Dekker, New York.
- Smith, B., 1999. *Infrared Spectral Interpretation: A Systematic Approach*. CRC Press.
- Smythe, W., Carlson, R., Ocampo, A., Matson, D., McCord, T., NIMS, T., 1998. Galileo NIMS measurements of the absorption bands at 4.03 and 4.25 microns in

- distant observations of Europa. American Astronomical Society, DPS Meeting #30, #55. P07; *Bulletin of the American Astronomical Society*, 30, 1448.
- Socrates, G., 2001. *Infrared and Raman characteristic group frequencies*. Wiley New York.
- Sohl, F., Spohn, T., Breuer, D., Nagel, K., 2002. Implications from Galileo Observations on the Interior Structure and Chemistry of the Galilean Satellites. *Icarus* 157 (1), 104–119.
- Spencer, J., Calvin, W., 2002. Condensed O₂ on Europa and Callisto. *Astron. J* 124, 3400–3403.
- Spencer, J., Calvin, W., Person, M., 1995. Charge-coupled device spectra of the Galilean Satellites: Molecular oxygen on Ganymede. *Journal of Geophysical Research* 100 (E9), 19049–19056.
- Spencer, J., Grundy, W., Dumas, C., Carlson, R., McCord, T., Hansen, G., Terrile, R., 2006a. The nature of Europa's dark non-ice surface material: Spatially-resolved high spectral resolution spectroscopy from the Keck telescope. *Icarus* 182 (1), 202–210.
- Spencer, J., Pearl, J., Segura, M., Flasar, F., Mamoutkine, A., Romani, P., Burratti, B., Hendrix, A., Spilker, L., Lopes, R., 2006b. Cassini Encounters Enceladus: Background and the Discovery of a South Polar Hot Spot.
- Spencer, J., Tamppari, L., Martin, T., Travis, L., 1999. Temperatures on Europa from Galileo Photopolarimeter-Radiometer: Nighttime Thermal Anomalies. *Science* 284 (5419), 1514–1516.
- Spohn, T., Schubert, G., 2003. Oceans in the icy Galilean satellites of Jupiter. *Icarus* 161 (2), 456–467.
- Squyres, S., Reynolds, R., Cassen, P., Peale, S., 1983. Liquid water and active resurfacing on Europa. *Nature* 301 (5897), 225–226.

- Srivastava, S., 1965. Method of Interpretation of Magnetotelluric Data When Source Field Is Considered. *Journal of Geophysical Research* 70, 945–954.
- Srivastava, S., 1966. Theory of the magnetotelluric method for a spherical conductor. *Geophysical Journal Research Astronomical Society* 11, 373–387.
- Stacey, F., 1992. *Physics of the Earth*. Wiley New York.
- Stein, C., Stein, S., 1994. Constraints on hydrothermal heat flux through the oceanic lithosphere from global heat flow. *J. Geophys. Res* 99, 3081–3095.
- Strazzulla, G., Calcagno, L., Foti, G., 1983. Polymerization induced on interstellar grains by low-energy cosmic rays. *Royal Astronomical Society, Monthly Notices (ISSN 0035-8711)*, 204, 59P–62P.
- Strazzulla, G., Palumbo, M., 1998. Evolution of icy surfaces: an experimental approach. *Planetary and Space Science* 46 (9), 1339–1348.
- Takeya, S., Nagaya, H., Matsuyama, T., Hondoh, T., Lipenkov, V., 2000. Lattice constants and thermal expansion coefficient of air clathrate hydrate in deep ice cores from Vostok, Antarctica. *J. Phys. Chem. B* 104 (4), 668–670.
- Thomson, R., Delaney, J., 2001. Evidence for a weakly stratified European ocean sustained by seafloor heat flux. *Journal of Geophysical Research* 106 (E6), 12355–12365.
- Tiscareno, M., Geissler, P., 2003. Can redistribution of material by sputtering explain the hemispheric dichotomy of Europa? *Icarus(0019-1035)* 161 (1), 90–101.
- Turcotte, D., Schubert, G., 1982. *Geodynamics*. John Wiley & Sons, New York.
- Turcotte, D., Schubert, G., 2002. *Geodynamics*. Cambridge University Press.
- Turtle, E., Pierazzo, E., 2001. Thickness of a European Ice Shell from Impact Crater Simulations. *Science* 294, 1326–1328.

- van der Waals, J., Platteeuw, J., 1959. Clathrate solutions. *Adv. Chem. Phys* 2 (1), 1–57.
- Vidal, R., Bahr, D., Baragiola, R., Peters, M., 1997. Oxygen on Ganymede: Laboratory Studies. *Science* 276 (5320), 1839–1842.
- Waite, J., Combi, M., Ip, W., Cravens, T., McNutt, R., Kasprzak, W., Yelle, R., Luhmann, J., Niemann, H., Gell, D., et al., 2006. Cassini Ion and Neutral Mass Spectrometer: Enceladus Plume Composition and Structure.
- Walker, J., 1977. *Evolution of the Atmosphere*. New York: McMillan.
- Washburn, E., Klemenc, A., 1936. Electrical conductivity of aqueous solutions. In: *CRC Handbook of Chemistry and Physics Tables*. CRC Press, Cleveland, OH.
- Weast, R., Astle, M., 1981. *CRC Handbook of Chemistry and Physics Tables*, 61st Edition. CRC Press, Boca Raton, FL.
- Wielicki, B., Harrison, E., Cess, R., King, M., Randall, D., 1995. Mission to Planet Earth: Role of Clouds and Radiation in Climate. *Bulletin of the American Meteorological Society* 76 (11), 2125–2153.
- Wielicki, B., Wong, T., Loeb, N., Minnis, P., Priestley, K., Kandel, R., 2005. Changes in Earth's Albedo Measured by Satellite. *Science* 308 (5723), 825.
- Winter, M., 1994. *Chemical bonding*. Oxford University Press New York.
- Zahnle, K., Schenk, P., Levison, H., Dones, L., 2003. Cratering rates in the outer Solar System. *Icarus* 163 (2), 263–289.
- Zheng, W., Jewitt, D., Kaiser, R., 2006. Formation of Hydrogen, Oxygen, and Hydrogen Peroxide in Electron-irradiated Crystalline Water Ice. *The Astrophysical Journal* 639 (1), 534–548.
- Zimmer, C., Khurana, K., Kivelson, M., 2000. Subsurface oceans on Europa and Callisto: constraints from Galileo magnetometer observations. *Icarus* 147 (2), 329–347.

Zolotov, M., Shock, E., 2001. Composition and stability of salts on the surface of Europa and their oceanic origin. *J. Geophys. Res* 106, 32815–32827.

Zolotov, M., Shock, E., 2003. Energy for biologic sulfate reduction in a hydrothermally formed ocean on Europa. *J. Geophys. Res* 108 (10.1029).

Zolotov, M., Shock, E., 2004. A model for low-temperature biogeochemistry of sulfur, carbon, and iron on Europa. *J. Geophys. Res* 109, 2003JE002194.